

Modeling and Monitoring of Cardiovascular Dynamics for Patients in Critical Care

by

Tushar Anil Parlikar

B.S. Engineering, Swarthmore College (2001)

B.A. Mathematics, Swarthmore College (2001)

S.M., Massachusetts Institute of Technology (2003)

Submitted to the Department of Electrical Engineering and Computer Science
in partial fulfillment of the requirements for the degree of

Doctor of Philosophy

at the

MASSACHUSETTS INSTITUTE OF TECHNOLOGY

June 2007

© Massachusetts Institute of Technology, MMVII. All rights reserved.

Author _____
Department of Electrical Engineering and Computer Science
May 25, 2007

Certified by _____
Professor George C. Verghese
Professor of Electrical Engineering
Thesis Supervisor

Certified by _____
Dr. Thomas Heldt
Postdoctoral Associate
Thesis Supervisor

Accepted by _____
Professor Arthur C. Smith
Chairman, Department Committee on Graduate Students

Modeling and Monitoring of Cardiovascular Dynamics for Patients in Critical Care

by
Tushar Anil Parlikar

Submitted to the Department of Electrical Engineering and Computer Science
on May 25, 2007, in partial fulfillment of the
requirements for the degree of
Doctor of Philosophy

Abstract

In modern intensive care units (ICUs) a vast and varied amount of physiological data is measured and collected, with the intent of providing clinicians with detailed information about the physiological state of each patient. The data include measurements from the bedside monitors of heavily instrumented patients, imaging studies, laboratory test results, and clinical observations. The clinician's task of integrating and interpreting the data, however, is complicated by the sheer volume of information and the challenges of organizing it appropriately. This task is made even more difficult by ICU patients' frequently-changing physiological state.

Although the extensive clinical information collected in ICUs presents a challenge, it also opens up several opportunities. In particular, we believe that physiologically-based computational models and model-based estimation methods can be harnessed to better understand and track patient state. These methods would integrate a patient's hemodynamic data streams by analyzing and interpreting the available information, and presenting resultant pathophysiological hypotheses to the clinical staff in an efficient manner. In this thesis, such a possibility is developed in the context of cardiovascular dynamics.

The central results of this thesis concern averaged models of cardiovascular dynamics and a novel estimation method for continuously tracking cardiac output and total peripheral resistance. This method exploits both intra-beat and inter-beat dynamics of arterial blood pressure, and incorporates a parametrized model of arterial compliance. We validated our method with animal data from laboratory experiments and ICU patient data. The resulting root-mean-square-normalized errors – at most 15% depending on the data set – are quite low and clinically acceptable. In addition, we describe a novel estimation scheme for continuously monitoring left ventricular ejection fraction and left ventricular end-diastolic volume. We validated this method on an animal data set. Again, the resulting root-mean-square-normalized errors were quite low – at most 13%. By continuously monitoring cardiac output, total peripheral resistance, left ventricular ejection fraction, left ventricular end-diastolic volume, and arterial blood pressure, one has the basis for distinguishing between cardiogenic, hypovolemic, and septic shock.

We hope that the results in this thesis will contribute to the development of a next-generation patient monitoring system.

Thesis Supervisor: Professor George C. Verghese
Title: Professor of Electrical Engineering

Thesis Supervisor: Dr. Thomas Heldt
Title: Postdoctoral Associate

Dedication

To my mother Anjana

You will always be a source of strength and inspiration.

Acknowledgements

It is almost impossible to capture in only a few pages the contributions of the many well-wishers I've had during my tenure at MIT. I can only hope that I do justice to those who have supported me while I completed this work.

I'll begin with my senior thesis co-supervisor, **Professor George Verghese**. George is a fantastic advisor – the best anyone could have. What makes George even more special is that he is an extremely compassionate individual. I first spoke with George when I was admitted to MIT in March 2001 – he sent all the Area I admits an e-mail, and I spent many hours that night e-mailing him back and forth. Those e-mail sprees and conversations in person continued once I started my thesis work with him. George's door is always open. He's always been willing to take (or, make!) time to see me and chat about anything – from research, to MIT, to life – both its ups and downs. George has been very understanding, and I have to say – I *couldn't* have done this without him.

My junior thesis co-supervisor, *Herr* **Dr. Thomas Heldt**, has been a source of inspiration. I met Thomas a short time before his thesis defense, and he's been extremely supportive of my work, especially as I struggled through the tail end of the research. He has been invaluable to our group, both in terms of his scientific abilities, and as a mentor. He encouraged the use of animal data to validate the methods presented in this thesis, and helped us secure the permission to use this data. Thomas is a wonderful person. He is willing to take the time to help out anyone. He's become a very good friend, and was particularly supportive during the good and bad times of this past year.

Both George and Thomas were willing to get involved in my research. I will fondly recall the countless number of times George jumped to the board with an *interesting* idea and/or explanation – be it about *integration*, *stabilization*, or finding a *corollary*. Together, George and Thomas have taught me two fundamental lessons about research: first, that research is about learning and teaching, as much as it is about contributing to a certain field. Second, that the details of every idea must be worked out meticulously before rushing to publish the idea. Without working out the details, one will surely publish and perish!

My other thesis committee members – **Dr. Cohen** and **Dr. Mark** – have been equally supportive of my work. As is the case with George, **Dr. Roger Mark** has also served as a great mentor. His door, too, is always open. Roger's knowledge of physiology is legendary – the extent of this knowledge was apparent when I TA'ed 6.022j a year ago. Roger pushed me towards simpler models and human ICU data, both of which paid off. He was kind enough to provide me with a quiet, secluded office in which I've written most of this dissertation.

Dr. Richard Cohen's wit is very impressive. Richard's insights at thesis committee meetings and at his group meetings provided new research directions and kept me from wandering too far off the path. He also kept me honest on the material on calibrating our cardiac output estimates.

I will be forever indebted to **Dr. Ramakrishna Mukkamala** of Michigan State University. Rama has been supportive of the work in this thesis in many ways – providing us with almost all the animal data we analyzed, having conversations with me about my work, and helping introduce us to ejection fraction estimation – a variant of his method was used in this thesis. Without his data, this thesis would have been

quite different.

I owe much gratitude to **Dr. Robert Marini**, veterinarian “extraordinaire”. Much of the animal data came to use via experiments conducted at MIT with Dr. Bob’s help. His talent in the OR, and his unparalleled sense of humor, made some of my days at MIT unforgettable.

I couldn’t have asked for a better home than the **Laboratory for Electromagnetic and Electronic Systems**. My research group members have always been supportive of this endeavor. Many parts of this thesis would not have been written without support from the group: **Zaid**, **Carlos R**, eventually-to-be **Dr. Gireeja**, **Shirley**, **Said**, soon-to-be **Dr. Faisal**, and **Ahmad**.

Gireeja did all the initial explorations with cardiac output estimation on the porcine data set, and for that I’ll have to be forever grateful. **Said** and **Faisal** helped out with the literature search on arterial compliance and Altman-Bland plots.

Marilyn Pierce deserves more acknowledgement than I can give her in this paragraph. She attended my defense and I feel honored. She will be sorely missed in the EECS Graduate Office, and I wish her the best as she begins her retirement, and hope that her new Steinway grand piano helps with the transition.

I’ll remember several current and former LEES staff and students wherever I go. If I forget to list someone here, please don’t take it personally! A special thanks to **Wayne** and **Vivian** – two of the most hard-working staff and the kindest people, I’ve ever encountered.

Vivian in particular has been wonderful these past six years. I don’t know what LEES would do without her. She’s been like a big sister to me, and I am extremely appreciative of the support, care, and friendship.

I’d like to thank some of my extraordinary LEES lab mates (and some of the smartest people in the world!) – **Tim**, **Ivan**, **Robert**, **Babak**, **Sandip**, **Laura**, **Ale**, **Bill**, **Arvind**, and **Victor**. My S.M. advisors, **Dr. Keim**, and **Prof. Kassakian**, have always been good to me, as have the other LEES faculty, some of whom I did research with, or took classes with – **David Perreault**, **Jeff Lang**, and **Joel Schindall**.

My second home at MIT, the **Laboratory for Computational Physiology**, has also been welcoming. I would like to thank **Ken** for helping whenever necessary – including creating some of the images used in this document. **Mauro**, **Dr. Gari**, **Dr. Andrew**, **Dr. Mohammed**, **George Moody**, and **Dr. Li-wei** were always helpful with providing data and other technical support/advice. **Dewang**, **Sherman**, **Katie**, **James**, **Tin**, **Dr. Wei Zong**, and **Ali** provided entertainment and encouragement on demand.

I’d also like to thank some of the professors I interacted with during my time at MIT. I took 6.435 with **Munzer Dahleh**, and the conversations I’ve had with him since then have always encouraged me. He and I agree that I had the best advisor at MIT. My academic advisor, **Sasha Megretski**, has stuck with me (when others didn’t!) and now, after all these years, finally has an answer to his ever-so-polite question: “So, when are you getting done?”.

My friends – in- and outside of MIT – have kept me going all these years, making my life more interesting, complicated, and fun, depending on how one looks at it. I’ve listed some of you here (in no particular order).

Vasanth and **Shubham** – your kind words over numerous dinners, M.O.S. breakfasts, and drinks encour-

aged me not to give up. You guys have been there for me in more ways than I can thank you for. I'm looking forward to having your friendship as I undertake the next stage(s) of life.

Leslie and **Sophia**, your caring friendship over the years has been phenomenal. I wish you both all the best as you finish up in the next few months and move on to Berkeley. It's worth it!

Amy, you have been incredibly caring while I've been stressed-out these past few months. That caring will always be appreciated!

Robert (thanks for the circuit help!), **Brooke** (you are very thoughtful), **Bill** (thanks for reading parts of this thesis!), and **Cara** (thanks for those wonderful cookies you made for my defense!), I wish you the best as you too try to finish up at MIT. I am happy that the spirit in LEES continues to remain strong. I'll fondly remember our lunches and conversations.

Shirli, I'm glad that I TA'ed 6.022j – it was the start of some wonderful friendships – both in- and outside of lab. And, yes, the joy you bring into my life will be sorely missed next year.

Pat and **Kiyomi** – I'll be visiting you soon, and I'll give you a copy of this dissertation when I get there. A lot of the introductory parts of this thesis were written in Building 4 classrooms with Pat and Vasanth at my side. Those were fun times!

Gireeja, you've made an impact in the past year. In particular, you've strongly encouraged me to reach my full potential and feel proud of my achievements – something that I haven't always aimed for, but will try to henceforth. I wish you all the best as you start your graduate school career at Berkeley.

To the Swatties – **Nii**, **Mike**, **Emily**, **Vasya**, **Jassi**, **Alice**, **Jesse**, **Allison**, **Marc**, and **Bjorn** – here's to the good times we've shared since we graduated.

I would like to acknowledge some Professors at my alma mater, Swarthmore College. A special thanks to **Professor Orthlieb** and his wife **Vera** Orthlieb, for staying in touch all these years. Prof. O is a firm believer in my research ability and was a strong influence on my decision to go to graduate school, and to come to MIT in particular.

Thanks also to Professors **Molter** and **Cheever**. You taught me the fundamentals of Electrical Engineering, both theory and practice, and encouraged me to pursue my dreams. I am glad we have stayed in touch.

My family have been amazing, especially in the last stretches of this marathon. My mother **Anjana**, to whom this thesis is dedicated, has been an inspiration my entire life. I am the person that I am because of her hard work and sacrifice. Mamma, I'm looking forward to taking some time off this summer and spending it with you.

My brothers **Rajeev** and **Sanjeev** have been models of older brothers, available to help out or encourage at a moment's notice. I'm glad that Rajeev was able to represent the rest of the family at the defense, and am looking forward to having more time to see Sanjeev in New York.

My sister-in-law **Urmila** (and her immediate **family**, **Arvind**, **Sunanda**, **Aj**, and **Mo**) have been nothing but encouraging all these years. I'll always appreciate the family time we've shared.

My nephew **Rohan** has been a source of joy for our family these past three years. He was born a few months premature right when I started on my thesis. He's now a flourishing toddler – having grown as fast as the body of work in this dissertation. I'm looking forward to spending some time with him!

To **Amit**, and **Amar** – you've been there for me for a long time, and are just like family. It's been 10 years since we graduated from Saints, and I'm finally out of school?!

Finally, to **Gus**, **Martin**, **Lauren**, and the rest of the crew at Tosci's, and to the crew at the Miracle of Science – thanks for all the food and ice-cream. It got me going on this thesis, and helped me develop a thesis gut.

Some of the material in this thesis is based on two IEEE-copyrighted papers. The material has been reproduced with permission from the Institute of Electrical and Electronics Engineers Intellectual Property Rights Office.

Some of the figures in the background chapters of this thesis have been reproduced with permission from either the Lippincott, Williams and Wilkins Company (Levick's *Introduction to Cardiovascular Physiology*, 3rd Ed., 2000.), the Elsevier Health Sciences Division through the Mosby Monograph Series (Berne and Levy's *Cardiovascular Physiology*, 8th Ed., 2001), or the Hodder Education Company (McDonald's *Blood Flow in Arteries*, 2nd Ed., 1974).

This work was supported in part by Philips Research North America, in part by the National Institute of Biomedical Imaging and Bioengineering (NIBIB) under Grant 1 RO1 EB001659, and in part by the National Aeronautics and Space Administration (NASA) under the NASA Cooperative Agreement NCC 9-58 with the National Space Biomedical Research Institute (NSBRI).

The contents of this thesis are solely my responsibility and do not represent the official views of Philips Research North America, the NIBIB, the National Institutes of Health, the NSBRI, NASA, or anybody else.

I	Introduction and Background	27
1	Introduction and Contributions	29
1.1	The MIT Bioengineering Research Partnership	30
1.2	The MIMIC II ICU Patient Database	31
1.3	Model-based Intelligent Monitoring for the ICU	35
1.4	Specific Aims	38
1.5	Thesis Contributions	40
1.6	Intended Audience	41
1.7	Document Outline	41
2	Overview of Cardiovascular Physiology	45
2.1	Introduction to the Cardiovascular System	46
2.2	Electrical Activity of the Heart	48
2.3	The Cardiac Cycle	49
2.4	Ventricular Pressure-Volume Relationships	51
2.4.1	Ventricular Volumes, Stroke Volume, and Ejection Fraction	51
2.4.2	Ventricular Compliance	53
2.4.3	Pressure-Volume Loops/Diagrams	53
2.5	Stroke Volume and Ejection Fraction	54
2.6	Cardiac Output and Venous Return	55
2.7	Arterial Blood Pressure	57
2.8	Cardiovascular Control Loops	58
2.8.1	The Baroreflex Control Loop	59
2.8.2	The Cardiopulmonary Reflex	60
2.8.3	Neural Coupling to Heart Rate	60
2.8.4	Local Metabolic Control of Cardiac Output	60

2.8.5	The Chemoreflex Loop	61
2.8.6	The Renin–Angiotensin II–Aldosterone System	61
2.9	Medications used in the ICU	61
II Lumped-Parameter Electrical Circuit Models of Cardiovascular Dynamics		65
3 Pulsatile Models of Cardiovascular Dynamics		67
3.1	Lumped-Parameter Electrical Circuit Analogs for the Cardiovascular System	68
3.2	The Windkessel Model	69
3.3	The Modified Windkessel Model	71
3.4	Limitations of the Windkessel Model	73
3.4.1	Distributed Effects	73
3.4.2	Arterial Tree Compliance	74
3.5	The CVSIM Model	75
3.6	The CVSIMple Model	77
3.7	The Simple Pulsatile Cardiovascular Model	81
3.8	Conclusion	86
4 Averaged Models of Cardiovascular Dynamics		87
4.1	Background	88
4.2	Beat-to-Beat Averaged Models	89
4.2.1	Beat-to-Beat Averaged Windkessel Model	89
4.2.2	Beat-to-Beat Averaged Modified Windkessel Model	90
4.3	Cycle-Averaged Models	92
4.3.1	Cycle-Averaged Windkessel Model	92
4.3.2	Cycle-Averaged Modified Windkessel Model	95
4.3.3	The Simple Pulsatile Cardiovascular Model	96
4.3.4	Cycle-Average Expressions for the SPCVM	98
4.3.5	The Index-0 Cycle-Averaged Model	99
4.3.5.1	An approximation for t_D	99
4.3.5.2	Fourier analysis	101
4.3.5.3	The index-0 cycle-averaged model	104
4.3.6	Results and Discussion	106

4.4	Chapter Summary	111
III	Estimation and Monitoring of Cardiovascular Dynamics	113
5	Continuous Monitoring of Cardiac Output and Total Peripheral Resistance	115
5.1	Outline	116
5.2	The Windkessel Model Revisited	117
5.2.1	Model Description	117
5.2.2	Arterial Tree Compliance	118
5.3	Using the Beat-to-Beat Averaged Windkessel Model to Estimate Cardiac Output	119
5.3.1	Model Description	119
5.3.2	Linear Least-Squares Estimation Scheme	120
5.3.3	Calculation of Pulse Pressure	121
5.3.4	Estimation of Total Peripheral Resistance	122
5.4	Calibration Methods	123
5.4.1	Least-Squares Calibration	124
5.4.2	State-Dependent Least-Squares Calibration with Updates	125
5.4.3	Constant Calibration Factors	125
5.5	Error Criteria	126
5.6	CO Variability and Naïve CO Estimators	127
5.7	Sensitivity to Window Size and α	128
5.8	Results and Discussion with Porcine Data	128
5.8.1	Porcine Data Set	128
5.8.2	RMSNEs and Individual Porcine ECO Waveforms	129
5.8.3	CO Error Visualization and Analysis	137
5.8.4	Comparison to Mukkamala and Co-workers Method	139
5.8.5	Comparison to other CO Estimation Methods	141
5.8.6	Comparison of Mean and State-Dependent Calibration Factors	143
5.8.7	Results on the Effect of Beat-to-Beat Variability	146
5.9	Results and Discussion with Canine Data	151
5.9.1	Canine Data Set	151
5.9.2	Results	152
5.9.3	Comparison to Other CO Estimation Methods	153

Contents

5.9.4	Comparison of Mean and State-Dependent Calibration Factors	157
5.10	Results and Discussion with MIMIC I Human ICU Data	158
5.10.1	MIMIC I Data Set	158
5.10.2	Results and Comparisons to other Methods	159
5.11	Results and Discussion with MIMIC II Data	162
5.11.1	MIMIC II Data	164
5.11.2	Results and Comparisons to other CO Estimation Methods	165
5.12	Summary and Conclusions	173
6	Continuous Monitoring of Left Ventricular Ejection Fraction and End-Diastolic Volume	175
6.1	Background	175
6.2	Using Beat-to-Beat Variability to Estimate EF and LVEDV	176
6.3	Linear Least-Squares Estimation Scheme	178
6.4	Calibration Methods	179
6.5	Error Criteria	180
6.6	Naive Sample-and-Hold Estimators for EF and LVEDV	181
6.7	Canine Data Set	182
6.8	Results on EF Estimation	183
6.9	Results on LVEDV Estimation	189
6.10	Combining Estimates of CO, TPR, EF, and LVEDV	192
6.11	Conclusions and Future Work	196
IV	Conclusions, Future Work, and Appendices	197
7	Conclusions	199
7.1	Summary of Contributions	199
7.2	Summary of Thesis Document	200
7.3	Suggestions for Future Work	201
A	Nomenclature	203
A.1	Chapter 1	203
A.2	Chapter 2	205

A.3 Chapter 3	207
A.4 Chapter 4	209
A.5 Chapter 5	211
A.6 Chapter 6	213
A.7 Chapter 7	215
B CVSIM Equations and Parameters	217
C Circuit Analysis for the SPCVM	219
D Ancillaries for the Index-0 Cycle-Averaged Model	221
D.1 Expressions used in the Index-0 Model	221
D.2 Charge Conservation in the Simple Pulsatile Cardiovascular Model	223
D.3 Higher-Order Approximations for the Cycle-Averages	223
E MATLAB implementation for the SPCVM	225
F MATLAB implementation for the index-0 CAM	227
Bibliography	231

List of Figures

1.1	The data explosion or <i>information overload</i> in modern intensive care units. Clinicians must make informed decisions based on the interpretation of the data.	30
1.2	Data trends for a MIMIC II ICU patient. The data streams from top to bottom are HR; SAP, MAP, and DAP; DPAP; CVP; filtered CVP.	32
1.3	A shorter window of ABP waveform data for a MIMIC II patient. A variety of transients in mean ABP (white dashed line) can be observed, even in this short period of time.	34
1.4	A schematic showing the MIMICU group’s approach. The tasks range from cardiovascular modeling to robust model identification and alarm/hypothesis generation.	36
1.5	An example of a model hierarchy where the models share their parameters, states, and outputs.	37
1.6	A hierarchy of cardiovascular models – both probabilistic and deterministic – for use in the ICU setting.	38
1.7	Block diagram showing how one could use measurements of CO, EF, LVEDV and HR to distinguish between septic, cardiogenic, and hypovolemic shock.	39
2.1	A schematic of the human cardiovascular system showing the heart and the blood vessels. Veins, with unidirectional valves, appear on the left of the figure, while arteries, with no valves, appear on the right. The majority of the resistance to blood flow is concentrated in the arterioles (dark ovals before the capillaries). This figure was adapted with permission from Elsevier Health Sciences Division.	47
2.2	Schematic of the electrical conduction system of the heart. Normally, impulses originate from the SA node, and spread through the atria and AV node to the ventricles. This figure was adapted with permission from Elsevier Health Sciences Division.	48
2.3	Wiggers diagram depicting the cardiac cycle in the left ventricle showing the various stages of diastole and systole. This figure was adapted with permission from Elsevier Health Sciences Division.	50
2.4	The human cardiac cycle showing how changes in ventricular contractile state relate to ventricular volume. This figure was adapted with permission from the Lippincott, Williams, and Wilkins Company.	52
2.5	Typical ventricular systolic and diastolic elastance curves. This figure was adapted with permission from Elsevier Health Sciences Division.	53
2.6	Human left ventricular pressure-volume loops showing how pressure and volume in the ventricle change during the cardiac cycle. This figure was adapted with permission from the Lippincott, Williams, and Wilkins Company.	54
2.7	Cardiac output curves showing the effect of right heart failure on the Frank-Starling relationship.	56

List of Figures

2.8	Cardiac output and venous return determination posed as a load-line problem.	57
2.9	Cardiac output and venous return curves for a variety of conditions. The intersection of the cardiac output curve and venous return curve determines cardiac output.	57
2.10	ABP waveform from a MIMIC II patient. The systolic and diastolic pressures for one ABP wavelet are shown in the figure. Mean ABP is proportional to the area under this wavelet. This figure was adapted with permission from Elsevier Health Sciences Division.	58
2.11	Block diagram of the cardiovascular control system, including both the baroreflex and the cardiopulmonary reflex mechanisms, but neglecting the direct neural coupling between heart rate and respiration. The baroreceptors sense arterial blood pressure in the aortic arch and carotid sinus, while the cardiopulmonary receptors sense right atrial transmural pressure.	59
3.1	(a) A ventricular compartment showing a time-varying compliance, $C(t)$, two heart valves D_i and D_o , valvular resistances R_i and R_o , and an intrathoracic pressure source, V_{th} ; (b) A systemic circulation compartment with fixed compliance, C_s , and inflow and outflow resistances R_{in} and R_{out} , respectively.	69
3.2	Circuit representation for the Windkessel model with a representative pulsatile ABP waveform.	70
3.3	The modified Windkessel model in which the arterial tree is divided into a distal and a proximal compartment.	71
3.4	Proximal (top) and distal (bottom) ABP waveforms for a simulation of the modified Windkessel model with $V_{a,d}(0) = 0$ mmHg, $V_{a,p}(0) = 0$ mmHg, $SV_n = 100$ ml, $T=T_n=1$ s, $R_a = 1$ mmHg/(ml/s), $L_a = 0.025$ mmHg/ml/s, $C_{a,p} = 1.45$ ml/mmHg, and $C_{a,d} = 0.15$ ml/mmHg.	72
3.5	A schematic of a canine arterial tree showing the distributed nature of the arterial tree. This figure was adapted with permission from Hodder Education.	73
3.6	Thoracic aorta compliance-pressure curves for various age groups. Each curve is an average for a particular age group.	75
3.7	Cardiovascular model comprised of two heart compartments (the left and right ventricle) and four systemic circulation compartments for the lungs, arterial system, and venous system.	76
3.8	The CVSIMple model. This cardiovascular model has only one ventricular compartment and is represented by three nonlinear time-varying differential equations and seven model parameters.	78
3.9	Compliance and piecewise linear elastance functions for the CVSIMple model for $T = 1$ s.	78
3.10	Comparison of two elastance functions (piecewise linear and sinusoidal) in the CVSIMple for $T=1$ s. This simulation was performed in MATLAB R14 (The Mathworks Inc., Natick, MA).	80
3.11	Waveforms generated during a single cycle of the CVSIMple for $T=1$ s. This circuit has seven regions of operation (four of which are labeled in the figure).	82
3.12	The simple pulsatile cardiovascular model (SPCVM) uses a 3-way switch which allows for simpler analysis of the circuit.	82
3.13	Switching functions for the 3-way switch and diode in the pulsatile model for $T=1$ s. The diode turn-on time t_D is marked on the bottom panel.	83

3.14	Waveforms generated over a single cycle of the pulsatile model for $T=1$ s. This circuit has four regions of operation. Each region is uniquely defined by the switch position, the state of the time-varying compliance $C_h(t)$, and the diode state.	84
3.15	Comparison of the SPCVM to the CVSIMple and CVSIM models for $T=1$ s. These models were simulated in HSPICE circuit simulation software.	85
4.1	Response of the SPCVM to a step change in total peripheral resistance at time $t=5$ s. Both the pulsatile and continuous-time averaged ABP and LVP waveforms are shown.	88
4.2	Analysis of the modified Windkessel circuit model, showing the supernode that includes $V_{a,p}$, L_a , and $V_{a,d}$	91
4.3	Windkessel (top) and cycle-averaged Windkessel (bottom) model circuit representations with representative pulsatile and cycle-averaged ABP waveforms.	94
4.4	Comparison of the outputs of the pulsatile, beat-to-beat averaged, and cycle-averaged Windkessel models. The output of the beat-to-beat averaged model is a sampled version of the output of the cycle-averaged model.	95
4.5	Modified Windkessel (top left) and cycle-averaged modified Windkessel (bottom left) model circuit representations with representative pulsatile and cycle-averaged proximal (top right) and distal (bottom right) ABP waveforms.	96
4.6	The simple pulsatile cardiovascular model (SPCVM) uses a 3-way switch which allows for simpler analysis of the circuit. V_i and V_o are defined here for future reference. For simplicity, only one diode is used to facilitate development of the averaged model.	97
4.7	Circuit representation for the SPCVM in region I.	100
4.8	The left and right hand side of the approximation of the equation defining \hat{t}_D . The left-most intersection of V_h and V_a defines t_D , while the intersection of the LHS and RHS of (4.43) define \hat{t}_D	101
4.9	First- and second-order Fourier-series approximations for the steady-state SPCVM waveforms using the parameters in Table 3.1. Solid lines: actual waveforms; dash-dotted lines: Fourier series approximations thereof.	102
4.10	Index-0 cycle-averaged model with two-voltage dependent voltage sources and two current-dependent voltage sources.	105
4.11	Comparison of the transient responses of the index-0 cycle-averaged model to the calculated cycle-averaged SPCVM waveforms for several step changes in resistance R_a . At $t=15$ s, R_a was stepped up to 1.4 PRU, at $t=30$ s, R_a was stepped down to 1 PRU, and at $t=45$ s, R_a was stepped down to 0.6 PRU.	107
4.12	Comparison of the transient responses of the index-0 cycle-averaged model to the calculated cycle-averaged SPCVM waveforms for several step changes in T . At $t=15$ s, T was stepped down to 0.5 s. At $t=30$ s, T was stepped back up to its nominal value of 1 s, and at $t=45$ s, T was stepped up to 1.2 s.	109
4.13	Envelope of the ABP waveform from the cycle-averaged model (top) compared to that of the SPCVM (bottom) for several step changes in peripheral resistance R_a . At $t=15$ s, R_a was stepped up to 1.4 PRU, at $t=30$ s, R_a was stepped down to 1 PRU, and at $t=45$ s, R_a was stepped down to 0.6 PRU.	110

List of Figures

5.1	Circuit representation for the Windkessel model.	117
5.2	Porcine radial arterial blood pressure waveform showing quantities that are used, on a beat-to-beat basis, to estimate the time constant τ_n . Mean arterial blood pressure in beat n is the area under the pressure waveform in the n^{th} cardiac beat.	120
5.3	True and estimated CO (using rABP), HR, mean rABP, true and estimated TPR, and IV drugs for swine 4 with window size = 360 beats and a 100-beat state-dependent calibration.	131
5.4	True and estimated CO (using cABP), HR, mean cABP, true and estimated TPR, and IV drugs for swine 5 with window size = 360 beats and a 100-beat state-dependent calibration.	132
5.5	True and estimated CO (using fABP), HR, mean fABP, true and estimated TPR, and IV drugs for swine 6 with window size = 360 beats and a 100-beat state-dependent calibration.	133
5.6	True and estimated CO (using rABP), HR, mean fABP, true and estimated TPR, and IV drugs for swine 7 with window size = 360 beats and a 100-beat state-dependent calibration.	134
5.7	True and estimated CO (using cABP), HR, mean fABP, true and estimated TPR, and IV drugs for swine 8 with window size = 360 beats and a 100-beat state-dependent calibration.	135
5.8	True and estimated CO (using fABP), HR, mean fABP, true and estimated TPR, and IV drugs for swine 9 with window size = 360 beats and a 100-beat state-dependent calibration.	136
5.9	True and estimated CO (using rABP), HR, mean rABP, estimated and true TPR, and IV drugs for swine 4 with window size = 360 beats, and a 10-beats of every 1000-beat window exponentially-weighted overlapping repeated state-dependent calibration.	138
5.10	Linear regression of TCO versus ECO (using rABP) over all six swine with window size = 360 beats, and a 100-beat state-dependent calibration.	139
5.11	Bland-Altman plot of CO estimation error versus the mean of TCO and ECO (using rABP) over all six swine with window size = 360 beats, and a 100-beat state-dependent calibration. The horizontal lines in the plot are the mean error, and the 1-SD and 2-SD lines.	140
5.12	True CO, 3-minute estimated CO (using rABP), and a sample-and-hold (S/H) version of the 3-minute estimated CO, HR, and mean rABP. 3-minute ECO was calculated with window size = 6 minutes, and a state-dependent calibration using all available 3-minute samples of TCO.	142
5.13	True and estimated CO (using cABP), HR, mean cABP, calibration factor C_a , and its components γ_1 and $\gamma_2\overline{V}_a$, and IV drugs for pig 4 with window size = 360 beats, and a 100-point state-dependent calibration.	147
5.14	True and estimated CO (using cABP), HR, mean cABP, calibration factor C_a , and its components γ_1 and $\gamma_2\overline{V}_a$, and IV drugs for pig 8 with window size = 360 beats, and a 100-point state-dependent calibration.	148
5.15	Plots of $\frac{\text{TCO}}{\text{ECO}}$ and our fit for the calibration factor C_a versus mean pressure \overline{V}_a for all six swine. The results were obtained using a window size = 360 beats and a 100-point state-dependent calibration.	149
5.16	True (intermittent echocardiography and flow probe measurements) and estimated CO (using cABP), HR, mean cABP, true and estimated TPR, and IV drugs for dog 1 with window size = 100 beats and a state-dependent calibration using all available echocardiography TCO measurements.	154

5.17 True (intermittent echocardiography measurements) and estimated CO (using cABP), HR, mean cABP, true and estimated TPR, and IV drugs for dog 2 with window size = 100 beats and a state-dependent calibration using all available echocardiography TCO measurements.	155
5.18 Bland-Altman plot of CO estimation error versus the mean of TCO and ECO (using cABP) over the three dogs with window size = 100 beats and a state-dependent calibration using all available echocardiography TCO measurements. The horizontal lines in the plot are the mean error, and the 1-SD and 2-SD lines.	156
5.19 True and estimated CO, mean rABP, HR, and true and estimated TPR for patient 411 with window size = 360 beats and a state-dependent calibration using all available thermodilution TCO measurements.	160
5.20 True and estimated CO, mean rABP, HR, and true and estimated TPR for patient 451 with window size = 360 beats and a state-dependent calibration using all available thermodilution TCO measurements.	161
5.21 Bland-Altman plot of our method's CO estimation error versus the mean of TCO and ECO over the set of MIMIC I patients with window size = 360 beats and a state-dependent calibration using all available thermodilution TCO measurements. The horizontal lines in the plot are the mean error, and the 1-SD and 2-SD lines.	163
5.22 Bland-Altman plot of the SHNECO estimation error versus the mean of TCO and ECO over the set of MIMIC I patients. No calibration was necessary for this estimate. The horizontal lines in the plot are the mean error, and the 1-SD and 2-SD lines.	164
5.23 True and estimated CO, mean rABP, HR, true and estimated TPR, and IV levophed infusion for patient b75092 with window size = 360 beats and a state-dependent calibration using the two available thermodilution TCO measurements. Data during the early parts of the patient's ICU stay are not plotted here.	167
5.24 True and estimated CO, mean rABP, HR, true and estimated TPR, and IV levophed infusion for patient b75092 with window size = 360 beats and a state-dependent calibration using the two available thermodilution TCO measurements. Only the patient data during the IV levophed infusion have been plotted.	168
5.25 True and estimated CO, mean rABP, HR, true and estimated TPR, and IV neosynephrine infusion for patient b63047 with window size = 360 beats and a state-dependent calibration using the two available thermodilution TCO measurements.	169
5.26 True and estimated CO, mean rABP, HR, true and estimated TPR, and IV neosynephrine infusion for patient b63047 with window size = 360 beats and a state-dependent calibration using the two available thermodilution TCO measurements.	170
5.27 Bland-Altman plots of CO estimation error versus the mean of TCO and ECO over the set of MIMIC II patients. The horizontal lines in the plots are the mean error, and the 1-SD and 2-SD lines.	171
6.1 Left ventricular pressure-volume loop showing the straight lines defining the end-diastolic, before-ejection, peak-systolic, and end-systolic compliances, as well as SAP, DAP, and the preload and afterload pressures. Note that the pressures in this graphic are measured with respect to intrathoracic pressure.	177

List of Figures

6.2	True and estimated CO (using cABP), HR, mean cABP, true and estimated EF (using cABP), and IV drugs for dog 2 with window size = 50 beats (using 2 points in each window), and a mean calibration. In the estimation, $Q_d=5\text{ml}$	185
6.3	Bland-Altman plot of EF estimation error (using cABP and mean calibration) versus the mean of true and estimated EF (using cABP) over the three dogs. The horizontal lines in the plot are the mean error, and the 1-SD and 2-SD lines.	186
6.4	True and estimated CO (using cABP), HR, mean cABP, true and estimated EF (using cABP), and IV drugs for dog 1 with window size = 50 beats (using 2 points in each window), and a single-point calibration.	187
6.5	Bland-Altman plot of EF estimation error (using cABP and single-point calibration) versus the mean of true and estimated EF (using cABP) over the three dogs. The horizontal lines in the plot are the mean error, and the 1-SD and 2-SD lines.	188
6.6	True and estimated CO (using cABP), HR, mean cABP, true and estimated LVEDV (using cABP), and IV drugs for dog 2 with a mean calibration.	190
6.7	True and estimated CO (using cABP), HR, mean cABP, true and estimated LVEDV (using cABP), and IV drugs for dog 3 with a mean calibration.	191
6.8	Bland-Altman plot of LVEDV estimation error (using cABP and mean calibration) versus the mean of true and estimated LVEDV (using cABP) over the three dogs. The horizontal lines in the plot are the mean error, and the 1-SD and 2-SD lines.	192
6.9	True and estimated CO, HR, mean cABP, true and estimated TPR, true and estimated EF, true and estimated LVEDV, and IV infusions for dog 1. The cABP waveform was used for each estimate.	193
6.10	True and estimated CO, HR, mean cABP, true and estimated TPR, true and estimated EF, true and estimated LVEDV, and IV infusions for dog 2. The cABP waveform was used for each estimate.	194
6.11	True and estimated CO, HR, mean cABP, true and estimated TPR, true and estimated EF, true and estimated LVEDV, and IV infusions for dog 3. The cABP waveform was used for each estimate.	195
C.1	SPCVM circuits for the different regions of operation: the top circuit is for regions I and III, the middle circuit is for region II, and the bottom circuit is for region IV.	220

List of Tables

3.1	Summary of parameters for the SPCVM and the CVSIMple models.	81
3.2	The seven regions of the CVSIMple model. Each region is uniquely determined by the diode states and the slope of the piecewise linear elastance function.	81
3.3	Definition of the four regions in the SPCVM.	83
4.1	Values of cycle-averages in steady-state.	102
4.2	Steady-state error for the values of R_a from Fig. 4.11.	106
4.3	Time constants in steady-state for the transient responses for the values of R_a from Fig. 4.11.	108
4.4	Computational savings obtained using the index-0 cycle-averaged model.	109
5.1	Population statistics for the porcine data set. The data was obtained from Professor Ramakrishna Mukkamala at Michigan State University.	129
5.2	RMSNEs for a 360 beat window size and a 100-beat state-dependent calibration.	130
5.3	Correlation coefficients for linear regressions of ECO versus TCO. The results are for a 360 beat window size and a 100-beat state-dependent calibration.	137
5.4	Correlation coefficients for linear regressions of estimation error (TCO-ECO) versus \bar{V}_a , HR, and TCO. The results are for a 360 beat window size and a 100-beat state-dependent calibration.	137
5.5	RMSNEs reported in Mukkamala and co-workers' paper with aggregate RMSNEs calculated based on our weighted-mean RMSNE equation.	140
5.6	RMSNEs for the porcine data set (using the rABP waveform) comparing our 3-minute ECO to Mukkamala and co-workers CO estimate, as well as our sample-and-hold ECO. Errors for the first three estimates were compared to 3-minute samples of TCO, while that for the sample-and-hold estimate was compared to the entire TCO waveform.	141
5.7	Mean RMSNEs for various static CO estimates, as well as Mukkamala's method. Each estimate was calibrated using a mean calibration. Note that Mukkamala's results are based on intermittent CO estimates i.e., every 3 minutes, while the others are continuous CO estimates.	143
5.8	Aggregate RMSNEs for the porcine data set (using the rABP waveform) with either mean calibration using all available TCO points or state-dependent calibration using 100 TCO points evenly-spaced throughout each record. Results obtained with the fABP waveform follow the trends in this table.	144

List of Tables

5.9	Aggregate RMSNEs for the porcine data set (using the rABP waveform) with either mean or state-dependent calibrations using 10 points out of the first half of the available TCO points to calibrate, and the second half of the records to test the predictive value of the calibration factor. Results obtained with the fABP waveform follow the trends in this table.	144
5.10	Aggregate RMSNEs for the porcine data set (using the rABP waveform) with either mean or state-dependent calibrations using 10 points out of the central half of the available TCO points to calibrate, and the outer fourths of the records to test the predictive value of the calibration factor. Results obtained with the fABP waveform follow the trends in this table.	145
5.11	Aggregate RMSNEs for the porcine data set (using the rABP waveform) with either mean or state-dependent calibrations using 10 points out of the second half of the available TCO points to calibrate, and the first half of the records to test the predictive value of the calibration factor. Results obtained with the fABP waveform follow the trends in this table.	145
5.12	RMSNEs for the rABP waveform-based estimate taken over points at which the beat-to-beat variability index was larger than 5%. 100-point state-dependent calibrations were used for our estimate and for the Herd estimate.	150
5.13	RMSNEs for the rABP waveform-based estimate taken over points at which the beat-to-beat variability index was larger than 5%. Mean calibrations were used for our estimate and for the Herd estimate.	150
5.14	Population statistics for the canine data set. The data was obtained from Professor Ramakrishna Mukkamala at Michigan State University.	152
5.15	Aggregate RMSNEs for the dog data set with a 100 beat window size and a state-dependent calibration using all available echocardiography TCO points in each record. The parenthetical numbers in the first row are those obtained from comparisons to TCO from the aortic flow probe using a 10 point state-dependent calibration.	153
5.16	Aggregate RMSNEs for the canine data set with either mean or state-dependent calibrations using all available echocardiography TCO points.	156
5.17	Aggregate RMSNEs for the canine data set with either mean or state-dependent calibrations using the first half of the available echocardiography TCO points to calibrate, and the second half to test the predictive value of the calibrated CO estimate.	157
5.18	Aggregate RMSNEs for the canine data set with either mean or state-dependent calibrations using the second half of the available echocardiography TCO points to calibrate, and the first half to test the predictive value of the calibrated CO estimate.	157
5.19	Population statistics and clinical class (if available) for our set of MIMIC I patients; NA=not available. The data was obtained from http://www.physionet.org .	159
5.20	Aggregate RMSNEs for the MIMIC I data set comparing our method to the SHNECO, and to Mukkamala’s method, for which the mean RMSNE for their selection of 15 patients was 15.3%. We calibrated our estimates with a state-dependent calibration using all available thermodilution TCO measurements.	162
5.21	Population statistics for the MIMIC II patients.	165

5.22	Aggregate RMSNEs for the MIMIC II ICU patient data set comparing our method to the best-performing of the other methods. We calibrated each estimate with a state-dependent calibration using all available thermodilution TCO measurements. The SHNECO estimator does not need calibration.	166
6.1	Population statistics for the canine data set. The data was obtained from Professor Ramakrishna Mukkamala at Michigan State University.	182
6.2	RMSNEs for our mean-calibrated EF estimate using cABP, fABP, or carABP, with window size = 50 beats (using 2 points in each window) and $Q_d=5\text{ml}$	184
6.3	RMSNEs for our single-point calibrated EF estimate, with window size = 50 beats and $Q_d=5\text{ml}$. In each record, the second reference EF measurement was used for calibration.	184
6.4	RMSNEs for Mukkamala's EF estimate using cABP and $Q_d=5\text{ml}$	188
6.5	RMSNEs for our mean-calibrated LVEDV estimate, for which EF was calculated with window size = 50 beats and $Q_d=5\text{ml}$	189
B.1	Nominal parameters of the CVSIM model.	218

Part I

Introduction and Background

Introduction and Contributions

WITH recent improvements in both computer and medical devices technology, modern critical care units or intensive care units (ICUs) measure and collect a vast and varied amount of data, with the intent of providing clinicians with detailed information about the pathophysiological state of each patient. The data include measurements from the bedside monitors of heavily instrumented patients, imaging studies, laboratory test results, medication records, fluid balance records, and other clinical observations.

Because the data come from several diverse sources, e.g., digital data from bedside monitors, paper copies of images and laboratory tests, and data entered at the nurses station, and are thus not well-organized, an *information overload* results, as illustrated in Fig. 1.1, making the clinician's task of integrating and interpreting the data very time-consuming. Quite often, this may lead to human errors in clinical decision-making as it is difficult to recognize the non-stationary complex relationships among the diverse data. Clinicians often miss significant physiological trends and early warning signs for diseases. For instance, a recent study by Donchin *et al.* [1] showed that at least one error in patient care occurs per patient day in the ICU.

While patient monitoring systems have come a long way, state-of-the-art bedside patient monitoring systems do not integrate the information from individual data streams to provide clinicians with reasonable hypotheses and/or alarms, nor do they correlate information from different data streams. Current ICU patient monitor alarms, for example, are highly sensitive, with an approximately 80% false positive rate [2]. The clinician's task of data integration and interpretation is further complicated by the frequently-changing physiological state of patients in critical care, and the lack of time for clinician-patient interaction. For instance, while current patient monitoring systems can be used to track the dynamics of a single variable (e.g., mean arterial blood pressure) over time, monitoring the trajectories of several frequently-changing variables or variables derived from them usually requires more time than a clinician can devote to a single ICU patient. In the current ICU environment, important clinical information can be easily overlooked as it is very difficult for humans to keep track of and make routine sense of multiple data time series [3].

In the near future, the clinician's task will only become more difficult. The amount of data collected in the ICU has been growing rapidly in recent years [4, 5], and thus the information overload is expected to increase dramatically. In addition, there is a projected shortage in nursing staff expected in the next 10 years [6]. These projections, when combined with a U.S. population that has a growing percentage of elderly citizens with accompanying growing health care costs, make the need to address the information

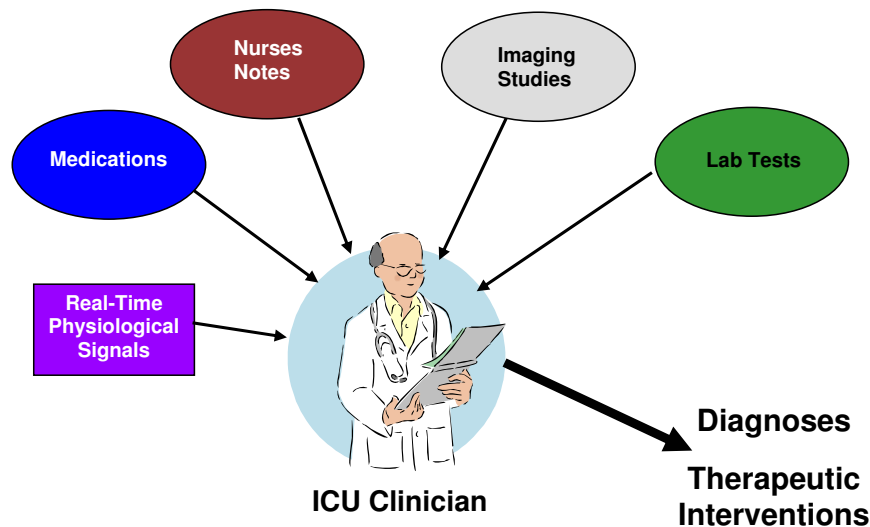


Figure 1.1: The data explosion or *information overload* in modern intensive care units. Clinicians must make informed decisions based on the interpretation of the data.

overload problem quite urgent.

Fortunately, the vast amount of clinical information, ranging from nurses' notes and blood chemistry tests to arterial blood pressure (ABP) and electrocardiogram (ECG) waveforms, allow for the development of a next-generation patient monitoring system. Ideally, such a monitoring system would assimilate and interpret the available data to provide clinicians with a list of differential diagnoses and timely and highly-specific alarms related to a patient's pathophysiological state.

1.1 The MIT Bioengineering Research Partnership

The goal of the National Institutes of Health-funded Bioengineering Research Partnership (BRP) project on *Integrating Data, Models, and Reasoning in Critical Care* at the Massachusetts Institute of Technology (MIT) is to develop the patient monitoring system of the 21st century. We envision a modern ICU having a patient monitoring system that provides clinicians in the ICU with a real-time comprehensive assessment of patient pathophysiological state. Ideally, this system would facilitate the clinician's task of reasoning by issuing patient-specific pathophysiological hypotheses and alarms, thereby allowing for more rapid diagnoses and treatments, i.e., we anticipate that such a system would identify the complex relationships among data elements and patterns, and suggest feasible differential diagnoses to make sense of the data.

This project is a large collaborative effort between researchers in three MIT laboratories (Computer Science and Artificial Intelligence Laboratory, Laboratory for Computational Physiology, Laboratory for Electromagnetic and Electronic Systems), a hospital in Boston (Beth-Israel Deaconess Medical Center), and a manufacturer of ICU patient monitoring systems (Philips Medical Systems, Inc.).

1.2 The MIMIC II ICU Patient Database

One of the specific aims of the MIT BRP project is to create an annotated database of ICU patients. The development of this Multi-parameter Intelligent Monitoring for the Intensive Care II (MIMIC II) database is underway, headed by researchers in the Laboratory for Computational Physiology (LCP) [7], and assisted by their colleagues in the Computer Science and Artificial Intelligence Laboratory (CSAIL). The LCP group is focused mainly on database development, while the group in CSAIL is heavily involved in the de-identification of patient data, i.e., the removal of protected health information (PHI) from the patient records, a task that must be completed before the database can be made public. Both groups are also involved in research projects that use the MIMIC II database to develop novel tools for an advanced patient monitoring system.

The MIMIC II database will serve two purposes. First, a publicly available annotated ICU patient database does not currently exist. Thus, once made public, this database will serve as a resource for medical researchers worldwide. Second, the annotated database will be used in the development and evaluation of a next-generation patient monitoring system.

The MIMIC II database will contain thousands of de-identified patient records from several ICUs [7]. Some of these records will be annotated. To annotate a patient record, a clinician is asked to mark critical events during the patient's stay and evaluate the patient's pathophysiological state, based on all of the available data. These events are then confirmed by other clinicians. The result of the annotation process is a *gold-standard* patient record that can be used to evaluate ICU patient monitoring techniques/systems. By gold-standard patient record, we mean a patient record in which the available measurements and interventions have been analyzed and interpreted accurately.

The annotation process is quite time-intensive and it is therefore a daunting task to complete the annotations for even a hundred patient records. For this thesis research, we could not rely on annotated patient data to verify our estimation methods because relatively few patient records have so far been annotated.

The types of data that are currently collected from the various hospital critical care units include:

- High-resolution *waveform data* recorded with 8-bit resolution at 125 samples/sec. At the moment, up to four waveforms can be simultaneously recorded. These recordings could include one or two surface electrocardiogram (ECG) traces, arterial blood pressure (ABP) waveforms, central venous pressure (CVP) waveforms, and pulmonary artery pressure (PAP) waveforms. Waveform data tend to be quite noisy and heavily prone to artifacts caused by patient movement and other sources.
- Less frequently obtained *data trends*. We may obtain up to 30 averaged physiological measurements that are usually derived from the waveform data streams and recorded at a rate of 1 sample/min. Examples include heart rate (HR), mean, systolic, and diastolic arterial blood pressure (MAP, SAP,

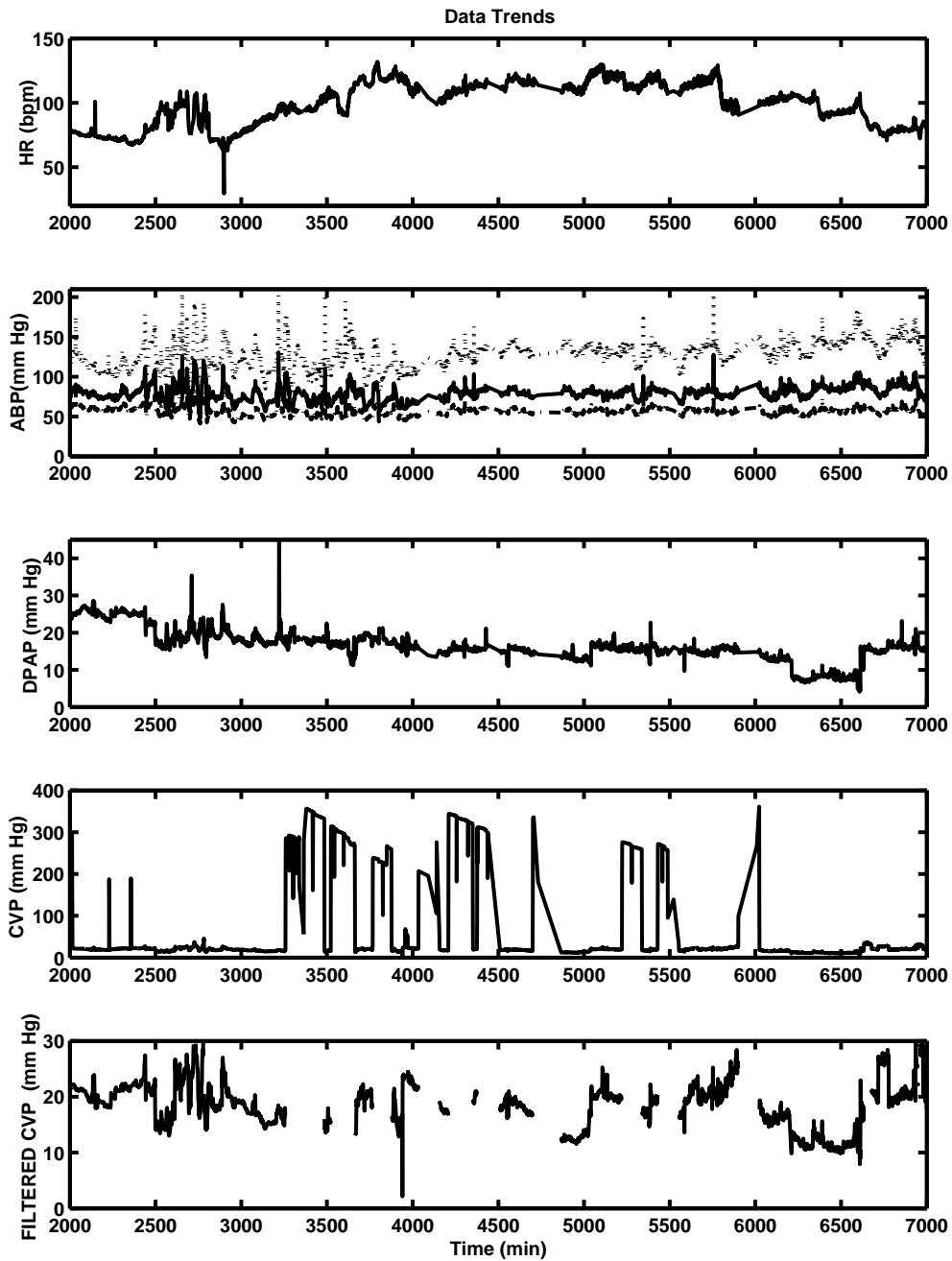


Figure 1.2: Data trends for a MIMIC II ICU patient. The data streams from top to bottom are HR; SAP, MAP, and DAP; DPAP; CVP; filtered CVP.

DAP, respectively), and diastolic pulmonary artery pressure (DPAP)¹.

- Other *intermittent data*, which may be recorded only as often as once a day. Examples include results from blood chemistry tests, results from imaging studies, provider-order-entry (POE) medications ordered, changes in medication infusion rates, changes in fluids administered, urine output, nurses notes, nurse-verified ABP and HR recordings, and hospital discharge summaries. Some of the intermittent data is machine-generated, e.g., changes in medication infusion rates, but most is human-entered data, e.g., nurses’ notes. For the human-entered data, the time stamping is not always accurate as human data recorders are not always meticulous about entering their observations in a timely manner.

There are two issues to point out related to this database. First, although the current size of the database stands at approximately 17000 patients, of which approximately 2500 have waveform data, the database is quite sparse in terms of gold-standard (accurately measured and recorded) trend data, i.e., there is little, if any, data in the MIMIC II database that could potentially be used to validate some of the estimation methods we propose below. For example, while evaluating our CO estimation method, we discovered in a set of 1510 MIMIC II patient records that had waveform data, all have at least one ECG lead recorded, while only 58% have at least one ECG recording *and* an ABP recording, and only 8% have one ECG recording *and* an ABP recording *and* one or more cardiac output (CO) recordings. Second, there is a lack of noise-free waveform data, making it critical that we filter and/or use a signal quality assessment algorithm to pre-process any data we intend to use with our model-based estimation methods.

Figure 1.2 shows typical ICU data trends (at 1 sample/minute) from the MIMIC II database. This patient is a 74-year old female admitted to the ICU with critical aortic stenosis and congestive heart failure (CHF). She stayed in the ICU for seven days and in the hospital for a total of twenty-six days. However, we only have four days worth of waveform data. During her hospital stay, she underwent surgery to replace her aortic valve. From top to bottom, the data streams available are HR, SAP, MAP, DAP, DPAP, CVP, and filtered CVP (i.e., the trend at the bottom of the figure is the CVP waveform where many of the artifacts have been removed²).

From Fig. 1.2, we can observe many transients in the data trends. Most of these transients occur at timescales of minutes to hours. There are also some problems with these data streams. At times, there are artifacts in the data caused by patient movements or by equipment malfunctions. For example, large parts of the CVP waveform are at values greater than 200 mm Hg – values that are physiologically impossible. In addition, there may be data streams that are not recorded at certain times because the measurement sensors are disconnected. For example, the catheter that measures ABP is quite often disconnected, perhaps to remove blood clots (catheter “flushing”).

Figure 1.3 is a shorter timescale view of the same patient’s ABP waveform data, at a sampling rate of 125

¹For blood pressure waveforms, the minimum value over one cardiac cycle is referred to as the diastolic blood pressure, whereas the maximum is termed the systolic blood pressure.

²Central venous pressure is usually less than 30 mm Hg, so all CVP values above this threshold were removed.

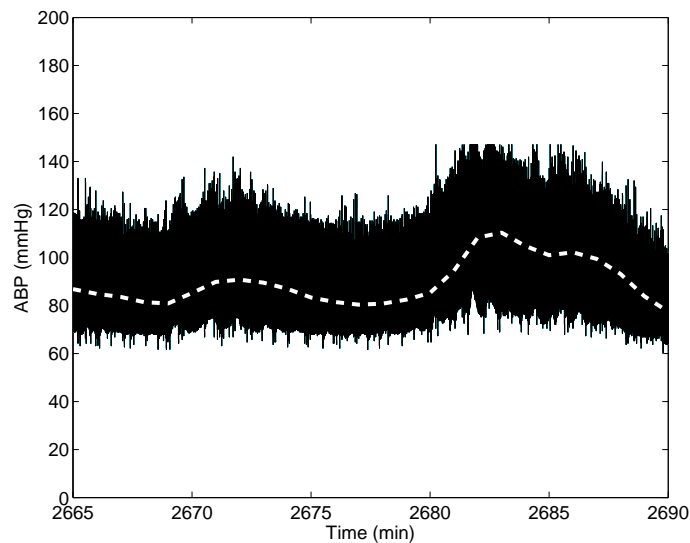


Figure 1.3: A shorter window of ABP waveform data for a MIMIC II patient. A variety of transients in mean ABP (white dashed line) can be observed, even in this short period of time.

Hz, where we can see a variety of transients in the *mean* blood pressure. Transients such as these could have signified important events during the patient’s ICU stay. Ideally, we envision our models and model-based estimation methods as being capable of tracking these transients in terms of clinically important variables. In particular, later we show how *averaged* models of cardiovascular dynamics can be used to track transients in MAP as opposed to the ABP waveform itself.

Of the hemodynamic variables measured in modern ICUs, the most important for the purposes of cardiovascular system modeling and monitoring [3, 8] are:

- The surface electrocardiogram, which is a very important diagnostic tool for determining heart function, and a measure of the electrical activity in the heart. It is a noninvasive measurement – three or more leads are attached to the patient’s skin. Patient heart rate, measured in beats per minute, is derived from ECG waveforms. The ECG can be used to detect cardiac arrhythmias, as well as heart diseases/conditions such as myocardial infarctions, ischemia, and ventricular hypertrophy.
- Arterial blood pressure, which is used as a diagnostic tool for cardiovascular function. ABP is tightly controlled by cardiovascular control mechanisms, making it an important indicator of cardiovascular system function. ABP is usually measured invasively by inserting a pressure-measuring catheter into one of the body’s main arteries, e.g., the radial or femoral artery. Intermittent noninvasive blood pressure measurements are also frequently recorded using an oscillometric system. The systolic, diastolic, and mean ABP are all derived from these pressure measurements.
- Pulmonary artery pressure, from which a measure of left-heart preload (or *filling* pressure at the left

atrium) can be determined³, and an indicator of left ventricular function. PAP is measured invasively using a Swan-Ganz catheter inserted into the pulmonary artery [9].

- Central venous pressure, which is a measure of preload (or *filling* pressure at the right atrium) of the right ventricle, and is important in diagnosing cardiac function. It is measured invasively using a catheter inserted into one of the large veins near the heart, e.g., the jugular vein. It may also be measured using a Swan-Ganz catheter.
- Cardiac output, which is the blood volume pumped by the heart per minute. It is measured only infrequently in the ICU, usually using an indicator-dilution technique known as thermodilution, or with an echocardiography imaging study [3].

In the ICU setting, the most readily available signals are the ECG and ABP. PAP measurements, and to a lesser extent, CVP measurements, are generally much less readily available in the ICU. For the purposes of the model development for this research, we have focused primarily on ECG and ABP, and the trends derived from these signals.

In addition to these variables, it would be prudent to monitor vasoactive medications, i.e., medications that alter total peripheral resistance (TPR), also referred to as systemic vascular resistance (SVR). Knowing the amounts of these medications that were administered is critical for the validation of model-based estimation methods for CO and TPR. For example, norepinephrine causes smooth muscle contraction (by stimulating α receptors in the muscle), and thus increases TPR, while isoproterenol and nitroglycerine cause smooth muscle relaxation (by stimulating β_2 receptors in the muscle), and thus lower TPR. Isoproterenol also acts to increase ventricular contractility (by stimulating β_1 receptors in the heart).

1.3 Model-based Intelligent Monitoring for the ICU

The research described in this thesis was pursued as part of the ongoing work in the BRP model-based intelligent monitoring for the ICU (MIMICU) group in the Laboratory for Electromagnetic and Electronic Systems (LEES). The overarching goal of the MIMICU group is to investigate the use of models of cardiovascular dynamics, model-based estimation methods, and knowledge-based clinical reasoning systems to identify and track a patient's cardiovascular state⁴. Previous work on intelligent patient monitoring, such as the SIMON project [11, 12], has focused on artificial intelligence (AI) methods, with no emphasis on lumped-parameter electrical circuit models of cardiovascular dynamics.

The specific questions the MIMICU group is addressing are:

³Diastolic PAP is a surrogate for Pulmonary Capillary Wedge Pressure (PCWP), which is a measure of left atrial transmural pressure.

⁴Another goal of the MIMICU group is to investigate better means of displaying data (see [10] for example) in the ICU, but this work will not be described here.

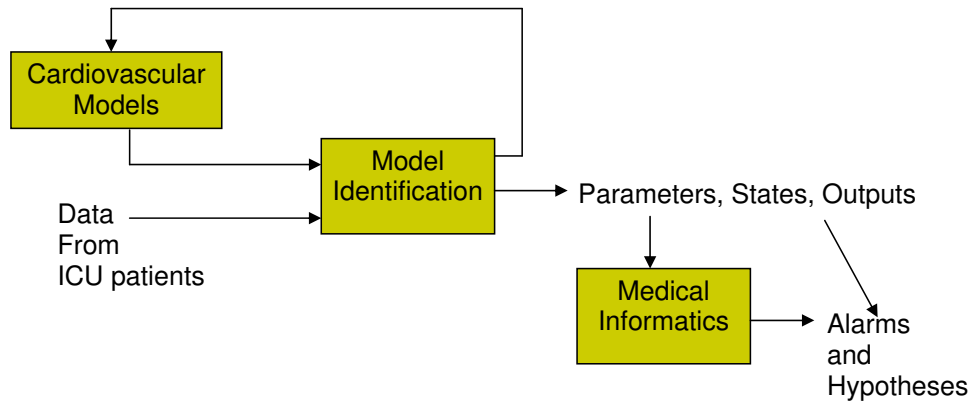


Figure 1.4: A schematic showing the MIMICU group’s approach. The tasks range from cardiovascular modeling to robust model identification and alarm/hypothesis generation.

- Given some set of ICU patient data, how effectively can one use models of cardiovascular dynamics to infer the patient’s pathophysiological state?
- Furthermore, how can this information be integrated to generate pathophysiological hypotheses and/or alarms?

We envision the BRP MIMICU group task to be that shown schematically in Fig. 1.4.

Because of the different types of data present in the ICU – both in terms of data format, e.g., textual or numerical, and in terms of timescale, e.g., continuously monitored ECG waveforms versus once-a-day laboratory tests – data analysis would potentially require several different types of models. In addition, the wide variety of pathologies seen in the ICU implies that the cardiovascular models we develop have to be capable of robustly tracking hemodynamic parameters for varying patient conditions. Finally, the model-based estimation must be carried out in real-time in the presence of artifacts and noise in the data.

In Fig. 1.4, we see that ICU patient data is fed into a model identification block that will estimate parameters and states of the cardiovascular dynamics models. The estimated parameters and states, and other model outputs are then used to give an estimate of the patient’s current hemodynamic state and to predict the patient’s hemodynamic trajectory. When combined with a clinical reasoning system, the outputs of the model identification block can be used to generate alarms and pathophysiological hypotheses that could be used by clinicians to make an informed assessment of patient cardiovascular function.

Due to the varying timescales on which measurements and observations are recorded in the ICU, the models themselves need to span the gamut of resolutions in time – from intra-beat (or, equivalently, intra-cycle) timescales typical of waveforms in the ICU, to inter-beat (or, equivalently, inter-cycle) timescales of the trends of these waveforms, through infrequently acquired measurements, such as radiology reports. To capture patient dynamics on these timescales, we envision a hierarchy of models with the basic structure as shown in Fig. 1.5 – a so-called *multi-scale* model hierarchy – where each level in the hierarchy operates

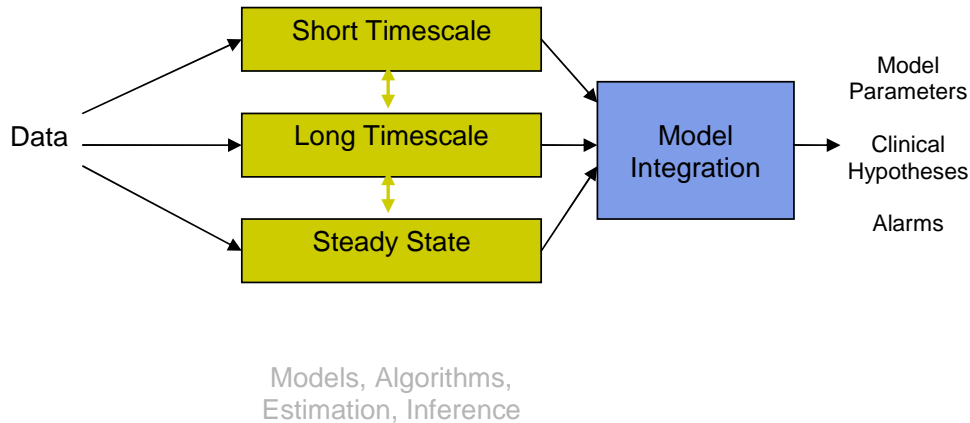


Figure 1.5: An example of a model hierarchy where the models share their parameters, states, and outputs.

on a different timescale. For instance, one cardiovascular model is used for waveform data analysis and another for trend data analysis.

In addition, for more robust model state and parameter identification, we envision that identified parameters, states, and model outputs are passed from one level of the hierarchy to another. Thus, outputs from one model can then be used to estimate parameters in another model. Clinical reasoning systems can also be used to determine which model is used to analyze a particular set of data, although we envision their primary use to be in the “model integration” block in this hierarchy.

Our group has begun work on all these fronts, some of which has already been published [8, 10, 13, 14, 15, 16], and some of which will be reported in documents to be published shortly [17, 18]. In particular, we are pursuing projects in which we are using models of cardiovascular dynamics at three different timescales:

- Intra-beat timescales: we are investigating parameter identification schemes using pulsatile models of cardiovascular dynamics;
- Inter-beat timescales: we are investigating model-based estimation methods using averaged models – both discrete-time beat-to-beat averaged and continuous-time cycle-averaged;
- Steady-state or coarse timescales: we are trying to estimate/predict/infer unobservable states and parameters on coarse timescales using probabilistic models. In particular, we are exploring both Bayesian Belief Networks (BBNs) and Hidden Markov Models (HMMs).

This detailed model hierarchy is illustrated in Fig. 1.6, where we show the approach we have taken for model-based ICU patient monitoring.

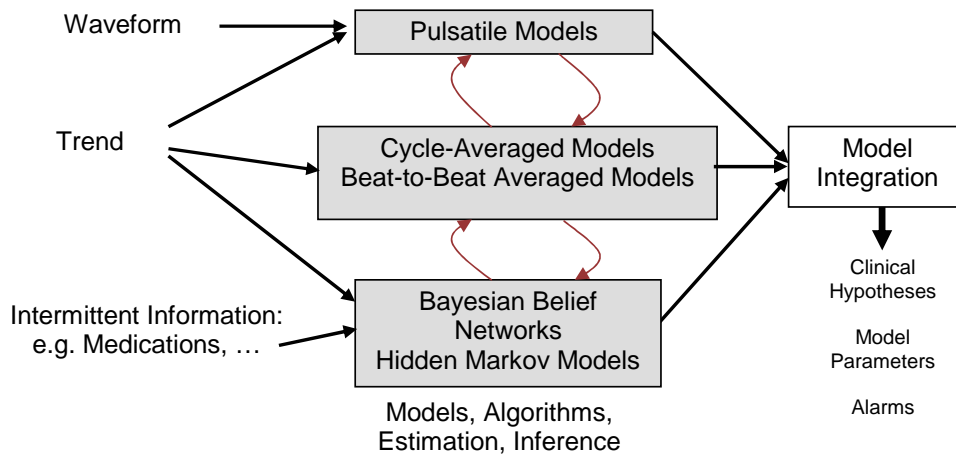


Figure 1.6: A hierarchy of cardiovascular models – both probabilistic and deterministic – for use in the ICU setting.

1.4 Specific Aims

For the purposes of this research, we restrict ourselves to the task of tracking patient cardiovascular dynamics, which is particularly useful in the ICU setting [3]. As mentioned above, we believe that computational models of cardiovascular dynamics can be incorporated into a next-generation monitoring system, and we are pursuing research avenues in this direction.

In particular, we hope that a next-generation monitoring system that incorporates cardiovascular dynamics models will also reduce the use of invasive procedures in the ICU. For example, if one could continuously estimate cardiac output (CO) from a less invasively obtained measurement, i.e., without inserting a catheter into the pulmonary artery, this would eliminate the need for expensive and invasive intermittent thermodilution measurements.

The specific aims of this thesis research are:

1. To develop models of cardiovascular dynamics for tracking patient hemodynamics and cardiovascular function in the ICU.
2. To explore parameter and state estimation methods for these models in order to track important clinical variables in the ICU.
3. To validate our model-based estimation methods with numerical simulations, data from laboratory animal experiments, and human ICU data.

The focus of this research, therefore, is the development of models and model-based estimation methods for better understanding and tracking of patient cardiovascular dynamics in the ICU. While we intend our

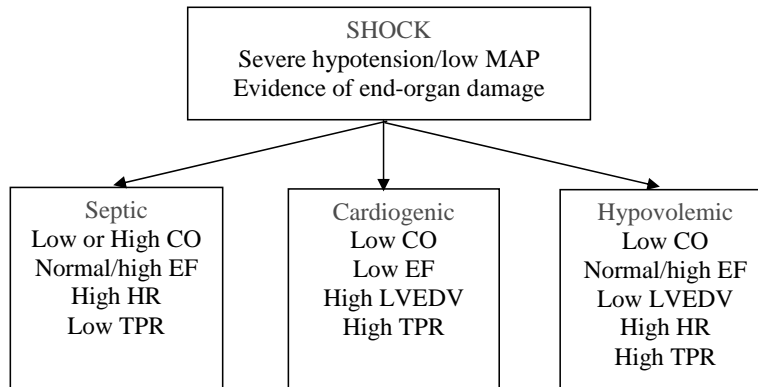


Figure 1.7: Block diagram showing how one could use measurements of CO, EF, LVEDV and HR to distinguish between septic, cardiogenic, and hypovolemic shock.

models and estimation methods to be used as aids in the clinical decision-making process in the ICU, the validation of our work in the clinical setting is beyond the scope of the research.

Of particular relevance is the problem of distinguishing between three types of *shock*, i.e., severe hypotension (or dangerously low MAP): septic shock (due to infections in the systemic vasculature), cardiogenic shock (relating to heart (pump) failure associated with myocardial infarction, cardiomyopathy, cardiac tamponade, etc.), and hypovolemic shock (relating to low blood volume, e.g., as a consequence of hemorrhage). Figure 1.7 is a block diagram showing how one can distinguish between septic, cardiogenic and hypovolemic shock using trends of HR, CO, TPR, left ventricular ejection fraction (EF)⁵, and left ventricular end-diastolic volume (LVEDV).

CO and LVEDV (or left-ventricular end-diastolic pressure, LVEDP) by themselves are two of the most important quantities for monitoring critically ill patients [19]. For instance, low CO and high LVEDV would indicate left ventricular failure, while low CO and low LVEDV would be indicative of hypovolemia. Ejection fraction allows for the additional distinction between sepsis, cardiac failure and hypovolemia, since sepsis and hypovolemia are usually not associated with low EF.

Of the patient data collected so far, we have observed that many MIMIC II ICU patients suffer from at least one (if not many) acute hypotensive episodes during their ICU stay. In the ICU, clinical interventions for each of these types of hypotension are different. In the case of hypovolemic shock, for example, one would try to increase the patient’s blood volume, perhaps with a saline infusion. With cardiogenic shock, on the other hand, one would try to reduce the load, i.e., either the inlet (preload) or outlet (afterload) pressures acting on the patient’s heart, perhaps by administering drugs that would reduce the patient’s vascular resistance or increase cardiac contractility. For patients with sepsis, intravenous saline infusions and/or medications that increase MAP by increasing TPR are given.

⁵Left ventricular ejection fraction is the ratio of blood volume ejected by the left ventricle in a single cardiac cycle to the ventricular blood volume at the instant prior to ejection – the left ventricular end-diastolic volume.

Introduction and Contributions

The therapeutic interventions given to patients for low MAP can often be incorrect if the relevant clinical information is not available. For instance, for patients with CHF, one would attempt diuresis (say, by giving a drug such as furosemide (‘Lasix’) to reduce the preload on the heart and remove any water that may have accumulated in the lungs (a condition known as *pulmonary edema*). On the other hand, for patients with hypovolemia, one would give the patient a bolus of fluid, e.g., saline infusion, in an attempt to increase distending blood volume, and in turn, MAP. If one were to give a patient with CHF a fluid bolus, this would worsen the preload on the heart and probably worsen the patient’s pulmonary edema symptoms [20].

Currently, it is quite difficult to determine the root cause of a patient’s shock, mainly for two reasons. First, CO, EF, and LVEDV are not frequently measured in the ICU. Of these, CO can be measured with relative ease once a pulmonary artery catheter is in place, but this is an invasive procedure that is reserved for the sickest of patients [3]. Second, for many ICU patients, there is always the possibility that the shock is a result of multiple organs failing, i.e., they may be suffering from heart failure *and* a systemic infection.

Our hope is that with estimates of CO, TPR, EF, and LVEDV, we will be able to distinguish between these three types of shock. Furthermore, by providing robust and continuous estimates of these variables, clinicians can track a patient’s response to therapeutic interventions. Therefore, the central parts of this thesis are devoted to estimating these three critically important clinical variables.

1.5 Thesis Contributions

We see the contributions of this thesis as being threefold:

- We have developed and applied novel averaging methodology to existing lumped-parameter continuous-time (pulsatile) electrical circuit models of cardiovascular dynamics. The resulting averaged models – discrete-time beat-to-beat averaged and continuous-time cycle-averaged models – are capable of tracking cardiovascular dynamics on timescales larger than a single cardiac beat (*inter-beat* rather than *intra-beat* timescales), are computationally efficient, and allow for model-based estimation methods that would be difficult to develop with existing models of intra-beat cardiovascular dynamics.
- We have developed and used a discrete-time beat-to-beat averaged model-based estimation method to estimate cardiac output and total peripheral resistance from central *or* peripheral arterial blood pressure waveforms. We have validated this estimation method on two animal data sets: a porcine data set comprising six swine with 82,734 ultrasound flow-probe based CO measurements, and a canine data set comprising three dogs with 10,743 reference ultrasound flow-probe and/or echocardiography-based CO measurements, and on two human ICU data sets: one with 12 patients and 124 reference thermodilution-based CO measurements, and another with 120 patients and 1378 reference thermodilution-based CO measurements. The errors obtained on application of our CO estimation method are well within the

margin of clinically-acceptable error.

- We also used the steady-state ventricular pressure-volume relationship to develop a novel method for estimating left ventricular ejection fraction and left ventricular end-diastolic volume from a central or peripheral arterial blood pressure waveform. We applied these estimation methods to a canine data set with three dogs and 64 reference echocardiography-based EF and LVEDV measurements. The errors obtained on application of our EF and LVEDV estimation methods are close to the margin of clinically-acceptable error.

Thus, the central results of this thesis concern averaged models and novel, simple, minimally-invasive, model-based estimation methods for tracking CO, TPR, left ventricular EF, and LVEDV. By tracking these variables over time, one can distinguish between cardiogenic, hypovolemic, and septic shock.

1.6 Intended Audience

This thesis is intended for engineers with a strong interest in systems level physiology and cardiovascular pathophysiology in particular. Wherever possible, we have included tutorials on the main physiological concepts – mainly from cardiovascular physiology – that were used to obtain the central results in this thesis. A beginner would do well to start by browsing some of the chapters in Costanzo’s physiology text [21] or the Berne *et al.* Physiology text [22], before moving on to a more detailed exposition, by Berne and Levy [23], for example.

This thesis could also be read by practicing clinicians or clinical researchers with a strong interest in physiological modeling and model-based parameter estimation. The engineering concepts – primarily electrical circuit analysis tools, least squares estimation, and systems of differential equations – described herein can be mastered with some effort, and appropriate references are provided throughout the document.

1.7 Document Outline

This document is made up of four parts, with a total of nine chapters and several appendices. The document outline is as follows:

- **Part I:** Introduction and Background

In this part, we give an introduction to and the background for the thesis research described later in the document. The focus in this part is on the specific aims of the thesis, the thesis contributions, and the necessary background in cardiovascular physiology.

- In **Chapter 1**, we placed the thesis research in context, and provided a description of the thesis aims and contributions. We gave an overview of the MIT Bioengineering Research Partnership and the modeling group within that partnership. We also included details on the MIMIC II ICU patient database, explaining which signals are routinely collected and what types of gold-standard data are available to researchers who would use the database. We end this chapter with the specific aims and contributions of this thesis research, and an outline of the thesis document.
- **Chapter 2** gives a brief overview of cardiovascular physiology. We begin with a historical overview of studies of human circulation and experimental work on cardiovascular physiology. We then give a detailed description of the circulatory system and the heart, including ventricular pressure-volume loops, arterial blood pressure and mechanisms for its control, and cardiac output and its control. Readers familiar with this material should skip this chapter and move to Chapter 3.

- **Part II: Lumped-Parameter Electrical Circuit Models of Cardiovascular Dynamics**

We present lumped-parameter continuous-time electrical circuit models of cardiovascular dynamics in this part, where we describe pulsatile and averaged – both discrete-time beat-to-beat averaged and continuous-time cycle-averaged – models, many of which we developed.

- In **Chapter 3** we describe *pulsatile* models of cardiovascular dynamics. These models are used to simulate cardiovascular dynamics on an intrabeat timescale. The well-known Windkessel model is introduced in this chapter, and we show how electrical circuit analogs for the cardiovascular system can be used to create models such as the modified Windkessel model, the cardiovascular simulator (CVSIM) model, and its derivatives – the simple cardiovascular simulator (CVSIMple) model and the simple pulsatile cardiovascular model (SPCVM).
- We show how we can average pulsatile models of cardiovascular dynamics to obtain averaged models of cardiovascular dynamics in **Chapter 4**. We illustrate these averaging techniques on the linear, time-invariant Windkessel model, and also show how one could cycle-average a time-varying model such as the SPCVM.

- **Part III: Estimation and Monitoring of Cardiovascular Dynamics**

In this part, we describe our model-based estimation methods for cardiac output, total peripheral resistance, left-ventricular ejection fraction, and left-ventricular end-diastolic volume. This part contains the main, clinically important research results.

- **Chapter 5** presents the main results of this thesis. We show how the beat-to-beat averaged Windkessel model from Chapter 4 can be used to estimate cardiac output and total peripheral resistance, using both intra-beat and inter-beat variations in arterial blood pressure. We show that this estimation is possible using either a central or a peripheral arterial blood pressure waveform. A key feature of our method is its use of an arterial compliance model that is a parametrized function of MAP. In this chapter, we describe the validation of our estimation method on two animal data sets and two human ICU patient data sets.
- **Chapter 6** presents a novel method for estimating left ventricular ejection fraction based on the steady-state left ventricular pressure-volume relationship. This method requires either a central or

a peripheral arterial blood pressure waveform, and at least one reference EF measurement. As an extension of our EF estimation method, we also estimated left ventricular end-diastolic volume. This extension is also described in this chapter. We end the chapter with results on the performance of these methods on a canine data set.

- **Part IV:** Conclusions, Future Work, and Appendices

We conclude the thesis with a chapter describing the thesis research and potential avenues for further research, and several supporting appendices.

- **Chapter 7** concludes this document with a recapitulation of the thesis goals and contributions, and a brief description of potential directions for further research.
- In the **Appendices**, we give a description of the notation used in this thesis (Appendix A), and have placed ancillary material, such as derivations (Appendices B, C, D), and programming scripts (Appendices E and F).

Overview of Cardiovascular Physiology

WE have learned much about cardiovascular physiology in the 400 years since the English physician William Harvey published his treatise on the human circulation – *Exercitatio Anatomica de Motu Cordis et Sanguinis in Animalibus* (An Anatomical Exercise Concerning the Motion of the Heart and Blood in Animals), and our knowledge of the cardiovascular system is still growing¹.

William Harvey made his observations using vivisections of humans and other animals, and was thus a pioneer in experimental systems-level physiology. In *De Motu Cordis*, Harvey proposed that the circulation was comprised of two closed circuits – a pulmonary circulation from the heart to the lungs, and a main circulation from the heart to the other organs. In proposing these circuits, he also showed, with a simple calculation involving a crude estimate of cardiac output, that blood is constantly recycled through the system. At the time, the common belief was that blood was constantly produced by the liver.

The pioneering work of William Harvey and others, such as the Italian histologist Marcello Malphigi, lay the foundation for the physiological experiments performed by Stephen Hales in the 18th century. Stephen Hales studied both animal and plant physiology, and published the two-volume collection *Statical Essays* in 1733 detailing his work, with *Vegetable Staticks*, the first volume, on plant physiology, and *Haemastaticks*, the second volume, on animal physiology. Hales is also credited with the first blood pressure measurement taken – in 1718 – by inserting a brass tube into a horse’s carotid artery and measuring the height of the resulting pressure column [24].

Our knowledge of cardiovascular (CV) physiology has steadily grown since the pioneering work by Harvey, Malphigi, and Hales. It has literally exploded in the latter part of the last century when cardiovascular diseases became the leading cause of death in the United States – accounting for approximately 1 million deaths/year² – and in many other industrialized countries. A significant portion of national resources are therefore consumed by the cost of patient care and basic research of CV physiology, and its aberrations under pathological conditions.

In this chapter, we give a brief overview of the fundamentals of CV systems physiology, including an overview of the human circulation, the cardiac cycle, and a description of the control mechanisms that

¹Much of this historical perspective is based on *Harvey, William*. Encyclopedia Britannica Online at <http://search.eb.com/eb/article-9106277>, and *Hales, Stephen*. Encyclopedia Britannica Online at <http://search.eb.com/eb/article-9038874>, site accessed on April 22, 2007.

²American Heart Association. *2002 Heart and Stroke Statistical Update*. 2002.

tend to maintain cardiac output and mean arterial blood pressure constant. For those interested in getting into more detail than provided here, a good start would be either Costanzo's *Physiology* [21] or the Berne *et al.* physiology text [22], before moving on to the more detailed cardiovascular physiology text by Berne and Levy [23]. Readers familiar with this material should move on to Chapter 3.

2.1 Introduction to the Cardiovascular System

The human cardiovascular system (CVS) performs several key functions, the most important being to carry oxygenated blood and other nutrients to the body's organs, particularly the brain and central nervous system, and to remove carbon dioxide and other waste products from them.

The CVS is comprised of the heart, which is responsible for pumping blood, and the various blood vessels, which serve as the distribution system – the “plumbing” – for blood to go from the heart to the main organs in the body, as illustrated in the schematic in Fig. 2.1. As we see in Fig. 2.1, the heart is comprised of two distinct pumps: the left heart and the right heart. Each of these pumps can be further divided into two chambers: an atrium and a ventricle. There are unidirectional valves (the tricuspid and mitral valves) between the atria and ventricles in both the left and right heart, and between the right ventricle and the pulmonary artery (pulmonic valve), and the left ventricle and the aorta (aortic valve). The right heart pumps deoxygenated blood from the systemic circulation to the lungs, while the left heart pumps oxygenated blood from the lungs to the various parts of the systemic circulation.

As William Harvey observed in his experimental work, the circulation can be divided into two parts: the pulmonary circulation referring to blood flow through the lungs where gas exchange occurs, and the systemic circulation referring to blood flow through rest of the body. These two parts are connected in series i.e., the flow through each part is equal. The various vascular beds in the circulation are connected to the heart in parallel i.e., approximately the same arterial blood pressure drives flow through each vascular bed.

There are three main types of blood vessels: arteries, capillaries, and veins. The arteries are thick-walled vessels that carry blood away from the heart, usually at high pressures. The largest of the arteries, the aorta, branches out successively into smaller arteries which carry blood to the various organs in the body (see Fig. 2.1). Within these organs the arterioles feed the capillaries across whose walls the exchange of oxygen/carbon dioxide and nutrients takes place. The veins are thin-walled vessels that carry blood from the capillary networks to the heart at low pressures. Many of the body's veins have unidirectional valves that only allow blood to flow back to the heart. Approximately two-thirds of the blood in the body resides in the veins [22].

Blood vessels offer resistance to the flow of blood from the heart, with most of this resistance concentrated at the level of the smaller arterioles (shown in Fig. 2.1), which are often modeled as resistance elements. As

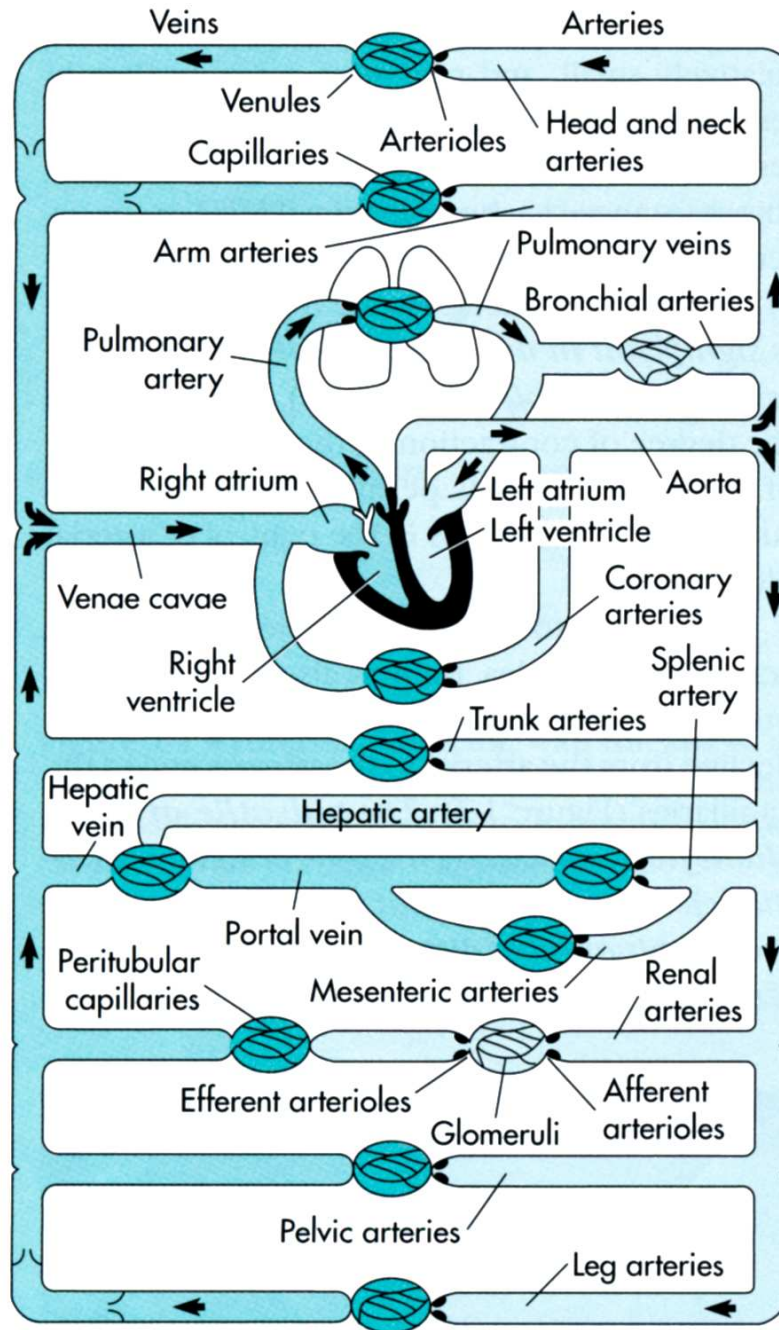


Figure 2.1: A schematic representation of the human cardiovascular system showing the heart and the blood vessels, including major vascular beds. The venous system, comprised of veins that may have unidirectional valves, appear on the left of the figure, while the arterial tree, with no valves, appears on the right. The majority of the resistance to blood flow is concentrated in the arterioles (dark ovals before the capillaries). This figure appears as Fig 1.4 in [23] and was reproduced with permission from Elsevier Health Sciences Division.

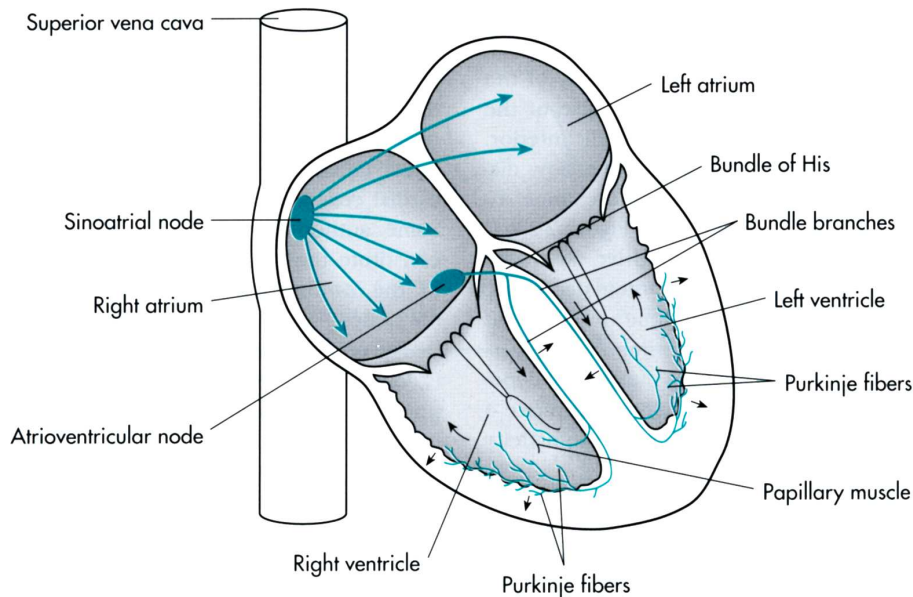


Figure 2.2: Schematic of the electrical conduction system of the heart. Normally, impulses originate from the SA node, and spread through the atria and AV node to the ventricles. This figure appears as Fig 2.28 in [23] and was reproduced with permission from Elsevier Health Sciences Division.

the body's blood vessels, especially the larger arteries, have elastic tissue, they have an inherent capacitive property i.e., the ability to store blood. This is commonly referred to as compliance (the change in volume per unit of change in pressure). (Note that compliance is the inverse of elastance, which is an indicator of the blood vessel elasticity.) The resistance to blood flow of the arterioles is much higher than the resistance of the main arteries or veins. The compliance of the veins is generally much higher than that of the arteries [25]. In Chapter 3, we show how electrical circuit analogs of the cardiovascular system can be constructed by appropriately combining resistance and capacitance (or compliance) elements. In the circuit models we present later, the large arteries and veins are modeled as compliance elements, while the arterioles are modeled as resistance elements. In some of the circuits, inductance elements are used to model the blood's inertia as it propagates through the arterial tree.

2.2 Electrical Activity of the Heart

The pumping action of the heart is a culmination of an electromechanical coupling that begins with electrical pulses that are initiated by the sinoatrial (SA) node. These pulses spread through the atria and the atrioventricular (AV) node and eventually reach the ventricular walls (via the bundle of His and the Purkinje fibers), as shown in Fig. 2.2. At the level of the individual myocyte, the electrical pulses initiate a sequence of events that ultimately lead to the shortening of the contractile cellular elements. It is the coordinated contraction of all myocardial cells that gives rise to the heart's macroscopic pumping action.

The surface electrocardiogram (ECG) (see bottom of Fig. 2.3) is based on the detection of the cardiac electrical activity – de- and re-polarization of the atria and ventricles, leading to contraction and relaxation, respectively – at the body’s surface, making it an essential tool in diagnosing cardiac abnormalities, including cardiac arrhythmias, some of which are exacerbated by underlying cardiovascular disease. For example, the ECG can be used to diagnose acute cardiovascular conditions such as an acute myocardial infarction (MI) quite often results in an elevated ST-segment in the ECG. Other salient features of the ECG are also used to detect heart rhythm abnormalities. For instance, a normal QRS complex, as seen in Fig. 2.3, is indicative of normal ventricular depolarization. Thus, abnormalities in the QRS complex can be indicative of abnormalities in the electrical conduction system in the heart or in the ventricle itself. For more on the ECG and heart arrhythmias, see [21] or [23].

2.3 The Cardiac Cycle

The *cardiac cycle* refers to the sequence of events ensuing from the cyclical quasi-periodic pumping action of the heart. Two descriptions, both from the perspective of the left ventricle, have gained particular popularity: the description of the temporal evolution of pressures, flows, and volumes as encompassed in the Wiggers diagram, and the description in terms of the pressure-volume loops of the left ventricle. We turn to the latter in Section 2.4.

The cardiac cycle can be divided into two distinct phases: *diastole* and *systole*. During diastole, the ventricles relax (isovolumic relaxation) and fill with blood (filling), while during systole, the ventricles contract (isovolumic contraction) and eject blood into the circulation (ejection). Diastole is typically two thirds of each cardiac cycle [23]. When the ventricles start to contract, the tricuspid and mitral valves close. While the pulmonic and aortic valves are still closed, the ventricles go through a brief period of isovolumic (or isovolumetric) contraction. The opening and closing of the aortic valve correlates with the first and second heart sounds in the thoracic cavity.

The cardiac cycle for the left ventricle is shown in Fig. 2.3, where the regions labeled isovolumic contraction, rapid ejection, and reduced ejection correspond to systole, and the regions labeled isovolumic relaxation, rapid ventricular filling, diastasis, and atrial systole correspond to diastole. From Fig. 2.3, we can also easily pick out the the systolic and diastolic ABP (SAP and DAP). SAP roughly corresponds to the peak-systolic³ left ventricular pressure.

³By *peak* we mean the local maximum of the ventricular pressure waveform.

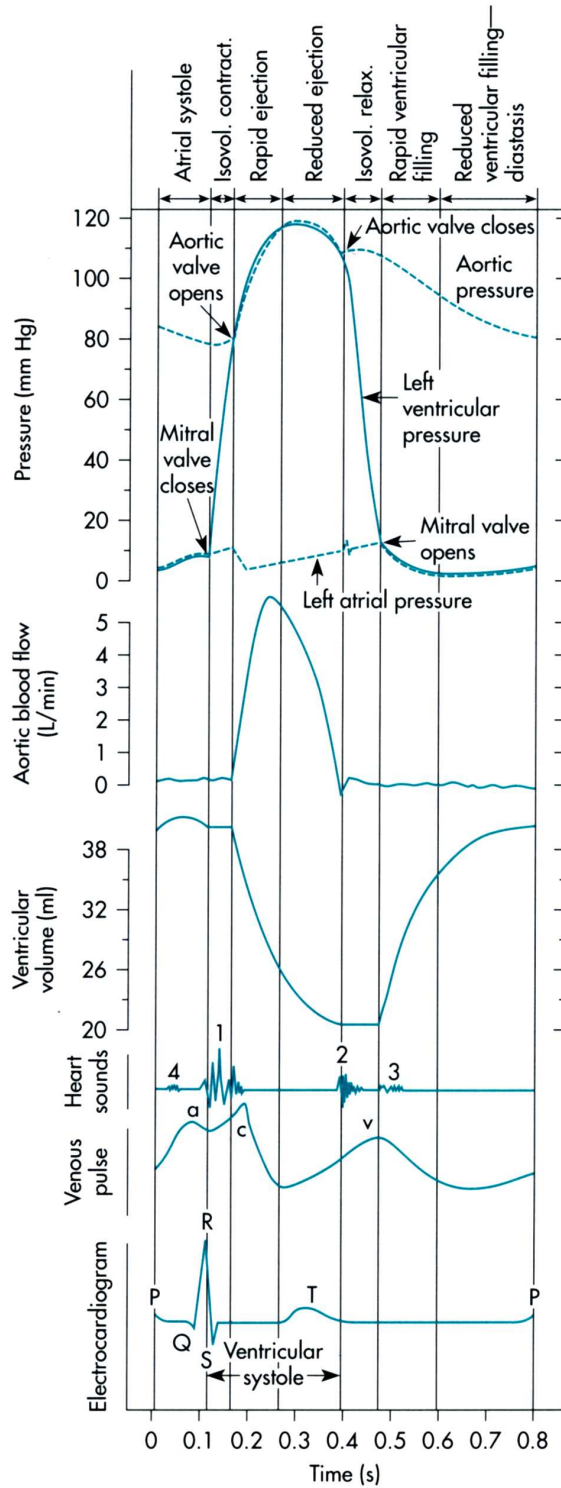


Figure 2.3: Wiggers diagram depicting the cardiac cycle in the left ventricle showing the various stages of diastole and systole. This figure appears as Fig 3.11 in [23] and was reproduced with permission from Elsevier Health Sciences Division.

2.4 Ventricular Pressure-Volume Relationships

In this section, we focus on the ventricle in the heart, and on the ventricular pressure-volume relationship in particular.

2.4.1 Ventricular Volumes, Stroke Volume, and Ejection Fraction

The electrical activity in the heart is translated to mechanical activity by myocardial cells in the heart. These cells have a pressure-dependent initial length as explained below, with larger forces, and thus larger pressures for cardiac contraction occurring when the initial length of the myocardial fibers is large. Figure 2.4 shows how changes in ventricular contraction during the cardiac cycle relate to changes in ventricular volume.

The ventricular end-diastolic volume (EDV) is the amount of blood in the ventricle at the end of filling. Ventricular end-systolic volume (ESV) is the amount of blood in the ventricle at the end of ejection. Similarly, ventricular end-diastolic pressure (EDP) is the transmural pressure across the ventricular walls at the end of filling, and ventricular end-systolic pressure (ESP) is the transmural pressure across the ventricular walls at the end of ejection. When describing these pressures or volumes, we quite often specify whether we are referring to left ventricular (LV) or right ventricular (RV) quantities. LVEDV refers to left ventricular end-diastolic volume, for example.

Stroke volume (SV) is defined as the difference between EDV and ESV, i.e., the amount of blood ejected by the right or left ventricle during a single cardiac cycle:

$$SV = EDV - ESV \tag{2.1}$$

These three volumes – EDV, ESV, and SV – are labeled in Fig. 2.4.

Left ventricular ejection fraction (EF) is the ratio of SV to EDV, i.e., the fraction of blood ejected from the heart during systole:

$$EF = \frac{SV}{EDV} \tag{2.2}$$

Ejection fraction is expressed as a percentage, with typical values for normal, healthy individuals ranging from 40–60%. Left ventricular ejection fraction is a strong indicator of heart function, perhaps the most significant index that is currently in clinical use [27]. Low ejection fraction is usually indicative of heart failure. Monitoring EF, even for outpatients, can be quite useful. For instance, Curtis and co-workers (see [28]) describe a powerful relationship between EF and mortality in heart failure outpatients – the lower the EF, the worse the patient outcome.

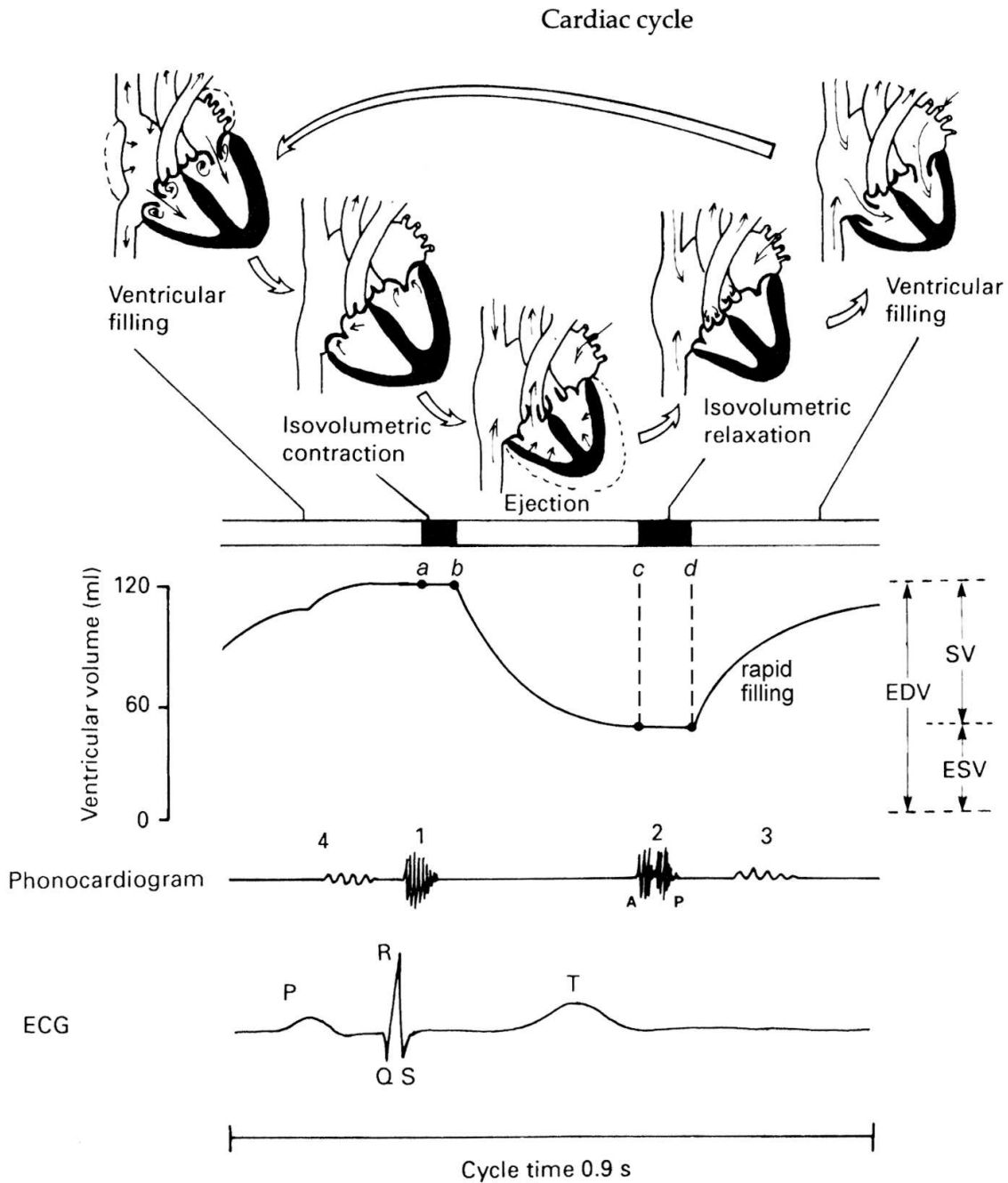


Figure 2.4: The human cardiac cycle (adapted from Fig. 2.3 in [26]) showing how changes in ventricular contractile state relate to ventricular volume. This figure appears as Fig 2.3 in [26] and was reproduced with permission from the Lippincott, Williams, and Wilkins Company.

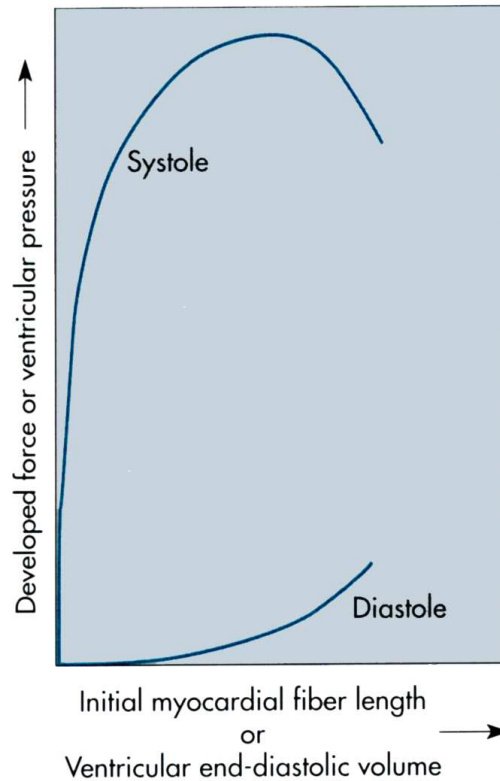


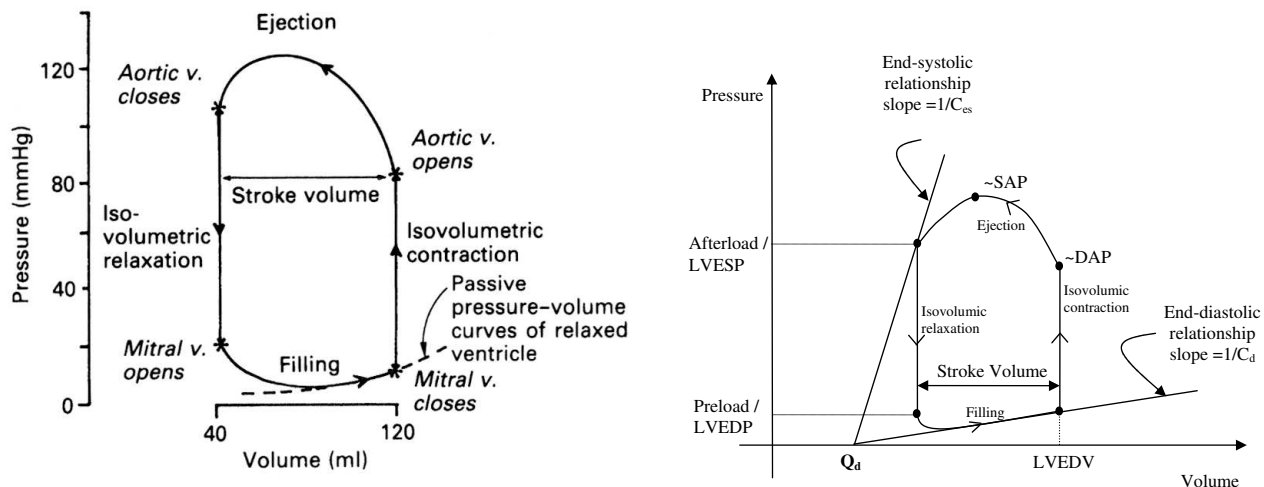
Figure 2.5: Typical ventricular systolic and diastolic elastance curves. This figure appears as Fig 3.4 in [23] and was reproduced with permission from Elsevier Health Sciences Division.

2.4.2 Ventricular Compliance

Figure 2.5 shows typical ventricular systolic and diastolic elastance curves, but in terms of developed force (or, equivalently, ventricular pressure) and initial fiber length in the myocardium (or, equivalently, ventricular EDV). The diastolic curve is quite flat, i.e., the incremental diastolic compliance is large, such that small increases in pressure lead to large increases in volume. On the other hand, the systolic curve has a large positive slope, i.e., the incremental systolic compliance is small. The positive slope on the systolic curve is quite often called the *Frank-Starling* curve or relationship. For normally functioning hearts, we can assume the incremental compliance to be constant during diastole and systole. However, for many disease conditions, this may not be true at the extreme of very large end-diastolic volumes.

2.4.3 Pressure-Volume Loops/Diagrams

Ventricular pressure-volume diagrams are frequently used to explain the pumping action of the heart and to study the effects of *preload* (pressure at the inlet of a particular atrium or EDP), *afterload* (pressure at the outlet of a particular ventricle or ESP), and ventricular compliance or capacitance (change in volume per unit of change in transmural pressure across wall of the ventricle) on the heart's ability to pump blood



(a) Typical human left ventricular pressure-volume loop. Stroke volume is defined as the width of the loop, while stroke work is the area of the loop. This figure appears as Fig. 2.5 in [26] and was reproduced with permission from the Lippincott, Williams, and Wilkins Company.

(b) Pressure-volume loop showing the straight lines defining the end-diastolic and end-systolic compliances, as well as the preload and afterload pressures. Note that the pressures in this figure are measured with respect to V_{th} , and that Q_d is ventricular dead volume.

Figure 2.6: Human left ventricular pressure-volume loops showing how pressure and volume in the ventricle change during the cardiac cycle.

[23]. The diastolic and systolic compliances of the ventricle define several points on the pressure-volume diagram [29]. A typical pressure-volume diagram for the left ventricle during the cardiac cycle is shown in the left panel of Fig. 2.6. An annotated schematic of the same pressure-volume loop is shown in the right panel of Fig. 2.6 with lines defining the end-diastolic and end-systolic compliances, as well as the EDP and ESP. In this panel, the slopes of the two lines define the fixed compliances C_d (end-diastolic compliance) and C_{es} (end-systolic compliance), and their intersection with the volume axis defines the ventricular dead volume, or Q_d . (Note that we assume in this thesis that the ventricular systolic and diastolic dead volumes are equal to Q_d .) Q_d is the blood volume in the ventricle when there is no transmural pressure applied to it. Note that the pressures in pressure-volume diagrams are transmural pressures and since the ventricles are inside the thorax, any pressures measured in that cavity are referenced to the intrathoracic pressure, V_{th} .

2.5 Stroke Volume and Ejection Fraction

Stroke volume in the right panel of Fig. 2.6 is defined by

$$SV = C_d(LVEDP - V_{th}) - C_{es}(LVESP - V_{th}) . \quad (2.3)$$

Although the incremental compliances C_s and C_d are fixed, this assumes a linear volume-pressure relationship in the ventricles in Fig. 2.6, an assumption that is valid only when the heart is pumping normally,

that is, when preload and afterload in steady-state are within a certain range of the typical LV elastance curve shown in Fig. 2.5 [23]. For other conditions, e.g., at higher preload, end-systolic compliance becomes very large, and SV can be severely impaired.

Assuming the same fixed incremental end-diastolic and end-systolic compliances as above, ejection fraction can be defined as

$$EF = \frac{SV}{EDV} = \frac{C_d(LVEDP - V_{th}) - C_{es}(LVESP - V_{th})}{C_d(LVEDP - V_{th}) + Q_d}. \quad (2.4)$$

Note the prominence of both Q_d and V_{th} in Equation (2.4), something we discuss when we use a variant of (2.4) in Chapter 6 to estimate EF.

EF can be estimated in two ways in the ICU. The first, an imaging technique, involves obtaining a 2- or 3-dimensional image of the ventricle during the cardiac cycle, and estimating EDV and ESV from the images. The second is based on the thermodilution technique (described in Section 2.6), in which a thermistor-bearing *Swan-Ganz* catheter is inserted into the pulmonary artery. A cold solution of dextrose or saline is then injected into the right atrium and the resultant temperature-time waveform recorded in the pulmonary artery is used to estimate ejection fraction. In particular, the difference between the two temperature peaks in the waveform is proportional to ejection fraction [3].

2.6 Cardiac Output and Venous Return

Cardiac output (CO), the amount of blood pumped by the heart per minute, is given by

$$CO = HR \cdot SV \quad (2.5)$$

where HR is heart rate.

In the ICU, CO is estimated using the thermodilution technique, in which a balloon-tipped catheter with a temperature-sensing thermistor (a Swan-Ganz catheter) is placed in the pulmonary artery via the right atrium. A cold solution of dextrose or saline is then injected into the right atrium. CO is inversely proportional to the area under the resultant pulmonary artery temperature-time curve waveform recorded by the thermistor [3].

In the clinical setting, CO can be used with MAP to obtain total peripheral resistance (TPR) defined as

$$TPR = \frac{MAP}{CO} \quad (2.6)$$

This relationship links CO to MAP through TPR, a fact that is exploited when using certain drugs in the ICU, e.g., vasodilators which decrease TPR. We shall see later that this relationship can be derived from the Windkessel model under steady-state assumptions.

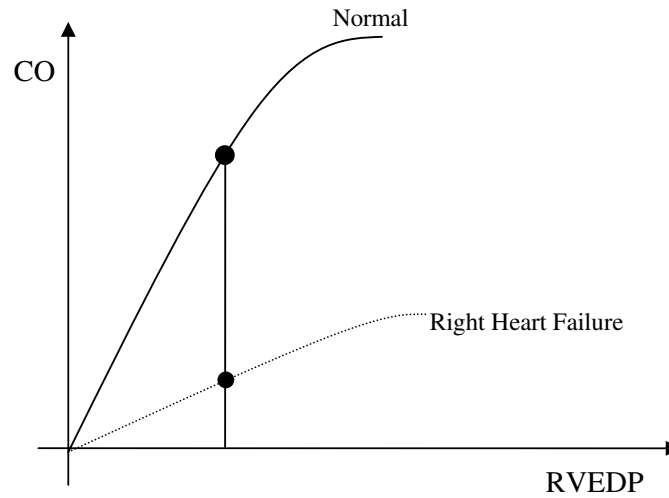


Figure 2.7: Cardiac output curves showing the effect of right heart failure on the Frank-Starling relationship.

Under normal operating conditions of the heart, i.e., with both the right and left ventricles functioning well, stroke volume (and hence cardiac output) is a strong function of right ventricular filling pressure or RVEDP. All other things being equal, increases in RVEDP result in increases in CO, except at very high RVEDP. When one or both of the ventricles fail, stroke volume is severely limited, and as a consequence, so is cardiac output. Figure 2.7 is a schematic showing CO-RVEDP curves (also called Frank-Starling curves) under normal conditions and during right heart failure. Both curves have been drawn assuming open-chest conditions i.e., neglecting V_{th} .

In general, CO is a complex function of many variables – heart rate, total blood volume, venous compliance, venous resistance, intrathoracic pressure, and the end-diastolic compliance of the right ventricle [25]. All other things being unperturbed, as heart rate or total blood volume or right ventricular end-diastolic compliance increase, CO increases. On the other hand, as arteriolar resistance or venous resistance or intrathoracic pressure increase, CO decreases. A typical value of cardiac output for a 70 kg human male is 5 l/min [23].

One way to envision what determines CO is shown in Fig. 2.8, in which the *heart-lung pumping unit* – the combination of the heart and lungs in the cardiovascular system – appears on the left, and the peripheral circulation appears on the right. The output of the heart-lung pumping unit is cardiac output, while that of the peripheral circulation is venous return (VR). Each of these units may be, in general, nonlinear and time-varying. Under normal conditions, we can plot CO and VR *curves* as a function of RVEDP [30]. Cardiac output itself is determined by the intersection of the CO and VR curves, analogous to the load-line analysis of the combination of two nonlinear circuits.

Figure 2.9 shows CO and VR curves for a variety of conditions – normal, right heart failure, hypovolemia, and right heart failure (left heart failure would result in a similar curve) and hypovolemia. (The VR curve has a negative slope, while the CO curve has a positive slope.) Each of these conditions results in

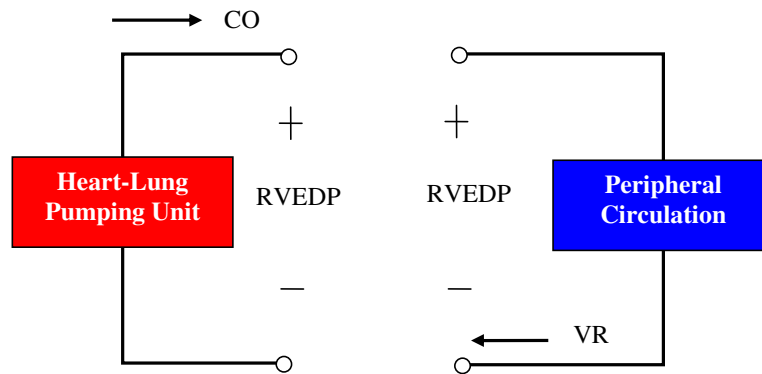


Figure 2.8: Cardiac output and venous return determination posed as a load-line problem.

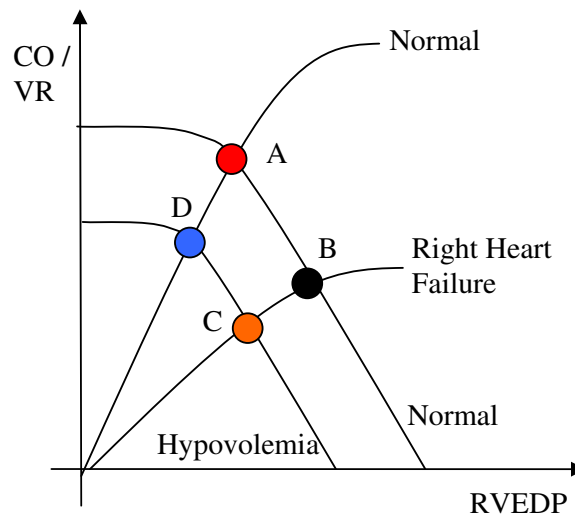


Figure 2.9: Cardiac output and venous return curves for a variety of conditions. The intersection of the cardiac output curve and venous return curve determines cardiac output.

a different intersection or operating point – A, B, C, or D – and thus a different cardiac output. Cardiac output decreases during hypovolemia or right heart failure, however, the values of RVEDP in each of these conditions is quite different.

2.7 Arterial Blood Pressure

Arterial blood pressure is probably the most important vital sign in any clinical setting, and is especially so in the ICU. While the arterial blood pressure wavelet morphology may change as blood travels from the aorta to the peripheral arteries (due to the reflections of the arterial pulse wave and changes in arterial impedance), mean arterial blood pressure (MAP) is essentially constant in the large arteries, and is normally around 100 mmHg at the level of the heart. This value is surprisingly common to all mammals except giraffes, which, given their unique anatomy, need a much higher mean ABP at the level of the heart in order to perfuse their neck and brain [31, 32].

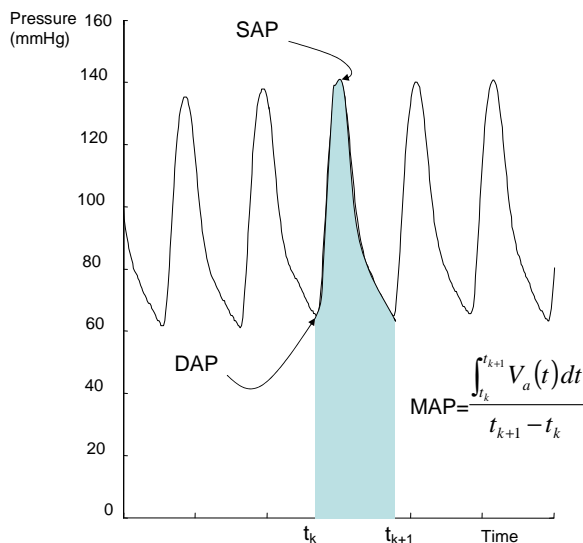


Figure 2.10: ABP waveform from a MIMIC II patient. The systolic and diastolic pressures for one ABP wavelet are shown in the figure. Mean ABP is proportional to the area under this wavelet. This figure was adapted with permission from Elsevier Health Sciences Division, i.e., the superimposition and integral are adapted from Fig. 6.7 in [23]).

Figure 2.10 shows a radial ABP waveform from an ICU patient record where we have annotated the ABP wavelet in the center with the systolic and diastolic arterial blood pressures. Mean arterial blood pressure over one cardiac beat is calculated using the area under that wavelet (shaded in the figure) as shown by the formula in Fig. 2.10, where we use $V_a(t)$ to denote ABP. Note that we have not drawn in the value of MAP for the center ABP wavelet.

2.8 Cardiovascular Control Loops

In this section we discuss the main control loops of the cardiovascular system. The principal control system we discuss is the arterial *baroreflex* control loop, which, on a beat-to-beat basis (short timescale i.e., seconds to minutes), tightly controls mean ABP. We also discuss the cardiopulmonary reflex, the chemoreflex, and the direct neural coupling between heart rate and respiration. The Ph.D. theses of both Mukkamala [33] and Heldt [34] can serve as good references on how to model and implement these control loops. For many ICU patients, a common problem is that certain disease conditions result in the saturation of the baroreflex control system, and an appropriate MAP can no longer be maintained [3]. For such patients, therapeutic interventions must be performed to regulate MAP.

Figure 2.11 is a block diagram of the cardiovascular control system we discuss here. The sensors for arterial blood pressure are the baroreceptors (located in the aortic arch and carotid sinus). The sensors for right atrial pressure are the cardiopulmonary receptors (located in the walls of the right atrium). The effectors for the control system are the heart (modulating heart rate and contractility), the arterioles (modulating

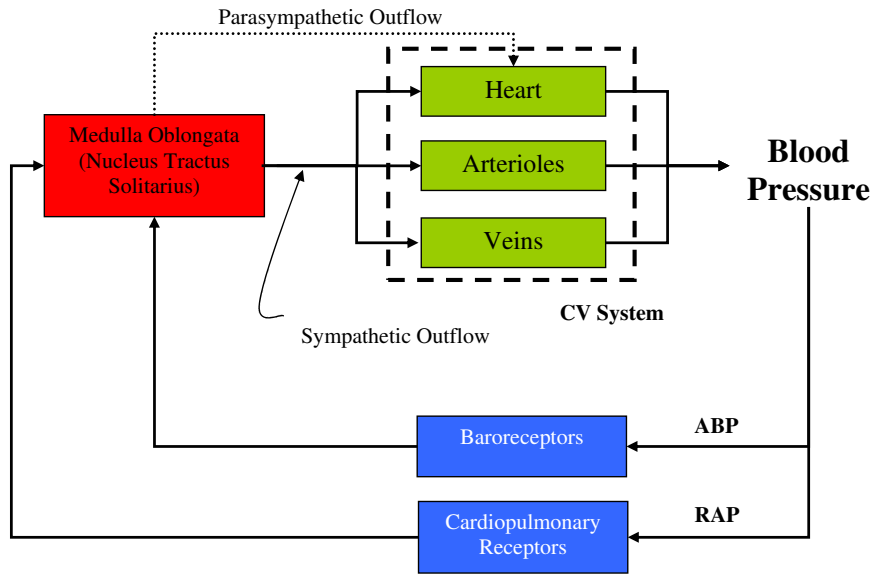


Figure 2.11: Block diagram of the cardiovascular control system, including both the baroreflex and the cardiopulmonary reflex mechanisms, but neglecting the direct neural coupling between heart rate and respiration. The baroreceptors sense arterial blood pressure in the aortic arch and carotid sinus, while the cardiopulmonary receptors sense right atrial transmural pressure.

TPR), and the veins (modulating zero-pressure filling volume or venous tone). The control inputs to the system are synthesized in the nucleus tractus solitarius (NTS), a part of the medulla oblongata in the autonomic nervous system (ANS) [34]. We very briefly discuss this system below.

2.8.1 The Baroreflex Control Loop

The arterial baroreflex control loop tightly controls mean arterial blood pressure on a short-term beat-to-beat basis. It is a global, hard-wired feedback loop that attempts to maintain mean arterial blood pressure close to constant. By regulating MAP in this manner, the baroreflex also indirectly changes (but does not regulate) cardiac output through the interaction summarized by (2.6).

The ANS attempts to alter heart rate, arterial resistance, ventricular contractility, and the body's venous unstressed blood volume (the *zero-pressure filling volume*) to regulate blood pressure. The sensor mechanisms for the baroreflex are the stretch receptors in the carotid sinus and aortic arch, which link to the NTS in the medulla oblongata in the ANS. An increase in arterial blood pressure corresponds to an increase in the firing rate of these receptors.

There are two parts of the autonomic nervous system that react to changes in arterial blood pressure: the *sympathetic* and the *parasympathetic* systems. When the sympathetic nervous system, which is responsible for the so-called *fight and flight* response, is stimulated, the primary effects are increased arterial resistance (primarily by stimulating the secretion of the vasoactive neurotransmitter norepinephrine which binds to

Overview of Cardiovascular Physiology

α receptors in the smooth muscle causing vasoconstriction in both the arteries and the veins), increased heart contractility (by stimulating the secretion of epinephrine with stimulates β_1 and β_2 receptors in the myocardium to decrease ventricular end-systolic compliance), increased heart rate (by speeding up SA node firing by increasing calcium uptake in the SA node), and increased distending blood volume (by decreasing the zero-pressure filling volume with α receptor stimulation). The overall effect of these changes is to increase the arterial blood pressure. These changes allow for the potentially dramatic increase in metabolic activity that would accompany the actions taken to combat the perceived threats, e.g., running away from a threatening person or situation. The primary effect of the parasympathetic nervous system is to slow down the heart, i.e., reduce the SA node firing rate – via acetylcholine release mediated by the *vagus* nerve [34].

2.8.2 The Cardiopulmonary Reflex

The cardiopulmonary reflex loop can be thought of as an additional part of the blood pressure control mechanism. The cardiopulmonary receptors are located in the right atrial walls and sense right atrial transmural pressure. An increase in right atrial transmural pressure (RAP), however, primarily affects the arteries and veins, with little to no effect on the heart [33]. When right atrial transmural pressure increases, for example, the ANS acts to decrease TPR and decrease distending blood volume.

2.8.3 Neural Coupling to Heart Rate

A neurally-mediated interaction exists between respiration and heart rate. This interaction is partly responsible for *sinus arrhythmia* i.e., the cyclical respiratory modulation of the ECG seen in human ECGs [33]. During inspiration, as lung volume increases, parasympathetic outflow from the ANS decreases. The converse occurs during expiration. In addition, there are perturbations induced in heart rate that can be modeled [33], but we ignore them here.

2.8.4 Local Metabolic Control of Cardiac Output

Blood flow to tissue in the body is regulated locally based on the oxygen demand in the tissue [30]. Although the exact mechanism for this autoregulation is not known, we know that the blood flow to tissue increases as oxygen demand in the tissue increases.

2.8.5 The Chemoreflex Loop

In addition to the baroreceptors, there are *chemoreceptors* in the carotid sinus and aorta which sense the oxygen content, carbon dioxide content, and blood pH, as blood flows through the vessels. If the oxygen content in these vessels is low, for example, the firing of these fast-acting receptors results in outflow from the ANS that increases mean ABP, and thus CO, via Equation (2.6). The mechanisms for this loop are discussed in [21].

2.8.6 The Renin–Angiotensin II–Aldosterone System

Another mechanism that responds, albeit slower, i.e., on the order of days and weeks, than the baroreflex, to changes in arterial blood pressure is the *renin–angiotensin II–aldosterone* system [21]. When aortic arterial blood pressure decreases, for example, renal arterial blood pressure decreases, which causes the hormone renin to be secreted. Renin causes the production of the hormone angiotensin I, which is converted to the hormone angiotensin II, which in turn directly increases arterial resistance and stimulates the secretion of the hormone aldosterone. Aldosterone causes the blood volume in the body to increase (through actions on the kidneys), which in turn increases RVEDP and LVEDP. The increased preload of the heart increases stroke volume and tends to return mean ABP to normal values.

2.9 Medications used in the ICU

In this section we give an overview of medications commonly used in the intensive care unit. Most of these medications can be classified by their chemical composition or their effect, e.g., a β_2 -agonist causes vasodilation by stimulating β_2 receptors in the smooth muscle, while *nitrates* such as nitroprusside cause vasodilation via nitric oxide (NO) to stimulate the production of guanosine triphosphate (GTP).

Here, we list the most common hemodynamic drugs in the ICU and describe their effect in terms of stimulating α (vasoconstriction), β_1 (increased contractility and/or heart rate), and β_2 (vasodilation) receptors. Both [3] and [20] are excellent references for this material.

Hemodynamic drugs

Amrinone is a calcium (Ca_{2+}) channel blocker and β_2 agonist that increases contractility in the heart and causes vasodilation in the vascular smooth muscle, respectively.

Diltiazem is a β_1 and β_2 agonist that results in reduced heart rate and increased vasodilation.

Overview of Cardiovascular Physiology

Dobutamine is primarily a β_1 agonist, increasing contractility in the heart, but also has mild β_2 vasodilation effects.

Dopamine has different effects depending on its dosage. In small doses, it causes increased salt-water excretion by the kidneys. In intermediate doses, it has both β_1 and β_2 effects i.e., increased contractility and vasodilation, while at high doses, it is primarily an α agonist (with mild β_1 effects), causing a dose-dependent vasoconstriction – higher doses causing progressively larger vasoconstriction.

In low doses, **Epinephrine** is a β_1 and β_2 agonist, while in high doses, it is primarily an α agonist (with mild β_1 effects).

Esmolol is very fast-acting β antagonist i.e., a β *blocker* which induces a reduction in heart rate and an increase in arterial resistance by reducing β_2 receptor stimulation.

Isoproterenol (commonly known as “Isuprel”) is a β agonist, with both β_1 and β_2 effects.

Labetalol causes vasodilation by reducing the amount of α -mediated vasoconstriction.

Levophed is an α agonist that causes increased arteriolar resistance.

Milrinone and **Natrecor** are β agonists, with both β_1 and β_2 effects.

Neosynephrine (also called **Phenylephrine** because of its chemical name Phenylephrine Hydrochloride) is primarily an α agonist that causes increased arteriolar resistance, but also has mild β_1 effects.

Nitroprusside and **Nitroglycerin** are both potent vasodilators. Their vasodilation effects are mediated by nitric oxide. Nitroprusside, however, has many more adverse side effects, and is thus not as commonly used as Nitroglycerin.

Norepinephrine is an α agonist that causes widespread vasoconstriction.

Propofol is a sedative used for mechanically-ventilated patients. It also has β_2 effects i.e., it causes vasodilation.

Drugs that affect body fluids

Furosemide (commonly known as “Lasix”) is a very strong diuretic which acts on the loop of Henle in the kidney to quickly remove fluid from the body. The result is a temporary reduction in distending blood volume. Furosemide also binds to β_2 receptors and thus has a slight vasodilation effect.

Vasopressin or anti-diuretic hormone (ADH) makes the body conserve water by reducing water reabsorp-

tion in the kidneys, which may cause a temporary increase in distending blood volume. It also has mild vasoconstrictor effects i.e., it binds to α receptors.

Other drugs

In addition to these drugs, many ICU patients are on pain-relieving medications (analgesics) such as **Ativan** and **Morphine**, while others are on drugs that are anticoagulants and/or anti-platelet forming agents, e.g., **Aggrastat** and **Integrelin**.

Part II

Lumped-Parameter Electrical Circuit Models of Cardiovascular Dynamics

Pulsatile Models of Cardiovascular Dynamics

MEDICAL teaching and research have a rich tradition of using simple mechanical or electrical models to describe and elucidate cardiovascular phenomena¹. This tradition dates back over a century to the work of Moens and Korteweg, who modeled arterial pulse propagation in 1878, and the work of Otto Frank and his associates in 1899, who used a lumped-parameter mechanical model of the arterial system – the Windkessel (meaning air chamber in German) – to analyze the arterial pressure pulse [35, 36] and estimate cardiac stroke volume [37].

Some of these cardiovascular models were later implemented on analog computers [38], and subsequently in software on digital computing platforms. Such *computational* models of cardiovascular dynamics vary in complexity, ranging from simple models (see [39, 40, 41, 41, 42]), to more complicated models such as those developed from experiments by Dr. A. Guyton and his associates [30, 43, 44, 45]. These models, particularly in the form of electrical circuit analogs (see [46, 47, 48] for some early work in this area), have been used in teaching physiology [49, 50, 51, 52], as well as in the research setting.

In the past, these models have generally been used to interpret experimental observations, serving as a rational framework that links an intervention to the observed system-level response (the *forward* problem, see [53, 54, 55] for examples). The forward problem involves tweaking model parameters so that the model output matches observed data. Thus, the modeler is required to have a deep physiological understanding, as one is building a model that is capable of simulating realistic hemodynamic responses. The focus in medical school classes, for example, is mostly on the forward problem, i.e., simulating CV disease conditions by changing model parameters [49].

More recently, however, these models have been used to link a system-level observation to the underlying changes in the cardiovascular system (the *inverse* problem), which involves estimating the *states*, or the *parameters*, or both, of a given computational model using the available hemodynamic data. There are a plethora of inverse problems to which we can apply our cardiovascular models (see the work of Heldt [34, 56], Mukkamala [57, 58], Clark [59], and Guarini [60] for examples), ranging from investigating the effect of micro-gravity on an astronaut’s cardiovascular system [56] to estimating cardiac output in a hospital ICU, one of the goals of this thesis research.

In the ICU setting, we believe that computational cardiovascular models can be used to provide clinicians

¹This chapter is partially based on two IEEE papers [15, 16]. The material has been reproduced with permission.

with a more comprehensive assessment of patient hemodynamic state. These cardiovascular models would be used to estimate a patient’s cardiovascular parameters such that the model’s response matches, in some sense, the available patient data, i.e., a subset of these parameters would be measured and the rest would be estimated using a model-based estimation method.

It is particularly convenient to model the cardiovascular system using lumped-parameter electrical circuit models representations for the different cardiac and vascular segments. Such electrical circuit analogs can be analyzed using Kirchhoff’s current and voltage laws, making them a particularly convenient representation. In this chapter, we describe a particular class of such models, namely *pulsatile* electrical circuit models of cardiovascular dynamics. (Models of cardiovascular dynamics are called pulsatile if they capture the intra-beat (or intra-cycle) features of individual pressure, flow, and volume waveforms.) We begin with an overview of prior work in this area, and then describe several pulsatile cardiovascular models including the well-known Windkessel model, the cardiovascular simulator (CVSIM) model [49], and simplifications of the CVSIM model – the simple CVSIM model (CVSIMple) and the simple pulsatile cardiovascular model (SPCVM). Of particular relevance to our work are the Windkessel and SPCVM models, as we use these models to develop the averaging methodology described in Chapter 4, and employ them in the estimation problem detailed in Chapter 5.

3.1 Lumped-Parameter Electrical Circuit Analogs for the Cardiovascular System

Under lumped-parameter approximations for the distributed cardiovascular system, the computational cardiovascular dynamics models that result allow for the simulation of hemodynamic waveforms that are reasonable approximations of those measured in the human cardiovascular system.

Figure 3.1 shows lumped-parameter electrical circuit analogs for a single ventricular compartment (Fig. 3.1(a)) and a systemic circulation compartment (Fig. 3.1(b)). The electric circuit analogs for cardiovascular variables and parameters are (not all shown in Fig. 3.1): current I for blood flow, voltage V for blood pressure, charge Q for blood volume, ideal diodes D for heart valves, resistance R for valvular or vascular resistance to blood flow, inductance L for blood inertia, and capacitance C for vascular or compartmental compliance. Elastance, E , is defined as the inverse of capacitance or compliance.

The pressures $V_{\text{in}}(t)$, $V_{\text{s}}(t)$, and $V_{\text{out}}(t)$ can be related using Kirchhoff’s current law. Thus, for the circuit in Fig. 3.1(b), we obtain:

$$C_s \frac{dV_{\text{s}}(t)}{dt} = \frac{V_{\text{in}}(t) - V_{\text{s}}(t)}{R_{\text{in}}} + \frac{V_{\text{out}}(t) - V_{\text{in}}(t)}{R_{\text{out}}} \quad (3.1)$$

In the circuit analogs presented in this thesis, pulsatile behavior is simulated with lumped-parameter circuit models in which the ventricular compartment is comprised of a time-varying capacitor that cycles between

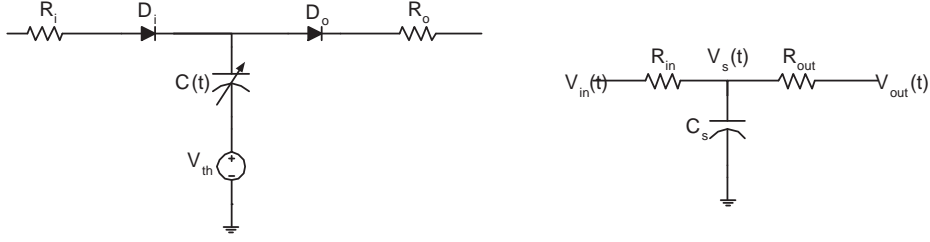


Figure 3.1: (a) A ventricular compartment showing a time-varying compliance, $C(t)$, two heart valves D_i and D_o , valvular resistances R_i and R_o , and an intrathoracic pressure source, V_{th} ; (b) A systemic circulation compartment with fixed compliance, C_s , and inflow and outflow resistances R_{in} and R_{out} , respectively.

a low (systolic or ejection) state and a high (diastolic or filling) state. We describe such time-varying capacitance functions, e.g., Equation (3.18), in Section 3.6.

There are several simplifying assumptions we make in some of the circuit analogs presented here. We neglect ventricular interactions in all our models, for example. Except for the modified Windkessel model, we ignore the effects of inertia in the blood flow (as captured by inductors in the circuit analogs). This is a reasonable assumption as we are not interested in the finer structure of the blood pressure waveforms, such as the presence of the dichrotic notch in the central ABP waveform. In addition, since we assume our models capture only the steady-state values of the hemodynamics – the slow inter-cycle dynamics we are interested in modeling in the ICU setting – we neglect the baroreflex and cardiopulmonary control mechanisms which, on an inter-cycle timescale, tightly control the arterial blood pressure by varying heart rate, ventricular elastance, peripheral resistance, and venous tone. The inclusion of the baroreflex is easily done (see the theses of Samar [8], Mukkamala [33], Heldt [34], or the work of deBoer [61]). Finally, we neglect the time-varying nature of intrathoracic pressure, i.e., whenever we include the intrathoracic pressure source V_{th} , we keep it fixed. In fact, we neglect all other cardiopulmonary interactions in our models as well.

3.2 The Windkessel Model

The Windkessel model describes the basic morphology of an arterial pressure pulse [62]. It lumps the distributed resistive and capacitive properties of the entire arterial tree into two elements, as seen in electrical circuit analog in Fig. 3.2: a single resistor, R_a , representing total peripheral resistance (TPR), and a single capacitor, C_a , representing the aggregate elastic properties of all arteries (see [25, 36, 63] for examples of Windkessel-type models).

The pumping action of the heart is represented by an impulsive current source, $I(t)$, that deposits a stroke volume, SV_n , into the arterial system during the n^{th} cardiac beat (or cycle):

$$I(t) = \sum_n SV_n \cdot \delta(t - t_n) \quad (3.2)$$

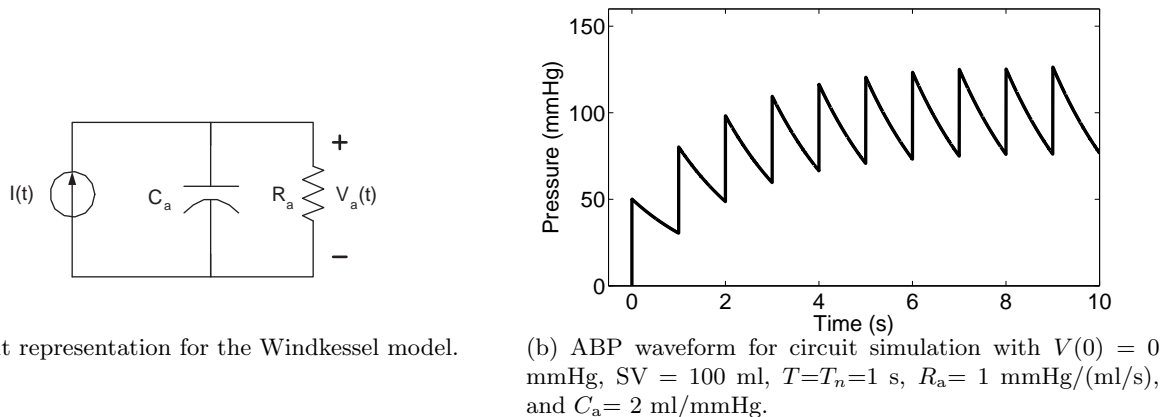


Figure 3.2: Circuit representation for the Windkessel model with a representative pulsatile ABP waveform.

where t_n is the onset time of the n^{th} cardiac cycle and $\delta(t)$ is a unit Dirac impulse at time $t=0$. The differential equation representing the Windkessel circuit at time t is given by

$$C_a \frac{dV(t)}{dt} + \frac{V(t)}{R_a} = I(t) \quad (3.3)$$

where $V(t)$ represents arterial blood pressure at the aortic root at time t . This equation shows that the time constant $\tau=R_a C_a$ governs the intra-cycle dynamics of the Windkessel model. The same time constant also governs the inter-cycle dynamics, as noted in [57, 16] and shown in Chapter 4. For now, we assume both R_a and C_a are fixed, though we will relax this assumption in Chapter 4.

If we assume that $V_a(0)=0$, we can iteratively solve the Windkessel model equation such that we have the following expression for $V_a(t)$ within each cycle:

$$V_a(t) = \frac{SV}{C_a} \frac{\exp\left(-\frac{t-t_n}{R_a C_a}\right)}{\left[1 - \exp\left(-\frac{t_{n+1}-t_n}{R_a C_a}\right)\right]} \quad \text{for } t_n < t < t_{n+1}. \quad (3.4)$$

Pulse pressure in the n^{th} cardiac cycle, PP_n , is defined as the difference between the systolic and the diastolic arterial blood pressures in the cycle, SAP_n and DAP_n , respectively. Due to the impulsive nature of the modeled cardiac ejection in the Windkessel model, pulse pressure is directly related to stroke volume through the arterial compliance:

$$PP_n = SAP_n - DAP_n = \frac{SV_n}{C_a}. \quad (3.5)$$

The pulsatile ABP waveform that results from simulating the model (3.3) with $V(0)=0$ mmHg, $T_n=1$ s (such that heart rate in the n^{th} cycle $HR_n=60$ beats/min), $SV_n=100$ ml, $R_a=1$ mmHg/(ml/s), and $C_a=2$ ml/mmHg, is shown in Fig. 3.2. The resulting steady-state PP equals 50 mmHg.

The Windkessel model has been the basis of several methods for estimating cardiac output ([37, 54, 64, 65]),

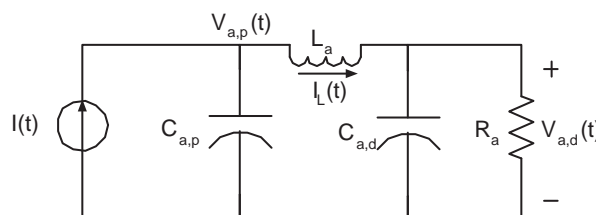


Figure 3.3: The modified Windkessel model in which the arterial tree is divided into a distal and a proximal compartment.

and is also the basis for our model-based CO estimation method described in Chapter 5. For instance, using Equation (2.5), we can write an expression for cardiac output:

$$\text{CO} = \frac{SV_n}{T_n} = C_a \frac{PP_n}{T_n} = f_n C_a PP_n . \quad (3.6)$$

where

$$T_n = t_{n+1} - t_n \quad (3.7)$$

is the duration of the n^{th} cardiac cycle. Equation (3.6) states that cardiac output in the Windkessel model is directly proportional to pulse pressure times heart rate, f_n . The proportionality constant is the lumped arterial compliance. The last expression in Equation (3.6) is the basis for the Windkessel method of estimating proportional cardiac output.

3.3 The Modified Windkessel Model

The modified Windkessel model² shown in Fig. 3.3 is a slightly more elaborate version of the Windkessel model.

In this model, the arterial tree compliance is split into a distal compliance, $C_{a,d}$, representing the less elastic arteries distal from the heart, and a proximal compliance, $C_{a,p}$, representing the highly elastic arteries proximal to the heart. These two compliances are separated by an inductor, L_a , which captures the effects of ABP pulse propagation on the distal and proximal ABP waveforms.

The main difference between the modified and the usual Windkessel models is the additional L_a - $C_{a,d}$ branch in the modified Windkessel model. If we assume that $L_a=0$, and define $C_a=C_{a,p} + C_{a,d}$, the modified Windkessel model reduces to the Windkessel model.

Due to these additional two energy-storage elements in the modified Windkessel model, the state space

²This model is the subject of further work in our group [17], which will not be described here.

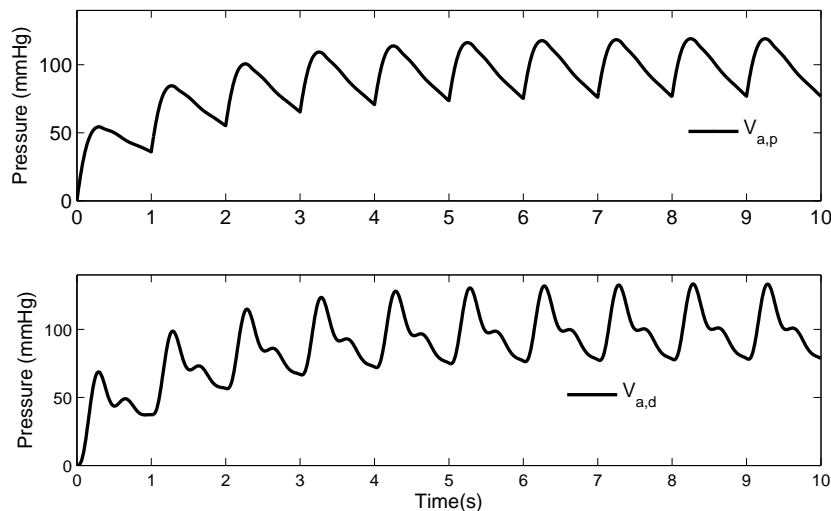


Figure 3.4: Proximal (top) and distal (bottom) ABP waveforms for a simulation of the modified Windkessel model with $V_{a,d}(0) = 0$ mmHg, $V_{a,p}(0) = 0$ mmHg, $SV_n = 100$ ml, $T=T_n=1$ s, $R_a = 1$ mmHg/(ml/s), $L_a = 0.025$ mmHg/ml/s, $C_{a,p} = 1.45$ ml/mmHg, and $C_{a,d} = 0.15$ ml/mmHg.

representation for this model is given by three equations:

$$C_{a,p} \frac{dV_{a,p}}{dt} = -I_L + I \quad (3.8)$$

$$L_a \frac{dI_L}{dt} = V_{a,p} - V_{a,d} \quad (3.9)$$

$$C_{a,d} \frac{dV_{a,d}}{dt} = -\frac{V_{a,d}}{R_a} + I_L \quad (3.10)$$

where the time argument t has been dropped for notational simplicity. As with the Windkessel model, we assume that the heart is modeled as an impulsive current source $I(t)$, given by Equation (3.2). Note that when $L_a=0$ we recover the usual Windkessel model, with $C_a=C_{a,p} + C_{a,d}$.

The modified Windkessel model can be summarized more compactly using vector-matrix notation:

$$\frac{d}{dt} \mathbf{x} = \begin{bmatrix} 0 & -\frac{1}{C_{a,p}} & 0 \\ \frac{1}{L_a} & 0 & -\frac{1}{L_a} \\ 0 & \frac{1}{C_{a,d}} & -\frac{1}{R_a C_{a,d}} \end{bmatrix} \mathbf{x} + \begin{bmatrix} \frac{I}{C_{a,p}} \\ 0 \\ 0 \end{bmatrix} \quad (3.11)$$

where $\mathbf{x}=[V_{a,p} \ I_L \ V_{a,d}]'$ is the vector of state variables.

Figure 3.4 shows the pulsatile ABP waveforms that result from simulating the modified Windkessel model (3.11) with $V_{a,d}(0) = 0$ mmHg, $V_{a,p}(0) = 0$ mmHg, $SV_n = 100$ ml, $T=T_n=1$ s, $R_a = 1$ mmHg/(ml/s), $L_a = 0.025$ mmHg/ml/s, $C_{a,p} = 1.45$ ml/mmHg, and $C_{a,d} = 0.15$ ml/mmHg.

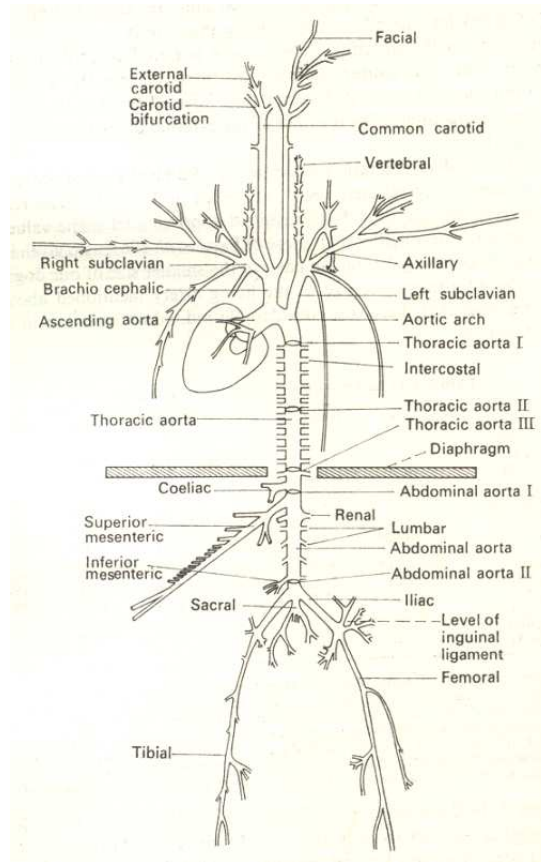


Figure 3.5: A schematic of a canine arterial tree showing the distributed nature of the arterial tree. This figure appears as Fig. 2.10 in [66] and was reproduced with permission from Hodder Education.

3.4 Limitations of the Windkessel Model

In this section we describe some limitations of the Windkessel and modified Windkessel models. The main limitations can be summarized as those pertaining to lumped-parameter modeling – in particular to the lumped arterial compliance – which ignores the distributed effects of blood flow in the arterial tree.

3.4.1 Distributed Effects

One of the main drawbacks of the Windkessel model is that the distributed arterial tree impedance (see Fig. 3.5) is described by just two lumped components. Thus, the transmission line-type effects, e.g., wave propagation, wave speed, etc., in the arterial system are not captured by the usual Windkessel model. For example, the Windkessel model assumes that ABP rises instantaneously in the entire arterial tree instead of becoming successively larger as the ABP wavelet propagates through the lower levels of the arterial tree. In particular, as this wave propagation occurs, arterial blood pressure wavelets become narrower, and have a higher systolic and pulse pressure [33].

Nonetheless, the simple Windkessel model captures the low-frequency dynamics of the central and peripheral arterial blood pressure waveforms quite well [67]. In fact, it captures the morphology of the aortic blood pressure wavelet quite well, aside from the high-frequency dichrotic notch [33]. To capture high-frequency dynamics in the central and/or peripheral arterial blood pressure waveforms (e.g., the dichrotic notch and/or pulse wave reflections which originate at bifurcation or termination points along the peripheral arteries and propagate back to the aorta) along the arterial tree branches, the arterial tree is perhaps better modeled with two or more arterial compartments – one representing the larger, more elastic arteries, and one or more representing the smaller, more muscular arteries [67].

The modified Windkessel model, for example, attempts to improve on the simple Windkessel model by adding on the L_a - $C_{a,d}$ branch. This addition, however, is still only an approximation that is not capable of capturing all the distributed effects. To do so, one would have to add a large number of R - L - C branches in parallel with the usual arterial tree compliance in the Windkessel model, or go to a distributed model based on solving the Navier-Stokes equation [68].

In addition to being unable to capture the distributed nature of the arterial tree, the Windkessel model compliance and resistance are elements with fixed values. While this assumption may be valid for the lumped arterial tree resistance, it is not necessarily true for the lumped arterial tree compliance, as we discuss below.

3.4.2 Arterial Tree Compliance

The lumped arterial tree compliance is a function of arterial blood pressure, and is perhaps better modeled as such rather than as a constant. Furthermore, it is well-known that arterial tree compliance depends on age (as we grow older, our arteries get less elastic and arterial compliance increases [69, 70]), gender, and disease state, e.g., acute arteriosclerosis results in lower compliance [71]. However, this compliance also depends on arterial blood pressure. Figure 3.6 shows mean compliance-pressure curves for thoracic aortas of various age groups presented. Each curve is an average for a particular age group. This figure was constructed using *ex vivo* measurements from eighteen human thoracic aortas, as presented in [69].

If we assume that pulse pressure variations around MAP are small, then we can model the arterial tree compliance to be a function of *mean* arterial blood pressure. Some previous work on CO estimation suggests that the arterial tree compliance is constant over a wide range of mean arterial blood pressures [72, 73, 74]. However, there is no consensus on this observation. While it may hold true for the largest arteries in the body, it does not necessarily hold true for the smaller arteries, as shown by Liu *et al.* [75]. (Since our modeling work is intended for the less invasive peripheral arterial blood pressure waveforms, we need to understand any nonlinearities in the arterial tree compliance.) In addition, researchers such as Burattini *et al.* [76], who conducted canine experiments, have shown that arterial compliance can change drastically in response to vasoactive drugs – partly due to the effect of these drugs on the mean arterial blood pressure and partly due to drug-induced changes in the mechanical properties of the arterial wall.

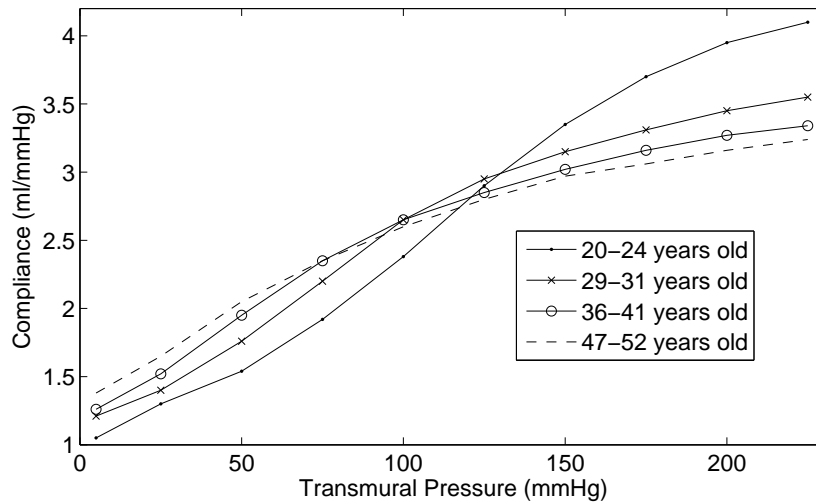


Figure 3.6: Thoracic aorta compliance-pressure curves for various age groups. Each curve is an average for a particular age group. This figure was constructed using *ex vivo* measurements from eighteen human thoracic aortas, as presented in [69].

Several researchers have investigated total arterial compliance and its dependence on mean arterial blood pressure. Westerhof and co-workers [63, 77, 78, 79], for example, have argued that the arterial tree volume depends strongly on pressure – falling sharply at lower pressures and asymptotically converging to a maximum at high pressures. The (incremental) compliance, therefore, is large at low mean pressures and steadily decreases with increasing pressure. In their work, they explored the use of such a nonlinear arterial tree volume-pressure function in various incarnations of the Windkessel model. Liu *et al.* [75] compared several nonlinear arterial volume-pressure relationships, including logarithmic, piecewise-parabolic, and exponential relationships, and a specific linear volume-pressure relationship – with corresponding constant compliance. They argue that for the larger arteries, e.g., the aortic arch and thoracic aorta, a linear fit to the volume-pressure data was sufficient, but for the carotid, femoral, and brachial arteries, a nonlinear relationship fit the volume-pressure data better. In [80, 81], the authors proposed several nonlinear arterial volume-pressure functions and evaluated them using simulated and human data.

In this chapter, we assume that C_a is fixed; however, we relax this assumption later in this thesis, when the compliance C_a plays a critical role in our model-based CO estimation method.

3.5 The CVSIM Model

Circuit analogs for the cardiac chambers and peripheral circulation compartments can easily be combined to create larger, more complex lumped-parameter cardiovascular circuit models, such as the cardiovascular simulator [49], which has been used extensively as a teaching tool for undergraduates, graduates, and medical school students.

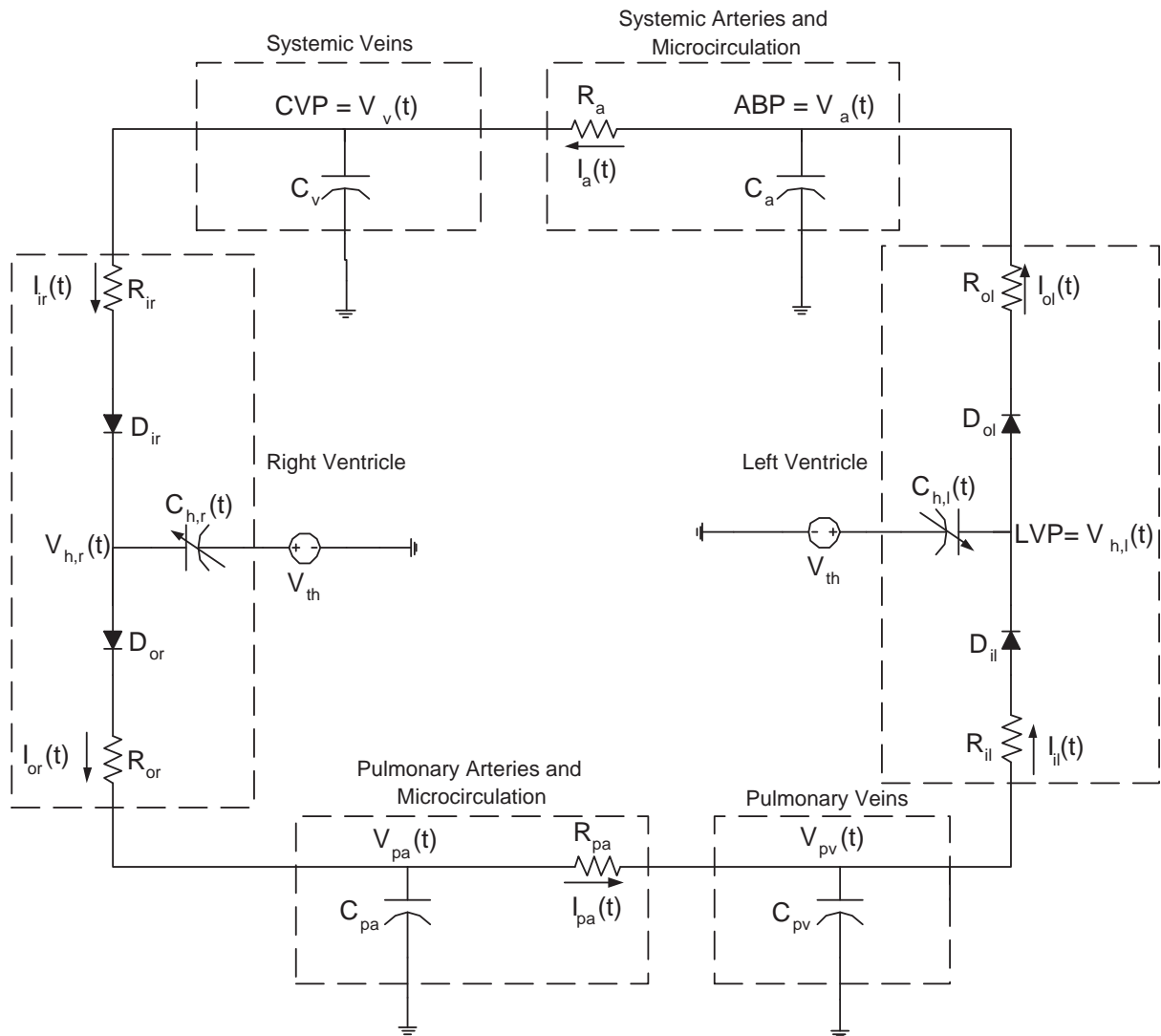


Figure 3.7: Cardiovascular model comprised of two heart compartments (the left and right ventricle) and four systemic circulation compartments for the lungs, arterial system, and venous system.

A block diagram of the CVSIM model is shown in Fig. 3.7, where the ABP, left ventricular pressure (LVP), and CVP³ are labeled. This model is comprised of six compartments including the left and right ventricles, the systemic arteries and veins, and the pulmonary arteries and veins. CVSIM is capable of representing the hemodynamic manifestations of a variety of cardiovascular diseases such as myocardial infarction, hemorrhage, valvular disease, and pulmonary edema.

CVSIM can be fully described by six coupled first order differential equations. These equations are nonlinear, as the circuit contains ideal diodes, and are time-varying because of the ventricular compliances. The equations for the CVSIM model, and the nominal parameters are listed in [49], as well as in the theses of Mukkamala [82, 83] and Samar [8], that describe the more recent incarnations of the CVSIM model. We have included the model equations and nominal parameters in Appendix B.

As with the Windkessel-type models above, we again do not describe the baroreflex and cardiopulmonary control mechanisms that, on a beat-to-beat timescale, tightly control mean arterial blood pressure. These reflex mechanisms have been incorporated into other implementations of the CVSIM model [8, 49, 56, 82, 83]. If we were to simulate short-term responses to parameters in the CVSIM model, we would need to, at least, wrap the baroreflex control loop around the model shown in Fig. 3.7, as is done in the work of Samar [8] and Heldt [34].

3.6 The CVSIMple Model

It is possible to use simpler lumped-parameter models of the cardiovascular dynamics to simulate reasonable approximations of hemodynamic waveforms. A simpler version of the CVSIM model that was recently proposed ([41, 42]) provides an abstracted view of the body's circulation (similar models were proposed by Guyton and co-workers in 1963 [25], and by a group at Penn. State University in 1982 [84]). This model, which we will refer to as the *CVSIMple* model, combines the pulmonary and cardiac compartments from CVSIM into a single ventricular compartment, which we can usually think of as the left ventricle. In doing so, it is assumed that the right-heart, pulmonary, and left-heart compartments act as a single functional unit. This assumption is justified if the model is intended for use mainly in simulating systemic vascular disease conditions, e.g., hemorrhaging in the systemic circulation.

Figure 3.8 shows the circuit for the CVSIMple model where C_a is the arterial compliance, C_v is the venous compliance, $C_h(t)$ is the time-varying ventricular compliance, R_1 is the inflow resistance to the ventricle, R_2 is the outflow resistance from the ventricle, and R_a is the total peripheral resistance.

³The pressure across C_v is more analogous to peripheral venous pressure, but we nevertheless refer to it as CVP here.

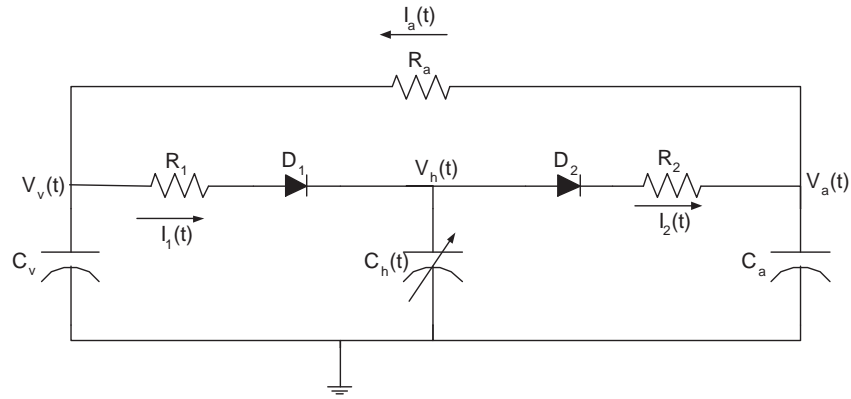


Figure 3.8: The CVSIMple model. This cardiovascular model has only one ventricular compartment and is represented by three nonlinear time-varying differential equations and seven model parameters.

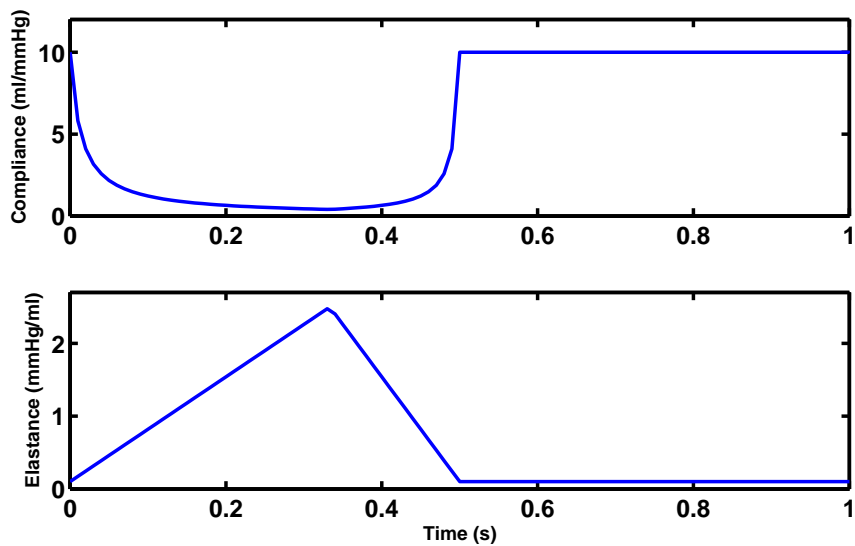


Figure 3.9: Compliance and piecewise linear elastance functions for the CVSIMple model for $T = 1$ s.

The state space equations for the CVSIMple model are as follows⁴:

$$\frac{dQ_h}{dt} = I_1 - I_2 \quad (3.12)$$

$$\frac{dV_a}{dt} = \frac{I_2 - I_a}{C_a} \quad (3.13)$$

$$\frac{dV_v}{dt} = \frac{I_a - I_1}{C_v} \quad (3.14)$$

where the time argument t has been dropped for notational convenience, and where the various flow rates are given by:

$$I_1 = \begin{cases} \frac{V_v - V_h}{R_1} & \text{if } V_v > V_h \\ 0 & \text{otherwise} \end{cases} \quad (3.15)$$

$$I_2 = \begin{cases} \frac{V_h - V_a}{R_2} & \text{if } V_h > V_a \\ 0 & \text{otherwise} \end{cases} \quad (3.16)$$

$$I_a = \frac{V_a - V_v}{R_a} \quad (3.17)$$

where, again, the time argument t has been dropped for notational simplicity.

The compliance and elastance for the ventricular compartment in the CVSIMple model are illustrated in Fig. 3.9. The elastance function $E_h(t) = 1/C_h(t)$ for the ventricle is represented as a piecewise linear (PWL) function given by:

$$E_h(t) = \begin{cases} \frac{3(E_s - E_d)}{T}t + E_d & \text{for } 0 \leq t \leq \frac{T}{3} \\ \frac{6(E_s - E_d)}{T}(\frac{T}{3} - t) + E_s & \text{for } \frac{T}{3} \leq t \leq \frac{T}{2} \\ E_d & \text{for } \frac{T}{2} \leq t \leq T \end{cases} \quad (3.18)$$

where T is the duration of the cardiac cycle, E_s is the end-systolic elastance, and E_d ($\ll E_s$) is the end-diastolic elastance. For now, we assume that T is fixed, but in general, for implementation purposes, one only needs to assume that T is fixed within each cardiac cycle. Such a time-varying elastance function approximates human data quite well [85, 86, 87, 88]. In the CVSIM model and in the models used in

⁴ $Q_h(t)$ is used as a state variable instead of $V_h(t)$ because it ensures smaller numerical errors, as the term $\frac{dC_h(t)}{dt}$ does not appear in the state-space model.

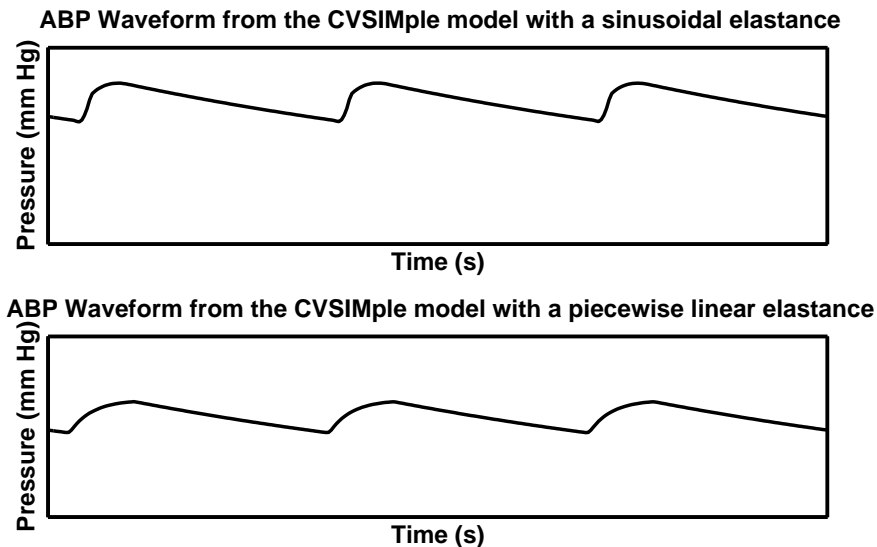


Figure 3.10: Comparison of two elastance functions (piecewise linear and sinusoidal) in the CVSIMple for $T=1$ s. This simulation was performed in MATLAB R14 (The Mathworks Inc., Natick, MA).

[56, 82, 83], a sinusoidal ventricular elastance function of the following form⁵:

$$E_h(t) = \begin{cases} \frac{1}{2}(E_s - E_d) \left(1 - \cos\left(\frac{\pi t}{0.3\sqrt{T}}\right)\right) + E_{d,1} & \text{for } 0 \leq t \leq 0.3\sqrt{T} \\ \frac{1}{2}(E_s - E_d) \left(1 - \cos\left(\frac{2\pi(t-0.3\sqrt{T})}{0.3\sqrt{T}}\right)\right) + E_d & \text{for } 0.3\sqrt{T} \leq t \leq \frac{0.9\sqrt{T}}{2} \\ E_d & \text{for } \frac{0.9\sqrt{T}}{2} \leq t \leq T \end{cases} \quad (3.19)$$

was used instead of the PWL elastance function. We have confirmed that using a PWL elastance instead of a sinusoidal elastance function does not result in waveforms with significantly different morphologies. Figure 3.10 shows ABP waveforms that we obtained using the PWL elastance (3.18) and the sinusoidal elastance (3.19) in the CVSIMple model. The main difference between the two waveforms is the larger initial slope of the ABP waveform from the CVSIMple model at the onset of systole. This larger initial slope results in a slightly larger steady-state pulse pressure.

The parameters used in the CVSIMple model, including the initial conditions (assuming the simulation begins at $t=0$) for our simulations, are shown in Table 3.1. These parameters represent typical values for a 70 kg male human [34], and, when used with Equation (3.18), result in reasonable *approximations* of the pressure waveforms during the cardiac cycle.

In the CVSIMple model, the PWL elastance function and the ideal diodes in the heart compartment result in a cardiac cycle with seven distinct regions as shown in Fig. 3.11. These regions of operation are

⁵The function (3.19) is used, with E_d and E_s from Table 3.1, for the left ventricle in the CVSIM model.

3.7 The Simple Pulsatile Cardiovascular Model

Parameter	Value
R_1	0.01 mmHg/(ml/s)
R_2	0.03 mmHg/(ml/s)
R_a	1 mmHg/(ml/s)
C_a	2 ml/mmHg
C_v	100 ml/mmHg
E_d	0.1 mmHg/ml
E_s	2.5 mmHg/ml
$V_a(0)$	91.2 mmHg
$V_v(0)$	15.0 mmHg
$Q_h(0)$	127.4 ml
T	1 s

Table 3.1: Summary of parameters for the SPCVM and the CVSIMple models [15].

Region	Slope of PWL Function	Diode D ₁ State	Diode D ₂ State
I (contraction)	Positive	On	Off
II (isovolumic contraction)	Positive	Off	Off
III (ejection)	Positive	Off	On
IV (ejection)	Positive	Off	On
V (isovolumic relaxation)	Negative	Off	Off
VI (relaxation)	Negative	On	Off
VII (filling)	Zero	On	Off

Table 3.2: The seven regions of the CVSIMple model. Each region is uniquely determined by the diode states and the slope of the piecewise linear elastance function.

determined by the states of the two diodes and the behavior of the PWL elastance function as displayed in Table 3.2.

3.7 The Simple Pulsatile Cardiovascular Model

Another pulsatile model that we recently proposed [15, 16], the *simple pulsatile cardiovascular model*, or SPCVM, is a simplification of the CVSIMple model, and is thus, again, justified for use mainly in simulating systemic vascular disease conditions. We modified the CVSIMple model to create the SPCVM so as to have a simpler model for applying the cycle-averaging methodology discussed in Chapter 4. Had we used the CVSIMple model as is, it would have been more difficult to derive the cycle-averaged model, explained in detail in Chapter 4.

Figure 3.12 illustrates the circuit for the pulsatile model, where C_a is the arterial compliance, C_v is the venous compliance, $C_h(t)$ is the time-varying ventricular compliance, R_1 is the inflow resistance to the ventricle, R_2 is the outflow resistance from the ventricle, and R_a is the total peripheral resistance. The voltage $V_h(t)$ is the ventricular pressure (VP), $V_v(t)$ is CVP, and $V_a(t)$ is ABP. The ventricular volume is $Q_h(t)$. The elastance $E_h(t)$ and the parameters for the SPCVM are the same as those in the CVSIMple

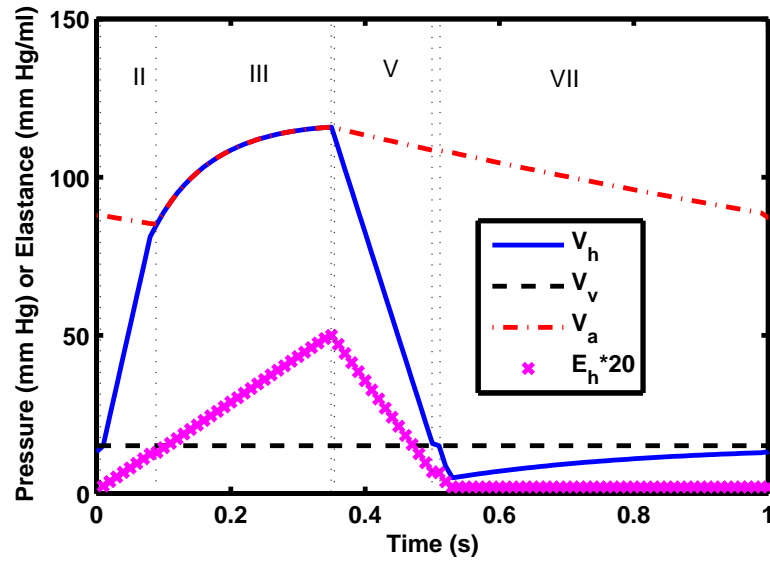


Figure 3.11: Waveforms generated during a single cycle of the CVSIMple for $T=1$ s. This circuit has seven regions of operation (four of which are labeled in the figure).

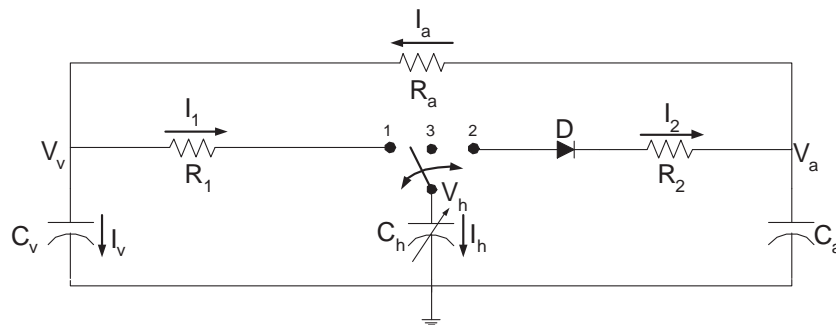


Figure 3.12: The simple pulsatile cardiovascular model (SPCVM) uses a 3-way switch which allows for simpler analysis of the circuit.

model, and are given in Table 3.1.

We can define switching functions for the switch and diode in the SPCVM. Figure 3.13 shows these switching functions for $T=1$ s where $s_1(t)$ equals 1 when the switch is in position 1, and 0 otherwise; $s_2(t)$ equals 1 when the switch is in position 2, and 0 otherwise; $s_3(t)$ equals 1 when the switch is in position 3, and 0 otherwise; and $s_D(t)$ equals 1 when the diode D is conducting (between $t=t_D$ and $t=\frac{T}{3}$), and 0 otherwise. The switching function $s_2(t)$ is redundant since $s_D(t)$ is sufficient for describing the flow through the diode D. The main reason for using a switch in the SPCVM instead of the two diodes in the CVSIMple model is to eliminate regions I, IV, and VI of the CVSIMple model. As we can observe in Fig. 3.11, these three regions have durations that are small compared to regions II, III, V, and VII. Furthermore, by eliminating regions I, IV and VI, we have a cardiovascular model whose regions of operation correspond directly to the four periods of the cardiac cycle: isovolumic contraction, ejection and isovolumic relaxation, and filling.

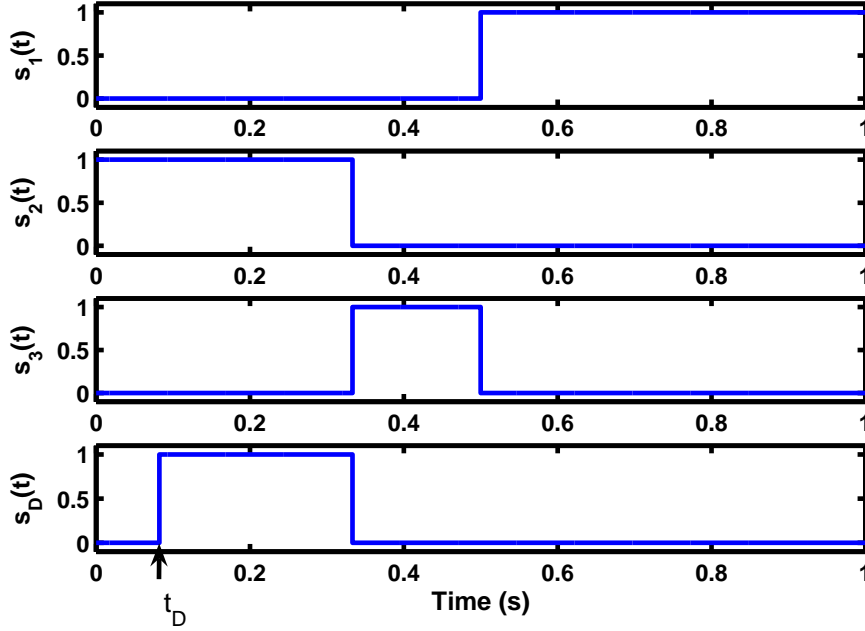


Figure 3.13: Switching functions for the 3-way switch and diode in the pulsatile model for $T=1$ s. The diode turn-on time t_D is marked on the bottom panel.

Region	Switch Position	Diode State
I (isovolumic contraction)	2	Off
II (ejection)	2	On
III (isovolumic relaxation)	3	Off
IV (filling)	1	Off

Table 3.3: Definition of the four regions in the SPCVM.

Therefore, the SPCVM has four regions of operation, corresponding directly to the four periods of the cardiac cycle: isovolumic contraction (I), ejection (II), isovolumic relaxation (III), and filling (IV), as shown in Fig. 3.14. The four regions are determined by the position of the switch and the state of the diode, as indicated in Table 3.3.

With the switching functions described above, and with $Q_h(t)$, $V_a(t)$ and $V_v(t)$ as state variables, we have a state-space description for the SPCVM given by

$$\frac{dQ_h}{dt} = \frac{s_1(V_v - E_h Q_h)}{R_1} + \frac{s_D(V_a - E_h Q_h)}{R_2} \quad (3.20)$$

$$C_a \frac{dV_a}{dt} = \frac{s_D(E_h Q_h - V_a)}{R_2} + \frac{(V_v - V_a)}{R_a} \quad (3.21)$$

$$C_v \frac{dV_v}{dt} = \frac{s_1(E_h Q_h - V_v)}{R_1} + \frac{(V_a - V_v)}{R_a} \quad (3.22)$$

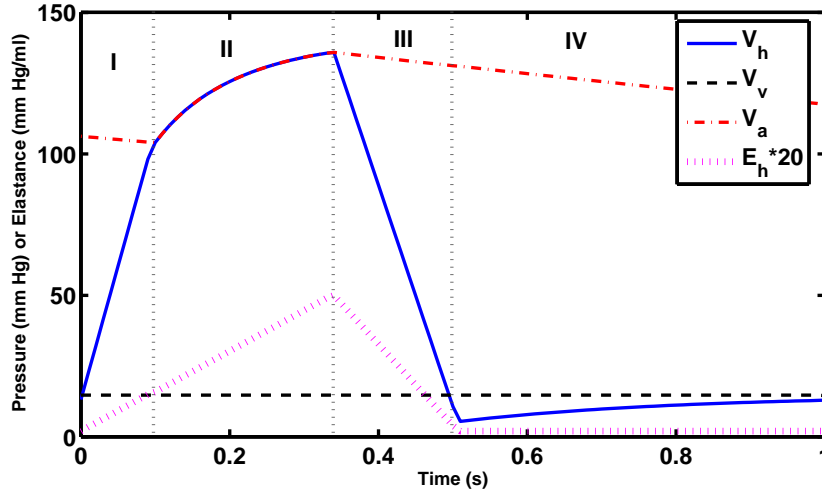


Figure 3.14: Waveforms generated over a single cycle of the pulsatile model for $T=1$ s. This circuit has four regions of operation. Each region is uniquely defined by the switch position, the state of the time-varying compliance $C_h(t)$, and the diode state.

More compactly, we can write

$$\frac{d}{dt} \mathbf{x} = \mathcal{A}(s_1, s_D, p) \mathbf{x} = \begin{bmatrix} -\frac{(s_1 R_2 + s_D R_1) E_h}{R_1 R_2} & \frac{s_D}{R_2} & \frac{s_1}{R_1} \\ \frac{s_D E_h}{C_a R_2} & -\frac{(s_D R_a + R_2)}{C_a R_2 R_a} & \frac{1}{C_a R_a} \\ \frac{s_1 E_h}{C_v R_1} & \frac{1}{C_v R_a} & -\frac{(s_1 R_a + R_1)}{C_v R_1 R_a} \end{bmatrix} \mathbf{x} \quad (3.23)$$

where $\mathbf{x}=[Q_h V_a V_v]'$ is the vector of state variables.

By making certain assumptions about $V_v(t)$, it is possible to find an analytical solution for the SPCVM similar to that previously published for the CVSIMple model [42]. For circuit analysis of the different regions of the SPCVM, see Appendix C. For an example of an implementation of the SPCVM in MATLAB R14 (The Mathworks Inc., Natick, MA), see Appendix E.

To confirm that using the SPCVM instead of the CVSIM model or CVSIMple models does not result in intolerable information loss, especially in terms of pressure waveform morphology, we simulated the CVSIM, CVSIMple, and the SPCVM using the parameter values from [49] (also in Appendix B) for the CVSIM model, and the values given in Table 3.1 for the CVSIMple model and the SPCVM. The piecewise linear elastance function (3.18) was used in all three models. The result of this simulation is shown in Fig. 3.15. It shows that there is little information loss as the waveforms from these three models are quite comparable.

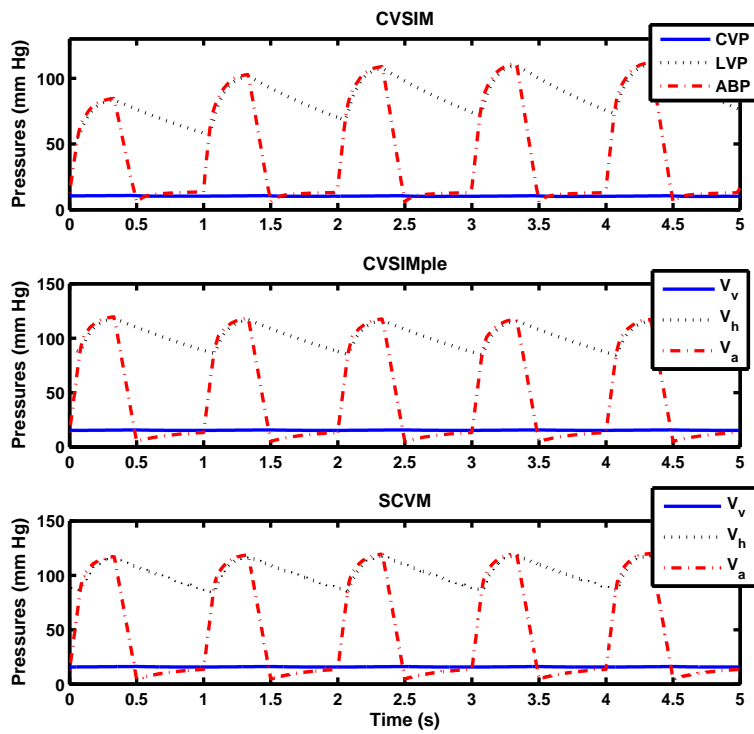


Figure 3.15: Comparison of the SPCVM to the CVSIMple and CVSIM models for $T=1$ s. These models were simulated in HSPICE circuit simulation software.

3.8 Conclusion

In this chapter we discussed several pulsatile electrical circuit models of cardiovascular dynamics, with emphasis on the Windkessel, the modified Windkessel, and the simple pulsatile cardiovascular models. Pulsatile models are frequently-used to understand and simulate inter-beat (or inter-cycle) dynamics, these models tend to be too detailed and computationally burdensome as the simulation time step generally has to be chosen much shorter than the cardiac cycle length.

Averaged models, on the other hand, are much less detailed and computationally burdensome and are more appropriate for settings such as the ICU in which dynamics occur over timescales of a few seconds to minutes. In these settings, blood pressure waveform morphology may be less important to track than average blood pressure. The Windkessel model, being the simplest model presented thus far, is the starting point for the application of the averaging methodology discussed in Chapter 4.

Averaged Models of Cardiovascular Dynamics

LUMPED-PARAMETER time-varying electrical circuit analogs for the cardiovascular system are frequently used in medical research and teaching for simulating and analyzing hemodynamic data¹. In Chapter 3, we studied pulsatile models of cardiovascular dynamics, which provide details of the *intra*-cycle dynamics of each heart beat. In some settings, however, e.g., in the ICU, it may be more useful to dynamically – either in discrete-time or in continuous-time – track the beat-to-beat or *inter*-cycle dynamics. Figure 4.1, for example, shows the pulsatile arterial blood pressure (ABP) and left ventricular pressure (LVP) waveforms, along with their calculated continuous-time *cycle-averages* from a simulation of the SPCVM of Chapter 3. In order to capture the transient changes in ABP or LVP, it would for many purposes suffice to capture their discrete-time or continuous time averages. In order to represent these averages dynamically we need to develop a *averaged* models of cardiovascular dynamics.

In this chapter, we study two types of averaged models of cardiovascular dynamics – discrete-time beat-to-beat averaged models and continuous-time cycle-averaged models. We begin by showing how to integrate the model equations for a pulsatile model of cardiovascular dynamics to obtain a beat-to-beat averaged model. This type of sampled-data model has wide-ranging applications as we shall see in Chapter 5. We then compare and contrast the beat-to-beat averaging methodology to cycle-averaging methodology. In particular, we show that rather than introducing heuristic averaging during the model-building step, as is done in existing *non-pulsatile* models, one can apply a short-term, cycle-averaging operation to the differential equations of the underlying pulsatile model to obtain cycle-averaged models. The cycle-averaging method preserves the dependence of the output variables on the model parameters. In particular, we apply cycle-averaging to a simple pulsatile cardiovascular model to derive a cycle-averaged model for cardiovascular dynamics. The resultant model captures the inter-cycle dynamics with relatively small approximation errors for a large range of perturbations in important system parameters.

In Section 4.2, we describe the beat-to-beat averaging methodology and apply it to the well-known Windkessel model and modified Windkessel models to derive beat-to-beat averaged Windkessel and modified Windkessel models, respectively. Beginning in Section 4.3, we describe cycle-averaged models. In Section 4.3.1, we describe the basic cycle-averaging methodology and also apply it to the Windkessel and modified Windkessel models. In Section 4.3.3, we again describe the SPCVM. After some additional background on cycle-averaging in Section 4.3.4, we derive in Section 4.3.5 a cycle-averaged representation for the SPCVM introduced in Chapter 3. Simulation results obtained using this cycle-averaged model are

¹This chapter is partially based on two IEEE papers [15, 16]. The material has been reproduced with permission.

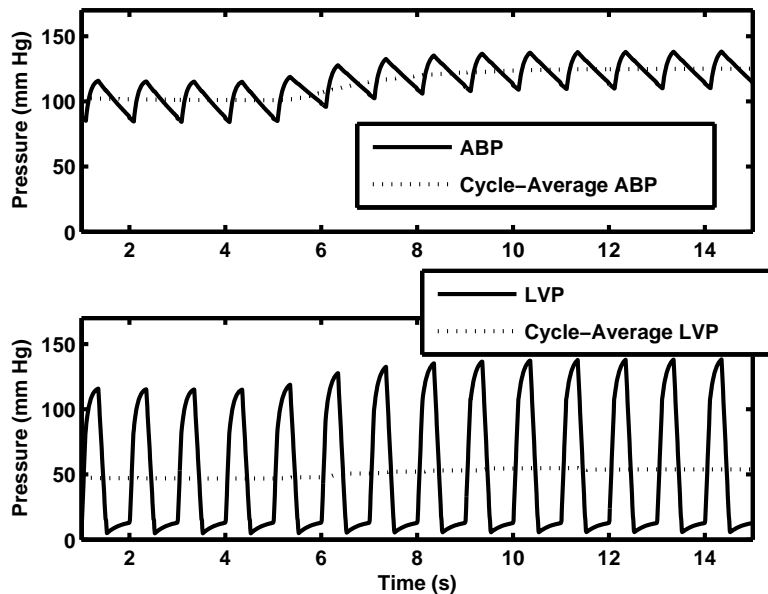


Figure 4.1: Response of the SPCVM to a step change in total peripheral resistance at time $t=5$ s. Both the pulsatile and continuous-time averaged ABP and LVP waveforms are shown.

presented and evaluated in Section 4.3.6. We conclude with a chapter summary.

4.1 Background

As mentioned in Chapter 1, integration and interpretation of hemodynamic data streams are particularly important in the clinical environment of the intensive care unit. Given the vast and varied amount of clinical information collected from each patient in intensive care, computational models have the potential to play an important role in integrating a patient’s hemodynamic data streams into a common framework, analyzing and interpreting the available information, and presenting resultant pathophysiological hypotheses to the clinical staff in an efficient manner [7]. To employ computational physiological models in such a way, one needs to match the model structure to the characteristics of the data streams collected at the patient’s bedside. This matching must be done both in terms of the time scales involved and the computational complexity of the forward and inverse problems to be solved. In developing discrete-time *beat-to-beat averaged* and continuous-time *cycle-averaged* models of cardiovascular dynamics from pulsatile ones, we aim to expand the repertoire of model structures available for matching to clinical data.

Unlike averaged models, *non-pulsatile models* simulate the time-average behavior of cardiovascular variables and thus reduce the computational overhead associated with pulsatile models [89, 90]. In order to derive non-pulsatile models, an implicit averaging step has to be taken to transform the pulsatile nature of cardiac outflow to an average flow over the cardiac cycle. Kappel and Peer [90], for example, based on work by

Grodins [89], used a heuristic formula to relate stroke volume to average ventricular end-diastolic volume, which in turn they related to average pre- and after-load and average cardiac contractility. Similarly, Boyers and co-workers [91] made stroke volume a function of average central blood volume and average autonomic activity.

Similar to the pulsatile models described in Chapter 3, there are several simplifying assumptions we have made in our models of cardiovascular dynamics. We, again, assume the elements of the systemic (or peripheral) circulation to be linear and time-invariant (LTI). Although LTI inertial and distributed-parameter effects are easily incorporated into the averaging framework, we omit them as they are relatively insignificant for the slow inter-cycle variations we intend to capture with our beat-to-beat or cycle-averaged models. Similarly, we neglect the baroreflex and cardiopulmonary control mechanisms that, on an inter-beat timescale, tightly control mean arterial blood pressure. These mechanisms act on time scales of a heart cycle or longer. However, they typically use beat-to-beat-averaged rather than instantaneous (or pulsatile) quantities as their inputs [92, 93]. Thus, it is not necessary to model them for purposes of deriving an averaged model. Instead, once an averaged model has been obtained, the various control loops can be wrapped around it if required.

4.2 Beat-to-Beat Averaged Models

Discrete-time beat-to-beat averaged models can be used to track the averages of the waveforms of an underlying pulsatile model in discrete-time. To derive the beat-to-beat average model for a pulsatile model, one simply finds the average of the pulsatile model over a single cardiac cycle, as we show below with the Windkessel and modified Windkessel models.

4.2.1 Beat-to-Beat Averaged Windkessel Model

As mentioned in Chapter 3, the Windkessel model describes the beat-to-beat variations that occur in arterial blood pressure. The differential equation representing the Windkessel circuit at time t is given by Equation (3.3), repeated here for convenience:

$$C_a \frac{dV(t)}{dt} + \frac{V(t)}{R_a} = I(t) \quad (4.1)$$

where, as before, $I(t)$ is given by:

$$I(t) = \sum_n SV_n \cdot \delta(t - t_n) . \quad (4.2)$$

We define T_n to be the duration of the n^{th} cardiac cycle (or beat), i.e., the beat that begins at some distinct time t_n (which we take to be the end-diastolic minimum that precedes the cycle), and ends at the

corresponding distinct time t_{n+1} of the next cycle:

$$T_n = t_{n+1} - t_n . \quad (4.3)$$

Average cardiac output in the n^{th} cycle is then given by:

$$\text{CO}_n = \frac{\text{SV}_n}{T_n} = C_{an} \frac{\text{PP}_n}{T_n} \quad (4.4)$$

where C_{an} is the lumped arterial tree compliance in the n^{th} cardiac cycle.

Equation (4.4) can be used to estimate beat-to-beat values proportional to cardiac output, given pulse pressure. However, we proceed here to derive an alternative expression – that for the beat-to-beat averaged Windkessel model. The derivation proceeds as follows: as R_a and C_a are assumed to be constant within each cardiac cycle, we may average Equation (4.1) from the onset of the beat at t_n to the onset of the next beat at t_{n+1} as follows:

$$\frac{C_{an}}{T_n} \int_{t_n}^{t_{n+1}} \frac{dV_a(t)}{dt} dt + \frac{1}{T_n R_{an}} \int_{t_n}^{t_{n+1}} V_a(t) dt = \frac{1}{T_n} \int_{t_n}^{t_{n+1}} I(t) dt . \quad (4.5)$$

where the time constant τ_n equals $R_{an} \cdot C_{an}$ and R_{an} is the lumped arterial tree resistance in the n^{th} cardiac cycle. (This application of beat-to-beat averaging is a simple example of a general method known as the modulating function technique [94], first proposed by Shinbrot [95].) Since stroke volume in the n^{th} cycle is

$$\text{SV}_n = \int_{t_n}^{t_{n+1}} I(t) dt \quad (4.6)$$

and the average arterial blood pressure over the n^{th} cycle is

$$\bar{V}_{an} = \frac{1}{T_n} \int_{t_n}^{t_{n+1}} V_a(t) dt \quad (4.7)$$

Equation (4.5) reduces to

$$C_{an} \frac{\Delta V_{an}}{T_n} + \frac{\bar{V}_{an}}{R_{an}} = \text{CO}_n \quad (4.8)$$

where $\Delta V_{an} = V_a(t_{n+1}) - V_a(t_n)$. This model captures the dynamic evolution of the beat-to-beat (or discrete-time) average arterial blood pressure, \bar{V}_{an} . Note that Equation (4.8) is a natural discrete-time counterpart to Equation (4.1). We compare and contrast this model to the continuous-time cycle-averaged Windkessel model below.

4.2.2 Beat-to-Beat Averaged Modified Windkessel Model

Along the same lines as above, we can also derive a beat-to-beat averaged modified Windkessel model in Fig. 4.2.

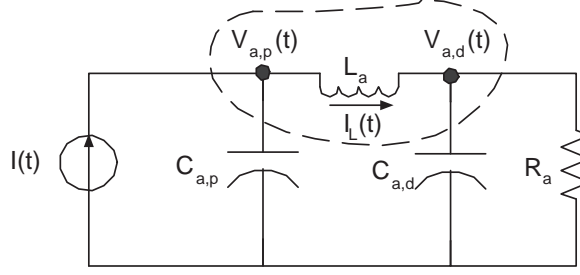


Figure 4.2: Analysis of the modified Windkessel circuit model, showing the supernode that includes $V_{a,p}$, L_a , and $V_{a,d}$.

The derivation proceeds as follows. Using Kirchhoff's current law to analyze the supernode that includes $V_{a,p}$, L_a , and $V_{a,d}$ in the modified Windkessel model circuit of Fig. 4.2 (marked in Fig. 4.2), we can write the following relation:

$$C_{a,p} \frac{dV_{a,p}(t)}{dt} + C_{a,d} \frac{dV_{a,d}(t)}{dt} + \frac{V_{a,d}(t)}{R_a} = I(t) . \quad (4.9)$$

By integrating (4.9) over a single cardiac cycle (or beat), we have:

$$\frac{C_{a,pn}}{T_n} \int_{t_n}^{t_{n+1}} \frac{dV_{a,p}(t)}{dt} dt + \frac{C_{a,dn}}{T_n} \int_{t_n}^{t_{n+1}} \frac{dV_{a,d}(t)}{dt} dt + \frac{1}{T_n R_{an}} \int_{t_n}^{t_{n+1}} V_{a,d}(t) dt = \frac{1}{T_n} \int_{t_n}^{t_{n+1}} I(t) dt \quad (4.10)$$

where T_n is defined by (4.3), $C_{a,pn}$ is the proximal arterial tree compliance, $C_{a,dn}$ is the distal arterial tree compliance, and R_{an} is the total peripheral resistance, all in the n^{th} cardiac cycle.

Again, since stroke volume in the n^{th} cycle is

$$SV_n = \int_{t_n}^{t_{n+1}} I(t) dt \quad (4.11)$$

and the average distal arterial blood pressure over the n^{th} cycle is

$$\overline{V_{a,dn}} = \frac{1}{T_n} \int_{t_n}^{t_{n+1}} V_{a,d}(t) dt \quad (4.12)$$

Equation (4.10) reduces to:

$$C_{a,pn} \frac{\Delta V_{a,pn}}{T_n} + C_{a,dn} \frac{\Delta V_{a,dn}}{T_n} + \frac{\overline{V_{a,dn}}}{R_{an}} = CO_n . \quad (4.13)$$

where $\Delta V_{a,pn} = V_{a,p}(t_{n+1}) - V_{a,p}(t_n)$ and $\Delta V_{a,dn} = V_{a,d}(t_{n+1}) - V_{a,d}(t_n)$. Note that (4.13) is the natural discrete-time counterpart to (4.9).

4.3 Cycle-Averaged Models

Cycle-averaged models can be used to track the averages of the waveforms of an underlying pulsatile model in continuous-time. To do so, one applies a short-term, cycle-averaging operation to the differential equations of the underlying pulsatile model. Such an approach, with certain systematic approximations, leads to cycle-averaged models, and has found much applicability in the area of power electronics [96]. The cycle-averaging process preserves the dependence of the output variables on the model parameters, which is a fundamental advantage over the *a priori* determination of such relationships during the model-building step for non-pulsatile models. In some cases, linear and time-invariant cycle-averaged models can be derived for nonlinear, time-varying pulsatile models [41]. A rich set of analysis tools can then be applied to these cycle-averaged models.

4.3.1 Cycle-Averaged Windkessel Model

In this section, we proceed to demonstrate our cycle-averaging methodology on the simple Windkessel model [35, 36], whose circuit representation appears in Fig. 4.3.

To derive this cycle-averaged model, we assume that stroke volume, SV_n , and the duration of the cardiac cycle, T_n , are fixed such that $SV_n=SV$ and $T_n=T$. While these assumptions are not necessary, they make it easier to understand our example here. It follows that $I(t)$, still modeled as an impulsive current source, given by

$$I(t) = SV \sum_n \delta(t - t_n) . \quad (4.14)$$

The state-space equation for the Windkessel circuit, repeated here for convenience, is as follows:

$$\frac{dV_a}{dt} + \frac{V_a}{R_a C_a} = \frac{I}{C_a} , \quad (4.15)$$

where the time argument t has been dropped for simplicity.

The pulsatile arterial blood pressure (ABP) waveform that results from simulating the model (4.15) with $V_a(0)=0$ is shown in Fig. 4.3. The pulse pressure in each cardiac cycle is given by

$$PP = \frac{SV}{C_a} . \quad (4.16)$$

We now describe the basic cycle-averaged methodology (see [96, 97, 98]) and apply it to the Windkessel model to derive the cycle-averaged Windkessel model. Our starting point is the complex Fourier series

representation for a signal $x(\tau)$ on the interval $[t - T, t]$, which can be written as

$$x(\tau) = \sum_{k=-\infty}^{\infty} X_k(t) e^{jk \frac{2\pi}{T} \tau} . \quad (4.17)$$

The $X_k(t)$ are the complex Fourier series coefficients, also referred to as the index- k cycle-averages of $x(\tau)$ and thus denoted by $\langle x \rangle_k(t)$. These complex coefficients are given by

$$X_k(t) = \langle x \rangle_k(t) = \frac{1}{T} \int_{t-T}^t x(\tau) e^{-jk \frac{2\pi}{T} \tau} d\tau \quad (4.18)$$

due to the orthogonality properties of the basis functions $\{e^{-jk \frac{2\pi}{T} \tau}\}$ on an interval of length T . For any real signal $x(t)$, X_k and X_{-k} are complex conjugates:

$$X_k = X_k^R + jX_k^I = X_{-k}^* \quad (4.19)$$

where the superscripts R and I denote real and imaginary parts, and $*$ denotes complex conjugation.

If $x(\tau)$ were strictly periodic with period T , then the $X_k(t)$ would be constants, independent of t . For waveforms that deviate only slowly and/or slightly from such strict periodicity, it is reasonable to assume that the $X_k(t)$ will have only slow and/or slight departures from constant values. This can be exploited when making modeling approximations.

From (4.18), with $k=0$, we obtain the standard formula for the cycle-average of the variable $x(t)$, namely

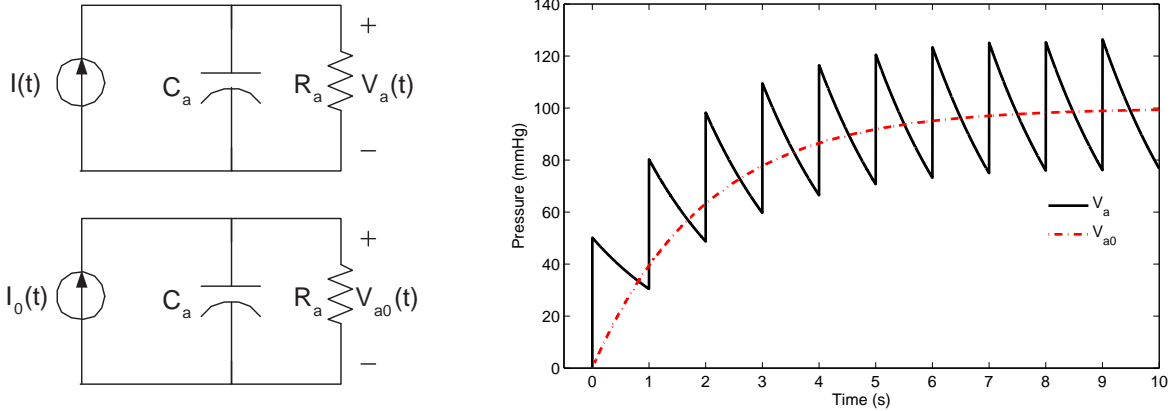
$$X_0(t) = \langle x \rangle_0(t) = \frac{1}{T} \int_{t-T}^t x(\tau) d\tau. \quad (4.20)$$

This index-0 cycle-average is simply the dc term in the Fourier series (4.17). It is also the short-term average of the variable $x(t)$ that we wish to track in our cycle-averaged models, and we will often simply write $\langle x \rangle(t)$ for $\langle x \rangle_0(t)$. In the cardiovascular models in which we apply these expressions, T is the length of the cardiac cycle, assumed to be known and essentially constant over the analysis interval of interest, though possibly different from one analysis interval to another.

By differentiating (4.18) under the assumption of constant T and setting $k=0$, we obtain an expression for the derivative of the index-0 cycle-average:

$$\frac{d}{dt} X_0(t) = \frac{d}{dt} \langle x \rangle_0(t) = \left\langle \frac{dx}{d\tau} \right\rangle_0 (t) . \quad (4.21)$$

By applying (4.20) and (4.21) to the state-space equation (4.15) for the Windkessel circuit, and taking note of (4.14), we obtain the following index-0 cycle-averaged Windkessel model (one could also directly



(a) Circuit representations for the pulsatile and cycle-averaged Windkessel model.

(b) Representative ABP waveforms – both pulsatile and cycle-averaged – for circuit simulations with $V_a(0) = 0$ mmHg, $SV = SV_n = 100$ ml, $T_n = 1$ s, $R_a = 1$ mmHg/(ml/s), and $C_a = 2$ ml/mmHg.

Figure 4.3: Windkessel (top) and cycle-averaged Windkessel (bottom) model circuit representations with representative pulsatile and cycle-averaged ABP waveforms.

average the circuit, see [99]):

$$\frac{dV_{a0}}{dt} + \frac{V_{a0}}{R_a C_a} = \frac{I_0}{C_a} = \frac{SV}{C_a T}. \quad (4.22)$$

It follows from (4.22) that in steady-state we have the following relation between SV and V_{a0} :

$$SV = \frac{V_{a0} T}{R_a}. \quad (4.23)$$

It follows from (4.16) and (4.23) that PP in terms of V_{a0} is given by

$$PP = \frac{V_{a0} T}{C_a R_a}. \quad (4.24)$$

Because the pulsatile Windkessel model is LTI, the cycle-averaged Windkessel model (4.22) has the same governing differential equation and circuit representation as the pulsatile Windkessel model (3.3). Of interest is the fact that the time constant in both the pulsatile and the cycle-averaged Windkessel models is $R_a C_a$.

Figure 4.3 shows the pulsatile ABP waveform from a simulation of the Windkessel model (an analytical solution is also straightforward), along with the cycle-averaged ABP waveform obtained from a simulation of the cycle-averaged Windkessel model. The time constant with which the average rises to its steady-state equals the time constant of the decay on each pulse. It is clear that in order to capture the transient dynamics in mean arterial blood pressure, V_{a0} , it would for many purposes suffice to use a model that is well-suited to efficiently representing the dynamics of the cycle-average.

Figure 4.4 shows how the ABP waveform from the continuous-time cycle-averaged Windkessel model differs

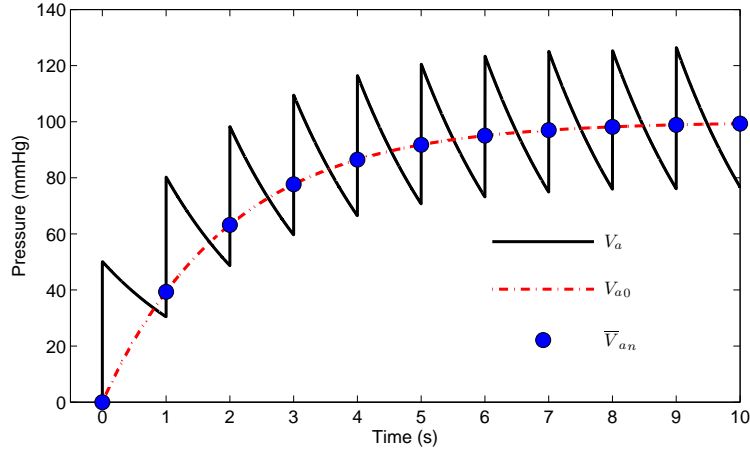


Figure 4.4: Comparison of the outputs of the pulsatile, beat-to-beat averaged, and cycle-averaged Windkessel models. The output of the beat-to-beat averaged model is a sampled version of the output of the cycle-averaged model.

from that in the discrete-time beat-to-beat averaged Windkessel model. The beat-to-beat averaged ABP (solid dots on Fig. 4.4) from the beat-to-beat averaged Windkessel model is a sampled version of the cycle-averaged ABP (dotted line on Fig. 4.4) from the cycle-averaged Windkessel model, where samples are taken at the end of each cardiac cycle.

4.3.2 Cycle-Averaged Modified Windkessel Model

We can easily apply the cycle-averaging methodology described above to the modified Windkessel model from Chapter 3, repeated here for convenience:

$$\frac{d}{dt}\mathbf{x} = \begin{bmatrix} 0 & -\frac{1}{C_{a,p}} & 0 \\ \frac{1}{L_a} & 0 & -\frac{1}{L_a} \\ 0 & \frac{1}{C_{a,d}} & -\frac{1}{R_a C_{a,d}} \end{bmatrix} \mathbf{x} + \begin{bmatrix} \frac{I}{C_{a,p}} \\ 0 \\ 0 \end{bmatrix} \quad (4.25)$$

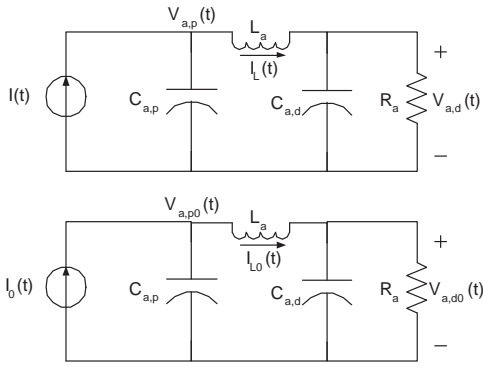
where $\mathbf{x}=[V_{a,p} \ I_L \ V_{a,d}]'$ is the vector of state variables.

By applying (4.20) and (4.21) to the state-space equation (4.25) for the modified Windkessel circuit, we obtain the following index-0 cycle-averaged Windkessel model:

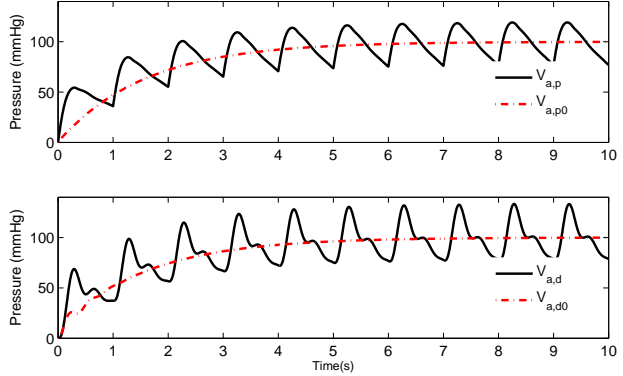
$$C_{a,p} \frac{dV_{a,p0}}{dt} = -I_{L0} + I_0 \quad (4.26)$$

$$L_a \frac{dI_{L0}}{dt} = V_{a,p0} - V_{a,d0} \quad (4.27)$$

$$C_{a,d} \frac{dV_{a,d0}}{dt} = -\frac{V_{a,d0}}{R_a} + I_{L0} \quad (4.28)$$



(a) Circuit representations for the pulsatile (top) and cycle-averaged (bottom) modified Windkessel models.



(b) Representative proximal and distal ABP waveforms – both pulsatile and cycle-averaged – for circuit simulations with $V_{a,p}(0) = 0$ mmHg, $V_{a,d}(0) = 0$ mmHg, $SV = SV_n = 100$ ml, $T = T_n = 1$ s, $R_{a,p} = 1$ mmHg/(ml/s), $L_a = 0.025$ mmHg/ml/s, $C_{a,p} = 1.45$ ml/mmHg, and $C_{a,d} = 0.15$ ml/mmHg.

Figure 4.5: Modified Windkessel (top left) and cycle-averaged modified Windkessel (bottom left) model circuit representations with representative pulsatile and cycle-averaged proximal (top right) and distal (bottom right) ABP waveforms.

where $V_{a,p0}$ is the index-0 cycle-average of the proximal ABP, $V_{a,d0}$ is the index-0 cycle-average of the distal ABP, I_{L0} is the index-0 cycle-average of the flow through the inductance L_a , and I_0 is the index-0 cycle-average of the flow out of the impulsive source representing the heart.

Because the pulsatile modified Windkessel model is LTI, the cycle-averaged modified Windkessel model has the same governing differential equations and circuit representation as the pulsatile modified Windkessel model (3.11).

Figure 4.5 shows the pulsatile proximal and distal ABP waveforms from a simulation of the modified Windkessel model (an analytical solution is also straightforward), along with the cycle-averaged proximal and distal ABP waveforms obtained from a simulation of the cycle-averaged modified Windkessel model. In this simulation, $V_{a,p}(0) = 0$ mmHg, $V_{a,d}(0) = 0$ mmHg, $SV = SV_n = 100$ ml, $T = T_n = 1$ s, $R_{a,p} = 1$ mmHg/(ml/s), $L_a = 0.025$ mmHg/ml/s, $C_{a,p} = 1.45$ ml/mmHg, and $C_{a,d} = 0.15$ ml/mmHg.

4.3.3 The Simple Pulsatile Cardiovascular Model

Applying the cycle-averaging operator to the Windkessel and modified Windkessel models was straightforward as these models are LTI and cycle-averaging is an inherently linear operation. When a circuit model has nonlinear and/or time-varying elements, such as the SPCVM, cycle-averaging is not as easily applied. Heldt and co-workers [41] applied cycle-averaging methodology to a version of the CVSimple model of Chapter 3 assuming a piecewise constant ventricular elastance. However, this assumption led to impulsive, and hence unrealistic, hemodynamic waveforms. Furthermore, the cycle-averaged model derived

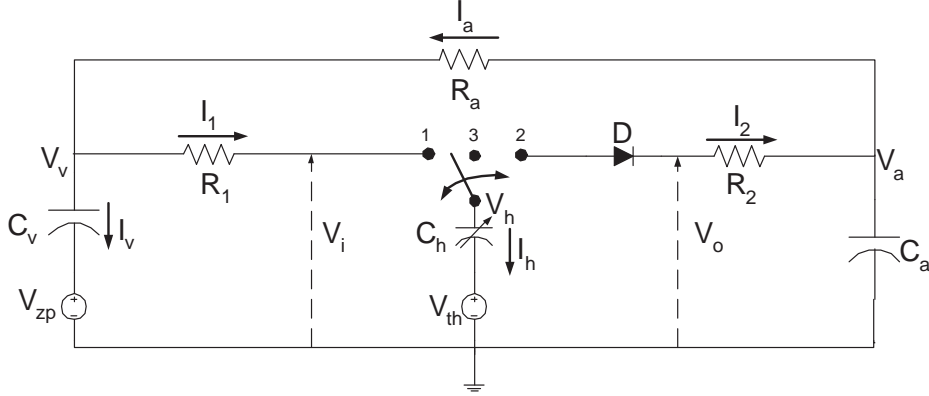


Figure 4.6: The simple pulsatile cardiovascular model (SPCVM) uses a 3-way switch which allows for simpler analysis of the circuit. V_i and V_o are defined here for future reference. For simplicity, only one diode is used to facilitate development of the averaged model.

there was dependent on the fine structure of the hemodynamic waveforms simulated by the pulsatile model. Thus, if one were to change the elastance function for the ventricle for example, the cycle-averaged model would have to be derived anew. The cycle-averaged model derived in this section remedies some of these shortcomings.

As mentioned in the previous chapter, the SPCVM has a single ventricular compartment, and is useful in studying systemic vascular conditions such as hemorrhaging in the peripheral circulation. Figure 4.6 illustrates the circuit representation for the SPCVM, but with two additional sources: V_{zp} and V_{th} . The source V_{zp} is the zero-pressure filling volume for the body's veins, while V_{th} is the pressure in the thoracic cavity.

The elastance function $E_h(t)=1/C_h(t)$ for the ventricular compartment in the SPCVM is taken to be the piecewise linear periodic function of Equation (3.18). The parameters used in the SPCVM, including the initial conditions for our simulations, are given in [16] and in Table 3.1 of Chapter 3. For simplicity, we set V_{zp} and V_{th} equal to 0 mm Hg. The derivation of a cycle-averaged model with non-zero V_{zp} and/or V_{th} would require only a trivial modification of the cycle-averaged model derived here.

The state space model for the SPCVM, repeated here for convenience is as follows:

$$\frac{dQ_h}{dt} = \frac{s_1(V_v - E_h Q_h)}{R_1} + \frac{s_D(V_a - E_h Q_h)}{R_2} \quad (4.29)$$

$$C_a \frac{dV_a}{dt} = \frac{s_D(E_h Q_h - V_a)}{R_2} + \frac{(V_v - V_a)}{R_a} \quad (4.30)$$

$$C_v \frac{dV_v}{dt} = \frac{s_1(E_h Q_h - V_v)}{R_1} + \frac{(V_a - V_v)}{R_a} \quad (4.31)$$

where the parameters $p=\{R_1, R_2, R_a, C_a, C_v, E_s, E_d, T\}$ are fixed or slowly varying and we have again dropped the time argument t for notational simplicity.

The cycle-averaging methodology for this model, to which we turn next, is considerably more involved than for the Windkessel or modified Windkessel models due to the presence of state-dependent switching functions.

4.3.4 Cycle-Average Expressions for the SPCVM

To apply the cycle-average operators ($\langle \bullet \rangle_k$) to our state-space model in (4.29)-(4.31), we need additional expressions for derivatives of index- k cycle-averages and for the cycle-averages of the products of two variables, such as $s_D(t)V_a(t)$, or three variables, such as $s_1(t)E_h(t)Q_h(t)$.

By differentiating (4.18) with T kept fixed, we easily obtain an expression for the derivative of the index- k cycle-average:

$$\frac{d}{dt}X_k(t) = \left\langle \frac{dx}{d\tau} \right\rangle_k (t) - jk \frac{2\pi}{T} X_k(t) . \quad (4.32)$$

The index- k cycle-average of the product of two signals, $x(t)$ and $y(t)$, is given by the easily verified discrete convolution formula for the product of the coefficients of two polynomials:

$$\langle xy \rangle_k = \sum_{m=-\infty}^{\infty} X_m Y_{k-m} . \quad (4.33)$$

The index- k cycle-average of the product of three signals, $x(t)$, $y(t)$, and $z(t)$, can be obtained by applying the discrete convolution relationship (4.33) to $[x(t)y(t)](z(t))$ to obtain:

$$\begin{aligned} \langle xyz \rangle_k &= \sum_{l=-\infty}^{\infty} Z_l \langle xy \rangle_{k-l} \\ &= \sum_{l=-\infty}^{\infty} Z_l \left(\sum_{m=-\infty}^{\infty} X_{k-l-m} Y_m \right) . \end{aligned} \quad (4.34)$$

In our application, we can neglect many of the Fourier series coefficients as their magnitude is relatively small, making these formulas much simpler to apply. Assuming only the index-0 and index-1 cycle-averages

are significant, as is the case for the pulsatile SPCVM waveforms, we have:

$$\langle xy \rangle_0 = X_0 Y_0 + 2(X_1^R Y_1^R + X_1^I Y_1^I) \quad (4.35)$$

$$\langle xy \rangle_1^R = X_0 Y_1^R + X_1^R Y_0 \quad (4.36)$$

$$\langle xy \rangle_1^I = X_0 Y_1^I + X_1^I Y_0 \quad (4.37)$$

$$\langle xyz \rangle_0 = X_0 \langle yz \rangle_0 + 2(X_1^R \langle yz \rangle_1^R + X_1^I \langle yz \rangle_1^I) \quad (4.38)$$

$$\begin{aligned} \langle xyz \rangle_1^R &= X_0 \langle yz \rangle_1^R + X_1^R \langle yz \rangle_0 + X_1^R (X_1^R Y_1^R \\ &\quad - X_1^I Y_1^I) - X_1^I (X_1^R Y_1^I + X_1^I Y_1^R) \end{aligned} \quad (4.39)$$

$$\begin{aligned} \langle xyz \rangle_1^I &= X_0 \langle yz \rangle_1^I + X_1^I \langle yz \rangle_0 + X_1^I (X_1^R Y_1^R \\ &\quad - X_1^I Y_1^I) + X_1^R (X_1^R Y_1^I + X_1^I Y_1^R). \end{aligned} \quad (4.40)$$

To obtain a cycle-averaged model, one can apply the formulas derived in Section 4.3.1 and in this section to a state-space model. If we represent circuit variables by their index-0 and index-1 (and, where necessary, their index-2) cycle-averages, but keep the index-1 and any index-2 cycle-averages constant, we end up with what we shall call an *index-0 cycle-averaged model*.

4.3.5 The Index-0 Cycle-Averaged Model

To obtain an index-0 cycle-averaged model for the SPCVM, we begin by deriving an approximation for the diode turn-on time t_D . This approximation is important since we need develop a cycle-averaged model in which all variables, including t_D , depend only on index-0 cycle-averaged quantities.

4.3.5.1 An approximation for t_D

We first need to express the index-0 cycle-average S_{D0} of the switching function s_D for the diode D in terms of cycle-averages of V_a , Q_h , and V_v . We do not require such an approximation for the other switching functions because their index-0 cycle-averages are not state-dependent. An approximation for t_D can be obtained on examination of the relevant circuit waveforms in region I (see Table 3.3) of the model's operation.

Figure 4.7 shows the SPCVM circuit in region I, where the switch is in position 2 and the diode D is open. In this region, the charge Q_h is fixed, but pressure V_h is increasing since the elastance function E_h is increasing linearly. At the same time, the arterial pressure V_a is decreasing as C_a discharges into C_v . The diode D begins conducting when V_h equals V_a .

Since the capacitance C_v is very large, we can assume V_v is essentially constant, and hence that $V_v = V_{v0}$,

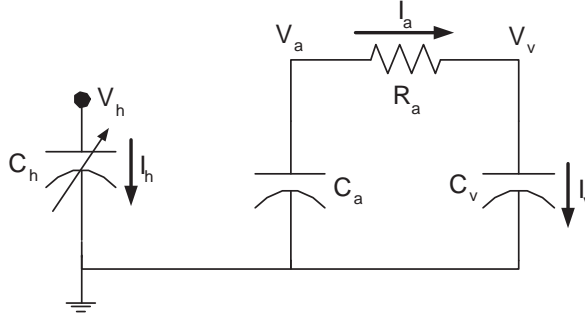


Figure 4.7: Circuit representation for the SPCVM in region I.

where V_{v0} is the index-0 cycle-average of V_v . Assuming region I begins at time $t = 0$, V_h in region I is given by

$$V_h = Q_h E_h = Q_h(0) \left(\frac{(E_s - E_d)}{T} t + E_d \right) \quad (4.41)$$

where we have used the fact that $Q_h = Q_h(0)$ in region I.

At the beginning of region I, $V_h \approx V_v$ and $E_h = E_d$, so

$$Q_h(0) \approx \frac{V_{v0}}{E_d}. \quad (4.42)$$

If we assume the relative ripple on the arterial pressure V_a to be small², we can assume that $V_a = V_{a0}$. The approximate diode turn-on time, \hat{t}_D , is then given by solving

$$\begin{aligned} V_h(\hat{t}_D) &= V_a(T + \hat{t}_D) \\ \frac{V_{v0}}{E_d} \left(\frac{3(E_s - E_d)}{T} \hat{t}_D + E_d \right) &= V_{a0} \end{aligned} \quad (4.43)$$

for \hat{t}_D , which yields

$$\hat{t}_D = \frac{E_d T}{3(E_s - E_d)} \left(\frac{V_{a0}}{V_{v0}} - 1 \right). \quad (4.44)$$

Figure 4.8 plots both sides of (4.43) on the same axes along with the steady-state waveforms for V_h and V_a obtained with the nominal SPCVM parameters in [16]. The actual t_D is given by the left-most intersection of V_h and V_a , while \hat{t}_D is given by the intersection of the lines representing the left- and right-hand sides of (4.43). The error in approximating t_D is only about 4% for the steady-state waveforms shown in Fig. 4.8.

The index-0 cycle-average of the s_D waveform is then given by applying the index-0 cycle-averaging operator

²Other approximations for t_D do not make this assumption; however, the improvement in results does not justify the added complexity.

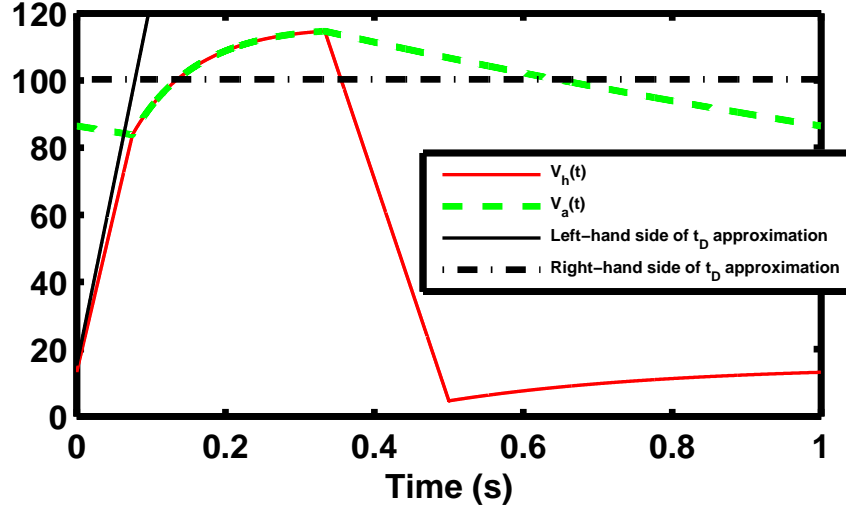


Figure 4.8: The left and right hand side of the approximation of the equation defining \hat{t}_D . The left-most intersection of V_h and V_a defines t_D , while the intersection of the LHS and RHS of (4.43) define \hat{t}_D .

to s_D to obtain

$$S_{D0} = \frac{1}{T} \int_{t_D}^{\frac{T}{3}} s_D(t) dt \approx \frac{1}{3} - \frac{E_d}{3(E_s - E_d)} \left(\frac{V_{a0}}{V_{v0}} - 1 \right). \quad (4.45)$$

If we were to approximate t_D as a fixed constant, the resulting index-0 cycle-averaged model would be linear and time-invariant. However, S_{D0} in (4.45) depends nonlinearly on state variables in the circuit, making the cycle-averaged model nonlinear, though still time-invariant.

4.3.5.2 Fourier analysis

To derive an index-0 cycle-averaged model, one needs to find nominal values at which to fix the index-1 and higher cycle averages. From simulations of the SPCVM, we justified that the index-2 and higher cycle-averages can be neglected for all the SPCVM waveforms except the ventricular volume, Q_h , and the ventricular elastance, E_h (see Appendix D.3 for derivations of the expressions we used). We then numerically (or partially analytically in the case of s_1 and E_h) calculated the relevant index-1 and index-2 cycle-averages using steady-state Fourier series representations of all the hemodynamic waveforms and switching functions from our simulations. The steady-state SPCVM waveforms we used were obtained from simulations with the nominal SPCVM parameters [16].

The results of this exercise are shown in Table 4.1. Since $s_1(t)$ is half-wave symmetric, it has no index- m cycle-averages for m even ($m \geq 2$). The first- and second-order Fourier series approximations we calculated for the steady-state V_a , V_h , and Q_h waveforms are shown in Fig. 4.9.

As noted above, we used exact analytical expressions for switching functions $s_1(t)$, $E_h(t)$, and $s_D(t)$. For

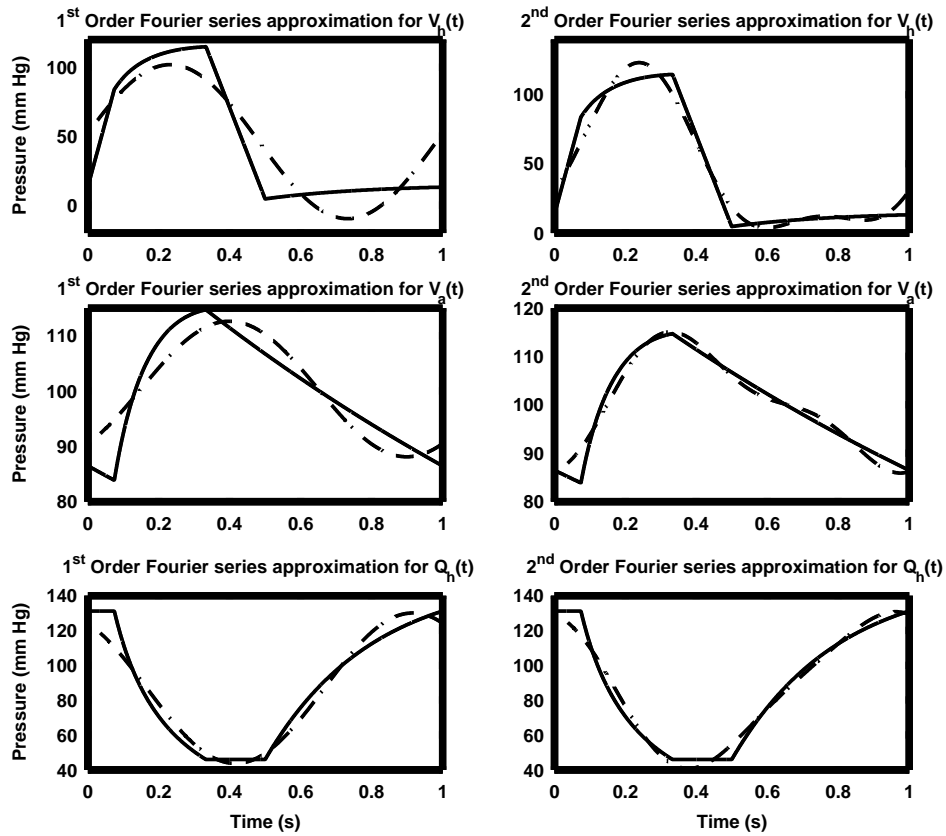


Figure 4.9: First- and second-order Fourier-series approximations for the steady-state SPCVM waveforms using the parameters in Table 3.1. Solid lines: actual waveforms; dash-dotted lines: Fourier series approximations thereof.

Variable	$\langle \bullet \rangle_0$	$\langle \bullet \rangle_1^R$	$\langle \bullet \rangle_1^I$	$\langle \bullet \rangle_2^R$	$\langle \bullet \rangle_2^I$
V_v	15.23	-0.09	-0.03	0.02	0.01
V_a	100.54	-4.91	-3.59	-1.91	0.83
Q_h	88.12	18.48	10.52	2.03	-2.52
E_h	0.70	-0.09	-0.47	-0.21	0.12
s_1	0.50	0.00	0.32	0.00	0.00
s_D	0.25	0.06	-0.22	-0.14	-0.08

Table 4.1: Values of cycle-averages in steady-state.

the $s_1(t)$ waveform in Fig. 3.13, for example, it is easy to show that:

$$S_{10} = \frac{T}{2}. \quad (4.46)$$

$$S_{11}^R = -\frac{\sin(2\pi S_{10})}{2\pi}. \quad (4.47)$$

$$S_{11}^I = -\frac{1}{2\pi} \left(\cos(2\pi S_{10}) - 1 \right). \quad (4.48)$$

Similarly, for the waveform for $s_D(t)$ displayed in Fig. 3.13, we could write:

$$S_{D1}^R = \frac{1}{2\pi} \left(\cos \left(2\pi \hat{t}_D \right) - \cos \left(2\pi \frac{T}{3} \right) \right) \quad (4.49)$$

$$S_{D1}^I = \frac{1}{2\pi} \left(\sin \left(2\pi \frac{T}{3} \right) - \sin \left(2\pi \hat{t}_D \right) \right) \quad (4.50)$$

where the expression for \hat{t}_D was derived in the previous section. In our simulations, however, we fixed S_{D1}^R and S_{D1}^I using $\hat{t}_D=0.0822$ seconds, which corresponds to the value of S_{D0} in Table 4.1.

Finally, E_{h0} is given by:

$$\begin{aligned} E_{h0} &= \frac{1}{T} \left(\int_0^T E_h(t) dt \right) \\ &= \frac{1}{4} E_s + \frac{3}{4} E_d. \end{aligned} \quad (4.51)$$

and E_{h1}^R and E_{h1}^I are given by finding the real and imaginary parts of:

$$E_{h1} = \frac{1}{T} \left(\int_0^T E_h(t) e^{j \frac{2\pi t}{T}} dt \right). \quad (4.52)$$

In addition, we implemented an index-0 dependence for the index-1 cycle-averages of the arterial blood pressure, V_{a1}^R and V_{a1}^I , and for the index-1 cycle-averages of the ventricular volume, Q_{h1}^R and Q_{h1}^I . These four index-1 cycle-averages were scaled by T and V_{a0} , since (4.24) and (4.23) respectively show that pulse pressure and stroke volume are proportional to $V_{a0}T$ in the Windkessel model. We therefore set:

$$V_{a1}^R = \frac{V_{a0}}{V_{a0\text{nominal}}} \frac{T}{T_{\text{nominal}}} (V_{a1}^R)_{\text{nominal}} \quad (4.53)$$

$$V_{a1}^I = \frac{V_{a0}}{V_{a0\text{nominal}}} \frac{T}{T_{\text{nominal}}} (V_{a1}^I)_{\text{nominal}} \quad (4.54)$$

$$Q_{h1}^R = \frac{V_{a0}}{V_{a0\text{nominal}}} \frac{T}{T_{\text{nominal}}} (Q_{h1}^R)_{\text{nominal}} \quad (4.55)$$

$$Q_{h1}^I = \frac{V_{a0}}{V_{a0\text{nominal}}} \frac{T}{T_{\text{nominal}}} (Q_{h1}^I)_{\text{nominal}} \quad (4.56)$$

where the nominal values of the index-1 cycle-averages were taken from Table 4.1. (One could also consider scaling the index-2 cycle-averages Q_{h2}^I and Q_{h2}^R by the same factor as in Equations (4.53)-(4.56). However, from simulations of the index-0 cycle-averaged model, we observed that such a scaling increases the resulting error, perhaps because the phase relations of the index-1 and index-2 terms change in the pulsatile circuit as conditions change.)

4.3.5.3 The index-0 cycle-averaged model

Using the values listed in Table 4.1 and applying the cycle-average operators from the previous section to (4.29-4.31), we obtain an index-0 cycle-averaged model for the SPCVM:

$$\frac{d}{dt}\mathbf{X}_0(t) = \frac{d}{dt} \begin{bmatrix} Q_{h0}(t) \\ V_{a0}(t) \\ V_{v0}(t) \end{bmatrix} = \begin{bmatrix} -\frac{\langle s_1 E_h Q_h \rangle_0}{R_1} - \frac{\langle s_D E_h Q_h \rangle_0}{R_2} + \frac{\langle s_D V_a \rangle_0}{R_2} + \frac{\langle s_1 V_v \rangle_0}{R_1} \\ \frac{\langle s_D E_h Q_h \rangle_0}{R_1 C_a} - \frac{(R_2 + R_a) V_{a0}}{R_2 R_a C_a} + \frac{V_{v0}}{R_a C_a} \\ \frac{\langle s_1 E_h Q_h \rangle_0}{R_1 C_v} + \frac{V_{a0}}{R_a C_v} - \frac{\langle s_1 V_v \rangle_0}{R_1 C_v} - \frac{V_{v0}}{R_a C_v} \end{bmatrix}. \quad (4.57)$$

Under our assumptions on the index-1 and higher cycle-averages, we can rewrite (4.57), using (4.35)-(4.40), as

$$\frac{d}{dt}\mathbf{X}_0(t) \approx \mathcal{C}(S_{10}, S_{D0}(t), p)\mathbf{X}_0(t) + \mathbf{d}(S_{10}, S_{D0}(t), S_{11}, S_{D1}, \mathbf{X}_1, \mathbf{X}_2, p) \quad (4.58)$$

where $\mathcal{C}(S_{10}, S_{D0}(t), p)$ is dependent on the index-0 cycle-averages of the switching functions and the parameters p , and where $\mathbf{d}(S_{10}, S_{D0}(t), S_{11}, S_{D1}, \mathbf{X}_1, \mathbf{X}_2, p)$ is dependent on the index-0 and index-1 cycle-averages of the switching functions, the index-1 cycle-averages, \mathbf{X}_1 , the index-2 cycle-averages of Q_h and E_h , \mathbf{X}_2 , and the parameters p . (Because of the index-1 adjustments in (4.53)-(4.56), \mathbf{X}_1 actually varies with $\mathbf{X}_0(t)$.) Exact expressions for $\mathcal{C}(S_{10}, S_{D0}(t), p)$ and $\mathbf{d}(S_{10}, S_{D0}(t), S_{11}, S_{D1}, \mathbf{X}_1, \mathbf{X}_2, p)$ are given in Appendix D.1.

Note that the state variables in this cycle-averaged model are the index-0 cycle-averages of the state variables in the SPCVM. Furthermore, it can be verified that the total charge in this cycle-averaged model is conserved, and is equal to the total cycle-averaged charge in the SPCVM, as shown in Appendix D.2.

In steady-state, the matrix \mathcal{C} has three eigenvalues: one that corresponds to a fast time constant (≈ 0.01 s), another that corresponds to a slower time constant (≈ 0.5 s), and one that is at zero³. Denoting the eigenvector of \mathcal{C} corresponding to this zero mode as v_3 , the index-0 cycle-averaged model state variables in steady state are given by:

$$\begin{bmatrix} Q_{h0} \\ V_{a0} \\ V_{v0} \end{bmatrix} = \zeta v_3 - \mathcal{C}^\dagger \mathbf{d} \quad (4.59)$$

where ζ is a constant that is determined by equating the total charge in the SPCVM to the total charge

³The left eigenvector u of the steady state matrix \mathcal{C} corresponding to this zero mode should be such that $u\mathbf{d}=0$, otherwise a steady state for (4.58) is not guaranteed.

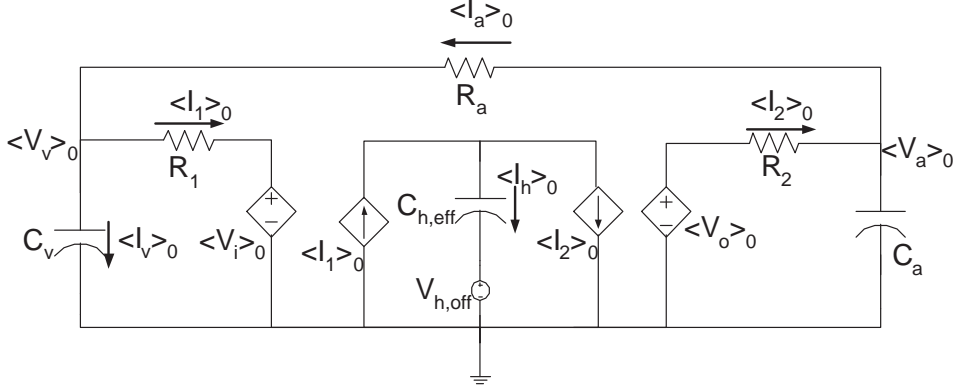


Figure 4.10: Index-0 cycle-averaged model with two-voltage dependent voltage sources and two current-dependent voltage sources.

in the index-0 cycle-averaged model, and \mathcal{C}^\ddagger is the pseudo-inverse of the steady-state matrix \mathcal{C} .

Initially, the parameters p in \mathcal{C} and \mathbf{d} are set to the nominal SPCVM parameters in Table 3.1 [15], which we shall call the nominal parameter set p_{nom} , and the index-1 and index-2 cycle-averages are fixed at the values given in Table 4.1. To start the cycle-averaged model in steady-state, the initial conditions $\mathbf{X}_0(0)$ for the index-0 cycle-averaged model are set equal to the numerically calculated cycle-averages of the steady-state simulated waveforms, \mathbf{x}_{ss} , of the SPCVM using the parameters p_{nom} .

Due to truncation error in the Fourier series approximations leading to (4.58)⁴, however, setting $\mathbf{X}_0(0) = \mathbf{x}_{\text{ss}}$ in the index-0 cycle-averaged model leads to a non-zero value for

$$\mathbf{e} = \mathcal{C}(S_{10}, S_{D0}(0), p_{\text{nom}})\mathbf{x}_{\text{ss}} + \mathbf{d}(S_{10}, S_{D0}(0), S_{11}, S_{D1}, \mathbf{X}_1, \mathbf{X}_2, p_{\text{nom}}) \quad (4.60)$$

in the index-0 cycle-averaged model. This violates the assumption that the circuit starts in steady-state with a certain fixed charge (or blood volume). To correct for this truncation error, we can subtract the fixed correction term \mathbf{e} from the right side of (4.58). The index-0 cycle-averaged model we propose is then given by

$$\frac{d}{dt}\mathbf{X}_0(t) = \mathcal{C}(S_{10}, S_{D0}(t), p)\mathbf{X}_0(t) + \mathbf{d}(S_{10}, S_{D0}(t), S_{11}, S_{D1}, \mathbf{X}_1, \mathbf{X}_2, p) - \mathbf{e} . \quad (4.61)$$

One alternative to using this correction term would be to use more index-2 Fourier series terms in (4.58); however, such higher-order approximations were only used for expressions involving Q_h and E_h .

We can also construct a circuit model that captures the dynamics of the index-0 cycle-averaged model using voltage-dependent voltage sources and current-dependent current sources. Such an index-0 cycle-averaged circuit, based on the SPCVM state space model in Equations (4.29) through (4.31) (or by direct averaging of the circuit in Fig. 4.6, see [99]), is shown in Fig. 4.10. Note that the LTI components of the

⁴For a brief discussion of the modeling error that results from truncating these Fourier series, please see [100].

R_a in PRU	Steady-state Error (%) for specified values of R_a in:		
	V_a	Q_h	V_v
1	0.00	0.00	0.00
0.6	0.54	0.55	0.04
1.4	1.33	0.86	0.14

Table 4.2: Steady-state error for the values of R_a from Fig. 4.11.

pulsatile circuit are unchanged by the cycle-averaging; they are in the same location, imposing the same constraints, but now on the averaged rather than instantaneous quantities. In this averaged circuit, the average compliance for the left ventricle, $C_{h,\text{eff}}$, is equal to $1/E_{h0}$ (see [41] for a derivation), and the source $V_{h,\text{eff}}$ is introduced to properly convert Q_{h0} into V_{h0} . Using V_i and V_o from the circuit in Fig. 4.6, we can write

$$V_{i0} = S_{10}V_{h0} + (1 - S_{10})V_{v0} + K_i \quad (4.62)$$

$$V_{o0} = S_{D0}V_{h0} + (1 - S_{D0})V_{a0} + K_o \quad (4.63)$$

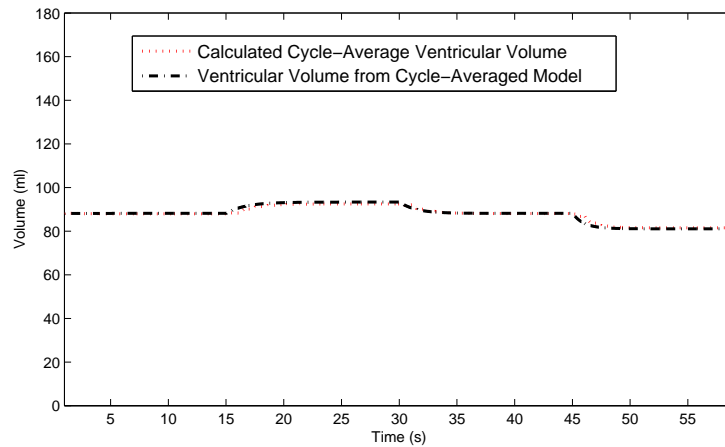
where K_i and K_o are variables that depend on the index-1 cycle-averages of s_D , V_h , V_a , and V_v , and fixed index-2 cycle-averages of E_h and Q_h .

4.3.6 Results and Discussion

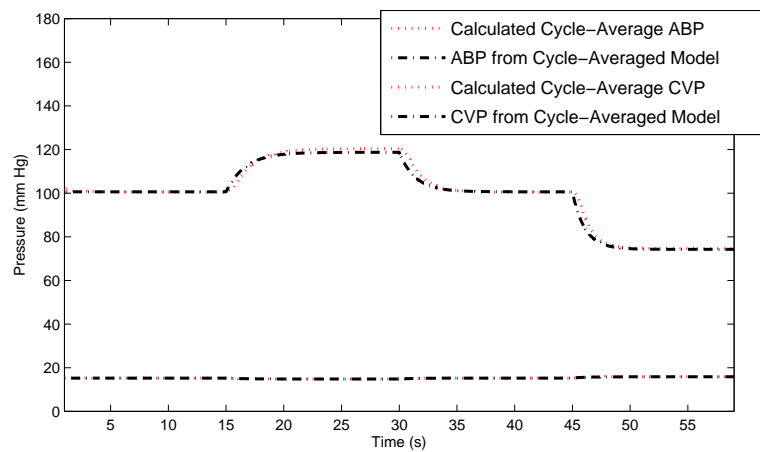
Using the index-0 cycle-averaged model (4.61), we obtained simulation results for typical transient responses to step changes in R_a , the systemic vascular resistance, and in T , the length of the cardiac cycle. We decided on these two parameters because both are significant hemodynamic variables in the clinical setting, and the cycle-averaged model is sensitive to both.

Figure 4.11 shows the transient responses of the index-0 cycle-averaged model for $T=1\text{s}$, during three step changes in systemic vascular resistance R_a [in peripheral resistance units (PRU) or equivalently mmHg/(ml/s)]: at $t=15$ s, R_a was stepped up to 1.4 PRU; at $t=30$ s, R_a was stepped down to 1 PRU; and at $t=45$ s, R_a was stepped down to 0.6 PRU. In Fig. 4.11, the index-0 cycle-averaged model responses are compared to the calculated index-0 cycle-averages from the SPCVM.

The errors inherent in the steady-state cycle-averaged waveforms for ABP, ventricular volume, and CVP from this simulation are shown in Table 4.2. The maximum error in the steady-state cycle-averaged waveforms (i.e., after each transient step response has settled) was approximately 1.3%, which is acceptable for the applications envisioned for this model. For this simulation, the transient error is lower than the steady-state error and is therefore not reported here. There was no error for the nominal condition of $R_a=1$ PRU because the initial conditions of the model (4.61) were set such that we began the simulation at the calculated cycle-averages from a simulation of the SPCVM with $p=p_{\text{nom}}$, and \mathbf{X}_1 and \mathbf{X}_2 set to the values given in Table 4.1.



(a) Ventricular Volume



(b) Arterial Blood Pressure and Central Venous Pressure

Figure 4.11: Comparison of the transient responses of the index-0 cycle-averaged model to the calculated cycle-averaged SPCVM waveforms for several step changes in resistance R_a . At $t=15$ s, R_a was stepped up to 1.4 PRU, at $t=30$ s, R_a was stepped down to 1 PRU, and at $t=45$ s, R_a was stepped down to 0.6 PRU.

R_a in PRU	Analytical	Calculated	$R_a C_a$
	Time Constant	Time Constant	
1.4	1.21 s	1.17 s	2.8 s
1	1.05 s	1.06 s	2 s
0.6	0.82 s	0.98 s	1.2 s

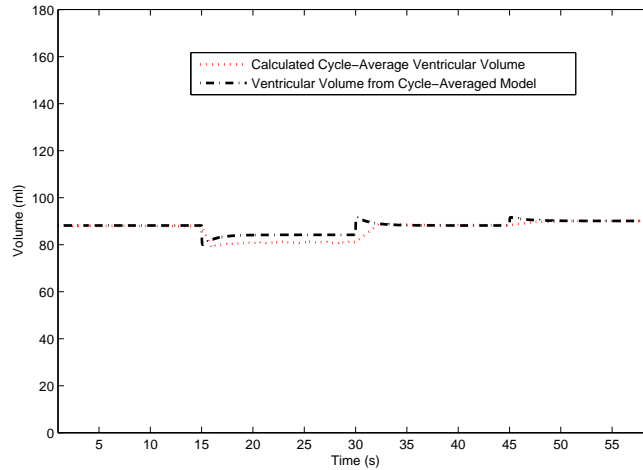
Table 4.3: Time constants in steady-state for the transient responses for the values of R_a from Fig. 4.11.

In steady-state, the matrix $\mathcal{C}(S_{10}, S_{D0}(t), p)$ has three eigenvalues: one corresponding to a fast time constant ($\approx 0.02s$), another to a slow time constant, and one that is zero [41]. The transient responses of our simulation are governed by the slow time constant. For the simulation of transients in R_a in Fig. 4.11, we determined the slow time constant both analytically and empirically in the neighborhood of steady-state. We computed analytical time constants by calculating the eigenvalues of $\mathcal{C}(S_{10}, S_{D0}(t), p)$ at $t=30$ s ($R_a=1.4$ PRU), $t=45$ s ($R_a=1$ PRU), and $t=60$ s ($R_a=0.6$ PRU). We also computed empirical time constants by fitting an exponential function to the calculated cycle-averaged ABP waveform for $24 < t < 30$ s ($R_a=1.4$ PRU), $39 < t < 45$ s ($R_a=1$ PRU), and $54 < t < 60$ s ($R_a=0.6$ PRU). Table 4.3 compares these two time constants to that obtained by estimating the time constant as $R_a C_a$, a reasonable assumption for the SPCVM since C_v is large and the SPCVM spends most of the cardiac cycle with $s_D(t)=0$. The empirical time constant for $R_a=0.6$ PRU does not match the analytical one as well as the other cases because the transient response for $45 < t < 60$ s settles to steady-state very quickly, making it difficult to estimate the time constant properly. Nonetheless, the analytical time constants we obtained are much more accurate than simply estimating the time constant as $R_a C_a$.

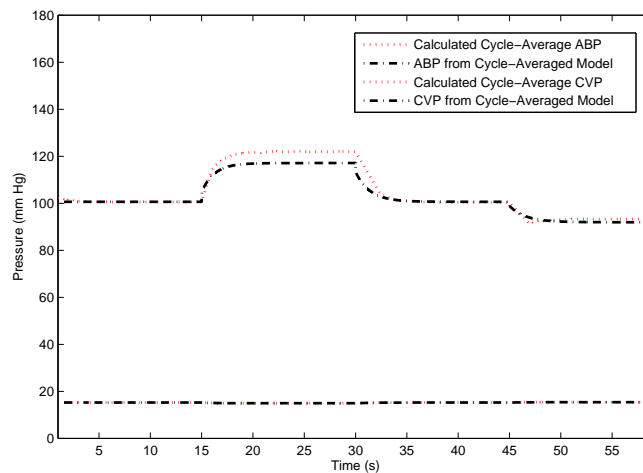
Figure 4.12 shows the transient responses of the index-0 cycle-averaged model for three step changes in cardiac cycle duration T : at $t=15$ s, T was stepped down to 0.5 s; at $t=30$ s, T was stepped back up to its nominal value of 1 s; and at $t=45$ s, T was stepped up to 1.2 s. These values of T correspond to heart rates of 50 beats/minute to 120 beats/min. In Fig. 4.12, the index-0 cycle-averaged model responses are compared to the calculated index-0 cycle-averages from the SPCVM. The maximum error in the steady-state cycle-averaged waveforms is larger than the simulation with transient changes in R_a – approximately 4%. This happens when the heart rate goes high, and where our approximation for t_D is poorest. For heart rate going low, the maximum error is 1.5%. Again, for this simulation, the transient error is lower than the steady-state error.

There are significant computational savings obtained when using the index-0 cycle-averaged model. Table 4.4 compares the CPU time for the simulation of Fig. 4.11 versus the time that it would take to simulate the SPCVM for the transients in R_a , not including the computational time for the calculated averages in Fig. 4.11. For the simulations, we used a Pentium M 1.7 GHz personal computer running Windows XP and MATLAB 7.01 (The Mathworks Inc., Natick, MA) with the “ode23” differential equation solver (see Appendix F). In the table, we also list the maximum step size limits that can be used in the simulations before output waveform degradation occurs.

Finally, we note that systolic and diastolic ABP, both important variables in clinical settings, can be



(a) Ventricular Volume



(b) Arterial Blood Pressure and Central Venous Pressure

Figure 4.12: Comparison of the transient responses of the index-0 cycle-averaged model to the calculated cycle-averaged SPCVM waveforms for several step changes in T . At $t=15$ s, T was stepped down to 0.5 s. At $t=30$ s, T was stepped back up to its nominal value of 1 s, and at $t=45$ s, T was stepped up to 1.2 s.

Model	CPU Time	Max. Step Size Limit
SPCVM	6.05 s	0.004 s
Index-0 CAM	0.61 s	0.5 s

Table 4.4: Computational savings obtained using the index-0 cycle-averaged model.

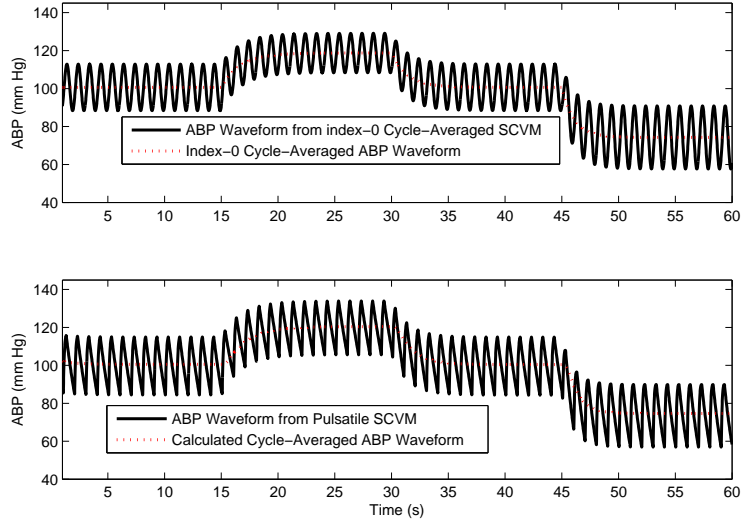


Figure 4.13: Envelope of the ABP waveform from the cycle-averaged model (top) compared to that of the SPCVM (bottom) for several step changes in peripheral resistance R_a . At $t=15$ s, R_a was stepped up to 1.4 PRU, at $t=30$ s, R_a was stepped down to 1 PRU, and at $t=45$ s, R_a was stepped down to 0.6 PRU.

estimated from the index-0 cycle-averaged model. Figure 4.13 is an example of such an approximation, where the ABP waveforms from the cycle-averaged model and the SPCVM are compared for the same transient as that in Fig. 4.11. The waveform in the top of Fig. 4.13 is sinusoidal, as it was calculated using the formula

$$V_a(t) \approx V_{a0}(t) + 2V_{a1}^R \cos\left(\frac{2\pi}{T}t\right) - 2V_{a1}^I \sin\left(\frac{2\pi}{T}t\right), \quad (4.64)$$

with V_{a1}^R and V_{a1}^I modulated as in (4.53) and (4.54), respectively.

We could also try to derive an index-1 cycle-averaged model to track the pulsatile arterial blood pressure waveform. However, this would require six additional state equations for tracking the index-1 cycle-averages.

4.4 Chapter Summary

In this chapter, we presented both discrete-time beat-to-beat and continuous-time cycle-averaging methodologies applicable to dynamic systems in close to periodic operation, and illustrated their application to the Windkessel, modified Windkessel, and, in the case of cycle-averaging, to a somewhat more elaborate cardiovascular model – the SPCVM – that has nonlinear and time-varying components.

The beat-to-beat averaged models were obtained by integrating the differential equations of the underlying pulsatile models over a single cardiac cycle. In Chapter 5, we show how the beat-to-beat averaged Windkessel model (4.8) can be used to estimate cardiac output.

The cycle-averaged models were derived by applying short-term averaging operators to the differential equations of the underlying pulsatile models. Despite the approximations needed to obtain the cycle-averaged version of SPCVM, our cycle-averaged model captures the inter-cycle cardiovascular dynamics of SPCVM with relatively small approximation errors for a large range of perturbations in important system parameters.

Further simplifications of the SPCVM — for instance, replacing V_v by a constant source, eliminating the remaining diode, and simplifying the logic for the switch — lead to pulsatile behavior that is still representative of cardiovascular dynamics, but that may have a simpler averaged model. These simplifications, and various extensions, and applications to fitting real data are beyond the scope of this thesis, but will hopefully be explored in future research work in our group.

Part III

Estimation and Monitoring of Cardiovascular Dynamics

Continuous Monitoring of Cardiac Output and Total Peripheral Resistance

CARDIAC output (CO) is an important hemodynamic variable that may be used to establish differential diagnoses, monitor disease progression, and titrate therapy in many cardiovascular conditions. CO can be measured in several ways, including echocardiography imaging studies, magnetic resonance imaging studies, and ventricular impedance catheter-based volume measurements. Unfortunately, the current clinical standard for measuring cardiac output is intermittent thermodilution – a highly invasive procedure in which a *Swan-Ganz* catheter [9] is advanced to the pulmonary artery, a bolus of cold saline is injected, and its mixing temperature with blood is observed over the time course of tens of seconds to a minute. Because of its invasive nature (and some controversy surrounding its effect on patient outcome [101, 102, 103, 104], thermodilution requires an expert operator and is usually reserved for only the sickest of patients [3].

Rather than intermittently estimating average cardiac output *invasively* via thermodilution, many attempts have been made to *noninvasively* obtain a continuous estimate of cardiac output from the arterial blood pressure (ABP) waveform [37, 54, 60, 62, 64, 65, 72, 105, 106]. Some of these CO estimation methods have since been deemed insufficiently reliable for clinical decision-making [107], while others claim to be reliable [65]. Since stroke volume is related to the arterial pressure wavelet through the properties of the arterial tree, realistic assumptions about the latter allow for the estimation of stroke volume, and thus cardiac output, on a beat-to-beat basis. One of the most basic models for the arterial tree is a Windkessel [62]: a single, leaky pressurized chamber that is filled intermittently with boluses of fluid. In fact, several methods for estimating stroke volume from the arterial pressure waveform (so-called *pulse contour methods*) are derivatives of the basic Windkessel model [37, 64, 65, 72]. Each of these methods assumes that the arterial tree behaves like a Windkessel on a beat-to-beat basis, and cardiac output is estimated using morphological features, e.g., systolic and/or diastolic values, of the arterial blood pressure waveform.

Recently, Mukkamala and co-workers [57, 58] pointed out that the arterial tree behaves like a Windkessel in the limit of inter-beat time scales, but not over intra-beat time scales, as wave reflections significantly distort the individual pressure wavelets, and therefore negatively affect stroke volume estimates derived using the Windkessel model. Other researchers disagree with this proposition [108]. Nonetheless, Mukkamala and co-workers intermittently, i.e., every 3 minutes, and with clinically acceptable precision, estimated relative changes in cardiac output from inter-cycle variations of the ABP waveform by finding the impulse

response function of the Windkessel model and, from it, the time constant of arterial outflow. Knowing the latter enables one to estimate proportional cardiac output, from which absolute CO can be obtained via calibration with true CO measurements.

The work by Mukkamala and co-workers on the problem of estimating cardiac output from beat-to-beat variations in ABP is consistent with our motivation in developing the averaged models of the cardiovascular system of Chapter 4. These models are capable of dynamically tracking the time-averaged behavior of various hemodynamic waveforms on a beat-to-beat basis.

5.1 Outline

This chapter is comprised of two parts: one describing our novel CO estimation method [109], and the second describing the application of this method to two animal and two human data sets. A full analysis of the errors obtained on application of our method is reported for one of the animal data sets.

In the first part of this chapter, we review the Windkessel model (Section 5.2), and then derive our beat-to-beat averaged Windkessel model-based CO estimation method (Section 5.3). We show that, following the example of Mukkamala and co-workers, we can directly apply the discrete-time beat-to-beat averaged Windkessel model of Chapter 4 to estimate the Windkessel model arterial time constant. In doing so, we exploit the beat-to-beat variability in arterial blood pressure and heart rate. Cardiac output estimates can then be calculated using this time constant and a value for the corresponding arterial compliance that is obtained via calibration with reference cardiac output measurements. This estimation method has a clear physiological basis, and is simple to understand and implement.

Calibration methods are discussed in detail in Section 5.4. In particular, unlike Mukkamala and co-workers, but consistent with other researchers [65, 110], we investigate the use of a parabolic arterial volume-*mean* pressure relationship, and compare this compliance to a constant arterial tree compliance. This compliance is the calibration factor for our CO estimate.

Error criteria used to compare our estimate to the reference cardiac output measurements are discussed in Section 5.5. We use these criteria to evaluate how our estimation method compares to several other model-based CO estimation methods when applied to animal and human data. Central to our CO estimation method are the notions of inter-beat and intra-beat arterial blood pressure variability. In Section 5.6, we discuss CO variability and some naïve CO estimators, as the estimation error that results from applying a naïve CO estimator is a strong indicator of CO variability.

In the second part of this chapter, we show the results obtained by applying our method to a porcine (Section 5.8), a canine (Section 5.9), and two human (Sections 5.10 and 5.11) ICU data sets. We also compare our results to those we obtained by applying a number of other CO estimation methods to the same data sets. We show that our method consistently outperforms all other methods we chose to apply

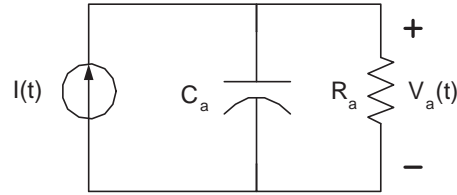


Figure 5.1: Circuit representation for the Windkessel model.

to the various data sets presented in this chapter. We conclude the chapter with Section 5.12 which summarizes the main results and presents some ideas for future work.

5.2 The Windkessel Model Revisited

In this section we revisit the discrete-time beat-to-beat averaged Windkessel model which is the basis of our CO estimation method described in Section 5.3.

5.2.1 Model Description

As mentioned in Chapters 3 and 4, the Windkessel model describes the basic phenomenon of an arterial pressure pulse [62]. It lumps the distributed resistive and capacitive properties of the entire arterial tree into two elements, as seen in the electrical circuit analog in Fig. 5.1: a single resistor, R_a , represents total peripheral resistance (TPR), and a single capacitor, C_a , represents the aggregate elastic properties of all arteries. Though C_a is expected to show a nonlinear dependence on arterial blood pressure, here we take this dependence to be on *mean* arterial blood pressure, \bar{V}_a . Equivalently, we assume pulse pressure is small relative to MAP, and the incremental compliance evaluated around MAP provides a sufficient approximation of the compliance characteristic for the entire ABP waveform over the cycle. Furthermore, we assume \bar{V}_a changes slowly enough that C_a may be assumed essentially constant over any window of a few beats duration.

The state space equation for the Windkessel model, repeated here for convenience, is:

$$C_a \frac{dV(t)}{dt} + \frac{V(t)}{R_a} = I(t) \quad (5.1)$$

In addition, the pulse pressure-stroke volume relationship for the Windkessel model, assuming impulsive

cardiac ejection, is as follows:

$$PP_n = SAP_n - DAP_n = \frac{SV_n}{C_{an}} \quad (5.2)$$

where C_{an} is the lumped arterial tree compliance in the n^{th} cardiac cycle.

5.2.2 Arterial Tree Compliance

As mentioned above and in Chapter 3, the arterial tree compliance C_a is perhaps better modeled as a function of arterial blood pressure, rather than as a constant. We observe below that a constant compliance is a reasonable assumption for modeling animal data, but a pressure-dependent compliance may be more relevant for ICU patients.

We mentioned several studies on arterial tree compliance in Section 3.4.2. Of particular relevance in terms of CO estimation, is the arctangent volume-pressure curve proposed by Langewouters *et al.* [110] based on *ex vivo* studies of human thoracic and abdominal aortas. Their work was further strengthened by the work of Tardy *et al.* [111] who describe *in vivo* studies on the mechanical properties of human peripheral arteries. The relationship proposed by Langewouters and co-workers, and used by Wesseling *et al.* [65] in their CO estimation method, yields the following (incremental) compliance:

$$C_a = \frac{\alpha_1}{\alpha_2 + \alpha_3(V_a - V^*)^2} \quad (5.3)$$

where α_1 , α_2 , and α_3 are constants, and V^* is the inflection point of their arctangent aortic volume-pressure relationship. In humans, a value $V^*=40$ mmHg is suggested [65]. The constants α_1 , α_2 , and α_3 depend on patient gender and age; nominal values of these constants can be extracted from regression analyses described in [110]. The CO estimation approach in [65] allows a further adjustment of α_1 when calibrating against available CO measurements.

There are other pressure-dependent compliances that have been used in CO estimation methods, e.g., the pressure-dependent compliances of Godje *et al.* [112] and Liljestrand and Zander [64]. In [64], compliance is simply modeled as being inversely proportional to the sum of the beat-to-beat systolic and diastolic arterial blood pressures, while in [112], compliance is modeled using a complicated expression that involves both mean and instantaneous arterial blood pressure.

In our work, we attempt to use either a *linear* arterial tree compliance:

$$C_{an} = \gamma_1 + \gamma_2 \overline{V_{an}} \quad (5.4)$$

where γ_1 and γ_2 are constants, C_{an} is arterial tree compliance and $\overline{V_{an}}$ is mean arterial blood pressure, both in the n^{th} cardiac cycle (or beat), or a *constant* arterial tree compliance:

$$C_{an} = \gamma_1 \quad (5.5)$$

which arises naturally from its linear counterpart as the special case of $\gamma_2=0$.

The function (5.4) corresponds to a parabolic volume-mean pressure relationship in the arterial tree, is simpler than the one used in [65], and facilitates estimation of patient- or animal-specific parameters from calibration data. A review of the literature (see Section 3.4.2) shows no significant advantages of a logarithmic or arctangent volume-*mean* pressure relationship over one that is parabolic or one that uses *instantaneous* arterial blood pressure. In our work, we compare the calibrated CO estimates obtained using (5.5) to those obtained using (5.4). We also allow for the total peripheral resistance to vary from cycle to cycle, denoting its value in the n^{th} cardiac cycle R_{an} .

5.3 Using the Beat-to-Beat Averaged Windkessel Model to Estimate Cardiac Output

In this section we work with the beat-to-beat averaged Windkessel model (4.8) from Chapter 4 and show how we use it to estimate cardiac output. It would also be possible to use the beat-to-beat averaged modified Windkessel model (4.13) to do such estimation; this is the subject of current research in our group [17].

5.3.1 Model Description

As derived in Chapter 4, the discrete-time beat-to-beat averaged Windkessel model equation is:

$$C_{an} \frac{\Delta V_{an}}{T_n} + \frac{\bar{V}_{an}}{R_{an}} = \text{CO}_n \quad (5.6)$$

where $\Delta V_{an} = V_a(t_{n+1}) - V_a(t_n)$. Note that (5.6) is a natural discrete-time counterpart to (5.1).

Average cardiac output in the n^{th} cycle is given by:

$$\text{CO}_n = \frac{\text{SV}_n}{T_n} = C_{an} \frac{\text{PP}_n}{T_n} \quad (5.7)$$

where we have invoked (5.2) to obtain the second equality.

Although, equation (5.7) can be used to estimate CO given pulse pressure, we proceed here to derive alternative expressions for cardiac output. As we show below, one such expression, Equation (5.9), results in much lower estimation error when applied to various human and animal data sets. Combining (5.7) and (5.6), we obtain

$$\frac{\Delta V_{an}}{T_n} + \frac{\bar{V}_{an}}{\tau_n} = \frac{\text{PP}_n}{T_n} \quad (5.8)$$

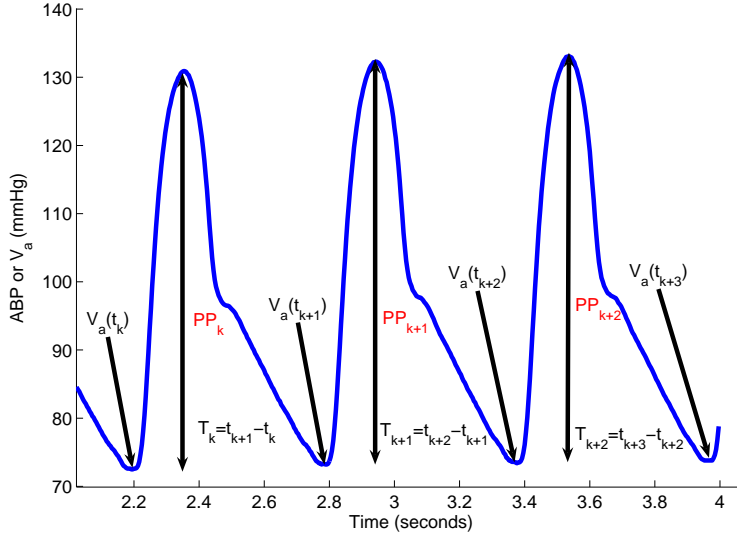


Figure 5.2: Porcine radial arterial blood pressure waveform showing quantities that are used, on a beat-to-beat basis, to estimate the time constant τ_n in Equation (5.8). Mean arterial blood pressure in beat n is the area under the pressure waveform in the n^{th} cardiac beat.

where $\tau_n = R_{an}C_{an}$ is the only unknown. Thus, Equation (5.8) can be used to estimate τ_n from knowledge of the remaining quantities, most of which are illustrated in Fig. 5.2.

CO_n can then be estimated from (5.6), rewritten below to show dependence on τ_n :

$$CO_n = C_{an} \left(\frac{\Delta V_{an}}{T_n} + \frac{\overline{V_{an}}}{\tau_n} \right) . \tag{5.9}$$

In steady-state, the first term on the right hand side of (5.9) vanishes and the equation reduces to:

$$CO_n = \frac{\overline{V_{an}}}{R_{an}} \tag{5.10}$$

which is simply the relation governing average flow through the resistor R_{an} given the mean pressure $\overline{V_{an}}$. The vanishing term $\frac{\Delta V_{an}}{T_n}$ in (5.9), represents the average flow through C_{an} . It is a measure of the beat-to-beat variability in CO and allows us to refine the estimate of τ_n .

5.3.2 Linear Least-Squares Estimation Scheme

In going from (5.8) to (5.9), we assume that τ_n varies slowly from beat-to-beat. Inherent in this assumption is that C_{an} , and hence $\overline{V_{an}}$, do not vary too much over the course of a few beats. Had we not assumed an impulsive cardiac ejection in Equation (5.2), we would have had two unknowns in Equation (5.8), and would have had to make the assumption that both τ_n and $\frac{SV_n}{C_{an}}$ vary slowly from beat-to-beat. Such an

5.3 Using the Beat-to-Beat Averaged Windkessel Model to Estimate Cardiac Output

assumption is invalid for stroke volume as it can change rapidly from one beat to the next. In addition, it turns out that for the human and animal data sets used in this chapter, the resulting two-parameter (SV_n and τ_n) least-squares estimation problem is ill-conditioned.

We estimated CO directly from (5.8) by computing a least-squares estimate of τ_n over a fixed-length data window, i.e., we calculated a least-squares estimate of τ_n for the n^{th} beat using a window comprising the $b/2$ adjacent beats on each side of this beat. This results in a total of b (even) equations in one unknown, a very well-conditioned least-squares estimation problem.

$$\begin{bmatrix} -\bar{V}_{an} \\ \cdot \\ \cdot \\ \cdot \\ -\bar{V}_{ab+n} \end{bmatrix} \begin{bmatrix} 1 \\ \tau_{n-1+\frac{b}{2}} \end{bmatrix} = \begin{bmatrix} \frac{\Delta V_a(n)}{T_n} - \frac{PP(t_n)}{T_n} \\ \cdot \\ \cdot \\ \cdot \\ \frac{\Delta V_a(b+n)}{T_{b+n}} - \frac{PP(t_{b+n})}{T_{b+n}} \end{bmatrix} \quad (5.11)$$

Note that we assign the estimated τ_n from each window to the midpoint of that window, and that in (5.11), $n > \frac{b}{2}$. We then estimated the uncalibrated beat-to-beat CO estimate, UCO_n , in the n^{th} window as:

$$UCO_n = \left(\frac{\bar{V}_{an}}{\tau_n} + \frac{\Delta V_{an}}{T_n} \right), \quad (5.12)$$

from which the calibrated beat-to-beat CO estimate, ECO_n , is:

$$ECO_n = C_{an} UCO_n. \quad (5.13)$$

The calibration factor C_{an} can be determined using one or more true or reference CO measurements, TCO_n , as described in Section 5.4.

5.3.3 Calculation of Pulse Pressure

The pulse pressure needed represented in the Windkessel model is that measured at the aortic root. Thus, calculation of PP_n from (5.2) for peripheral pressure waveforms can be problematic because these waveforms can exhibit pressure wave reflections leading to overestimation of SAP_n . Some of these reflections occur because of the tapering of vessels at the lower levels of the arterial tree. In addition, (5.2) assumes an impulsive model for cardiac ejection and thus (5.1) simulates blood pressure waveforms that morphologically do not represent real blood pressure waveforms. In previous work on SV estimation, Herd *et al.* [106] suggested using the following estimate for PP_n :

$$PP_n = \alpha (\bar{V}_{an} - DAP_n) \quad (5.14)$$

where α is a constant. Their expression for estimated CO is:

$$\text{CO}_n = \alpha \frac{\overline{V}_{an} - \text{DAP}_n}{T_n} . \quad (5.15)$$

Herd *et al.* [106] argue that Equation (5.14) is more accurate than the usual expression for pulse pressure because it takes into account not only the blood volume ejected into the arterial tree, but also the additional blood volume which “leaves the arterial tree during systole.” They also argue that their pulse pressure estimate is not confounded by wave reflections in the ABP wavelet.

In the results described in this thesis, we compare our estimate (5.13) to (5.15) – the *Herd estimate* for cardiac output. Herd *et al.* compared (5.14) to several other expressions for PP_n by performing canine experiments in which they measured ABP at the ascending aorta.

After we applied (5.2) and visually inspected the reflection-induced morphologies in the peripheral ABP waveforms in the two animal data sets used in this thesis, we decided to use (5.14) to calculate PP_n . We used $\alpha=2$ in (5.14) because for high enough HR (i.e., $T_n \ll \tau_n$) in the n^{th} cardiac cycle of the Windkessel model (5.1), a reasonable assumption for the representative values of T_n and τ_n observed in both animal data sets, we see that in the $(n+1)^{\text{st}}$ cardiac cycle, diastolic ABP is given by

$$\text{DAP}_{n+1} = \text{SAP}_n e^{-\frac{T_n}{\tau_n}} \approx \text{SAP}_n \left[1 - \frac{T_n}{\tau_n} \right] \quad (5.16)$$

such that the MAP in the n^{th} cardiac cycle can be approximated as

$$\overline{V}_{an} \approx \frac{1}{T_n} \left[\text{DAP}_{n+1} T_n + \frac{1}{2} T_n (\text{SAP}_n - \text{DAP}_n) \right] \quad (5.17)$$

which yields the following formula for pulse pressure in the n^{th} cardiac cycle:

$$\text{PP}_n = \text{SAP}_n - \text{DAP}_n \approx 2 (\overline{V}_{an} - \text{DAP}_n) . \quad (5.18)$$

For the human data sets, we used (5.2) to approximate pulse pressure.

5.3.4 Estimation of Total Peripheral Resistance

Total peripheral resistance is an important cardiovascular variable; it is used along with CO and mean ABP to generate differential diagnoses and monitor disease progression. TPR is especially useful in tracking conditions that affect the systemic vasculature such as septic shock. Even in conditions that do not affect the vasculature directly, e.g., hypovolemic shock, a patient’s TPR can change significantly. In the case of hypovolemic shock, it rises to compensate for blood loss. An estimate of TPR also allows clinicians to infer

the effects of any vasoactive medications. In the clinical setting, TPR is commonly defined as the ratio of mean arterial blood pressure to cardiac output:

$$\text{TPR}_n = \frac{\overline{V_{an}}}{\text{TCO}_n}, \quad (5.19)$$

which is essentially a rearrangement of Equation (5.10), with ΔV_{an} set to zero.

There are two ways in which we can obtain an estimate of TPR_n , or R_{an} , in our beat-to-beat averaged Windkessel model. First, given beat-to-beat estimates of τ_n and C_{an} , we can estimate TPR using:

$$R_{an} = \frac{\tau_n}{C_{an}}. \quad (5.20)$$

Both τ_n and C_{an} are outputs of our estimation method, making (5.20) particularly easy to implement. This estimate is relatively smooth given that τ_n and C_{an} are usually estimated in a least-squares sense over a window of many beats.

Second, similar to the Windkessel model-based formula used by Toorop and co-workers [77], we can calculate R_{an} by subtracting from ECO_n the proportion of ECO_n that goes into C_{an} and use this flow to estimate R_{an} :

$$R_{an} = \frac{\overline{V_{an}}}{\text{ECO}_n - C_{an} \frac{\Delta V_{an}}{T_n}}. \quad (5.21)$$

Since this formula uses beat-to-beat variations in the flow to C_{an} , it tends to be noisier than the estimate in (5.20).

For the results presented in this thesis, we use (5.21) to estimate TPR, though both (5.20) and (5.21) give acceptable TPR estimates.

5.4 Calibration Methods

The purpose of calibrating the UCO is to determine an appropriate value of C_{an} such that we can compare our CO estimate to the true or reference CO. If we did not calibrate, we would only be able to report relative changes in our CO estimate, i.e., how *relative* changes in ECO (or equivalently, how absolute changes in UCO) track *relative* changes in TCO, as opposed to how *absolute* changes in ECO track *absolute* changes in TCO.

5.4.1 Least-Squares Calibration

A natural calibration criterion is the root-mean-square-normalized error (RMSNE), in which we seek an optimal C_{an} such that we minimize

$$\sqrt{\text{sum}_n \frac{\epsilon_n}{\text{TCO}_n}} \quad (5.22)$$

This is equivalent to minimizing the commonly-used weighted least-squares error criterion. Specifically, we want to find a value for C_{an} such that the CO estimation error, ϵ_n , in

$$\text{TCO}_n = \text{ECO}_n + \epsilon_n = C_{an} \text{UCO}_n + \epsilon_n \quad (5.23)$$

is minimized. For example, one can find C_{an} such that the root-mean-square-normalized-error (RMSNE), described in the Section 5.5, is minimized, i.e., find the optimal C_{an} such that $\frac{\epsilon_n}{\text{TCO}_n}$ in

$$1 = \frac{C_{an} \text{UCO}_n}{\text{TCO}_n} + \frac{\epsilon_n}{\text{TCO}_n} \quad (5.24)$$

is minimized, in the least-squares sense, for all n of interest.

Note that this kind of *least-squares* calibration is easily done with (5.5) – a *constant* calibration factor. For instance, given a set of TCO measurements $\{\text{TCO}_{p_i}\}$ at points $\{p_1, \dots, p_m\}$, to find the least-squares optimal γ_1 in (5.5), we need to solve (5.24) using at least one reference TCO measurement, i.e., we need to solve:

$$\begin{bmatrix} \frac{\text{UCO}_{p_1}}{\text{TCO}_{p_1}} \\ \cdot \\ \cdot \\ \cdot \\ \frac{\text{UCO}_{p_m}}{\text{TCO}_{p_m}} \end{bmatrix} \gamma_1 = \begin{bmatrix} 1 \\ \cdot \\ \cdot \\ \cdot \\ 1 \end{bmatrix} . \quad (5.25)$$

The resulting value for γ_1 minimizes the RMSNE between ECO and TCO at points $\{p_1, \dots, p_m\}$.

It is also straightforward to extend this method in order to find the least-squares optimal γ_1 and γ_2 in (5.4) – a *state-dependent* calibration factor as it depends on mean arterial blood pressure. To do so, one needs to solve (5.24) using at least two reference TCO measurements:

$$\begin{bmatrix} \frac{\text{UCO}_{p_1}}{\text{TCO}_{p_1}} & \overline{V}_{ap_1} \frac{\text{UCO}_{p_1}}{\text{TCO}_{p_1}} \\ \cdot & \cdot \\ \cdot & \cdot \\ \cdot & \cdot \\ \frac{\text{UCO}_{p_m}}{\text{TCO}_{p_m}} & \overline{V}_{ap_m} \frac{\text{UCO}_{p_m}}{\text{TCO}_{p_m}} \end{bmatrix} \begin{bmatrix} \gamma_1 \\ \gamma_2 \end{bmatrix} = \begin{bmatrix} 1 \\ \cdot \\ \cdot \\ \cdot \\ 1 \end{bmatrix} \quad (5.26)$$

for $m \geq 2$. For (5.26) to be well-conditioned, there must be a sufficient degree of variation in mean pressure \overline{V}_{an} .

If we solve (5.26) using all the available TCO measurements, we call this a state-dependent calibration with all points. If we choose to solve (5.26) using an equally-spaced fixed number p of the available TCO measurements, we call this a state-dependent calibration with p points. From the perspective of conditioning of (5.26), it makes more sense to do a state-dependent calibration with p points since it is unlikely that $\overline{V_{an}}$ will be varying drastically from one beat to the next. Furthermore, a state-dependent calibration with p points is more realistic in settings such as the ICU where CO is measured only intermittently.

5.4.2 State-Dependent Least-Squares Calibration with Updates

It is also possible to carry out state-dependent (or even constant, though we don't discuss this here) calibrations on smaller windows of data, and update the calibration constants γ_1 and γ_2 in successive windows. This kind of calibration would also be particularly applicable in the ICU, where CO is measured only intermittently. If we use non-overlapping windows and re-calibrate the CO estimate in every window using an equally-spaced fixed number of the available TCO measurements in that window, we call this a repeated state-dependent calibration with p points. If instead, we use overlapping windows, we call this an overlapping repeated state-dependent calibration with p points. Finally, if we use exponentially-shaped overlapping windows such that older calibration data is emphasized more (and we solve a weighted least-squares calibration with tapering windows instead of (5.25) or (5.26)), we call this an exponentially-weighted overlapping repeated state-dependent calibration with p points. Repeatedly calibrating on overlapping or non-overlapping windows results in much lower RMSNEs, however, instead of reporting results with these low RMSNEs in Section 5.8, we report those obtained with state-dependent calibration with p points.

5.4.3 Constant Calibration Factors

The results reported by Mukkamala *et al.* [57] and some of the results quoted by Sun *et al.* [113] were generated using a C_{an} that is not optimal in the sense of (5.24). In [57], a *mean* calibration was done, i.e., C_{an} was estimated by dividing the mean of the true CO waveform by that of the estimated CO waveform as follows:

$$C_{an} = \frac{\text{mean}(\text{TCO})}{\text{mean}(\text{ECO})} = \frac{\sum_{i=1}^m \text{TCO}_i}{\sum_{i=1}^m \text{ECO}_i}. \quad (5.27)$$

Mean-calibrated CO estimates allow one to determine, in some sense, *relative* errors for the CO estimates, i.e., percent changes in TCO to percent changes in ECO after scaling one of these two waveforms to have the same mean as the other. Thus, the mean calibration errors reported in this document can be interpreted as relative errors in ours and others' estimation methods.

In some of the results in Sun *et al.* [113], a *single point* calibration was used i.e., estimate the calibration constant C_{an} by dividing a single point p in the true CO waveform by the corresponding point in the

estimated CO waveform as follows:

$$C_{an} = \frac{\text{TCO}_p}{\text{ECO}_p}. \quad (5.28)$$

We do not quote results using single point calibration in this chapter, however, we do compare results obtained with mean calibration and results obtained with state-dependent calibration. Note that the mean or single point calibration methods can only be used if one assumes that C_{an} is given by (5.5) for all n .

5.5 Error Criteria

In evaluating the goodness-of-fit of our calibrated CO estimates, i.e., to compare true cardiac output (TCO) to estimated cardiac output (ECO), we used the RMSNE criterion. For a particular subject or animal, s , given n_s points at which TCO was measured and ECO was estimated, the RMSNE (in %) for the ECO for subject or animal s , denoted RMSNE_s , is given by:

$$\text{RMSNE}_s = \sqrt{\frac{1}{n_s} \sum_{n=1}^{n_s} \left(\frac{100(\text{TCO}_n - \text{ECO}_n)}{\text{TCO}_n} \right)^2}. \quad (5.29)$$

Within each data set, the subject or animal data records are of varying lengths, and thus the *aggregate* RMSNE over all subjects or animals is calculated as the weighted mean of the individual RMSNEs. Assuming that a particular data set has N_S total data points across all the subjects or animals, the aggregate RMSNE is given by:

$$\text{Aggregate RMSNE} = \sqrt{\frac{1}{N_S} \sum_s n_s (\text{RMSNE}_s^2)}. \quad (5.30)$$

In the literature, for example in [57, 58], instead of the weighted mean (5.30), the following expression is used to compute RMSNE over all S subjects or animals:

$$\text{Mean RMSNE} = \frac{1}{S} \sum_s \text{RMSNE}_s. \quad (5.31)$$

Such a *mean* RMSNE can be skewed if a particular subject or animal record within a data set is significantly larger (or smaller) or error-ridden (or error-free) compared to others in the same data set. In this chapter, unless we are doing direct comparisons with the results in [57], we use the aggregate RMSNE expression (5.30).

RMSNE, even for a particular subject or animal, is an average measure of performance. While it represents how the TCO and ECO compare in an average sense, it does not classify the CO estimation error with regard to the particular values of CO, ABP, or HR, or even the particular interventions being performed on the animals. A linear regression of TCO versus ECO with a reported correlation coefficient would also

only be an aggregate measure of performance, as would a Bland-Altman (see [114, 115]) plot of CO error versus the mean of TCO and ECO.

While we use RMSNEs, linear regressions, and Bland-Altman plots to visualize our CO estimation error and do useful comparisons of our estimation method to other methods, wherever appropriate, we also present plots of our estimate to visualize how the time series for the estimate and the reference waveform compare. A measure that is less sensitive to outliers and perhaps better matched to the visual impression in the graphical plots would be the mean absolute normalized error (MANE) for a particular animal or subject s :

$$\text{MANE}_s = \frac{1}{n_s} \sum_{n=1}^{n_s} \frac{100|\text{TCO}_n - \text{ECO}_n|}{|\text{TCO}_n|}, \quad (5.32)$$

however, we do not use this criterion in this thesis.

5.6 CO Variability and Naïve CO Estimators

As a metric for the degree of variability in the TCO waveform, i.e., a measure of how variable TCO is and how well our CO estimation method captures this variability, we implemented two *naïve* CO estimators, one for the porcine data set, and another for the canine and human data sets. Neither of these estimators needs to be calibrated.

For the porcine data set, the naïvely estimated CO, NECO, for swine s is simply the mean of the beat-to-beat TCO values:

$$\text{NECO}_n = \text{NECO} = \frac{1}{n_s} \sum_{n=1}^{n_s} \text{TCO}_n, \quad (5.33)$$

such that the normalized error at each estimation point is simply the normalized standard deviation of the TCO at that point. If the RMSNE for the NECO is smaller than that of our ECO, it implies that our method does not add more information than can be naïvely obtained from the TCO values.

For the canine and human data sets, since we only have intermittent echocardiography- or thermodilution-based cardiac output measurements, we used a sample-and-hold naïve estimator, SHNECO, given by:

$$\text{SHNECO}_{n+1} = \text{TCO}_n, \quad (5.34)$$

for $n \geq 2$ and $\text{SHNECO}_1 = \text{TCO}_1$. Again, if the RMSNE for the SHNECO is smaller than that of the ECO, it implies that our ECO does not add more information than can be obtained by simply holding the value of the previous TCO sample until the next time instant TCO is measured.

5.7 Sensitivity to Window Size and α

We used various window sizes (i.e., number of beats) – ranging from about 6 seconds to 12 minutes of data – to estimate τ_n , and hence ECO_n in our data sets. We observed that aggregate RMSNEs do not increase significantly for window sizes above 50 beats, implying that we do not seem to need variability beyond the range of 50 beats (30 seconds at a resting porcine or canine heart rate of 100 bpm, or approximately 1 minute at a resting human heart rate of 60 bpm) to obtain reasonable estimates. These observations, however, could be strongly dependent on the particular data sets used. For the results on the porcine data set, for example, we used a window size of 360 beats. For the canine data set, we used a window size of 100 beats, while in the two human ICU patient data sets, we used a window size of 360 beats.

We also used various values for α in (5.14) to estimate CO in our animal data sets. We observed that mean RMSNEs in the animal data sets are not too sensitive to α except for small values of α . For example, with a window size equal to 360 beats, the aggregate RMSNE taken over the porcine data set for each value of α were about the same for α ranging from 1.5 to 100. For small α , e.g., $\alpha \approx 0.01 - 0.9$, the aggregate RMSNE is much higher than with $\alpha \geq 1.5$. For other window sizes, the same result holds for this data set, i.e., the aggregate RMSNE is not sensitive to the value of α except for small α . From a least-squares estimation point of view this is not surprising as the constant α must be large enough such that the term $\frac{1}{T_n} \text{PP}_n$ in (5.8) is of the same order of magnitude, i.e., as significant, as the term $-\frac{1}{\tau_n} \overline{V}_{an}$. For the results presented in this thesis, we use $\alpha=2$ in both the porcine and the canine data sets, as described above.

5.8 Results and Discussion with Porcine Data

In this section, we describe a porcine data set, and describe how we estimate cardiac output for the animals in this data set. We also describe the errors obtained using our method and present a comparison of these errors to those obtained with other model-based CO estimation methods.

5.8.1 Porcine Data Set

The estimation methods were tested on the same animal data set used by Mukkamala *et al.* [57] – a study on nine Yorkshire swine (weighing 30–34 kg) approved by the MIT Committee on Animal Care. The animals were intubated under anesthesia and mechanically ventilated. Once intubated, the animals’ chests were opened, pressure transducers and an ultrasonic flow probe were placed, and over the course of 2-3 hours, CO, ABP, and HR were varied by one or more of the following interventions: volume infusions, slow hemorrhage, intravenous (IV) drugs (one or more of phenylephrine, isoproterenol, esmolol, nitroglycerine, or dobutamine).

The resulting data set is comprised of measurements of ECG, central arterial blood pressure (cABP)

Swine	CO (l/min) Range	HR (bpm) Range	Mean cABP (mmHg) Range	Duration of record (min)
4	1.5-5.6	43-190	40-115	118
5	2.4-5.0	100-210	45-162	112
6	2.2-6.1	63-192	55-120	94
7	1.2-4.8	56-250	36-123	140
8	2.5-5.9	49-208	40-117	104
9	1.3-6.3	51-192	45-130	72

Table 5.1: Population statistics for the porcine data set. The data was obtained from Professor Ramakrishna Mukkamala at Michigan State University [57].

measured at the thoracic aorta, approximate “radial”¹ arterial blood pressure (rABP), femoral arterial blood pressure (fABP), and aortic flow (AF), all sampled at 250 Hz with 16 bit amplitude resolution.

The results from swines 1–3 are not reported here (or in [57]) due to insufficiencies in the experimental data. The cABP waveform for swine 4 and the fABP waveform for swine 7 were corrupted because the corresponding pressure transducers were mis-calibrated during the experimental protocol. In addition, as was done in [57], data points at the end of each record, after progressive hemorrhages were started, were neglected as TCO was too low in these regions for any serious analysis. Table 5.1 gives a summary of population statistics for the six swine we used in this thesis.

Using a standard open-source algorithm [116] on the AF waveform, we derived onset times for each cardiac beat and HR. We also calculated systolic and diastolic cABP, systolic and diastolic rABP, systolic and diastolic fABP, mean cABP, mean rABP, and mean fABP for each swine. True or reference beat-to-beat CO was calculated by integrating the AF waveform over each beat, and then applying a 50-beat median filter to the resulting output. All the data processing and cardiac output estimation algorithms were implemented in MATLAB R14 (Mathworks Inc., Natick, MA).

5.8.2 RMSNEs and Individual Porcine ECO Waveforms

We applied our method to each of the six swine in several experiments, i.e., the cABP, rABP, and fABP waveforms were used independently in the linear least squares estimation scheme described in the previous section to obtain an uncalibrated estimate of CO. This estimate was calibrated using the methods described in Section 5.4, and the resulting ECO waveform was filtered using a 50-beat median filter. We tried using both the end-diastolic and the peak-systolic pressures in ΔV_{an} . All the results reported in this paper were obtained using the end-diastolic pressures in ΔV_{an} as the end-diastolic pressure points are less affected by wave reflection phenomena. We tried various values of α and window size, as well the different calibration methods mentioned in Section 5.4. Unless noted otherwise, results reported in this section were generated with a 100-point state-dependent calibration, i.e., 100 beats (1% or less of each swine record) evenly-

¹This pressure was measured using a transducer placed as distal as possible from the brachial artery.

Continuous Monitoring of Cardiac Output and Total Peripheral Resistance

Swine	Number of comparisons	RMSNE (%) for NECO	RMSNE (%) using cABP	RMSNE (%) using rABP	RMSNE (%) using fABP
4	14604	36.8	–	15.4	10.2
5	14404	17.6	8.7	10.6	9.4
6	12088	23.2	8.8	9.7	8.8
7	18155	33.7	13.1	11.1	–
8	14113	24.4	10.6	8.4	12.6
9	9370	44.6	21.7	15.8	19.5
Aggregate	82734	30.8	12.8	11.9	12.1

Table 5.2: RMSNEs for a 360 beat window size with $\alpha=2$ in equation (5.14) and a 100-beat state-dependent calibration.

spaced throughout a particular swine’s record, were used in (5.26) for calibration. (The aggregate RMSNEs reported here do not change more than 1% if we use as few as 10 beats, or even as many as 1000 beats, for calibration.)

Table 5.2 summarizes the results obtained for a window size of 360 beats (or, approximately 6 minutes at a HR of 100 bpm) for the cABP, rABP, and fABP waveforms. Results obtained with window sizes ranging from 20 to 800 beats yield similar RMSNEs. We also list the RMSNEs for the NECO estimate described in Section 5.5. These RMSNEs reflect the high CO variability in the porcine data set. Were this not the case, it would be difficult to argue that the low RMSNEs obtained using our method are an improvement over the naïve CO estimate (5.33).

Figures 5.3, 5.4, 5.5, 5.6, 5.7, and 5.8 show results for each of the six swine – Swines 4, 5, 6, 7, 8, and 9, respectively. Note that the spikes in the HR and R_a waveforms are a result of not filtering either \overline{V}_{an} , T_n or ΔV_{an} to generate these results. Note that there are sections where our estimate performs very well, while there are sections in each record where our estimate performs poorly. Whenever our estimate performs poorly, it is the result of over- or underestimating the time constant τ . For instance, for a single cardiac beat, assuming $\Delta V_{an}=0$, Equation (5.8) can be rewritten to reflect the components of τ_n :

$$\tau_n = \frac{\overline{V}_{an}}{PP_n} T_n \quad , \quad (5.35)$$

from which it is clear that τ_n depends on the relative magnitudes and variability in mean ABP, PP, and HR. For example, in data sections where ABP and PP are not varying much, τ_n depends strongly on HR, e.g., between $t=2000$ s and $t=3000$ s in Fig. 5.5. On the other hand, in sections of data where HR is constant, τ_n depends on the ratio of mean ABP to pulse pressure – and if mean ABP is low, e.g., 50 mmHg, τ_n will vary primarily with pulse pressure, e.g., see the first and last 500 s of data in Fig. 5.4 and between $t=3800$ s and $t=4200$ s in Fig. 5.5.

Our results with 100-point state-dependent calibration have mean RMSNEs of 11–13% which is lower than the 15% reported in the literature [58] as being acceptable for clinical purposes. The CO estimate tracks all major transitions in TCO over a wide range of values for mean ABP and HR. In addition, across

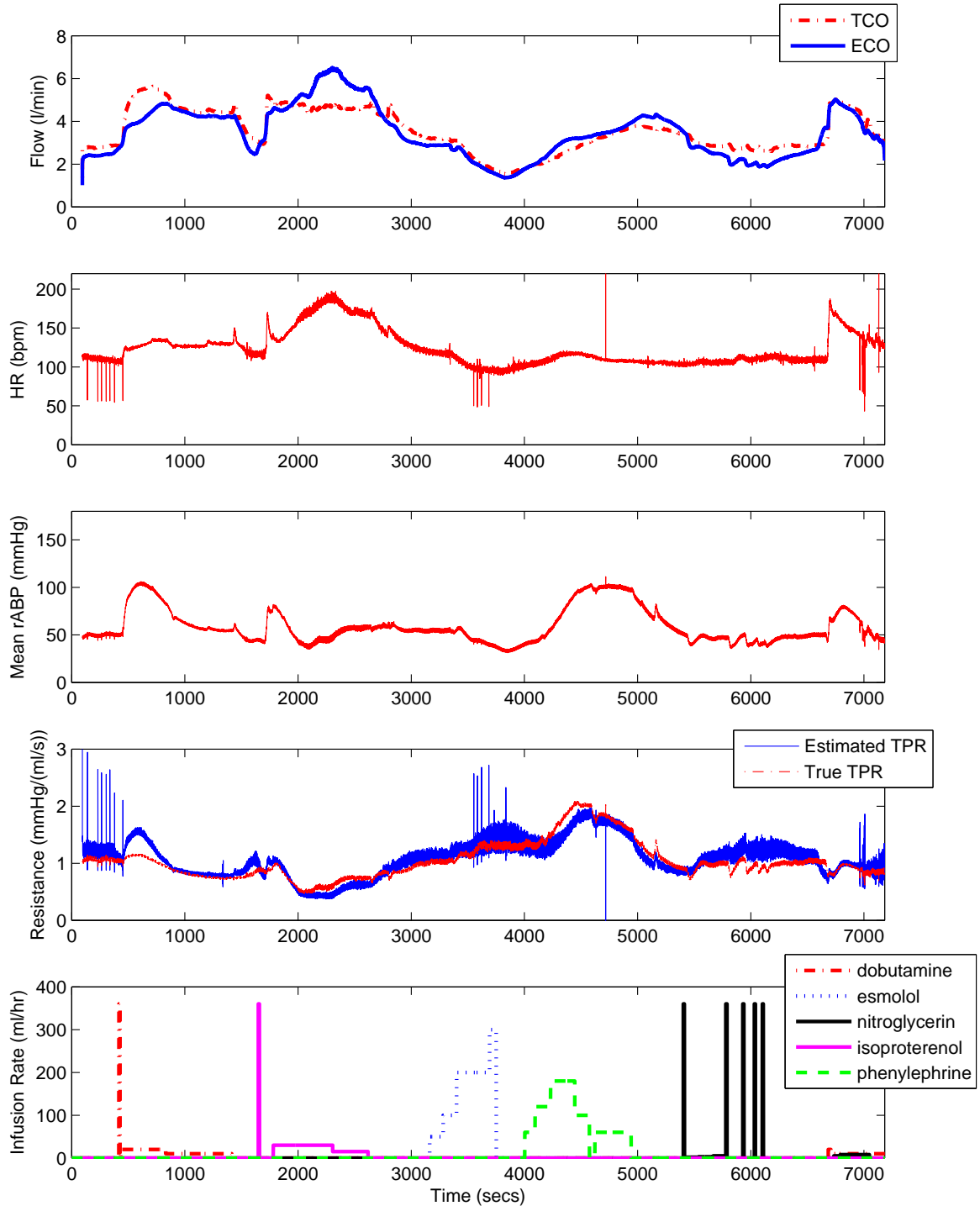


Figure 5.3: True and estimated CO (using rABP), HR, mean rABP, true and estimated TPR, and IV drugs for swine 4 with window size = 360 beats and a 100-beat state-dependent calibration.

Continuous Monitoring of Cardiac Output and Total Peripheral Resistance

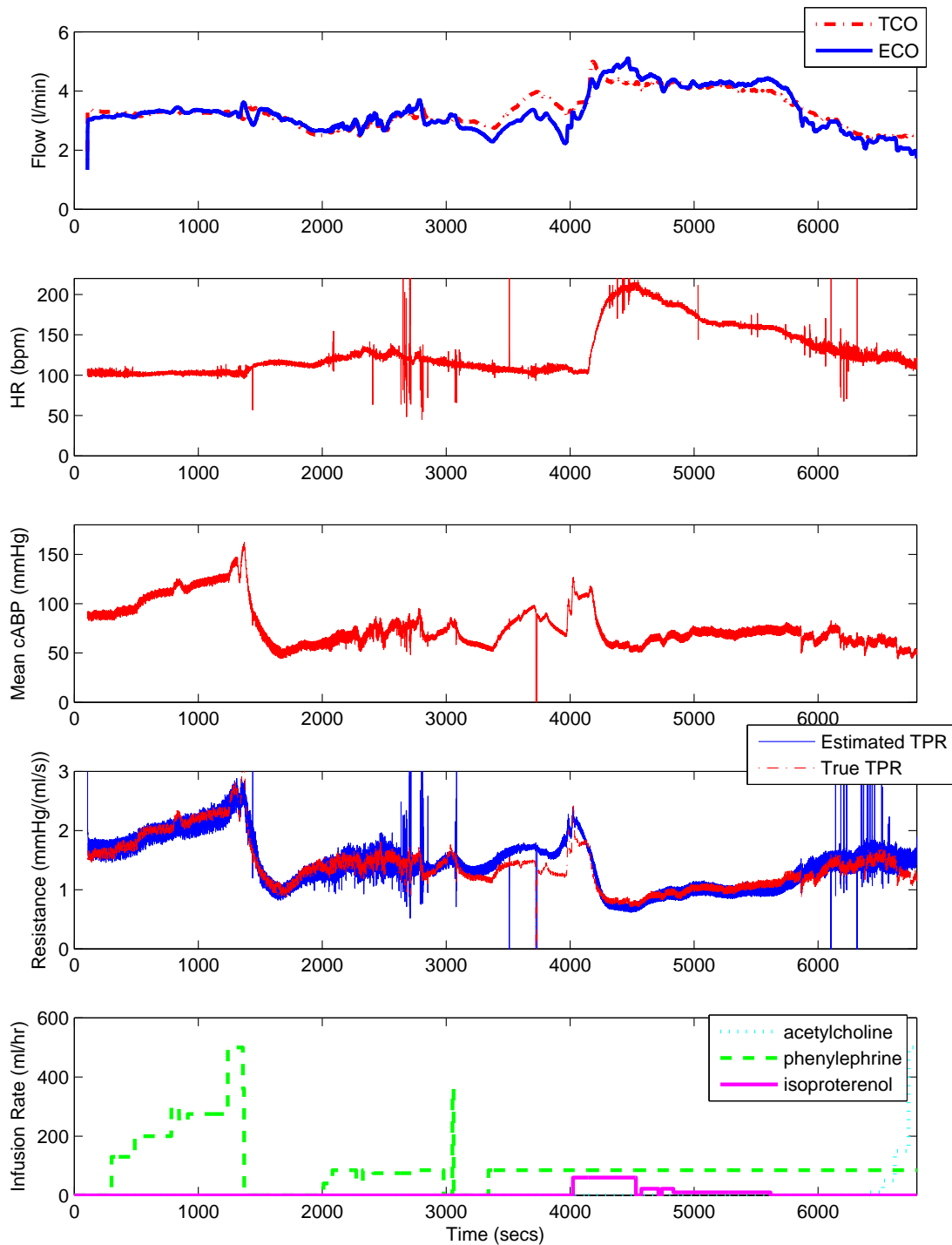


Figure 5.4: True and estimated CO (using cABP), HR, mean cABP, true and estimated TPR, and IV drugs for swine 5 with window size = 360 beats and a 100-beat state-dependent calibration.

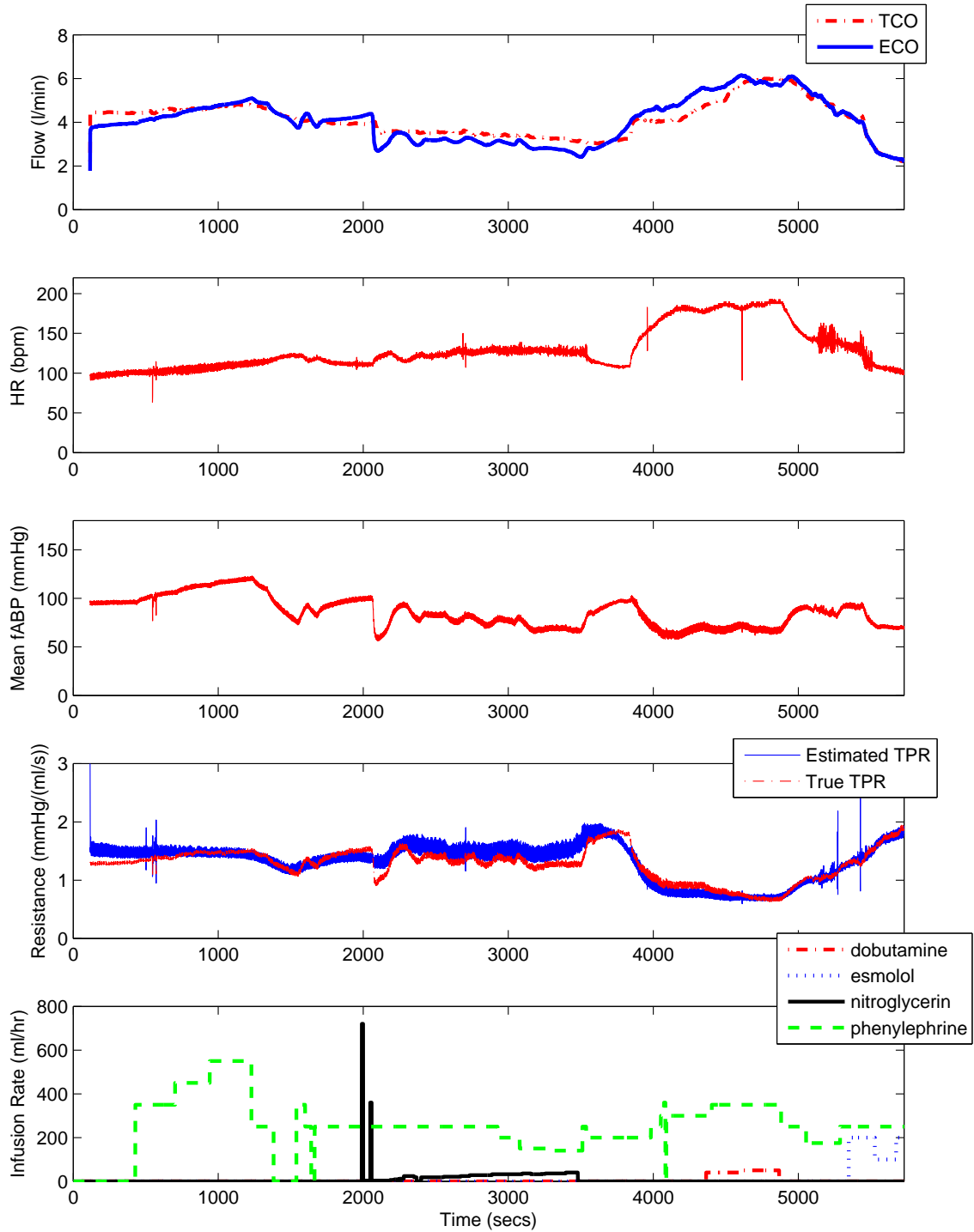


Figure 5.5: True and estimated CO (using fABP), HR, mean fABP, true and estimated TPR, and IV drugs for swine 6 with window size = 360 beats and a 100-beat state-dependent calibration.

Continuous Monitoring of Cardiac Output and Total Peripheral Resistance

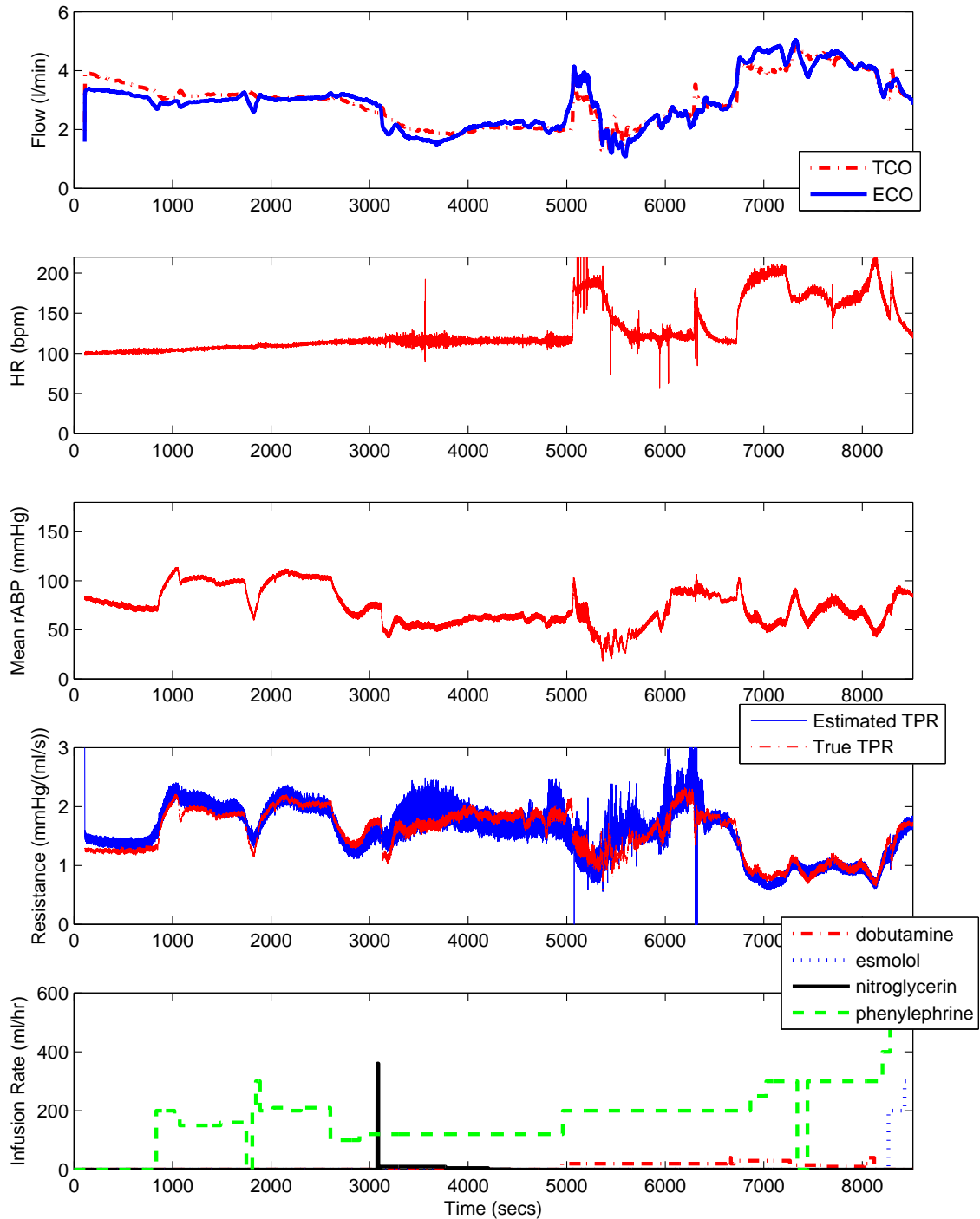


Figure 5.6: True and estimated CO (using rABP), HR, mean fABP, true and estimated TPR, and IV drugs for swine 7 with window size = 360 beats and a 100-beat state-dependent calibration.

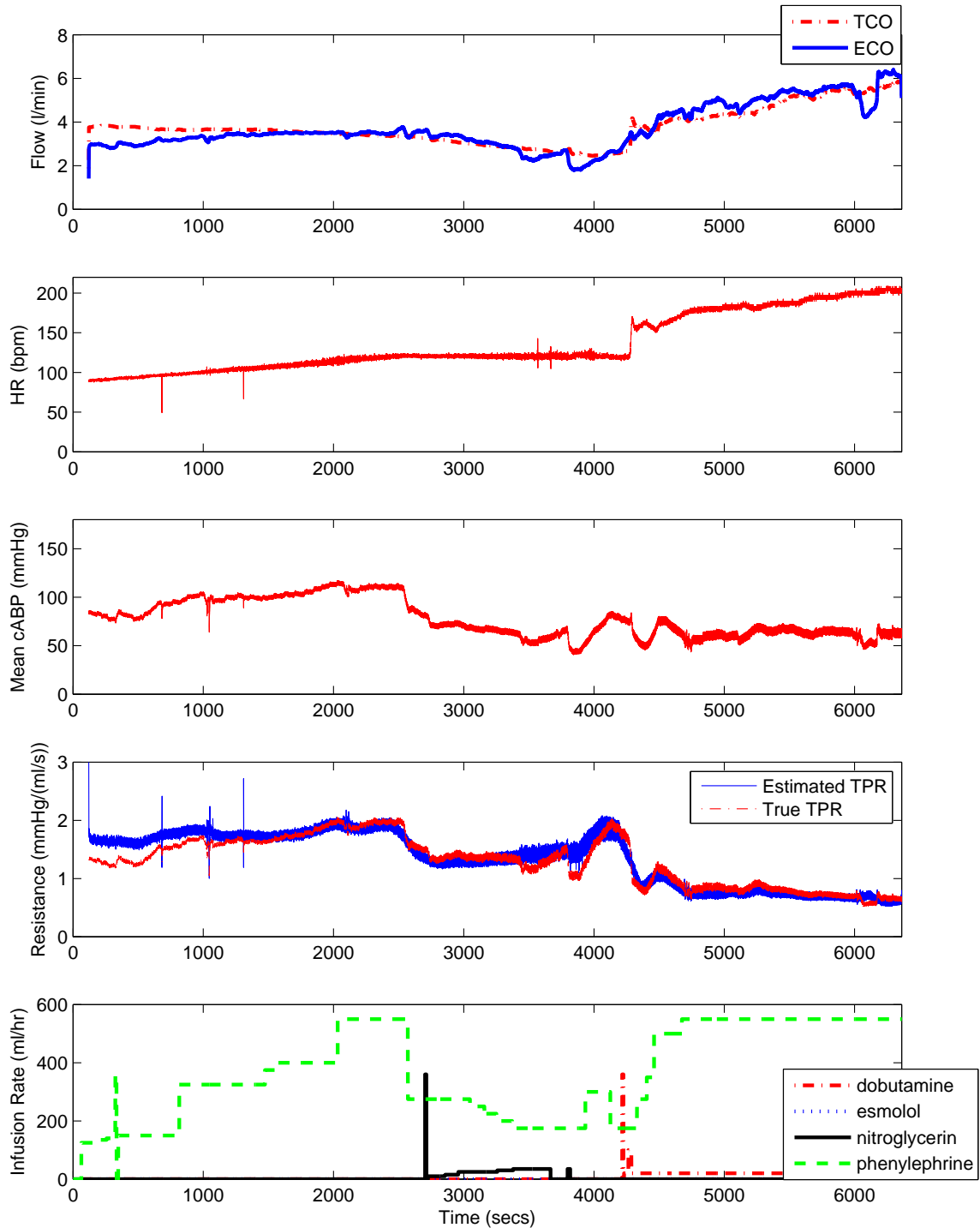


Figure 5.7: True and estimated CO (using cABP), HR, mean fABP, true and estimated TPR, and IV drugs for swine 8 with window size = 360 beats and a 100-beat state-dependent calibration.

Continuous Monitoring of Cardiac Output and Total Peripheral Resistance

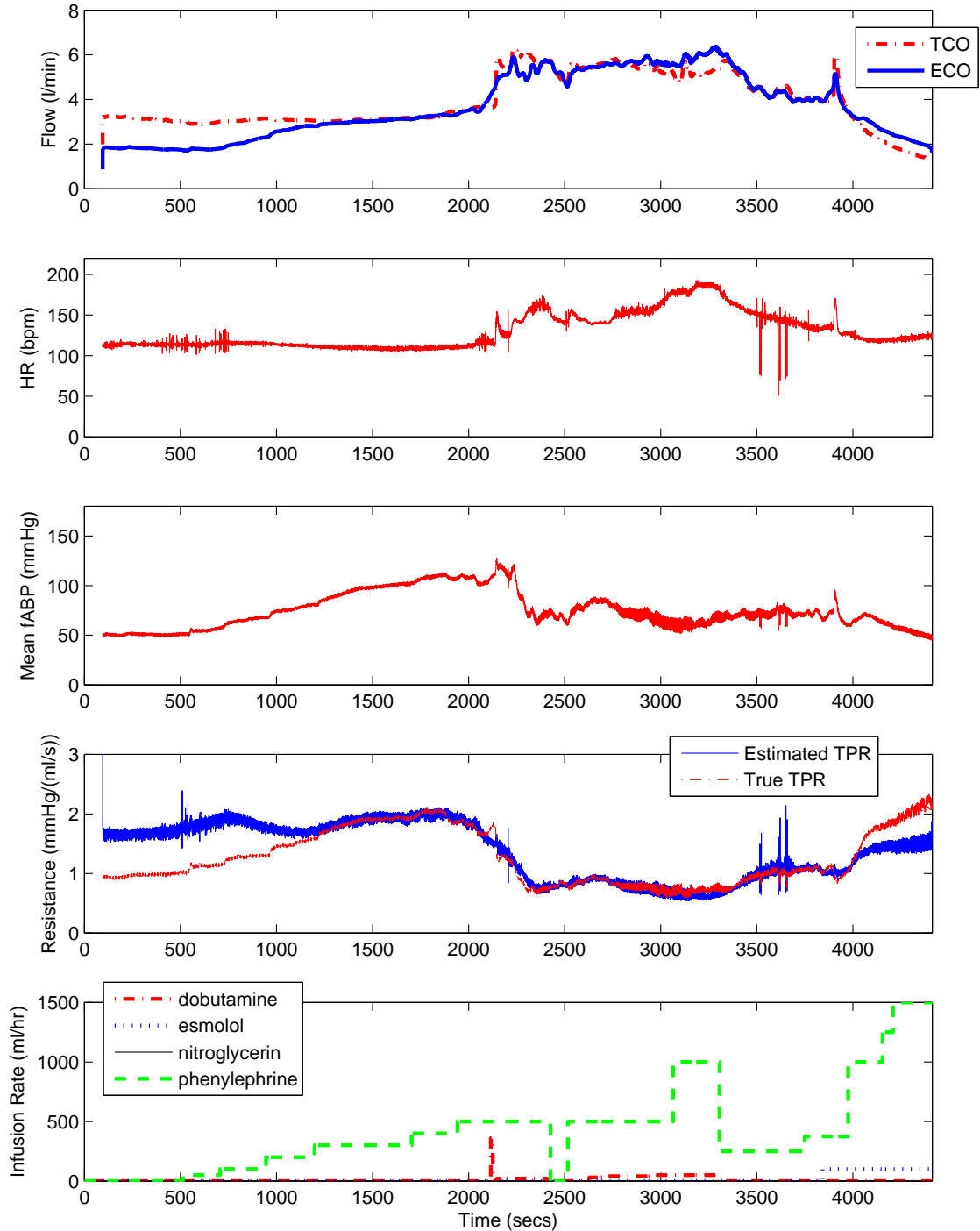


Figure 5.8: True and estimated CO (using fABP), HR, mean fABP, true and estimated TPR, and IV drugs for swine 9 with window size = 360 beats and a 100-beat state-dependent calibration.

–	ECO (for cABP)	ECO (for rABP)	ECO (for fABP)
TCO	0.917±0.001	0.9325 ± 0.005	0.887 ± 0.002

Table 5.3: Correlation coefficients for linear regressions of ECO versus TCO. The results are for a 360 beat window size and a 100-beat state-dependent calibration.

–	TCO-ECO (for cABP)	TCO-ECO (for rABP)	TCO-ECO (for fABP)
\bar{V}_a	0.072±0.006	0.051 ± 0.007	0.009 ± 0.007
HR	-0.470±0.005	-0.488 ± 0.005	-0.127 ± 0.006
TCO	-0.102±0.006	-0.198 ± 0.007	0.049 ± 0.007

Table 5.4: Correlation coefficients for linear regressions of estimation error (TCO-ECO) versus \bar{V}_a , HR, and TCO. The results are for a 360 beat window size and a 100-beat state-dependent calibration.

the entire data set, the estimated TPR, R_a , tracked the true TPR for a wide variety of pharmacological interventions, e.g., in Fig. 5.3, when phenylephrine is infused, we see a large increase in estimated TPR and a slight increase in HR. In Fig. 5.4, we again see larger estimated TPR when phenylephrine is infused.

If we allowed for updates in the calibration factor, e.g., with an exponentially-weighted repeated overlapping state-dependent calibration with 10 points in every window of 1000 points, as shown in Fig. 5.9, the ECO and R_a waveforms track the TCO and TPR waveforms, respectively, extraordinarily well. In the region around 6800s, the calibration factor is not updated as fast as the transient in TCO, and we see a spike in the ECO waveform.

5.8.3 CO Error Visualization and Analysis

Figure 5.10 shows a linear regression visualizing the CO estimation error. This plot is an aggregate of all 82,734 comparisons listed in Table 5.2 using the rABP waveform.

The correlation coefficients for ECO versus TCO (with 95% confidence intervals) are summarized in Table 5.3, while the correlation coefficients of the estimation error versus mean pressure, heart rate, and TCO, with 95% confidence levels, are summarized in Table 5.4. These correlation coefficients show that the estimation error is not strongly correlated with mean ABP, HR, or TCO.

Figure 5.11 is a Bland-Altman plot for the CO estimation error using rABP. Again, this plot is an aggregate of all 82734 comparisons listed in Table 5.2. Note that in both the regression and the Bland-Altman plots, there is a discernible path traced by the error in the plane showing some correlation between error and the underlying TCO waveform. Given our state-dependent calibration, this time correlation is expected.

From the Bland-Altman plot, we see that the mean estimation error (or *bias*) is 18 ml/min, while the 1-standard deviation (SD) of the estimation error is 429 ml/min. The flow probe (T206 with A-series attachment, Transonic Systems Inc., Ithaca, NY) used in the animal experiments had a relative precision of $\pm 2\%$, which at the instrument scale of ± 20 l/min is approximately 1 l/min. The 2-SD line for our

Continuous Monitoring of Cardiac Output and Total Peripheral Resistance

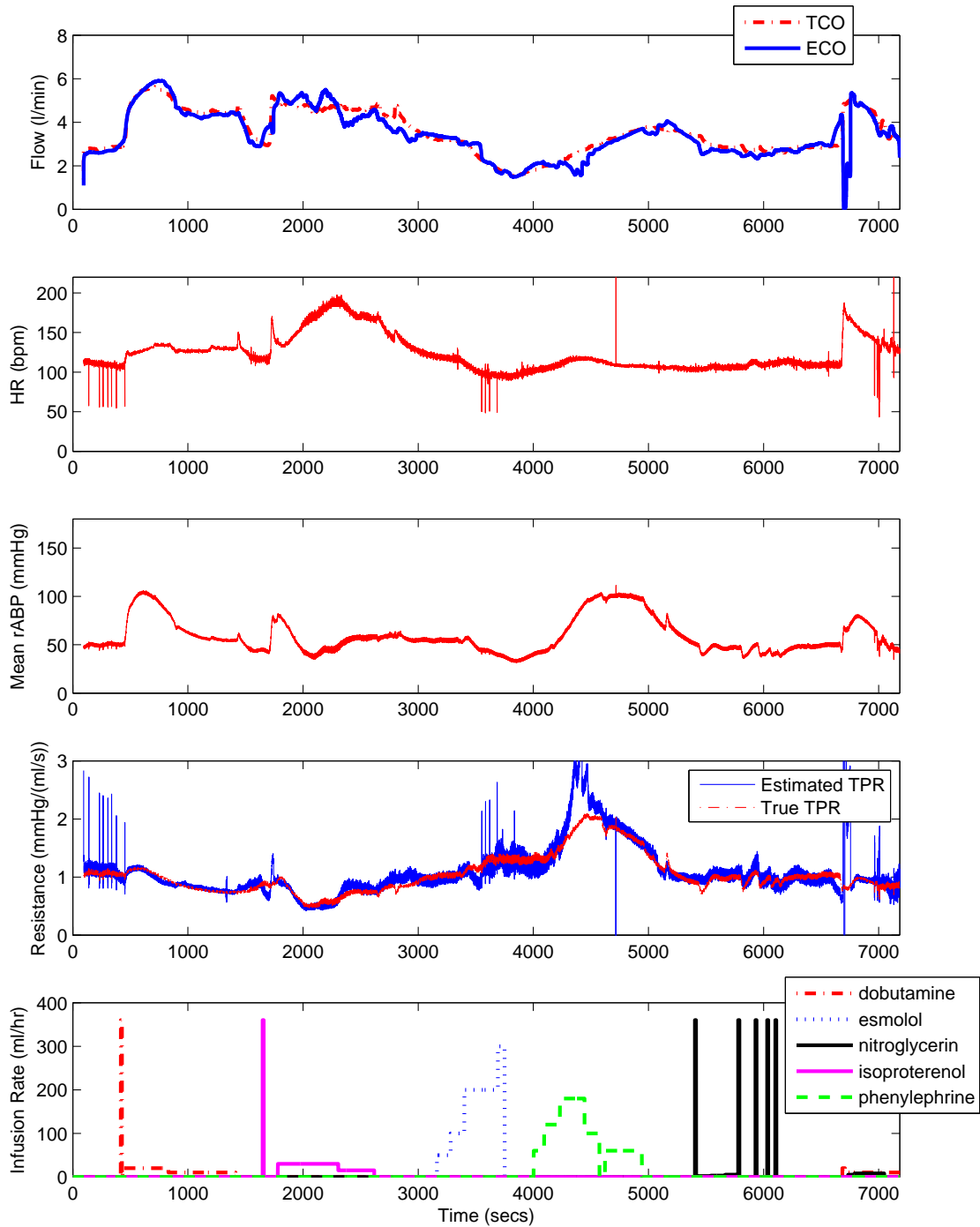


Figure 5.9: True and estimated CO (using rABP), HR, mean rABP, estimated and true TPR, and IV drugs for swine 4 with window size = 360 beats, and a 10-beats of every 1000-beat window exponentially-weighted overlapping repeated state-dependent calibration.

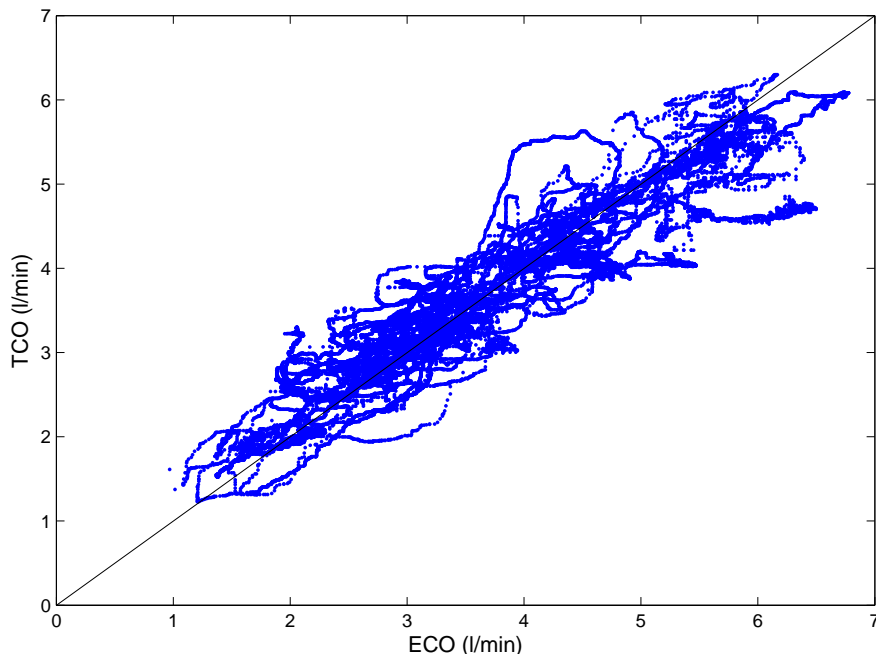


Figure 5.10: Linear regression of TCO versus ECO (using rABP) over all six swine with window size = 360 beats, and a 100-beat state-dependent calibration.

estimate lies 860 ml/min from the line representing mean estimation error, showing that, according to the criterion outlined in [114, 115], our estimated CO compares well with the reference aortic flow probe CO measurements.

5.8.4 Comparison to Mukkamala and Co-workers Method

Mukkamala *et al.* [57] reported the results shown in Table 5.5, where we calculated the aggregate RMSNEs using (5.30). They re-sampled the 250Hz data at 90 Hz, and used a 6-minute window size, with a 3-minute overlap between successive windows. In each 6-minute window, they estimated the time constant τ of the Windkessel model by assuming it could be represented by a 23-coefficient ARMA model [57].

Our results are significantly different by swine and are, in an aggregate sense, much better than those reported in [57]. In addition, instead of 6-minute windows, our method can use much less data, e.g., 10–50 beats to obtain an estimate of τ_n . A criticism of Mukkamala *et al.* put forward by van Lieshout *et al.* [108], and contended in [118] is that while CO estimates produced every 3 minutes may be good enough to track slower patient dynamics, they may not be good enough for large, sudden changes in CO, as is evident from patient data in the literature [119]. Furthermore, Mukkamala and co-workers' estimate assumes a constant arterial tree compliance, which is not necessarily a valid assumption, but does allow for the possibility of using only one TCO point for calibration.

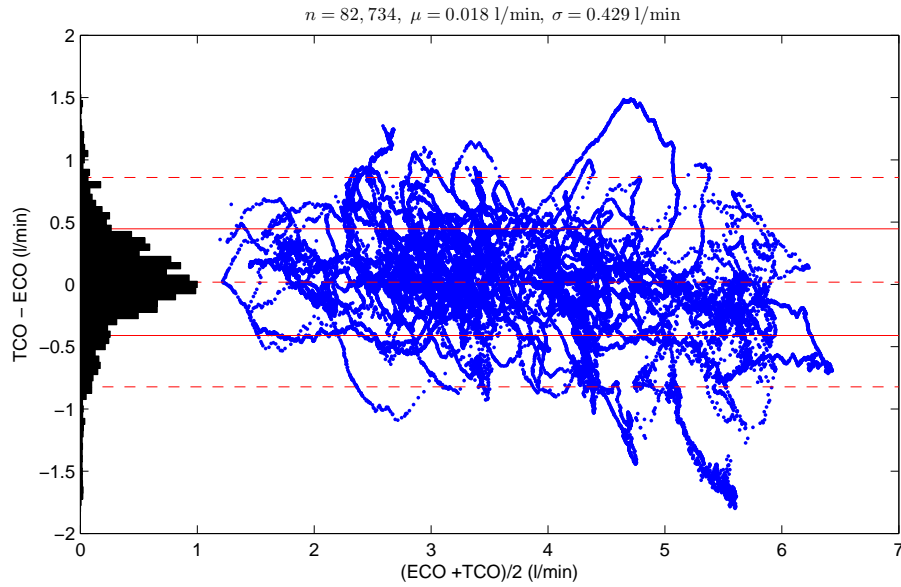


Figure 5.11: Bland-Altman plot of CO estimation error versus the mean of TCO and ECO (using rABP) over all six swine with window size = 360 beats, and a 100-beat state-dependent calibration. The horizontal lines in the plot are the mean error, and the 1-SD and 2-SD lines.

Swine	Number of comparisons	RMSNE (%) using rABP	RMSNE (%) using fABP
4	38	19.1	29.9
5	37	16.0	10.2
6	31	16.7	8.8
7	46	12.3	–
8	34	8.0	10.2
9	24	14.7	17.1
Aggregate	210	14.8	17.6

Table 5.5: RMSNEs reported in Mukkamala *et al.* [57] with aggregate RMSNEs calculated based on (5.30).

CO Estimation Method (calibration method)	RMSNE (%) using rABP	RMSNE (%) using fABP
Ours* (state-dependent using 3-minute sampled TCO points)	13.3	13.9
Ours (state-dependent using half of 3-minute sampled TCO points)	13.5	14.0
Mukkamala <i>et al.</i> [57] (mean using 3-minute sampled TCO points)	13.9	15.0
Sample-and-hold version of *	18.5	19.2

Table 5.6: RMSNEs for the porcine data set (using the rABP waveform) comparing our 3-minute ECO to Mukkamala and co-workers CO estimate, as well as our sample-and-hold ECO. Errors for the first three estimates were compared to 3-minute samples of TCO, while that for the sample-and-hold estimate was compared to the entire TCO waveform.

For a better comparison with Mukkamala *et al.* [57], we implemented our method using 6-minute windows to estimate the time constant and produced estimates of CO every 3 minutes. We compared this 3-minute CO estimate to the 3-minute samples of the TCO waveform. For our estimate, we performed a state-dependent calibration in two ways – using all the available 3-minute TCO points, and using only half of these points. We also computed a sample-and-hold 3-minute estimate and compared it to the TCO waveform. Table 5.6 presents the results of these analyses.

Fig. 5.12 is a plot of our 3-minute estimated CO (using rABP) and the sample-and-hold version of this 3-minute estimated CO versus true CO for swine 4. Note that the sample-and-hold version of the 3-minute estimated CO performs much worse than our beat-to-beat CO estimate.

5.8.5 Comparison to other CO Estimation Methods

We compared our and Mukkamala and co-workers’ methods to several other *static* intra-beat Windkessel-based CO estimation methods. We refer to these methods as static since they estimate CO at each beat using only information encoded in the pressure wavelet of that particular beat. To come up with a fair comparison, we used a mean calibration (5.27), as used by Mukkamala and co-workers, to calibrate all the estimates. In addition, as was done in [57], we calculated mean RMSNEs for each estimation method using (5.31), i.e., *without weighting* the individual swine RMSNEs by the number of comparisons in each swine record. The results of this analysis, for the fABP and rABP waveforms², are shown in Table 5.7.

From these results we can conclude that for this particular porcine data set, the Herd estimate performs quite well, while the other static estimation methods tend to perform quite poorly. Using rABP, the Herd estimate performs as well as the dynamic estimation method of Mukkamala *et al.* [57], and is comparable to our CO estimate. For the fABP waveform-based results, our method, Mukkamala and co-worker’s method,

²We do not report results with the cABP waveform here because they were not reported in [57].

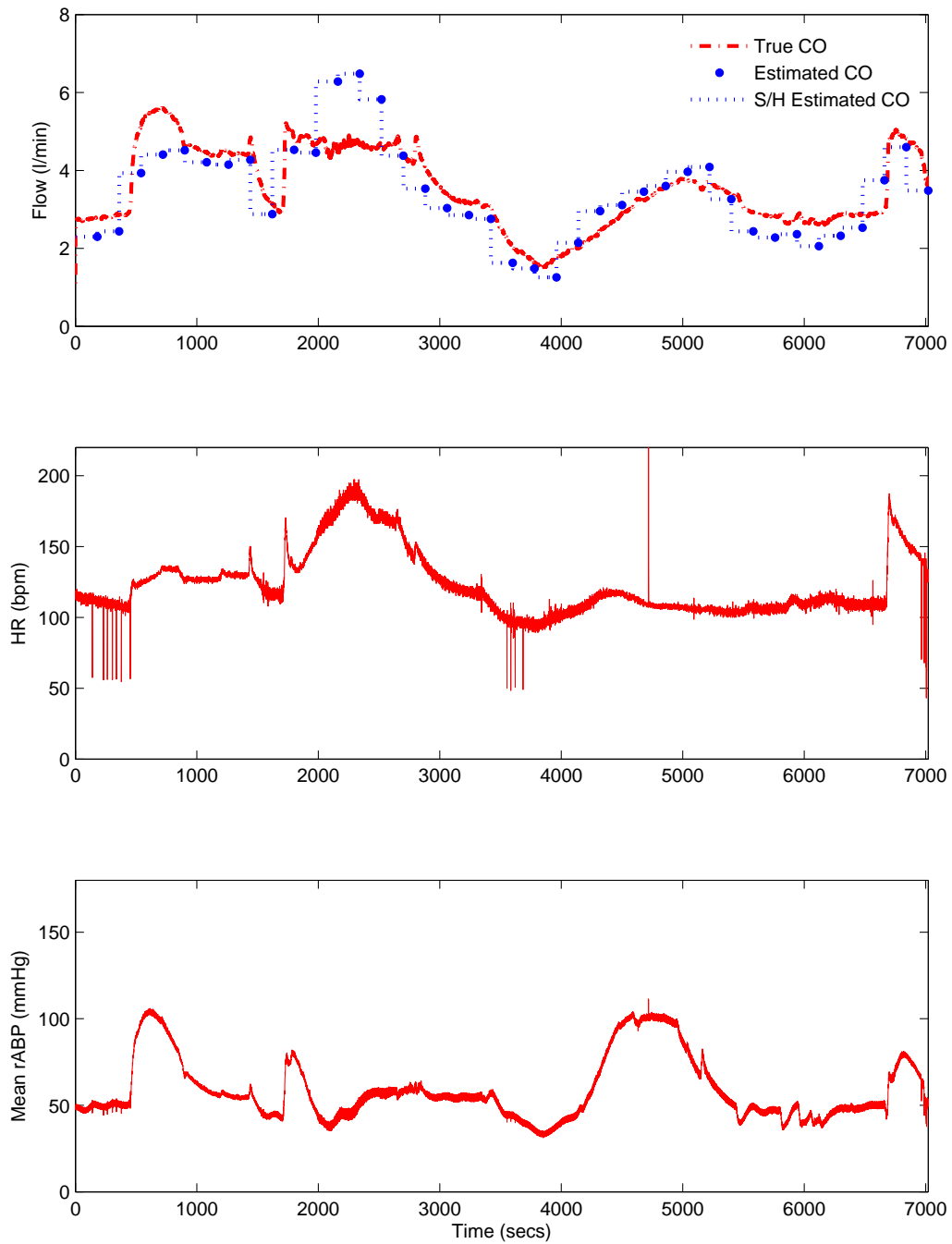


Figure 5.12: True CO, 3-minute estimated CO (using rABP), and a sample-and-hold (S/H) version of the 3-minute estimated CO, HR, and mean rABP. 3-minute ECO was calculated with window size = 6 minutes and $\alpha=2$ in (5.14), and a state-dependent calibration using all available 3-minute samples of TCO.

CO Estimation Method	Uncalibrated $CO_n =$	RMSNE (%) using rABP	RMSNE (%) using fABP
Our Method	(5.13)	13.5	15.2
Mukkamala <i>et al.</i> [57]	ARMA model	14.0	15.0
Herd [106]	$HR_n \cdot (\overline{V_{an}} - DAP_n)$	14.0	15.9
Modified Mean Pressure	$HR_n \cdot \overline{V_{an}}$	18.6	20.0
Static Windkessel [37]	$HR_n \cdot (SAP_n - DAP_n)$	21.1	18.8
Liljestrand and Zander [64]	$HR \cdot \left(\frac{SAP_n - DAP_n}{SAP_n + DAP_n} \right)$	30.0	25.1
Mean Pressure [113]	$\overline{V_{an}}$	31.6	33.6

Table 5.7: Mean RMSNEs for various static and dynamic CO estimates. Each estimate was calibrated using a mean calibration (5.27). Note that Mukkamala’s results are based on intermittent CO estimates i.e., every 3 minutes, while the others are continuous CO estimates.

In the next section, we show that if we apply the same 100-point state-dependent calibration to the Herd estimate, we obtain aggregate RMSNEs similar to those in Table 5.2. On the other hand, results obtained using human ICU data [113] show that the method of Liljestrand and Zander [64] outperforms the Herd estimate (we apply our method to human data in Sections 5.10 and 5.11). Our method, however, consistently outperforms all other methods we chose to apply to the various data sets presented in this chapter.

5.8.6 Comparison of Mean and State-Dependent Calibration Factors

At the outset, we wanted to investigate the use of both a constant and a mean pressure-dependent compliance C_a as the calibration factor for our CO estimates. While there is much disagreement in the research community, CO estimation methods exist which assume a constant arterial compliance, and there are others which assume a pressure-dependent compliance function – whether linear or nonlinear.

We applied our method and other methods from the literature to the porcine data set using both a 100-point state-dependent calibration, and a 100-point mean calibration. In each case, the points were spread evenly throughout each swine record. The results of this experiment are shown in Table 5.8. It is clear that a state-dependent calibration, even on just 100 points out of 10,000-15,000, yields better results than a mean calibration. It is also clear that for the Liljestrand and Zander, mean pressure, and modified mean pressure methods, the state-dependent calibration significantly reduces the aggregate RMSNEs.

In addition to calibrating the CO estimates with TCO points spread evenly through the entire length of each swine record, we also applied each CO estimation method from Table 5.8 to swine records in which half the data was used for calibrating (or “training”), and half was used for testing the predictive value of the calibration factor (or “testing”).

Table 5.9 shows the resulting RMSNEs for each of the CO estimation methods when 10 points out of the first half of each swine record were used for training, and the second half of each swine record was used for

Continuous Monitoring of Cardiac Output and Total Peripheral Resistance

CO Estimation Method	Aggregate RMSNE (%) using rABP state-dependent calibration	Aggregate RMSNE (%) using rABP mean calibration
Ours	11.8	13.5
Herd [106]	12.0	13.9
Mukkamala <i>et al.</i> [57]	N/A	14.0
Liljestrand and Zander [64]	14.6	30.0
Modified Mean Pressure	14.5	18.6
Mean Pressure [113]	26.6	31.6

Table 5.8: Aggregate RMSNEs for the porcine data set (using the rABP waveform) with either mean calibration using all available TCO points or state-dependent calibration using 100 TCO points evenly-spaced throughout each record. Results obtained with the fABP waveform follow the trends in this table.

CO Estimation Method	Aggregate RMSNE (%) using rABP state-dependent calibration	Aggregate RMSNE (%) using rABP mean calibration
Ours	19.8	18.3
Herd [106]	20.8	19.3
Liljestrand and Zander [64]	28.9	57.8
Modified Mean Pressure	19.8	21.1
Mean Pressure [113]	35.3	41.1

Table 5.9: Aggregate RMSNEs for the porcine data set (using the rABP waveform) with either mean or state-dependent calibrations using 10 points out of the first half of the available TCO points to calibrate, and the second half of the records to test the predictive value of the calibration factor. Results obtained with the fABP waveform follow the trends in this table.

testing.

Table 5.10 shows the resulting RMSNEs for each of the CO estimation methods when 10 points out of the central half of each swine record were used for training, and the outer quarters of the records were used for testing.

Table 5.11 shows the resulting RMSNEs for each of the CO estimation methods when 10 points out of the second half of each swine record were used for training, and the first half of each swine record was used for testing.

In all three scenarios described above, we tried the same analysis using 50 points or all points for calibration in the training set and observed similar results.

From Tables 5.8, 5.9, 5.10, and 5.11, it is evident that when the data records were divided into training and test sets, mean calibration resulted in lower RMSNEs than state-dependent calibration for the top two estimation methods, but when the records were not split in this manner, state-dependent calibration resulted in lower RMSNEs. While there may be some data dependency in these results, it is also clear that whatever data set we use for training/testing, our method is robust in the sense that it is consistently

CO Estimation Method	Aggregate RMSNE (%) using rABP state-dependent calibration	Aggregate RMSNE (%) using rABP mean calibration
Ours	17.9	15.2
Herd [106]	19.2	15.1
Liljestrand and Zander [64]	22.3	30.0
Modified Mean Pressure	21.6	18.9
Mean Pressure [113]	38.2	33.1

Table 5.10: Aggregate RMSNEs for the porcine data set (using the rABP waveform) with either mean or state-dependent calibrations using 10 points out of the central half of the available TCO points to calibrate, and the outer fourths of the records to test the predictive value of the calibration factor. Results obtained with the fABP waveform follow the trends in this table.

CO Estimation Method	Aggregate RMSNE (%) using rABP state-dependent calibration	Aggregate RMSNE (%) using rABP mean calibration
Ours	20.2	13.5
Herd [106]	22.3	14.0
Liljestrand and Zander [64]	23.1	32.7
Modified Mean Pressure	22.4	19.9
Mean Pressure [113]	46.7	52.8

Table 5.11: Aggregate RMSNEs for the porcine data set (using the rABP waveform) with either mean or state-dependent calibrations using 10 points out of the second half of the available TCO points to calibrate, and the first half of the records to test the predictive value of the calibration factor. Results obtained with the fABP waveform follow the trends in this table.

a top performer in each of the evaluations. Since these conclusions were true for both the fABP and the rABP waveform, we can conclude that our observations are not measurement site-dependent.

We analyzed our linear mean pressure-dependent arterial tree compliance for each of the six swine and discovered that, apart from swine 4, all the swines have an almost-constant, i.e., pressure-independent, arterial compliance. Figures 5.13 and 5.15(a) show a time series of our fit for the arterial compliance, and a plot of $\frac{\text{TCO}}{\text{ECO}}$ and our fit for the arterial compliance versus mean pressure, respectively, for swine 4. Note that in Fig. 5.15, we used 100 points spread evenly throughout each swine record to compute our fit for the arterial compliance C_a . Figures. 5.14 and 5.15e) show a time series of our fit for the arterial compliance, and a plot of $\frac{\text{TCO}}{\text{ECO}}$ and our fit for arterial compliance versus mean pressure, respectively, for swine 8. Plots of $\frac{\text{TCO}}{\text{ECO}}$ and our fits for the arterial compliance versus mean pressure for all six swine appear in Fig. 5.15.

It is clear from Figs. 5.13, 5.14, and 5.15, that the arterial tree compliance is essentially constant for all but one of the swine in this data set, i.e., that γ_2 in (5.4) can be assumed to be zero for all except swine 4. This may not be the case for the canine and human data sets as we discuss below, and thus, more investigation is needed to ascertain the need for a mean pressure-dependent compliance.

5.8.7 Results on the Effect of Beat-to-Beat Variability

We conclude this section with a brief discussion on beat-to-beat variability. While Tables 5.7, 5.8, 5.9, 5.10, and 5.11, all seem to imply that the static Herd estimate and our dynamic CO estimate are, in an aggregate sense, equivalent, the same is not true if we take a closer look at the TCO and ECO waveforms. Our dynamic CO estimation method incorporates beat-to-beat variability and we assumed therefore from the outset that it must produce more fine-tuned CO estimates than those produced by static estimation methods. If this assumption is valid, we can infer that the performance of the static Herd estimation method relative to our method may be because there is not enough beat-to-beat variability in these animals' ABP and/or HR.

To test the hypothesis, i.e., that beat-to-beat variability improves our CO estimate, we defined a beat-to-beat variability index, B2BVI_b (%), in each 360-beat window as follows:

$$\text{B2BVI}_b = \frac{1}{360} \sum_{n=b}^{b+360} \left(100 \frac{\Delta V_{an}}{\text{PP}_n} \right) . \quad (5.36)$$

We then calculated RMSNEs only using points on the ECO waveform where τ_n was calculated on windows where $\text{B2BVI}_b \geq 5\%$. The results obtained are summarized in Tables 5.12 and 5.13, where, for the rABP waveform, we compare our estimate to the Herd estimate. It is clear that on windows with high beat-to-beat variability, our dynamic CO estimate performs either comparably (in the case of swine 5) or somewhat better than the static Herd estimate.

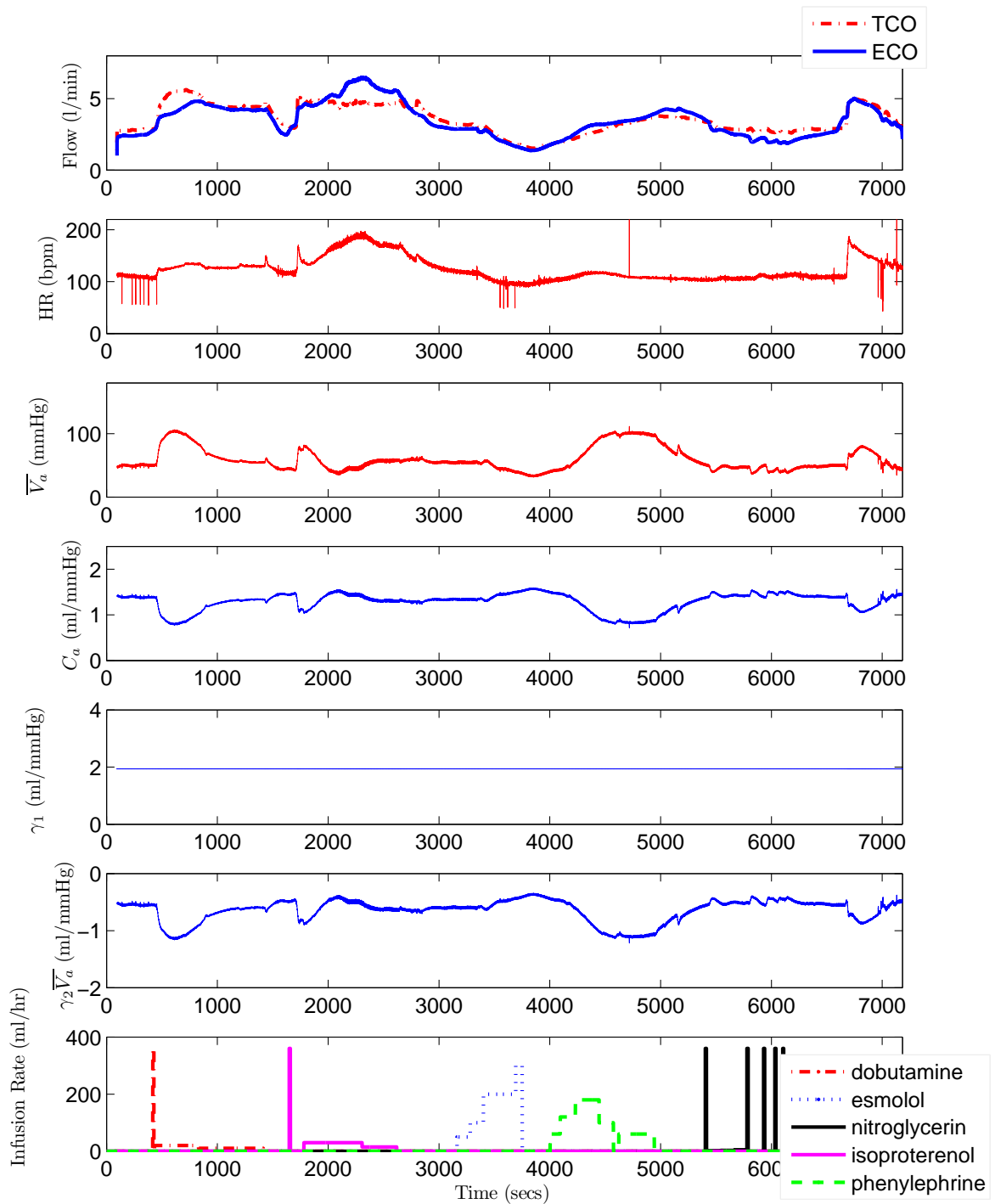


Figure 5.13: True and estimated CO (using cABP), HR, mean cABP, calibration factor C_a , and its components γ_1 and $\gamma_2 \bar{V}_a$, and IV drugs for pig 4 with window size = 360 beats, and a 100-point state-dependent calibration.

Continuous Monitoring of Cardiac Output and Total Peripheral Resistance

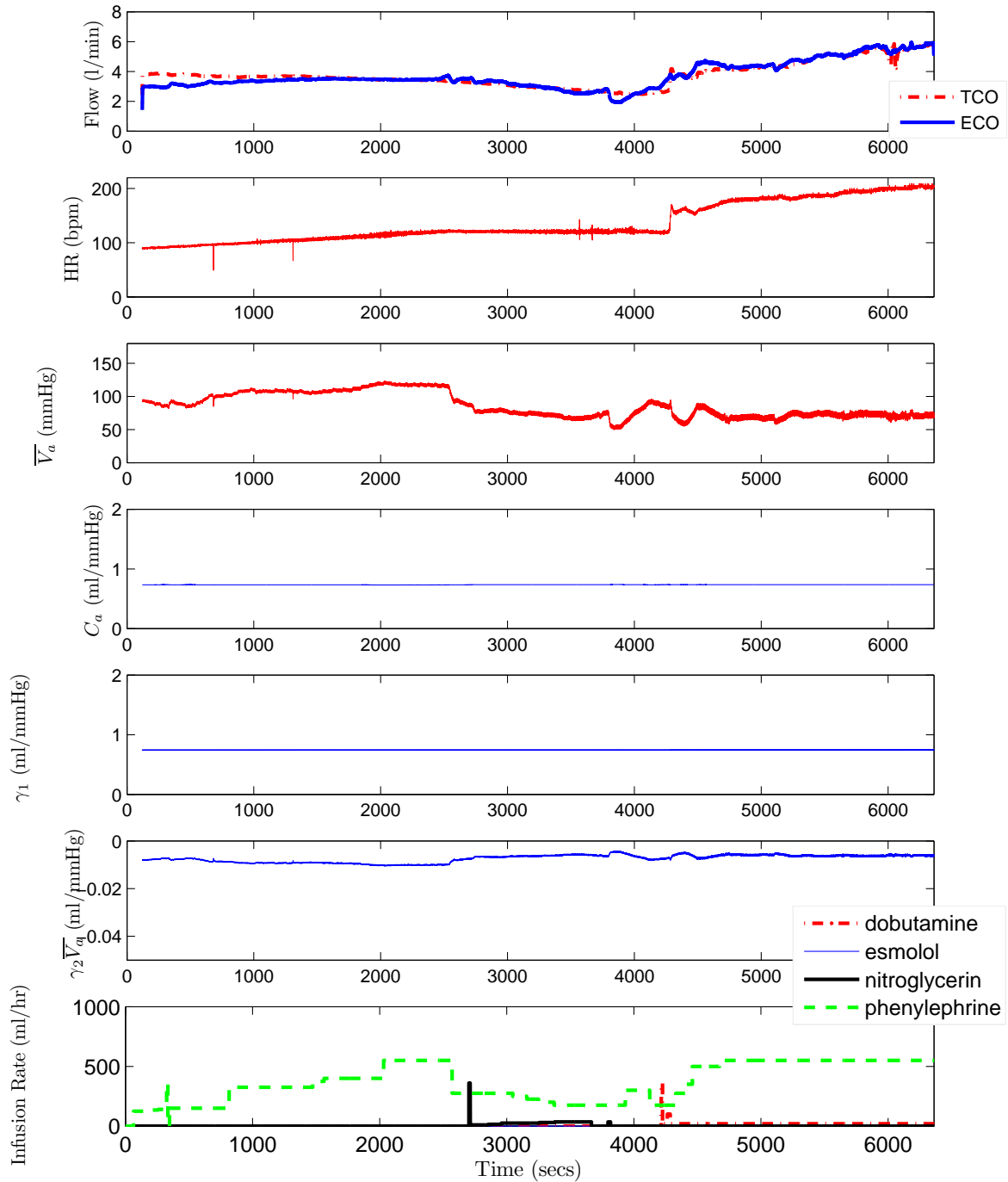


Figure 5.14: True and estimated CO (using cABP), HR, mean cABP, calibration factor C_a , and its components γ_1 and $\gamma_2\bar{V}_a$, and IV drugs for pig 8 with window size = 360 beats, and a 100-point state-dependent calibration.

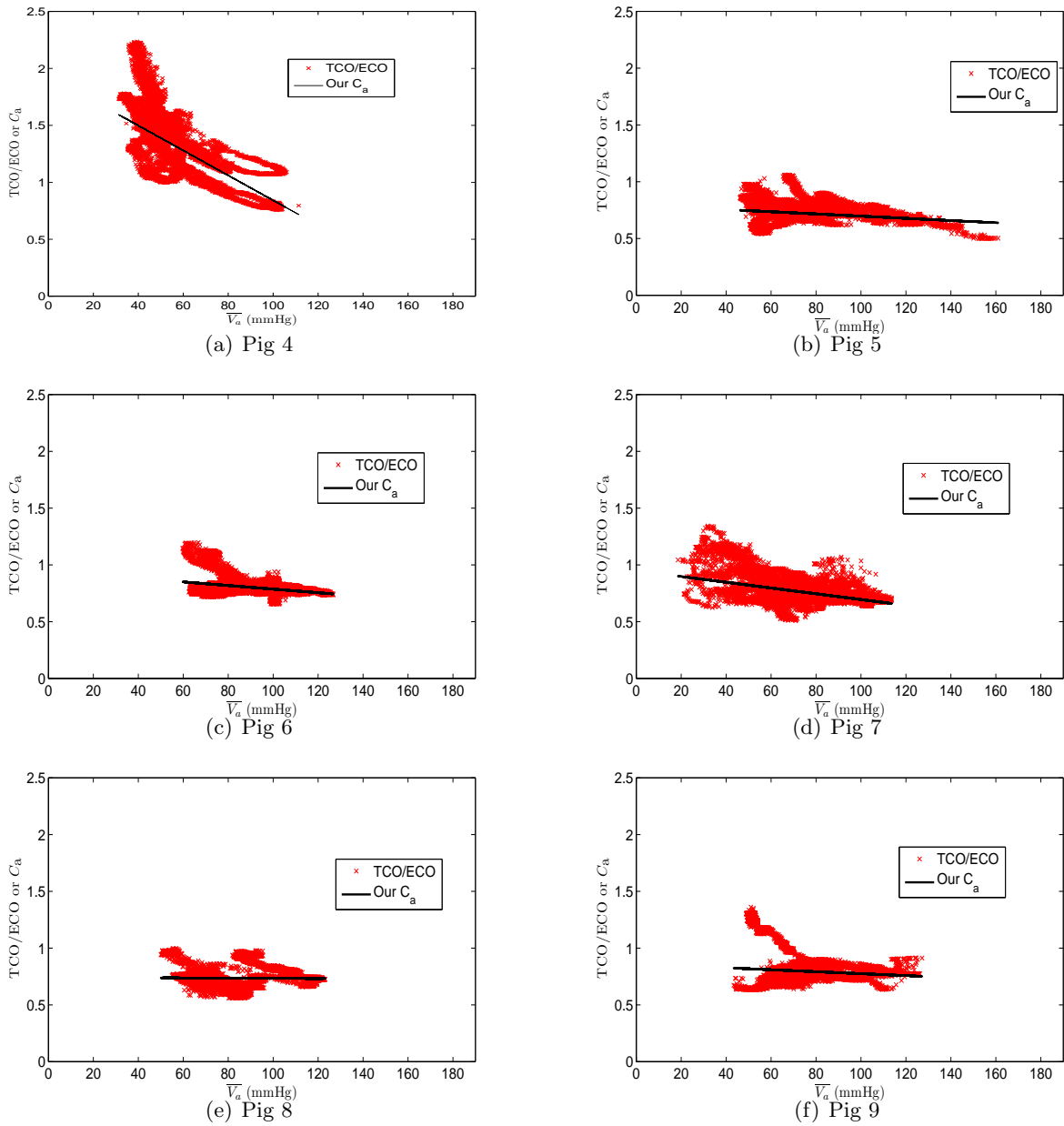


Figure 5.15: Plots of $\frac{TCO}{ECO}$ and our fit for the calibration factor C_a versus mean pressure \bar{V}_a for all six swine. The results were obtained using a window size = 360 beats and a 100-point state-dependent calibration.

Swine	Number of comparisons	RMSNE (%) for Herd estimate using rABP	RMSNE (%) for our estimate using rABP
4	3256	17.1	14.9
5	2608	5.1	5.2
6	0	–	–
7	6847	14.8	14.2
8	0	–	–
9	514	9.3	7.1
Aggregate	13225	13.9	12.9

Table 5.12: RMSNEs for the rABP waveform-based estimate taken over points at which the beat-to-beat variability index was larger than 5%. 100-point state-dependent calibrations were used for our estimate and for the Herd estimate.

Swine	Number of comparisons	RMSNE (%) for Herd estimate using rABP	RMSNE (%) for our estimate using rABP
4	3256	26.4	24.7
5	2608	5.5	6.0
6	0	–	–
7	6847	17.1	15.7
8	0	–	–
9	514	8.6	6.6
Aggregate	13225	18.2	16.9

Table 5.13: RMSNEs for the rABP waveform-based estimate taken over points at which the beat-to-beat variability index was larger than 5%. Mean calibrations were used for our estimate and for the Herd estimate.

We applied this variability index to all our data sets, but only report results with the porcine data set here. The beat-to-beat variability in the canine data set described below was less than the variability in the porcine data set.

Results in the literature imply that the performance of many CO estimation methods may be extremely data-dependent [65, 113]. In the next three sections, as encouraged in editorials by Mukkamala *et al.* [118] and van Lieshout *et al.* [108], we apply our estimation method to canine and human ICU patient data.

5.9 Results and Discussion with Canine Data

In this section, we describe a canine data set, and describe how we estimate cardiac output for the animals in this data set. We also describe the errors obtained using our method and present a comparison of these errors to those obtained with other model-based CO estimation methods.

5.9.1 Canine Data Set

The canine data set was obtained from Professor Ramakrishna Mukkamala of Michigan State University, and was the result of a study on three beagles (weighing 10–15 kg) approved by the Michigan State University All-University Committee on Animal Use and Care. Dog 1 was intubated under anesthesia and mechanically ventilated. Once intubated, the dog underwent a thoracotomy and an aortic flow transducer was placed. This dog was allowed ten days to recover from this major surgery.

The same experimental protocol was then applied to each of the three dogs – one with the chronic instrumentation described above, and two others. Each animal was anesthetized, but not mechanically ventilated. Catheters were placed in the thoracic aorta to measure cABP, and in the femoral artery to measure fABP. A syringe pump catheter was placed into a cephalic vein for drug administration, and ECG leads were placed on the animal. In each animal, over the course of approximately 1 hour, CO, EF, ABP, and HR were varied by one or more of the following interventions: volume infusions, fast hemorrhage, and intravenous (IV) drug infusions (one or more of phenylephrine, nitroprusside, or dobutamine).

Table 5.14 summarizes the population statistics for the canine data set. It is important to note that for dog 3, the variability in CO, HR, and mean cABP is particularly small. In fact, the beat-to-beat variability as measured by the index (5.36) does not exceed 1% for the entire record for dog 3. Furthermore, it does not exceed 3% for the entire record for dog 2, and only exceeds 5% for a few windows of data for dog 1, with most variability seen with the fABP waveform.

For dog 1, the data set is comprised of measurements of central arterial blood pressure (cABP) measured at the aorta, carotid arterial blood pressure (carABP), femoral arterial blood pressure (fABP), and aortic

Continuous Monitoring of Cardiac Output and Total Peripheral Resistance

Dog	Weight (kg)	CO (l/min) Range	HR (bpm) Range	Mean cABP (mmHg) Range	Duration of record (min)
1	14.5	0.9-6.7	94-181	50-160	92
2	10.5	0.7-3.9	88-179	56-99	49
3	12.5	1.8-3.5	142-197	57-120	74

Table 5.14: Population statistics for the canine data set. The data was obtained from Professor Ramakrishna Mukkamala at Michigan State University.

flow (AF), all sampled at 250 Hz with 16 bit amplitude resolution. In addition, there are intermittent echocardiography measurements of heart rate, left ventricular end-systolic volume (LVESV) and left ventricular end-diastolic volume (LVEDV), from which one can compute both CO and left ventricular ejection fraction (EF).

For dogs 2 and 3, the data set is comprised of measurements of central arterial blood pressure (cABP) measured at the aorta sampled at 250 Hz with 16 bit amplitude resolution. Similar to dog 1, there are intermittent echocardiography measurements of heart rate, left ventricular end-systolic volume (LVESV) and left ventricular end-diastolic volume (LVEDV), from which one can compute CO and EF. There are no peripheral arterial blood pressure waveforms available for dogs 2 and 3.

Using a standard open-source algorithm [117] on the cABP waveforms, we derived onset times for each cardiac beat and thus derived HR. We calculated systolic and diastolic cABP, and mean cABP for all three dogs. For dog 1, we also calculated systolic and diastolic carABP, systolic and diastolic fABP, mean carABP, and mean fABP. For dog 1, true or reference beat-to-beat CO was calculated by integrating the AF waveform over each beat, and applying a 50 beat median filter to the resulting TCO waveform. In addition, the intermittent echocardiography measurements were also used as reference CO measurements. For dogs 2 and 3, we used the echocardiography measurements of cardiac output as the reference or true CO. For dog 3 we averaged every three echocardiography CO measurements. All the data processing and cardiac output estimation algorithms were implemented in MATLAB R14 (Mathworks Inc., Natick, MA).

5.9.2 Results

The arterial blood pressure waveforms that were available were used independently in the linear least squares estimation scheme described in Section 5.3.2 to obtain an uncalibrated estimate of CO. This estimate was calibrated using a state-dependent calibration using all available echocardiography CO measurements.

Table 5.15 summarizes the results obtained for a window size of 100 beats (or, approximately 1 minute at a HR of 100 bpm) for the cABP, carABP, and fABP waveforms. Results obtained with other window sizes yield similar RMSNEs. In the table, we also list the RMSNEs for the SHNECO estimate (5.34) described in Section 5.5. The SHNECO RMSNEs reflect fairly low CO variability for dogs 2 and 3.

Dog	Number of comparisons	RMSNE (%) for SHNECO	RMSNE (%) using cABP	RMSNE (%) using fABP	RMSNE (%) using carABP
1	7 (10636)	31.6 (0.0)	11.2 (9.7)	9.0 (6.3)	13.7 (14.9)
2	30	19.0	11.7	–	–
3	7	15.1	9.1	–	–
Aggregate	44	20.8	11.1	–	–

Table 5.15: Aggregate RMSNEs for the dog data set with a 100 beat window size, $\alpha=2$ in Equation (5.14), and a state-dependent calibration using all available echocardiography TCO points in each record. The parenthetical numbers in the first row are those obtained from comparisons to TCO from the aortic flow probe using a 10 point state-dependent calibration.

Our results are comparable to results in the literature, e.g., in [120], Mukkamala and co-workers obtained a RMSNE of 10% for dog 1, but did not report errors for dogs 2 or 3.

Figures 5.16 and 5.17 show results for dogs 1 and 2, respectively. Note that the spikes in the HR and R_a waveforms are a result of not filtering either \bar{V}_{an} , T_n or ΔV_{an} to generate these results.

Note that there are sections where our estimate performs very well, while there are sections in each dog record, where we are over- or underestimating the time constant τ , as explained in (5.35). Our results with state-dependent calibration have aggregate RMSNEs of 11% which is much below the 15% reported in the literature [58] as being acceptable for clinical purposes. The CO estimate tracks all major transitions in TCO over the ranges of mean ABP and HR.

In addition, across the entire canine data set, the estimated TPR, R_a , tracked the true TPR for all the pharmacological interventions, e.g., in Fig. 5.16, when dobutamine is infused, estimated TPR decreases, while when phenylephrine is infused, estimated TPR increases. In the case of dog 2 in Fig. 5.17, we see a rapid rise in estimated TPR subsequent to the progressive hemorrhage procedure.

Figure 5.18 is a Bland-Altman plot for the CO estimation error using the cABP waveform. From the Bland-Altman plot, we see that the mean estimation error (or *bias*) is 53 ml/min, while the 1-standard deviation (SD) of the estimation error is 343 ml/min. The 2-SD line for our estimate lies 686 ml/min from the line representing mean estimation error, showing that, according to the criterion outlined in [114, 115], our estimated CO compares well with the reference echocardiography CO measurements.

5.9.3 Comparison to Other CO Estimation Methods

We compared the estimates produced by our CO estimation method for the canine data set to estimates produced by other methods. Table 5.16 shows the results of this exercise with either a state-dependent or a mean calibration using all available TCO points. Again, we see that our method outperforms the other CO estimation methods listed, and that state-dependent calibration yields better results than mean calibration.

Continuous Monitoring of Cardiac Output and Total Peripheral Resistance

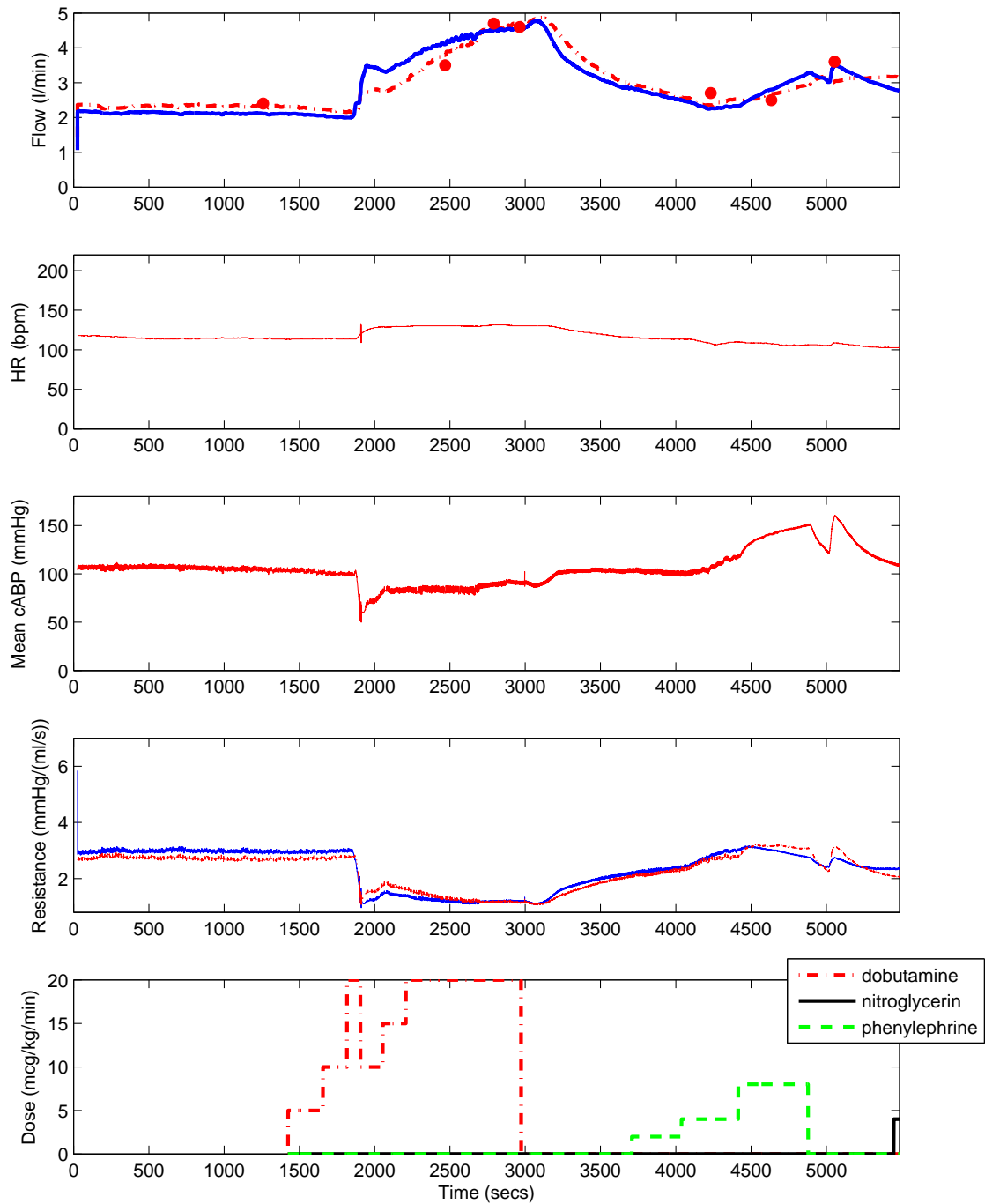


Figure 5.16: True (intermittent echocardiography and flow probe measurements) and estimated CO (using cABP), HR, mean cABP, true and estimated TPR, and IV drugs for dog 1 with window size = 100 beats and a state-dependent calibration using all available echocardiography TCO measurements.

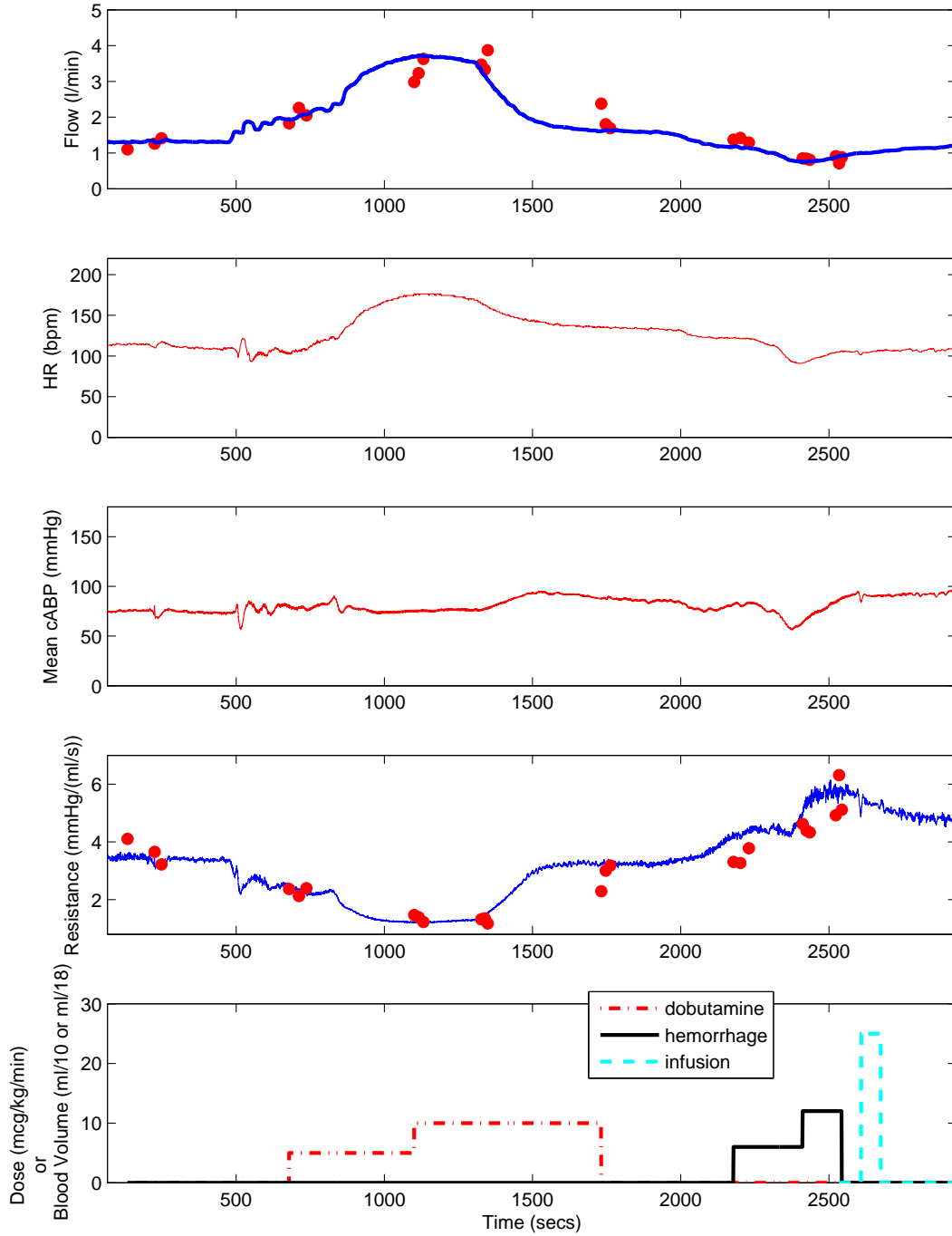


Figure 5.17: True (intermittent echocardiography measurements) and estimated CO (using cABP), HR, mean cABP, true and estimated TPR, and IV drugs for dog 2 with window size = 100 beats and a state-dependent calibration using all available echocardiography TCO measurements.

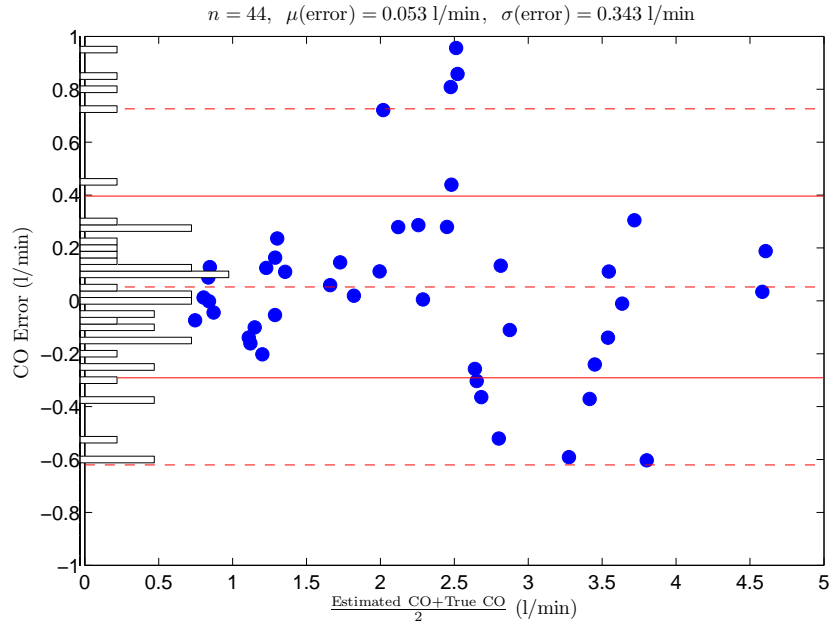


Figure 5.18: Bland-Altman plot of CO estimation error versus the mean of TCO and ECO (using cABP) over the three dogs with window size = 100 beats and a state-dependent calibration using all available echocardiography TCO measurements. The horizontal lines in the plot are the mean error, and the 1-SD and 2-SD lines.

CO Estimation Method	Aggregate RMSNE (%) using cABP state-dependent calibration	Aggregate RMSNE (%) using cABP mean calibration
Ours	11.1	13.3
Herd [106]	13.7	17.2
Liljestrand and Zander [64]	11.3	19.6
Modified Mean Pressure	25.6	39.9
Mean Pressure [113]	34.3	56.5

Table 5.16: Aggregate RMSNEs for the canine data set with either mean or state-dependent calibrations using all available echocardiography TCO points.

CO Estimation Method	Aggregate RMSNE (%) using cABP state-dependent calibration	Aggregate RMSNE (%) using cABP mean calibration
Ours	32.0	11.1
Herd [106]	16.0	15.9
Liljestrand and Zander [64]	24.2	20.3
Modified Mean Pressure	66.7	75.0
Mean Pressure [113]	93.7	119.7

Table 5.17: Aggregate RMSNEs for the canine data set with either mean or state-dependent calibrations using the first half of the available echocardiography TCO points to calibrate, and the second half to test the predictive value of the calibrated CO estimate.

CO Estimation Method	Aggregate RMSNE (%) using cABP state-dependent calibration	Aggregate RMSNE (%) using cABP mean calibration
Ours	13.3	12.2
Herd [106]	16.2	18.8
Liljestrand and Zander [64]	13.4	18.3
Modified Mean Pressure	45.7	41.0
Mean Pressure [113]	36.0	48.9

Table 5.18: Aggregate RMSNEs for the canine data set with either mean or state-dependent calibrations using the second half of the available echocardiography TCO points to calibrate, and the first half to test the predictive value of the calibrated CO estimate.

5.9.4 Comparison of Mean and State-Dependent Calibration Factors

To further investigate the efficacy of a state-dependent arterial compliance calibration factor, we applied each CO estimation method from Table 5.16 to dog records in which half the data was used for calibrating (training set), and half was used for testing the predictive value of the calibration factor (testing set).

Table 5.17 shows the resulting RMSNEs for each of the CO estimation methods when all points in the first half of each dog record were used for training, and the second half of each dog record was used for testing. Since the RMSNEs for the state-dependent calibrated estimates nearly doubled for all except the Herd estimate, we can infer that this particular training/testing data split was not rich enough for fitting the state-dependent compliance parameters.

Table 5.18 shows the resulting RMSNEs for each of the CO estimation methods when all points in the second half of each dog record were used for training, and the first half of each dog record was used for testing.

Again, as was the case with the porcine data set, it is evident that when the data records were divided into training and test sets, mean calibration resulted in lower RMSNEs than state-dependent calibration, but when the records were not split in this manner, state-dependent calibration resulted in lower RMSNEs. It

is also clear that whatever data set split we use for training/testing, our method is robust in the sense that it is consistently a top performer in the numerical experiments (except for Table 5.17 which was discussed above).

5.10 Results and Discussion with MIMIC I Human ICU Data

In this section, we describe the multi-parameter intelligent monitoring in intensive care (MIMIC) I database, and describe how we estimate cardiac output for some patients in this database.

5.10.1 MIMIC I Data Set

The MIMIC I database is freely available from an internet physiological signal database³. Based on the work of Lu *et al.* [58], we selected a set of 12 MIMIC I patients of different clinical classes. In Lu *et al.* [58], three more patients (ID 055, ID 410, and ID 480) were used, but we found the available data for these patients to be too noisy to be included in our analysis.

Each of the patients in this data set had 2 or more CO measurements obtained via thermodilution (giving a total of 124 reference or true CO measurements), a radial arterial blood pressure waveform, and two or more frontal electrocardiogram signals. In addition to these signals, some patients had a pulmonary arterial blood pressure waveform or pulmonary capillary wedge pressure measurements. While it would have been possible to use pulmonary signals to estimate CO as in [19], we did not do this as the goal of our work is to use signals that can be obtained less invasively than with right-heart catheterization.

It is commonly known that an average of 3 thermodilution CO measurements obtained in close succession constitutes the current clinical gold-standard for evaluating CO estimation methods on human ICU data [3]. In the case of the MIMIC I patient data set, and the MIMIC II patient data set that we use below, this averaging was rarely performed.

Table 5.19 summarizes the population statistics for the patients chosen from the MIMIC I database. It is important to note that the variability in CO, and the beat-to-beat variability in MAP for almost all of these patients is very low.

Using a standard open-source algorithm [117] on the rABP waveforms, we derived onset times for each cardiac beat and HR. We calculated systolic and diastolic rABP, and mean rABP for each of the 12 patients. All the data processing and cardiac output estimation algorithms were implemented in MATLAB R14 (Mathworks Inc., Natick, MA). For both the MIMIC I and MIMIC II data sets, we used PP=SAP-DAP to calculate pulse pressure for our least-squares estimation scheme.

³The database can be accessed at <http://www.physionet.org>.

MIMIC I Patient ID	Clinical Class	Number of TCO points	CO (l/min) Mean \pm SD	HR (bpm) Range	MAP (mmHg) Range
041	Hemorrhage	2	8.98 \pm 0.728	78-104	74-81
281	NA	5	4.37 \pm 0.438	100-114	94-99
411	Respiratory Failure	6	3.84 \pm 0.582	50-61	84-94
451	Congestive Heart Failure	6	5.18 \pm 0.583	74-84	51-58
453	Heart Valve Surgery	14	4.08 \pm 0.457	50-89	60-79
454	Heart Valve Surgery	11	4.18 \pm 0.398	49-70	67-74
456	Coronary Artery Bypass Graft	14	5.92 \pm 1.301	67-108	57-100
474	NA	6	4.21 \pm 0.414	86-94	72-79
476	Coronary Artery Bypass Graft	11	4.42 \pm 0.331	90-105	58-71
477	Coronary Artery Bypass Graft	10	5.40 \pm 0.554	79-111	54-75
484	NA	12	6.56 \pm 0.743	79-96	62-78
485	NA	27	3.54 \pm 0.562	94-126	69-87

Table 5.19: Population statistics and clinical class (if available) for our set of MIMIC I patients; NA=not available. The data was obtained from <http://www.physionet.org>. More descriptions of the data set are given in [58], where two more patients were used.

5.10.2 Results and Comparisons to other Methods

We applied our CO estimation method (using PP=SAP-DAP) to the available peripheral arterial blood pressure waveforms in the data set. We used the linear least squares estimation scheme described in Section 5.3.2 to obtain an uncalibrated estimate of CO. This estimate was calibrated with a state-dependent calibration using all available reference or true thermodilution CO measurements.

Table 5.20 summarizes the results obtained for a window size of 360 beats (or, approximately 3.5 minutes at a HR of 100 bpm). Results obtained with other window sizes yield similar RMSNEs – something to be expected given the lack of beat-to-beat variability in the ABP waveforms of the patients in this data set. In the table, we also list the RMSNEs for the SHNECO estimate (5.34) described in Section 5.5, and the errors reported by Lu *et al.* in [58].

From Table 5.20, we can see that for many patients, the SHNECO does better than both our method and the Mukkamala’s method. This is not surprising given the low CO variability in many of these patients.

Figures 5.19 and 5.20 are plots of true and estimated CO, mean rABP, HR, and true and estimated TPR for MIMIC I patients 411, and 451, respectively. In both figures, the estimated CO coincides quite well with the reference thermodilution TCO points. The accuracy of our estimate between two consecutive thermodilution measurements cannot be determined. In addition, we have marked the obvious artifacts in the rABP and HR waveforms in Fig. 5.19. There is very little variability in the thermodilution CO measurements for both these patients. Medication data was not available for the MIMIC I patients, so we were not able to verify medication-induced changes in hemodynamic variables.

Continuous Monitoring of Cardiac Output and Total Peripheral Resistance

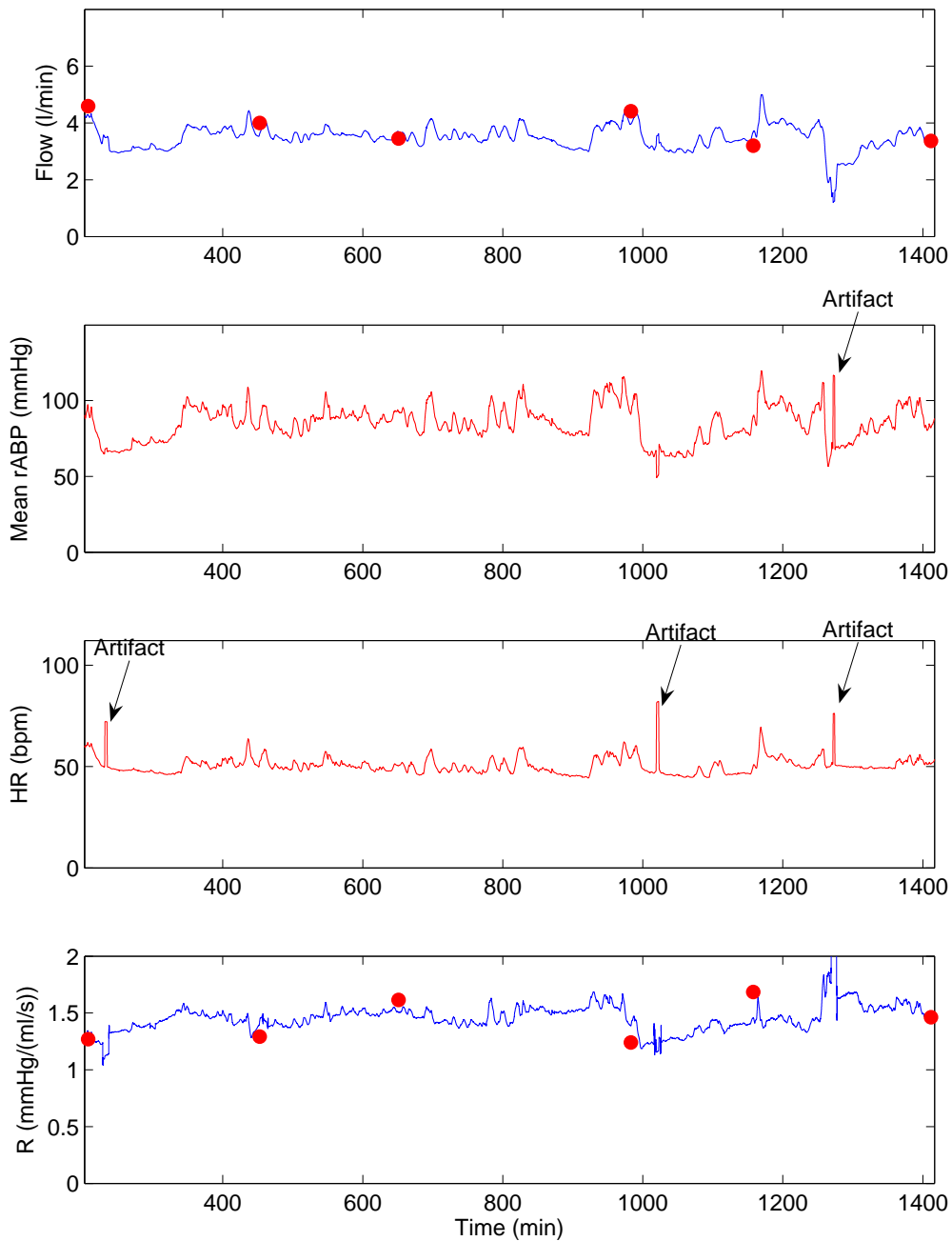


Figure 5.19: True and estimated CO, mean rABP, HR, and true and estimated TPR for patient 411 with window size = 360 beats and a state-dependent calibration using all available thermodilution TCO measurements.

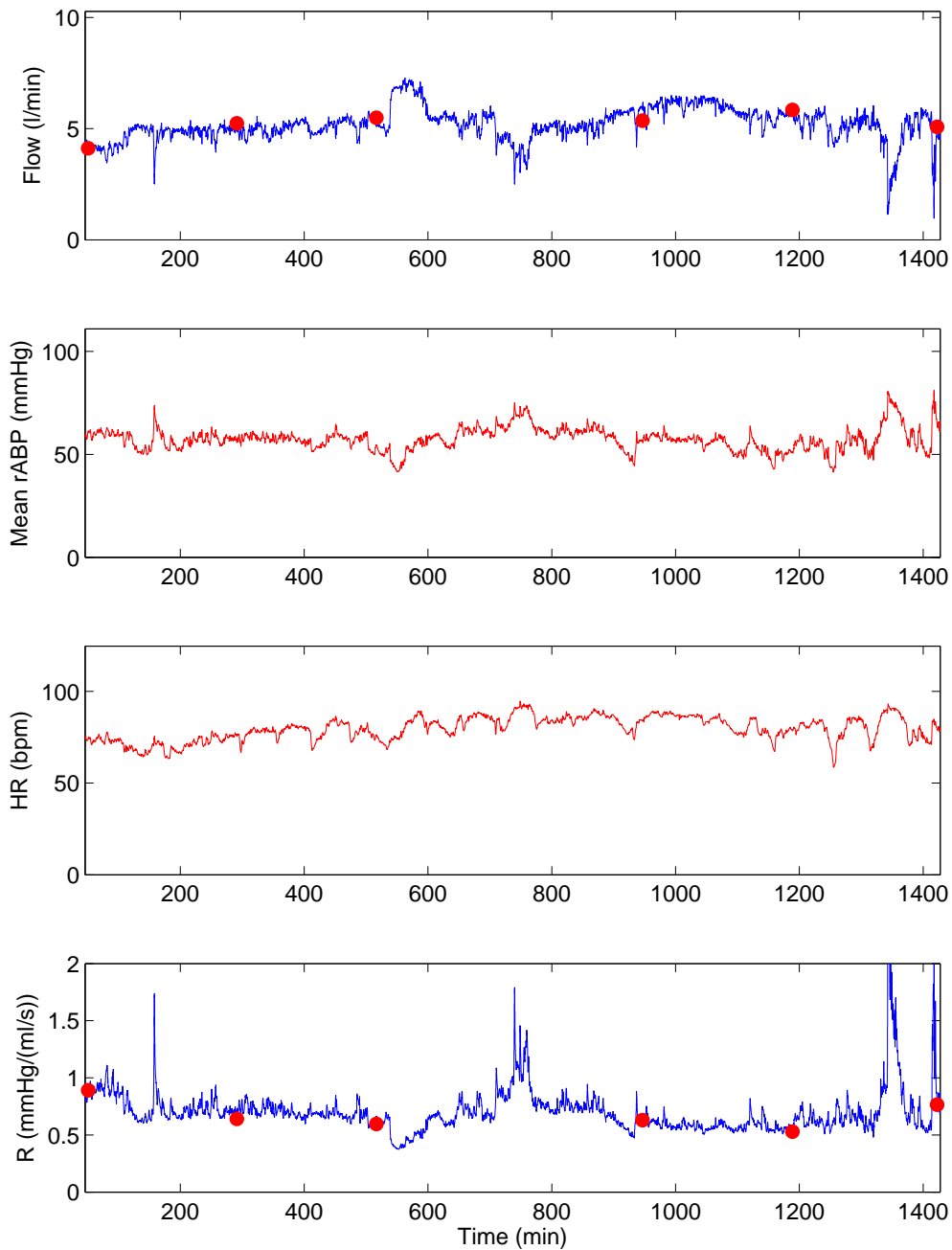


Figure 5.20: True and estimated CO, mean rABP, HR, and true and estimated TPR for patient 451 with window size = 360 beats and a state-dependent calibration using all available thermodilution TCO measurements.

MIMIC I Patient ID	Number of Comparisons	RMSNE (%) Our Method	RMSNE (%) SHNECO	RMSNE (%) reported in [58]
041	2	0.0	7.7	0.5
281	5	6.2	10.2	6.8
411	6	9.3	17.8	14.4
451	6	6.3	13.0	15.0
453	14	8.8	9.5	10.7
454	11	25.1	8.7	5.4
456	14	15.2	25.0	22.5
474	6	15.8	11.7	15.6
476	11	12.3	9.7	11.2
477	10	12.2	11.5	10.6
484	12	9.7	14.2	12.4
485	27	18.4	10.3	23.0
Aggregate	124	14.8	14.3	15.3

Table 5.20: Aggregate RMSNEs for the MIMIC I data set comparing our method to the SHNECO, and to Mukkamala’s method [58], for which the mean RMSNE for their selection of *15 patients* was 15.3%. We calibrated our estimates with a state-dependent calibration using all available thermodilution TCO measurements.

Figure 5.21 is a Bland-Altman plot for the CO estimation error using our CO estimation method. From Fig. 5.21, we see that the mean estimation error (or *bias*) is 119 ml/min, while the 1-standard deviation (SD) of the estimation error is 667 ml/min. While we do not know the inherent error in thermodilution CO measurements, we can assume it to be small (< 1 l/min), the 2-SD line for our estimate lies 1.334 l/min from the line representing mean estimation error, showing that, according to the criterion outlined in [114, 115], our estimated CO compares reasonably well with the reference thermodilution CO measurements.

Figure 5.22 is a Bland-Altman plot for the CO estimation error on the MIMIC I patients using the SHNECO estimation method. From Fig. 5.21, we see that the mean estimation error (or *bias*) is -24 ml/min, while the 1-standard deviation (SD) of the estimation error is 691 ml/min. From this plot, we can infer that the SHNECO estimator works almost as well as our CO estimation method.

Nevertheless, in an ICU setting where we expect a minimally-invasive CO estimation method to be useful, there would be few to no reference thermodilution measurements taken, making it difficult to make use of the SHNECO estimate.

5.11 Results and Discussion with MIMIC II Data

In this section, we describe the MIMIC II data set, and describe how we estimated cardiac output for our set of MIMIC II patients.

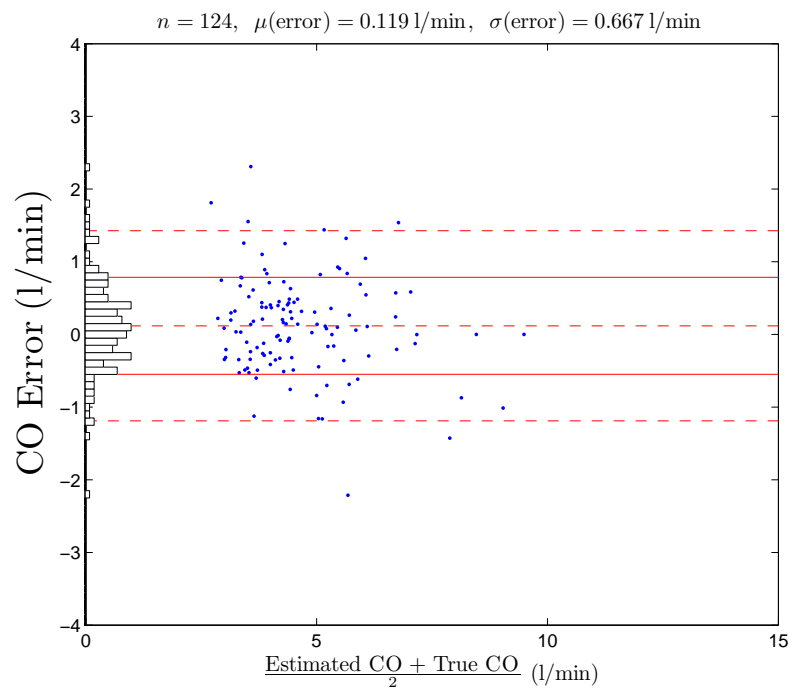


Figure 5.21: Bland-Altman plot of our method’s CO estimation error versus the mean of TCO and ECO over the set of MIMIC I patients with window size = 360 beats and a state-dependent calibration using all available thermodilution TCO measurements. The horizontal lines in the plot are the mean error, and the 1-SD and 2-SD lines.

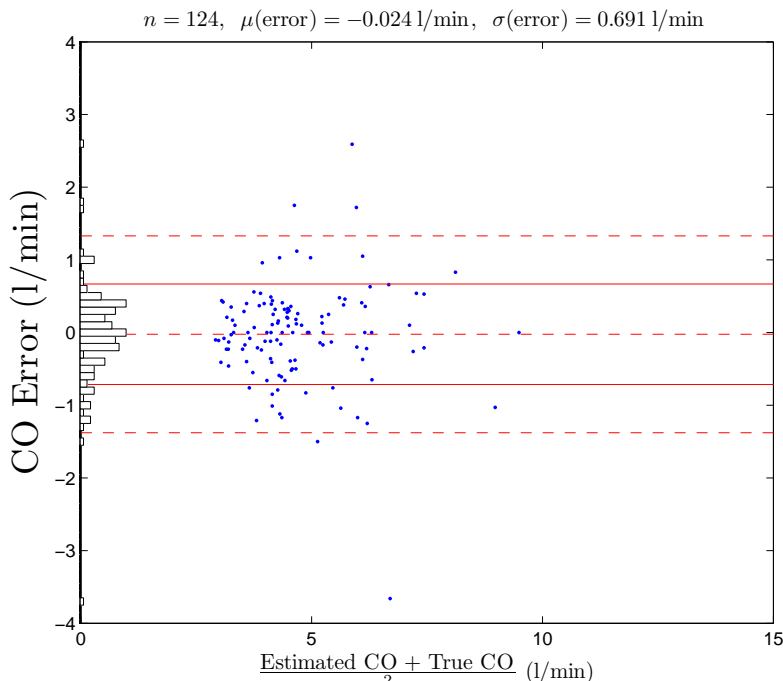


Figure 5.22: Bland-Altman plot of the SHNECO estimation error versus the mean of TCO and ECO over the set of MIMIC I patients. No calibration was necessary for this estimate. The horizontal lines in the plot are the mean error, and the 1-SD and 2-SD lines.

5.11.1 MIMIC II Data

The MIMIC II database is not yet publicly available, though we expect parts of it to be publicly available by June 2008. We obtained a de-identified⁴ MIMIC II data set from researchers at the Laboratory for Computational Physiology at MIT. Based on the work of Sun *et al.* [113], we selected a set of 120 MIMIC II patients, each of which had 2 or more CO measurements obtained via thermodilution (giving a total of 1378 reference or true CO measurements) and a radial arterial blood pressure waveform. Sun *et al.* [113] showed that on this set of ICU patients, the CO estimation method of Liljestrand and Zander [64] outperformed 10 other CO estimation methods, including the static Windkessel and the Herd estimates.

It is important to note three problems with the MIMIC II data set. First, as mentioned above, we note that the average of 3 consecutive thermodilution CO measurements constitutes the current clinical gold-standard for evaluating CO estimation methods on human ICU data. In the case of the MIMIC II data set this averaging was rarely performed. Second, based on the TCO ranges for each patient, we inferred that there is little to no CO variability in the MIMIC II data set. Finally, there was little to no beat-to-beat variability in other hemodynamic variables in the MIMIC II data set.

Table 5.21 summarizes the population statistics for the MIMIC II patients, some of which were adopted

⁴All protected health information (PHI) was removed.

Variable	Mean \pm SD
Age (years)	69 \pm 12
TCO (l/min)	5 \pm 2
Δ TCO (l/min)	2.5 \pm 1.2
HR (bpm)	90 \pm 20
MAP (mmHg)	75 \pm 10
Number of TCO measurements	1378

Table 5.21: Population statistics for the MIMIC II patients some of which were adapted from [113]. Δ TCO signifies the mean of the maximum deviation of each subject’s TCO measurements. The data was obtained via a personal communication from researchers at the Laboratory for Computational Physiology at MIT.

from [113].

Using a standard open-source algorithm [117] on the rABP waveforms, we derived onset times for each cardiac beat and thus derived HR. We calculated systolic and diastolic rABP, and mean rABP for each of the 120 patients. In addition, we implemented a signal quality index developed by Sun *et al.* [121, 122] on each rABP waveform, neglecting all low quality rABP wavelets, e.g., wavelets which had values beyond physiologically-possible values. All the data processing and cardiac output estimation algorithms were implemented in MATLAB R14 (Mathworks Inc., Natick, MA). For both the MIMIC I and MIMIC II data sets, we used PP=SAP-DAP to calculate pulse pressure for our least-squares estimation scheme.

5.11.2 Results and Comparisons to other CO Estimation Methods

We applied our CO estimation method to the rABP waveforms (using PP=SAP-DAP) to our MIMIC II patient data set. We used the linear least squares estimation scheme described in Section 5.3.2 to obtain an uncalibrated estimate of CO. This estimate was calibrated using a state-dependent calibration using all available reference or true thermodilution CO measurements.

For the MIMIC II patients, we were able to obtain information on IV and provider-order-entry (POE) medications for most of the 120 patients; we used this information to correlate our estimates of CO and TPR to changes in medications. While this analysis was conclusive for some patients, for many others it was too difficult to determine the effect of a particular medication.

Table 5.22 summarizes the results obtained for a window size of 360 beats (or, approximately 3.5 minutes at a HR of 100 bpm). Results obtained with other window sizes yield similar RMSNEs – something to be expected given the lack of beat-to-beat variability in the ABP waveforms of the patients in this data set.

In Table 5.22, we also list the RMSNEs and 1-SD Bland-Altman error for three other estimates: the SHNECO estimate (5.34), which performs quite well, and the two best-performing CO estimation methods: the Liljestrand and Zander [64] method, and the Modified Mean Pressure method, in which CO is proportional to the product of MAP and HR. Both these methods performed almost as well as our CO

CO Estimation Method	Number of Comparisons	$\sigma(\text{error})$ l/min	Aggregate RMSNE (%)
Our Method	1378	0.906	17.4
SHNECO (no calibration)	1378	0.906	17.2
Modified Mean Pressure	1378	1.027	19.8
Liljestrand and Zander [64]	1378	1.041	19.7

Table 5.22: Aggregate RMSNEs for the MIMIC II ICU patient data set comparing our method to the best-performing of the other methods. We calibrated each estimate with a state-dependent calibration using all available thermodilution TCO measurements. The SHNECO estimator does not need calibration.

estimation method. Note that we do not include the results for the Herd estimation method here because this method performed poorly on the MIMIC II data set.

While our method performs well on this ICU patient data set, the fact that the SHNECO estimator performs as well as our method implies that there is very little CO variability in the data set – something that discounts the performance of any CO estimation method on this data set.

Figure 5.23 is a plot of estimated and true waveforms for MIMIC II patient b75092. There were only two thermodilution CO measurements taken on this patient. Fortunately, these coincide with the infusion of levophed, which acts to increase TPR. Both the true and estimated TPR increase during the period of levophed infusion, something that is more clear in the Fig. 5.24, where only the period of levophed infusion is plotted.

Figure 5.25 is a plot of estimated and true waveforms for MIMIC II patient b63047, where we have marked a HR artifact at $t \approx 900$ minutes which affects both our CO and TPR estimates. There were 14 thermodilution CO measurements taken on this patient, all of which coincide with the infusion of neosynephrine (or phenylephrine), which acts to increase TPR. The estimated TPR tracks the neosynephrine infusion rate quite well for most of the patient data shown in the figure. Both the true and estimated TPR increase during the period of neosynephrine infusion, something that is more clear in the Fig. 5.26, where we zoom in on part of Fig. 5.25. Of more clinical relevance is the fact that in Fig. 5.26, the estimated TPR tracks the neosynephrine infusion rate, even between the intermittent thermodilution CO measurements.

Figure 5.21 shows Bland-Altman plots of CO estimation error using our CO estimation method, the Liljestrand and Zander method [64], the Modified Mean Pressure method, and the SHNECO estimator. From Fig. 5.27, we see that the mean estimation error in our method is 226 ml/min, in Liljestrand’s and Zander’s method is 292 ml/min, for the SHNECO estimator is 42 ml/min, and for the Modified Mean Pressure method is 325 ml/min. The 1-SD of our method’s estimation error is 906 ml/min, the same as that for the SHNECO estimator. The 1-SD error for the other two methods is about 100 ml/min more. (In an ICU setting, however, where we expect a minimally-invasive CO estimation method to be useful, there would be few to none reference thermodilution measurements taken, making it difficult to make use of the SHNECO estimate.)

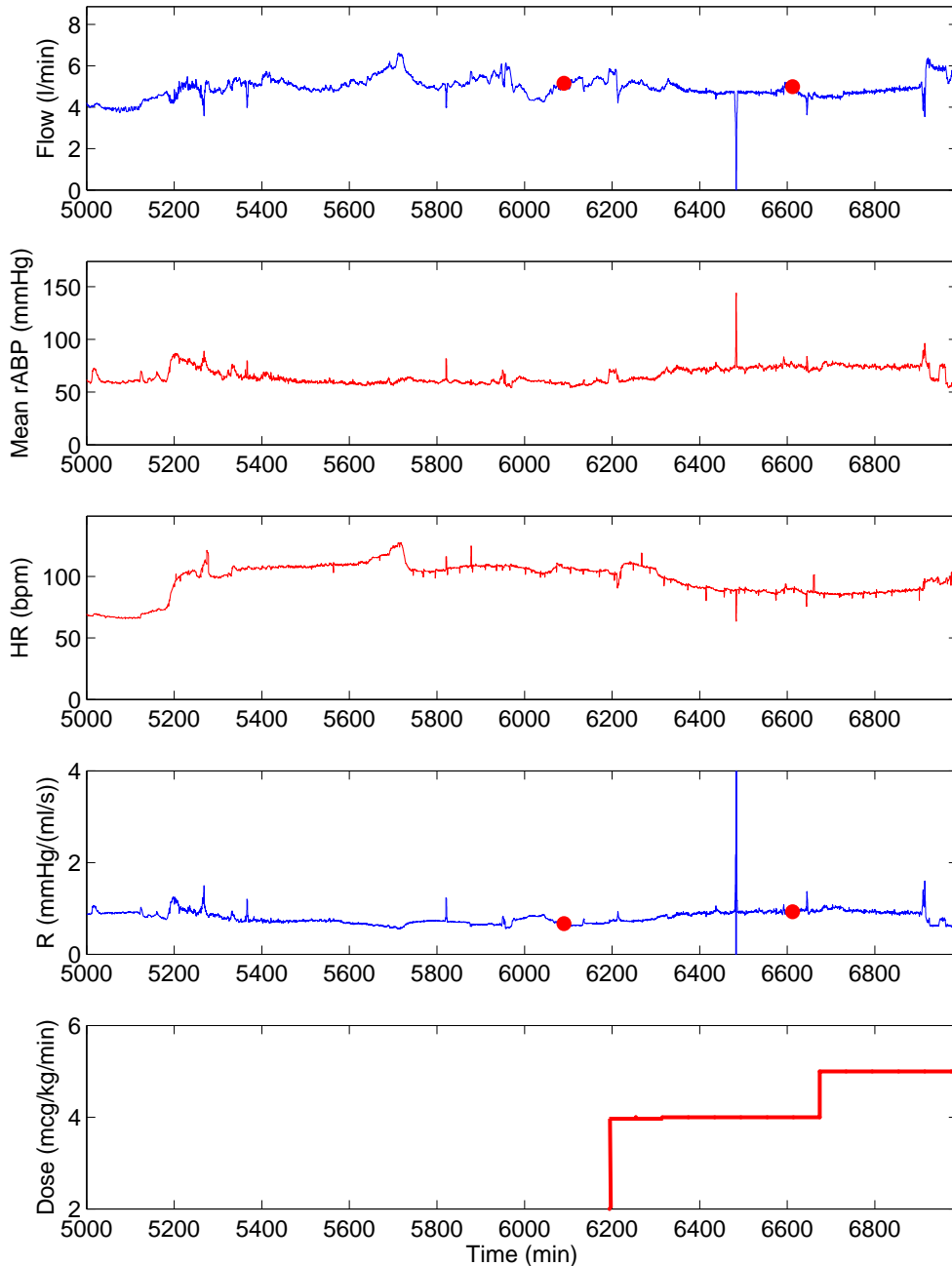


Figure 5.23: True and estimated CO, mean rABP, HR, true and estimated TPR, and IV levophed infusion for patient b75092 with window size = 360 beats and a state-dependent calibration using the two available thermodilution TCO measurements. Data during the early parts of the patient's ICU stay are not plotted here.

Continuous Monitoring of Cardiac Output and Total Peripheral Resistance

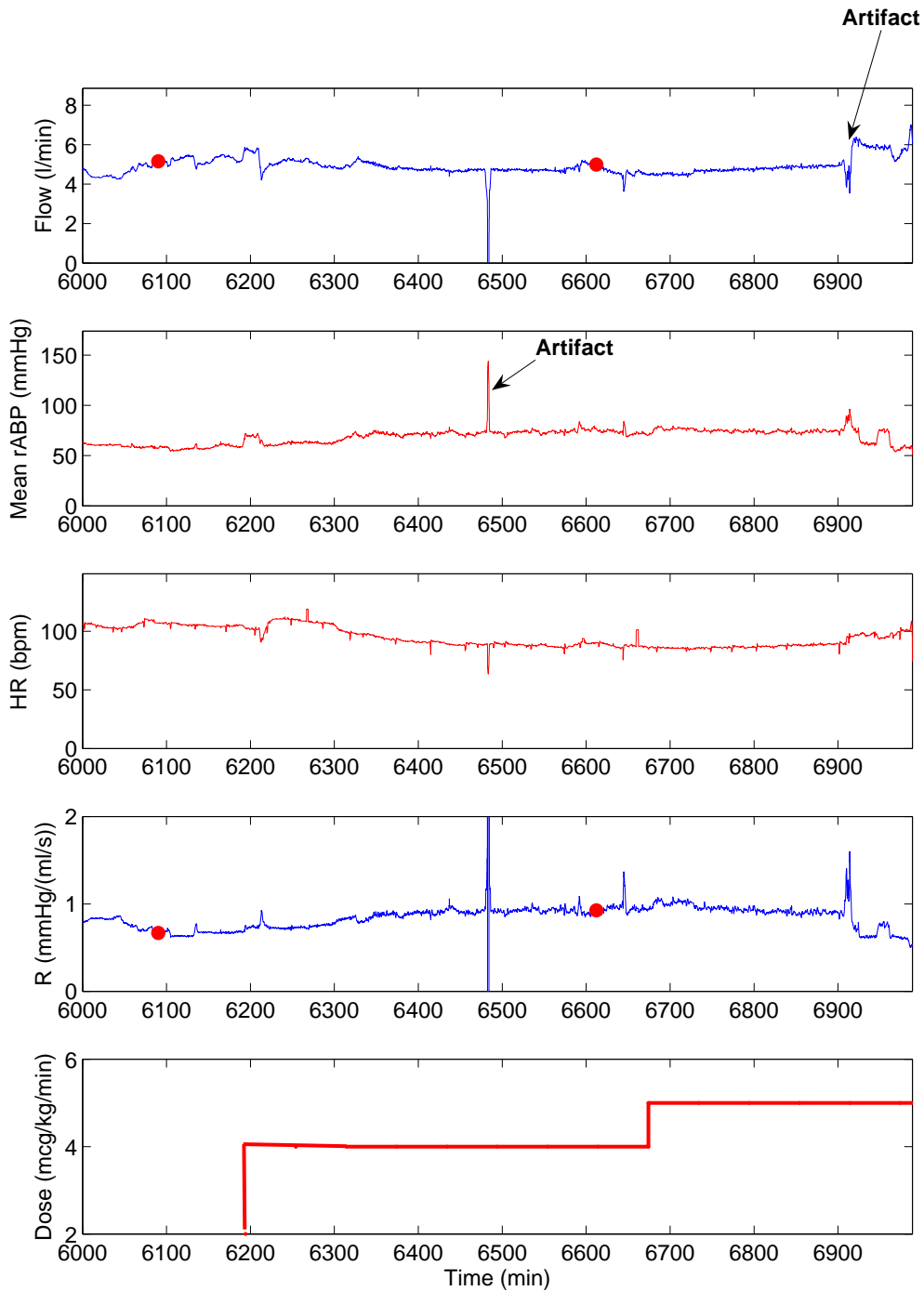


Figure 5.24: True and estimated CO, mean rABP, HR, true and estimated TPR, and IV levophed infusion for patient b75092 with window size = 360 beats and a state-dependent calibration using the two available thermodilution TCO measurements. Only the patient data during the IV levophed infusion have been plotted.

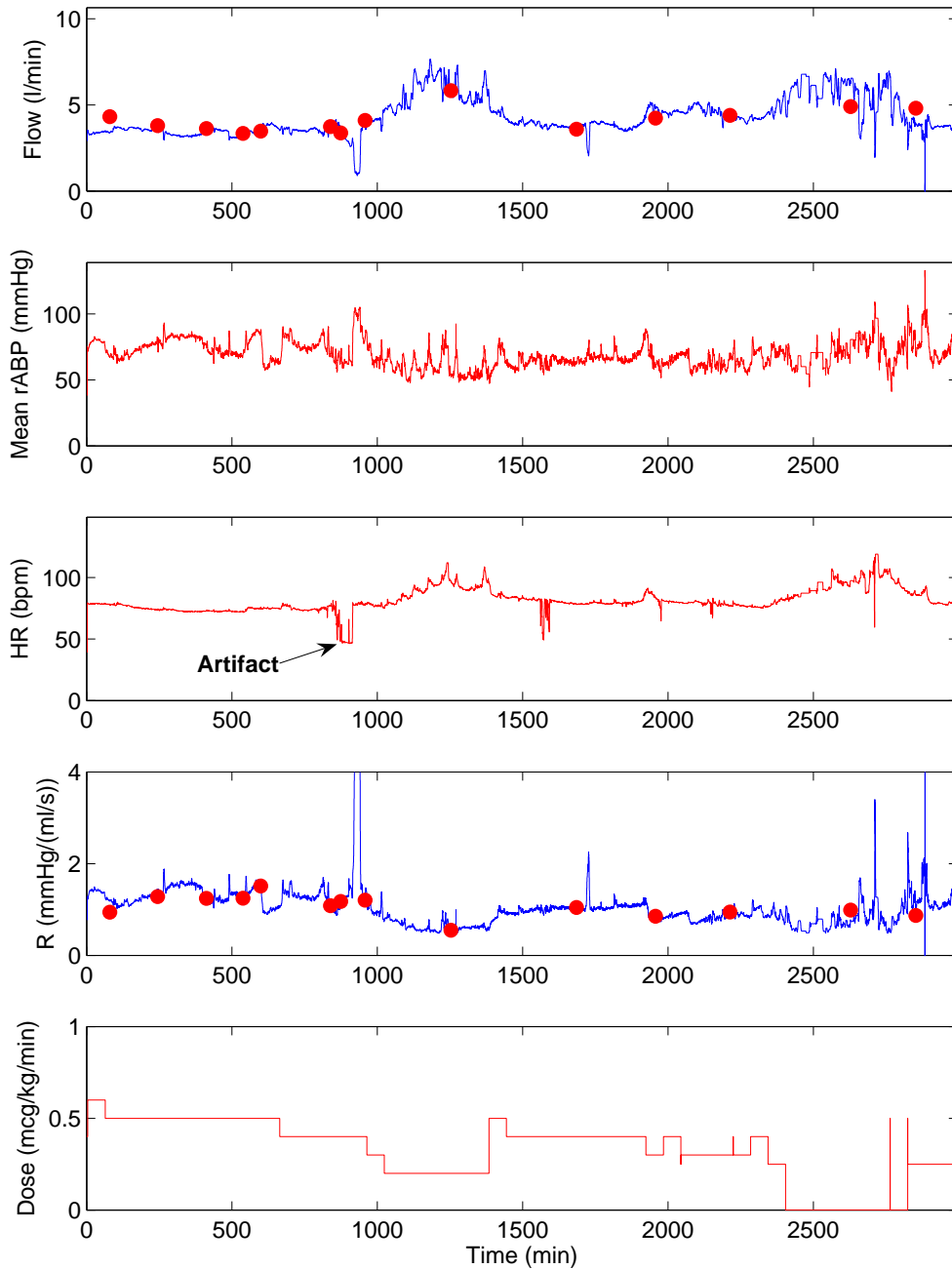


Figure 5.25: True and estimated CO, mean rABP, HR, true and estimated TPR, and IV neosynephrine infusion for patient b63047 with window size = 360 beats and a state-dependent calibration using the two available thermodilution TCO measurements.

Continuous Monitoring of Cardiac Output and Total Peripheral Resistance

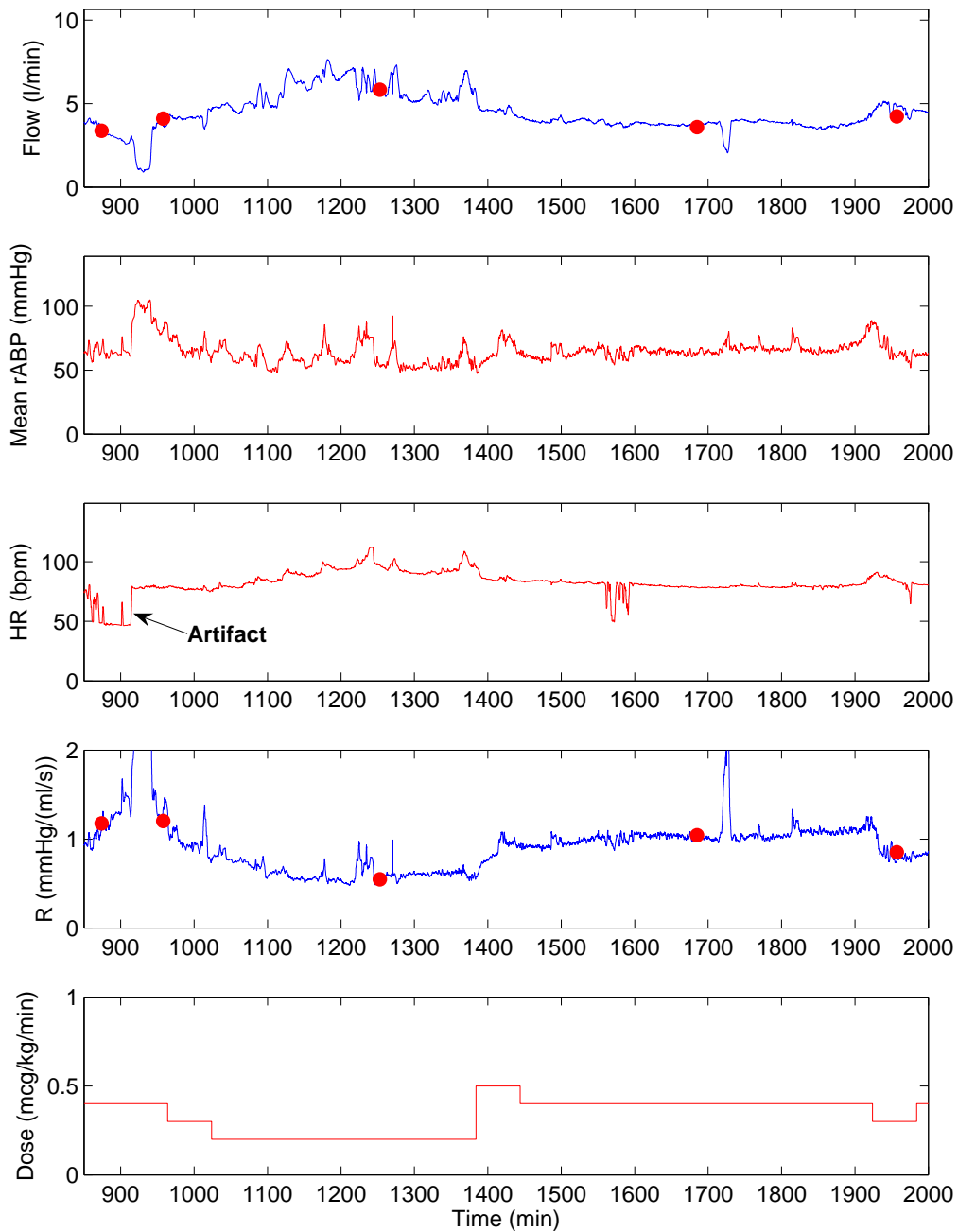


Figure 5.26: True and estimated CO, mean rABP, HR, true and estimated TPR, and IV neosynephrine infusion for patient b63047 with window size = 360 beats and a state-dependent calibration using the two available thermodilution TCO measurements.

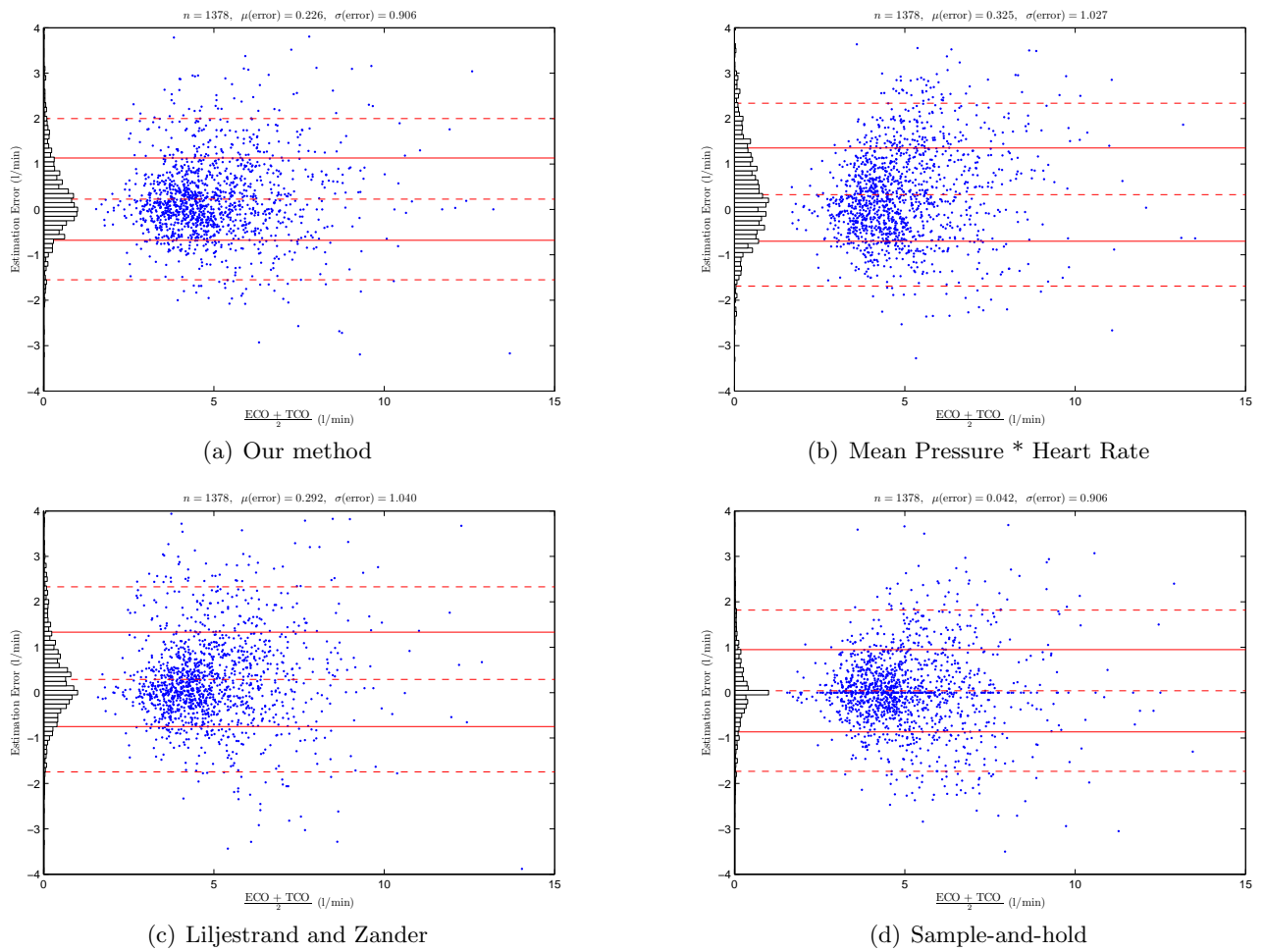


Figure 5.27: Bland-Altman plots of CO estimation error versus the mean of TCO and ECO over the set of MIMIC II patients. The horizontal lines in the plots are the mean error, and the 1-SD and 2-SD lines.

Continuous Monitoring of Cardiac Output and Total Peripheral Resistance

While we do not know the inherent error in the reference thermodilution CO measurements, if we assume it to be small (< 1 l/min), then the 2-SD lines for all four of the estimates presented here lie at least 1.8 l/min from the lines representing mean estimation errors, showing that, according to the criterion outlined in [114, 115], these estimates can probably not be used to robustly detect changes in true CO of magnitude < 1 l/min.

5.12 Summary and Conclusions

In this chapter, we described a novel beat-to-beat averaged model-based method for continuously estimating cardiac output from arterial blood pressure waveforms. This continuous cardiac output estimation method can easily be implemented in real time, works well on different window lengths of data, and is model-based, giving it a clear physiological basis. The method exploits the beat-to-beat variability in heart rate and arterial blood pressure to estimate the time constant for the Windkessel model. We applied the method to porcine, canine, and human data sets in which reference CO measurements were available. The resulting errors on each of the data set showed that our method is *robust* i.e., it performs well on each data set we used.

We investigated the use of both a constant and a mean pressure-dependent compliance when we applied our method. We observed that errors obtained using each of these compliance functions depend on the method used to obtain the results. In particular, when the data records were divided into training and test sets, mean calibration proved superior to state-dependent calibration. However, when the records were not split in this manner, state-dependent calibration resulted in lower RMSNEs. More investigation is needed to ascertain the need for a mean pressure-dependent compliance, possibly with more animal and human subject experiments.

Using the porcine central or peripheral arterial blood pressure waveforms, the aggregate RMSNE was at most 15-18%. Using the canine central or peripheral arterial blood pressure waveforms, the aggregate RMSNE was at most 13% (except for one case), while the aggregate RMSNE was at most 18% in the two human ICU patient data sets. These errors are on the order of those obtained using another beat-to-beat variability-based method in the literature [57], as well as some static intra-beat CO estimation methods. In addition, in the case of the animal data sets, we observed that the total peripheral resistance calculated from this estimate tracked the animals' expected hemodynamic responses to the intravenous drugs quite well. For the human data sets, it is more difficult to correlate the infusion of intravenous drugs to changes in patient hemodynamics as we discuss below.

We did not use the mean absolute normalized error criterion to evaluate our CO estimates, but this criterion could be used in future evaluations of our method as the MANE criterion does not exaggerate the effects of estimates that are outliers.

Continuous Monitoring of Left Ventricular Ejection Fraction and End-Diastolic Volume

LEFT ventricular ejection fraction (EF) and left ventricular end-diastolic volume (LVEDV) are clinically important variables that, together with cardiac output (CO) and total peripheral resistance (TPR), allow clinicians to make early diagnoses, track disease progression, and decide on therapeutic interventions. Of particular relevance in the ICU is distinguishing between cardiogenic, septic, and hypovolemic shock, which could potentially be done using continuous measurements of EF, LVEDV, and CO. Given the projected shortage of nurses in the coming decade [6], and the aging US population, it is essential that automated, continuous, and minimally-invasive methods for monitoring CO, TPR, EF, and LVEDV are developed.

In Chapter 5, we discussed a novel model-based method for continuously estimating CO and TPR from arterial blood pressure waveforms. In this chapter we describe two other novel, model-based methods, this time for continuously estimating EF and LVEDV [123]. We show how these methods work in practice on the canine data set we presented in Chapter 5. We conclude this chapter with a discussion on how we envision combinations of our CO, TPR, EF, and LVEDV estimates to make clinical assessments of hemodynamic state.

6.1 Background

Left ventricular ejection fraction (EF) is defined the ratio of stroke volume (SV) to LVEDV. Since SV can be written as the difference between left ventricular end-systolic and end-diastolic volumes, the following equality holds:

$$\text{EF} = \frac{\text{SV}}{\text{LVEDV}} = \frac{\text{LVEDV} - \text{LVESV}}{\text{LVEDV}}. \quad (6.1)$$

EF is usually expressed as a percentage, with typical normal values ranging from 40–60%. Left ventricular ejection fraction is a strong indicator of heart function – perhaps the most significant index that is currently in clinical use [27]. Low ejection fraction is indicative of compromised heart function or coronary artery disease [124, 125, 126]. Monitoring EF, even for outpatients, can thus be quite useful. For instance, Curtis and co-workers (see [28]) describe a powerful relationship between EF and mortality in heart failure outpatients – the lower the EF, the worse the patient outcome.

If the left-ventricular end-diastolic compliance is assumed to be large and constant, LVEDV is proportional to left ventricular end-diastolic pressure (LVEDP). LVEDP, usually approximated in the ICU by Pulmonary Capillary Wedge Pressure (PCWP) measurements, is a strong indicator of congestive heart failure [127, 128, 129, 130]. Hence, LVEDV, a quantity proportional to LVEDP, is also an important indicator of ventricular function, namely the left ventricular preload.

Although many techniques exist to measure ventricular volumes, e.g., magnetic resonance imaging (MRI), the current clinical gold-standard for determining ventricular volumes, i.e., LVEDV and LVESV, is echocardiography imaging [131, 132, 133]. While this is a noninvasive procedure, it is quite expensive because it requires an expert operator to perform the measurement and interpret the image. As a result, ventricular volumes are infrequently measured. While there are non-imaging methods, e.g., thermodilution-based EF mentioned in Chapter 2, one could use to continuously monitor ventricular volumes, these methods are highly invasive and would therefore only be used on the sickest of patients.

We propose that ventricular volumes, and hence EF, can be estimated from central or peripheral arterial blood pressure waveforms. Our estimation method would therefore allow for continuous, minimally-invasive measurements of EF and LVEDV. While Mukkamala and co-workers have successfully estimated EF using a central arterial blood pressure waveform [27, 120], they did so by assuming a particular ventricular elastance function and performing an intra-beat fit of this function to the central arterial blood pressure (cABP) waveform. Their method is thus still quite invasive. However, it does not require calibration against true or reference EF measurements.

Consistent with our development of beat-to-beat averaged cardiovascular models, instead of fitting an intra-beat cABP waveform, we propose a model-based method that used inter-beat information from the arterial blood pressure waveform – central or peripheral – to estimate EF and LVEDV. Such a method does not require one to assume a particular ventricular elastance function; it exploits the inter-beat variability in systolic and diastolic blood pressures to estimate important left ventricular parameters. To our knowledge, our method is the only inter-beat method for estimating EF and LVEDV.

6.2 Using Beat-to-Beat Variability to Estimate EF and LVEDV

In this section, we give a detailed description of our model-based technique for estimating EF and LVEDV. In the next section we discuss a linear least-squares estimation scheme based on the model of this section.

The starting point for this method is the left-ventricular pressure-volume loop shown in Fig. 6.1. In the figure, we have labeled straight lines defining the end-diastolic (C_d), before-ejection (C_{be}), peak-systolic (C_s), and end-systolic (C_{es}) compliances, as well as SAP, DAP, LVEDP, and LVESP. We have also exaggerated the distance between SAP and LVESP to emphasize the key elements in our method. Q_d is the ventricular dead volume during *either* systole or diastole; V_{th} is intrathoracic pressure.

6.2 Using Beat-to-Beat Variability to Estimate EF and LVEDV

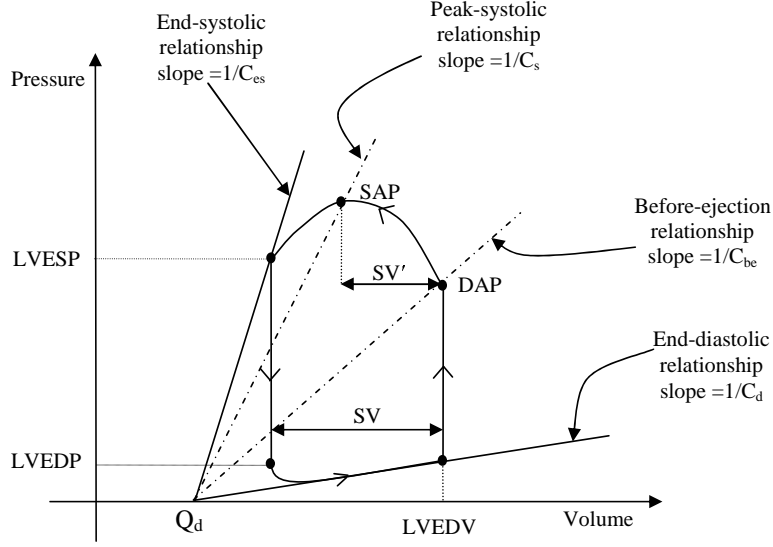


Figure 6.1: Left ventricular pressure-volume loop showing the straight lines defining the end-diastolic, before-ejection, peak-systolic, and end-systolic compliances, as well as SAP, DAP, and the preload and afterload pressures. Note that the pressures in this graphic are measured with respect to intrathoracic pressure.

In steady-state, ejection fraction can be computed as follows:

$$EF \equiv \frac{SV}{LVEDV} = \frac{C_d(LVEDP - V_{th}) - C_{es}(LVESP - V_{th})}{C_d(LVEDP - V_{th}) + Q_d} \quad (6.2)$$

where steady-state stroke volume is given by:

$$SV = C_d(LVEDP - V_{th}) - C_{es}(LVESP - V_{th}) \quad (6.3)$$

Note the prominence of both Q_d and V_{th} in Equation (6.2). The intrathoracic pressure variations during the respiratory cycle modulate left-ventricular and arterial blood pressures, LVP and ABP, respectively, and cause beat-to-beat variations in SV, which in turn cause beat-to-beat variations in EF [3].

If we assume $V_{th}=0$, we can (see Fig. 6.1) approximate stroke volume by:

$$SV' = C_{be}DAP - C_sSAP \quad (6.4)$$

and thus EF simplifies to:

$$EF \approx \frac{SV'}{LVEDV'} = \frac{C_{be}DAP - C_sSAP}{C_{be}DAP + Q_d}, \quad (6.5)$$

and LVEDV is approximated by:

$$LVEDV' \approx C_{be}DAP. \quad (6.6)$$

Continuous Monitoring of Left Ventricular Ejection Fraction and End-Diastolic Volume

Given beat-to-beat measurements of SAP, DAP, and SV and assuming a nominal value for Q_d , we can use Equation (6.5) to compute beat-to-beat estimates of C_{be} and C_s – the essence of our method for continuously estimating beat-to-beat EF from the ABP waveform. Furthermore, given beat-to-beat estimates of C_{be} and DAP, Equation (6.6) can be used to estimate LVEDV.

The main problem with this approach is that SV' does not in general equal SV (though we believe SV' may be proportional to SV), leading to bias errors in the estimates of C_{be} and C_s . We discuss calibration methods to correct for the inequality of the SV estimate (6.4) in Section 6.4.

If a measurement of SV is not available, one can use a proportional estimate of SV, e.g., $\frac{SV}{C_a}$, such that (6.4) reduces to:

$$\frac{SV'}{C_a} = \frac{C_{be}}{C_a}DAP - \frac{C_s}{C_a}SAP \quad (6.7)$$

and approximate EF is computed using:

$$EF \approx \frac{\frac{C_{be}}{C_a}DAP - \frac{C_s}{C_a}SAP}{\frac{C_{be}}{C_a}DAP + \frac{Q_d}{C_a}} \quad (6.8)$$

from which the proportionality constant C_a cancels out [27, 120]. Note that one now has to assume a nominal value for $\frac{Q_d}{C_a}$ in (6.8), and that to obtain LVEDV', one needs to perform a calibration.

We implemented least-squares estimation schemes in which we used absolute estimates of SV, and thus (6.4)-(6.6), as well as relative estimates of SV, and thus (6.7)-(6.8), but only present results using absolute SV estimates in this thesis.

6.3 Linear Least-Squares Estimation Scheme

In doing EF estimation from (6.5), we assume that C_{be} and C_s vary slowly from beat-to-beat. Thus, we ensure that the window size in our linear least-squares estimation scheme does not exceed half a minute (30 beats at a heart rate of 60 beats/min), which is probably slightly larger than the timescale on which C_{be} and C_s change. We estimated EF directly from (6.5) by computing least-squares estimates of C_{be_n} and C_{s_n} over a fixed-length data window, i.e., we calculated least-squares estimates of C_{be_n} and C_{s_n} for the n^{th} cardiac beat using a window comprising *every* m^{th} beat of the $b/2$ adjacent beats on each side of this beat. This results in a total of $\frac{b}{2m}$ (even) equations in two unknowns, leading to a reasonably well-conditioned

least-squares estimation problem:

$$\begin{bmatrix} \text{SAP}_n & \text{DAP}_n \\ \cdot & \cdot \\ \cdot & \cdot \\ \cdot & \cdot \\ \text{SAP}_{b+n} & \text{DAP}_{b+n} \end{bmatrix} \begin{bmatrix} C_{\text{be}_{n-1+\frac{b}{2}}} \\ C_{\text{sn}_{n-1+\frac{b}{2}}} \end{bmatrix} = \begin{bmatrix} \text{SV}_n \\ \cdot \\ \cdot \\ \cdot \\ \text{SV}_{b+n} \end{bmatrix} \quad (6.9)$$

where we estimated absolute SV estimates using the CO estimation method of Chapter 5. The end-result presented here does not change if we use proportional SV estimates, i.e., $\frac{\text{SV}_n}{C_{\text{an}}}$, instead of absolute SV estimates.

Furthermore, we assign the estimated C_{ben} and C_{sn} from each window to the midpoint of that window, and assume that in (6.9), $n > \frac{b}{2m}$, such that ejection fraction in the n^{th} cardiac cycle, EF_n , is given by:

$$\text{EF}_n \approx \frac{\text{SV}'_n}{\text{LVEDV}_n} \approx \frac{C_{\text{ben}}\text{DAP}_n - C_{\text{sn}}\text{SAP}_n}{C_{\text{ben}}\text{DAP}_n + Q_{\text{dn}}} \quad (6.10)$$

and estimated LVEDV in the n^{th} cycle, LVEDV'_n is given by:

$$\text{LVEDV}'_n \approx C_{\text{ben}}\text{DAP}_n \quad (6.11)$$

It is important to note that we could use the definition of SV from (6.4) in Equation (5.8) of Chapter 5 and attempt to compute beat-to-beat estimates of C_{be} , C_{s} , and τ in a three-parameter linear least-squares estimation scheme of the form:

$$\frac{\Delta V_{\text{an}}}{T_n} + \frac{\bar{V}_{\text{an}}}{\tau_n} = \frac{C_{\text{ben}}\text{DAP}_n}{T_n} - \frac{C_{\text{sn}}\text{SAP}_n}{T_n}, \quad (6.12)$$

where C_{ben} and C_{sn} are the before-ejection and end-diastolic compliances in the n^{th} cardiac cycle. Such a scheme, however, turns out to be severely ill-conditioned as there is an insufficient degree of variability in the data. In addition, this approach would also suffer from the modeling assumption above, namely that SV' does not in general equal SV, leading to bias errors in the estimates of C_{be} and C_{s} .

6.4 Calibration Methods

The formulae for EF and LVEDV in (6.10) and (6.11) seem to require no calibration to true or reference measurements. Once C_{ben} and C_{sn} are estimated, the only unknown in (6.10) is Q_{d} , for which we can assume a nominal value.

There are three problems with this approach, though, and we list them here in order of importance. First,

Continuous Monitoring of Left Ventricular Ejection Fraction and End-Diastolic Volume

as mentioned above, SV' does not equal SV (though we believe SV' may be proportional to SV), leading to bias errors in the estimates of C_{be} and C_s . Second, it is difficult to assume a good value for Q_d , as it can vary from between 5 ml to 200 ml depending on ventricular disease state. Third, because we are assuming $V_{th}=0$ and using (6.4) to estimate SV based on SAP and DAP , instead of LVE_{SP} and LVE_{DP} , respectively, there will be an additional component to the bias errors in our estimates of C_{be} and C_s , and thus, in our EF and $LVEDV$ estimates.

To attempt to correct for these bias errors, we use a constant calibration factor to relate estimated and reference EF or $LVEDV$, such that our estimate of EF in the n^{th} cardiac cycle, EF_n , is given by:

$$EF_n = \delta \frac{SV'_n}{LVEDV_n} = \delta \frac{C_{ben}DAP_n - C_{sn}SAP_n}{C_{ben}DAP_n + Q_{dn}} \quad (6.13)$$

and our estimate of $LVEDV$ in the n^{th} cardiac cycle, $LVEDV'_n$, is given by:

$$LVEDV'_n = \epsilon C_{ben}DAP_n \quad (6.14)$$

We could select the constants δ or ϵ to minimize the RMSNE between the true and estimated EF (or $LVEDV$). However, in this chapter we use two types of calibration: *mean* and *single-point* calibration. In mean calibration, we set δ (or ϵ) to be the ratio of the mean of the reference EF (or $LVEDV$) to the mean of the estimated EF (or $LVEDV$) waveform. In single-point calibration, we set δ (or ϵ) to be the ratio of a single reference EF (or $LVEDV$) point to the corresponding point in the estimated EF (or $LVEDV$) waveform.

6.5 Error Criteria

In evaluating the goodness-of-fit of our calibrated EF or $LVEDV$ estimates, i.e., to compare reference EF or $LVEDV$ to estimated EF or $LVEDV$, we used the root-mean-square-normalized-error criterion introduced in Chapter 5. For a particular animal, s , given n_s points at which EF (or $LVEDV$) was measured and estimated, the RMSNE (in %) for the EF (or $LVEDV$) for animal s , denoted $RMSNE_s$, is given by:

$$RMSNE_s = \sqrt{\frac{1}{n_s} \sum_{n=1}^{n_s} \left(\frac{100(\text{True } X_n - \text{Estimated } X_n)}{\text{True } X_n} \right)^2}, \quad (6.15)$$

where X denotes either EF or $LVEDV$.

Within the data set, the animal records contain varying numbers of reference EF or $LVEDV$ measurements, and thus the aggregate RMSNE over all animals is calculated as the weighted mean of the individual dog

RMSNEs. Assuming that there are N_S reference measurements, the aggregate RMSNE is given by:

$$\text{Aggregate RMSNE} = \sqrt{\frac{1}{N_S} \sum_s n_s (\text{RMSNE}_s^2)}. \quad (6.16)$$

In the literature [27, 120], instead of the weighted mean (6.16), the following expression is used to compute RMSNE over all S animals:

$$\text{Mean RMSNE} = \frac{1}{S} \sum_s \text{RMSNE}_s. \quad (6.17)$$

Such a mean RMSNE can be skewed if a particular animal record within the data set has a large number of reference EF or LVEDV measurements or is relatively error-ridden (or error-free) compared to others in the same data set. In this chapter, unless we are doing direct comparisons with the results in [120], we use the aggregate RMSNE expression (6.16).

RMSNE, even for a particular animal, is an average measure of performance. While it represents how the true and estimated quantities compare in an average sense, it does not classify the EF or LVEDV estimation error with regard to the particular values of ABP, HR, or even the particular interventions being performed on the animals. A linear regression of true EF (or LVEDV) versus estimated EF (or LVEDV) with a reported correlation coefficient would also only be an aggregate measure of performance, as would a Bland-Altman (see [114, 115]) plot of estimation error versus the mean of the reference and estimated quantities.

In this chapter, while we use RMSNEs and Bland-Altman plots to visualize our estimation error, wherever appropriate, we also present plots of our EF and LVEDV estimates to visualize how the time series for the estimates and the reference measurements compare. A measure that is less sensitive to outliers and perhaps better matched to the visual impression in the graphical plots would be the mean absolute normalized error (MANE) for a particular animal or subject s :

$$\text{MANE}_s = \frac{1}{n_s} \sum_{n=1}^{n_s} \frac{100 |\text{True } X_n - \text{Estimated } X_n|}{|\text{True } X_n|}, \quad (6.18)$$

where X denotes either EF or LVEDV. We do not use this criterion in this thesis.

6.6 Naive Sample-and-Hold Estimators for EF and LVEDV

As a metric for the quality of the estimated EF (or LVEDV) waveforms, i.e., a measure of how variable EF (or LVEDV) is and how well our EF (or LVEDV) estimation method captures this variability, we implemented a *naïve* sample-and-hold EF (or LVEDV) estimator.

For the canine data set, since we only had intermittent echocardiography-based EF (or LVEDV) measure-

Dog	EF (%) Range	LVEDV (ml) Range	LVESV (ml) Range	HR (bpm) Range	cABP (mmHg) Range
1	53-90	28-46	3-20	94-181	50-160
2	30-86	17-30	3-21	88-179	56-99
3	55-76	19-28	6-11	142-197	57-120

Table 6.1: Population statistics for the canine data set. The data was obtained from Professor Ramakrishna Mukkamala at Michigan State University and was also used in [120].

ments, we used the following sample-and-hold naïve estimator given by:

$$\text{SH } X_{n+1} = \text{True } X_n, \tag{6.19}$$

where $n \geq 2$, $\text{SH } X_1 = \text{True } X_1$, and where X denotes either EF or LVEDV. Again, if the RMSNE for the sample-and-hold naïve estimator is smaller than that of the estimated quantity itself, it implies that our estimate does not add more information than can be obtained by simply holding the value of the previous sample.

6.7 Canine Data Set

As described in Chapter 5, the canine data set was the result of a study on three beagles (weighing 10–15 kg) approved by the Michigan State University All-University Committee on Animal Use and Care. Dog 1 was intubated under anesthesia and mechanically ventilated. Once intubated, the dog underwent a thoracotomy and an aortic flow transducer was placed. This dog was allowed ten days to recover from this major surgery.

The same experimental protocol was then performed on each of the three dogs – one with the chronic instrumentation described above, and two others. Each animal was anesthetized, but not mechanically ventilated. Catheters were placed in the thoracic aorta to measure cABP, and in the femoral artery to measure fABP. A syringe pump catheter was placed into a cephalic vein for drug administration, and ECG leads were placed on the animal. In each animal, over the course of approximately 1 hour, CO, EF, ABP, and HR were varied by one or more of the following interventions: volume infusions, fast hemorrhage, intravenous (IV) drugs (one or more of phenylephrine, nitroprusside, or dobutamine). During the experiment, 2-dimensional echocardiography measurements [132] were intermittently used so as to obtain reference LVEDV, LVESV, and thus, EF measurements.

Table 6.1 summarizes the population statistics for the canine data set. It is important to note that for dog 3, the variability in HR and mean cABP is particularly small. In fact, the beat-to-beat variability as measured by the index (5.36) does not exceed 1% for the entire record for dog 3, does not exceed 3% for the entire record for dog 2, and only exceeds 5% for a few windows of data for dog 1, with most variability seen with the fABP waveform.

For dog 1, the data set is comprised of measurements of central arterial blood pressure (cABP) measured at the aorta, carotid arterial blood pressure (carABP), and femoral arterial blood pressure (fABP), all sampled at 250 Hz with 16 bit resolution. In addition, there are intermittent echocardiography measurements of heart rate, left ventricular end-systolic volume and left ventricular end-diastolic volume, from which one can compute left ventricular ejection fraction using (6.1).

For dogs 2 and 3, the data set comprised of measurements of central arterial blood pressure (cABP) measured at the aorta sampled at 250 Hz with 16 bit resolution. Similar to dog 1, there are intermittent echocardiography measurements of heart rate, left ventricular end-systolic volume (LVESV) and left ventricular end-diastolic volume (LVEDV), from which one can compute left ventricular ejection fraction (EF) using (6.1). There are no peripheral arterial blood pressure waveforms available for dogs 2 and 3. For dog 3, we averaged every 3 echocardiography measurements since they were taken very close together.

Using standard open-source algorithms [117] on the cABP waveforms, we derived onset times for each cardiac beat and HR. We calculated systolic and diastolic cABP, and mean cABP for all three dogs. For dog 1, we also calculated systolic and diastolic carABP, systolic and diastolic fABP, mean carABP, and mean fABP. We computed EF using the intermittent echocardiography measurements. For dog 3 we averaged every three EF (or LVEDV) measurements as each consecutive set of three measurements was taken at about the same time instant. All the data processing and EF and LVEDV estimation algorithms were implemented in MATLAB R14 (Mathworks Inc., Natick, MA).

6.8 Results on EF Estimation

We first used the available ABP waveforms in the canine data set to estimate beat-to-beat stroke volume using our CO estimation method from Chapter 5, and then used the estimated SV in the linear least squares estimation scheme (6.9), with a window size of 50 beats and two evenly spaced points per window¹, to obtain beat-to-beat estimates of C_{be} and C_s . We then computed an uncalibrated EF estimate assuming $Q_d=5$ ml, a plausible value for the animals in our data set [27, 120]. Note that other values of Q_d could have been used since an error in Q_d can to some extent be corrected by calibration. Varying Q_d from 5 to 150 ml only moderately affected the estimation results.

Table 6.2 summarizes the results obtained for a window size of 50 beats (or, approximately half a minute at a HR of 100 bpm) for the cABP, carABP, and fABP waveforms, using a mean calibration. In the table, we also list the RMSNEs for the SH EF estimate (6.19) described above. The RMSNEs for the SH EF estimate reflect fairly low EF variability for dogs 2 and 3. We believe that these low RMSNEs are sufficiently low to make our EF estimation method useful in clinical applications. In addition, the fact that results are reasonable whether we use the cABP, fABP or carABP waveforms for dog 1 implies that our method could be used in a minimally-invasive manner.

¹We used two beats per 50 beat window to improve the conditioning of the least-squares problem (6.9).

Continuous Monitoring of Left Ventricular Ejection Fraction and End-Diastolic Volume

Dog	Number of comparisons	RMSNE (%) for SH EF	RMSNE (%) using cABP	RMSNE (%) using fABP	RMSNE (%) using carABP
1	7	20.3	14.0	11.5	16.0
2	29	13.7	12.1	–	–
3	7	6.8	13.2	–	–
Aggregate	43	13.9	12.7	–	–

Table 6.2: RMSNEs for our mean-calibrated EF estimate using cABP, fABP, or carABP, with window size = 50 beats (using 2 points in each window) and $Q_d=5\text{ml}$.

Dog	Number of comparisons	RMSNE (%) using cABP	RMSNE (%) using fABP	RMSNE (%) using carABP
1	7	14.1	11.6	16.1
2	29	11.7	–	–
3	7	13.6	–	–
Aggregate	43	12.6	–	–

Table 6.3: RMSNEs for our single-point calibrated EF estimate, with window size = 50 beats and $Q_d=5\text{ml}$. In each record, the second reference EF measurement was used for calibration.

Figure 6.2 shows the true and estimated EF for dog 2 using a mean calibration. Note that the estimated EF tracks the true EF quite well during the infusions of dobutamine, which increases EF by decreasing C_{es} , and volume changes (hemorrhage results in a controlled response to lower C_{es} , while volume infusion results in a controlled response to increase C_{es}).

Figure 6.3 is a Bland-Altman plot for the EF estimation error across all three dogs using the cABP waveform with window size = 50 beats (using 2 points in each window) and a mean calibration.

From the Bland-Altman plot, we see that the mean estimation error (or *bias*) is 0%, while the 1-standard deviation (SD) of the estimation error is 8.2%. A review of the literature [132, 131] suggests that 2-dimensional echocardiography measurements of ventricular volumes, as were performed on the dogs of the canine data set, have a 13% root-mean-square error, which is approximately what our EF RMSNE is in Table 6.2. (3-dimensional echocardiography measurements have approximately 5% root-mean-square error.) Since the 2-SD line for our estimate lies 16.4% from the line representing mean estimation error, showing that, according to the criterion outlined in [114, 115], our estimated EF could be used to estimate EF changes of magnitude larger than $\pm 10\%$.

Table 6.3 summarizes the results obtained for a window size of 50 beats for the cABP, carABP, and fABP waveforms, by performing a single-point calibration using the second EF measurement in each canine record. We believe that these low RMSNEs are sufficiently low to make our estimation method useful in clinical applications, especially given that these results were obtained with only one reference measurement used for calibration. Note that the results in Table 6.3 are reasonable whether we use the cABP, fABP or carABP waveforms for dog 1, which implies that our method could be used in a minimally-invasive manner.

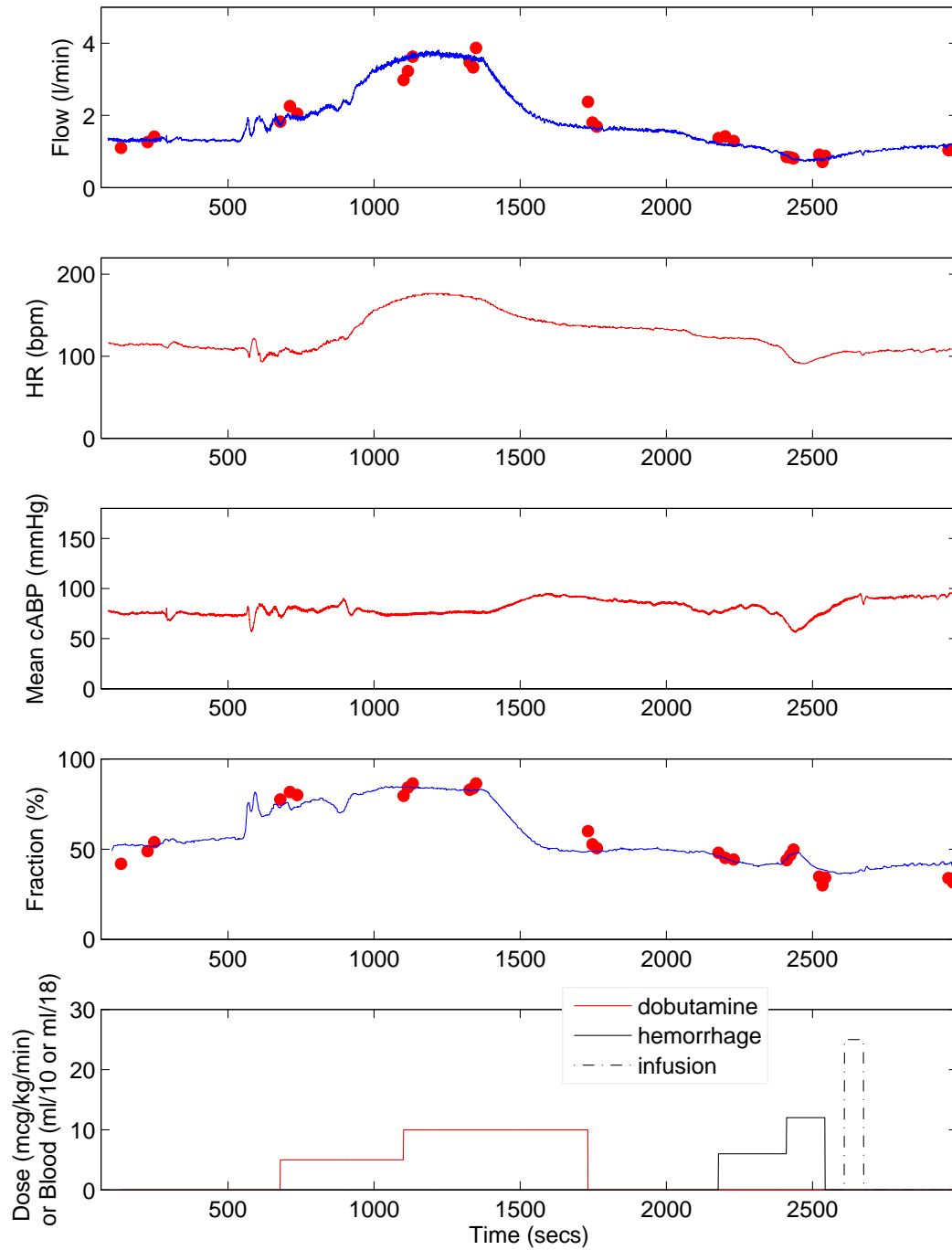


Figure 6.2: True and estimated CO (using cABP), HR, mean cABP, true and estimated EF (using cABP), and IV drugs for dog 2 with window size = 50 beats (using 2 points in each window), and a mean calibration. In the estimation, $Q_d=5\text{ml}$.

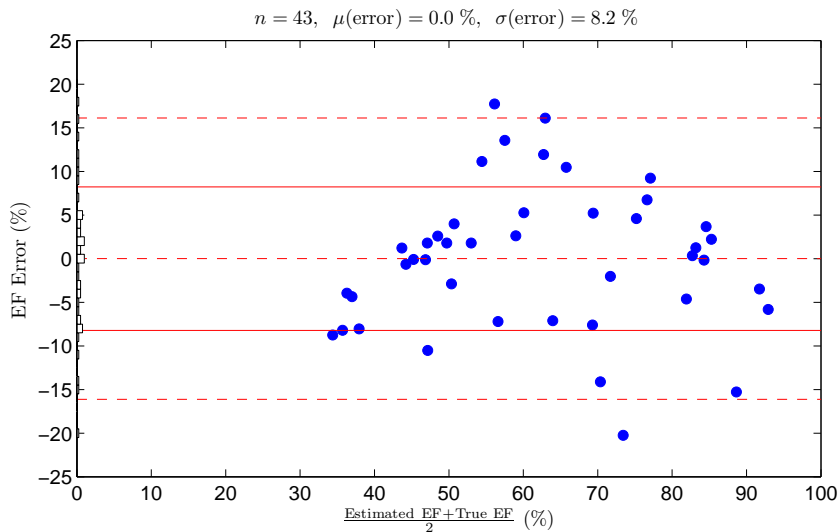


Figure 6.3: Bland-Altman plot of EF estimation error (using cABP and mean calibration) versus the mean of true and estimated EF (using cABP) over the three dogs. The horizontal lines in the plot are the mean error, and the 1-SD and 2-SD lines.

Figure 6.4 shows the true and estimated EF for dog 1 with a single-point calibration (using the second EF measurement). Note that the estimated EF tracks the true EF quite well during the infusions of dobutamine and phenylephrine (which increase EF by decreasing C_{es}).

Figure 6.3 is a Bland-Altman plot for the EF estimation error across all three dogs using the cABP waveform with window size = 50 beats (using 2 points in each window) and a single-point calibration using the second reference EF measurement in each record.

From the Bland-Altman plot, we see that the mean estimation error (or *bias*) is 2.7%, while the 1-standard deviation (SD) of the estimation error is 8.2%. The 2-SD line for our estimate lies 16.4% from the line representing mean estimation error, showing that, according to the criterion outlined in [114, 115], our single-point calibrated estimated EF could be used to estimate true EF changes larger than $\pm 10\%$.

In [120], Mukkamala and co-workers describe the results shown in Table 6.4. Note that these results were obtained without any calibration. However, this method cannot be implemented except on cABP waveforms². Our results from Tables 6.2 and 6.3 compare favorably to Mukkamala’s results, but are not as good, especially for dog 3. However, considering that we only use beat-to-beat values of DAP and SAP to compute our EF estimate, our method performs very well.

²Prof. Mukkamala obtained RMSNEs of $> 20\%$ when using the fABP waveform in dog 1 (personal communication, March 2007)

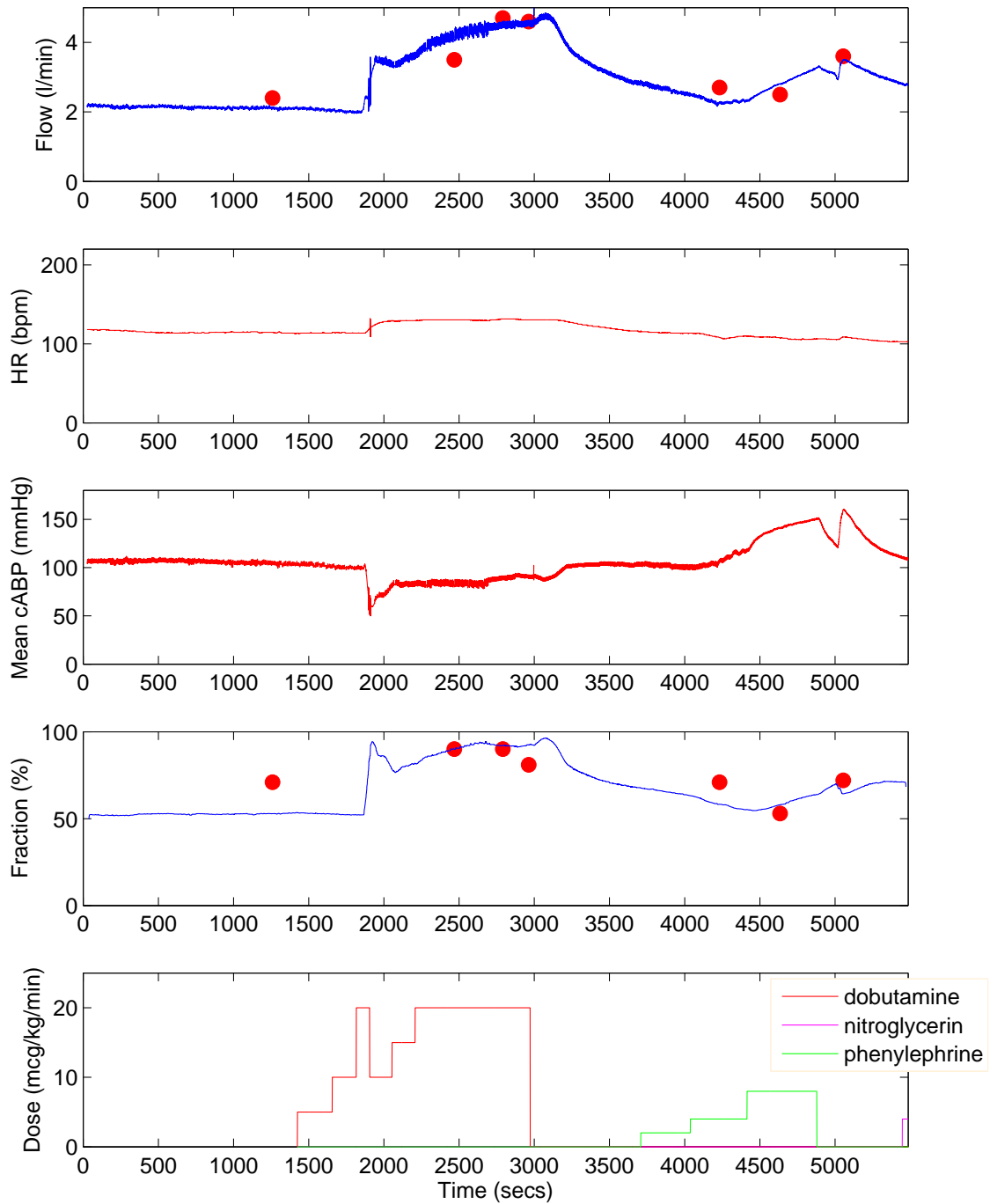


Figure 6.4: True and estimated CO (using cABP), HR, mean cABP, true and estimated EF (using cABP), and IV drugs for dog 1 with window size = 50 beats (using 2 points in each window), and a single-point calibration.

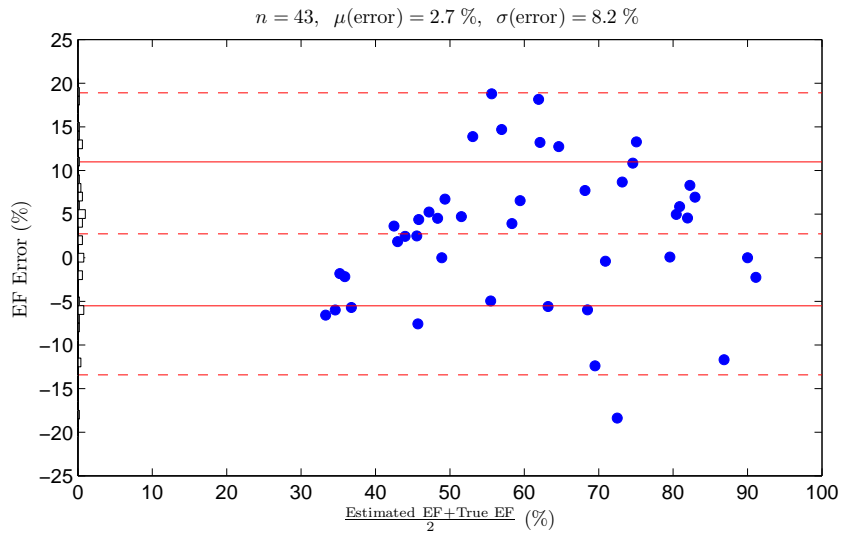


Figure 6.5: Bland-Altman plot of EF estimation error (using cABP and single-point calibration) versus the mean of true and estimated EF (using cABP) over the three dogs. The horizontal lines in the plot are the mean error, and the 1-SD and 2-SD lines.

Dog	Number of comparisons	RMSNE (%) using cABP
1	7	9.2
2	9	12.1
3	10	6.9
Mean	26	8.5

Table 6.4: RMSNEs for Mukkamala and co-workers' EF estimate using cABP and $Q_d=5\text{ml}$ [120].

Dog	Number of comparisons	RMSNE (%) for SH LVEDV	RMSNE (%) using cABP	RMSNE (%) using fABP	RMSNE (%) using carABP
1	7	17.5	14.3	15.5	15.4
2	29	14.0	9.8	–	–
3	7	6.1	14.0	–	–
Aggregate	43	13.3	11.9	–	–

Table 6.5: RMSNEs for our mean-calibrated LVEDV estimate, for which EF was calculated with window size = 50 beats and $Q_d=5\text{ml}$.

6.9 Results on LVEDV Estimation

Using the available ABP waveforms in the canine data set, we obtained beat-to-beat estimates of C_{be} , and used these estimates to compute beat-to-beat estimates of LVEDV using (6.14).

Table 6.5 summarizes the results obtained for the cABP, carABP, and fABP waveforms, using a mean calibration. In the table, we also list the RMSNEs for the SH LVEDV estimate (6.19) described above. The RMSNEs for the SH EF estimate reflect very low LVEDV variability for dogs 2 and 3. We believe that these low RMSNEs are sufficiently low to make our LVEDV estimation method useful in clinical applications. In addition, the fact that results are reasonable whether we use the cABP, fABP or carABP waveforms for dog 1 implies that our method could also be used in a minimally-invasive manner.

Figure 6.6 shows the true and estimated LVEDV for dog 2 with a mean calibration. Note that the estimated LVEDV tracks the true LVEDV quite well during the infusions of dobutamine (which indirectly increases LVEDV by reducing TPR) and volume changes (hemorrhage results in lower LVEDV, while volume infusion results in higher LVEDV).

Figure 6.7 shows the true and estimated LVEDV for dog 3 with a mean calibration. Note that the true LVEDV is essentially constant for this dog, making it difficult to conclude much about the estimated LVEDV.

Figure 6.8 is a Bland-Altman plot for the LVEDV estimation error across all three dogs using the cABP waveform and a mean calibration.

From the Bland-Altman plot, we see that the mean estimation error (or *bias*) is -0.01 ml, while the 1-standard deviation (SD) of the estimation error is 3.2 ml. The 2-SD line for our estimate lies 6.4 ml from the line representing mean estimation error, showing that, according to the criterion outlined in [114, 115], our mean-calibrated estimated LVEDV compares quite well with the reference echocardiography LVEDV measurements.

Continuous Monitoring of Left Ventricular Ejection Fraction and End-Diastolic Volume

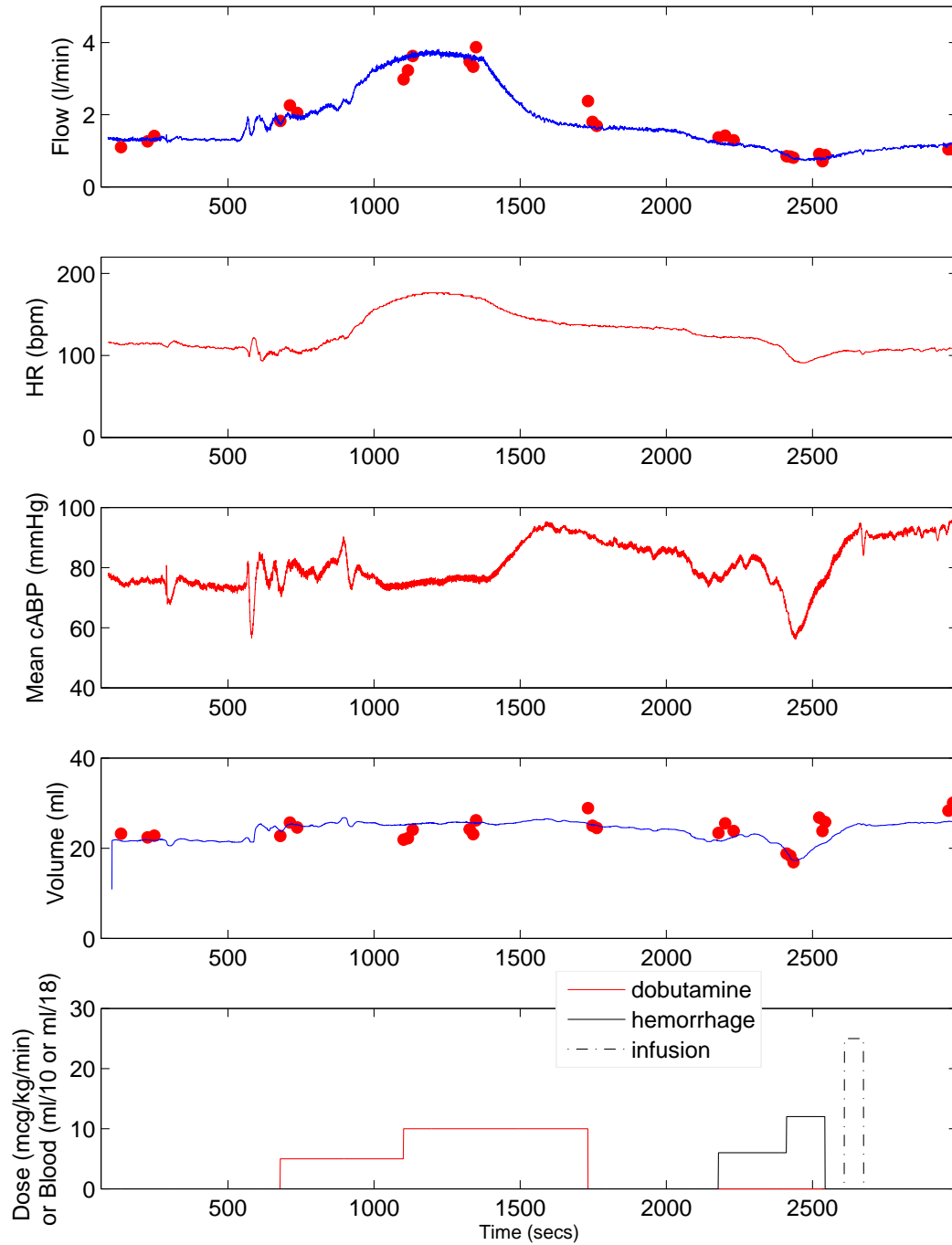


Figure 6.6: True and estimated CO (using cABP), HR, mean cABP, true and estimated LVEDV (using cABP), and IV drugs for dog 2 with a mean calibration.

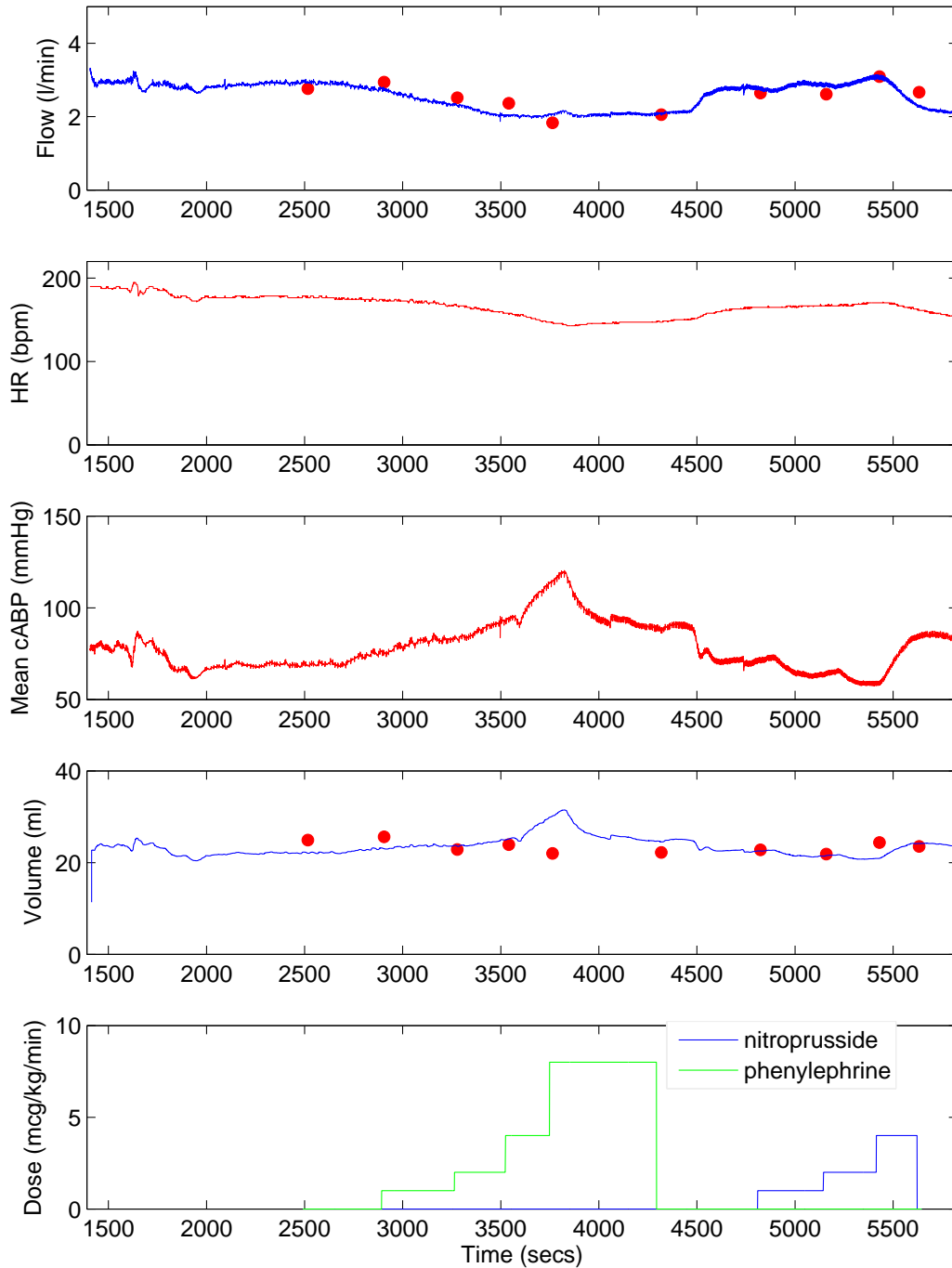


Figure 6.7: True and estimated CO (using cABP), HR, mean cABP, true and estimated LVEDV (using cABP), and IV drugs for dog 3 with a mean calibration.

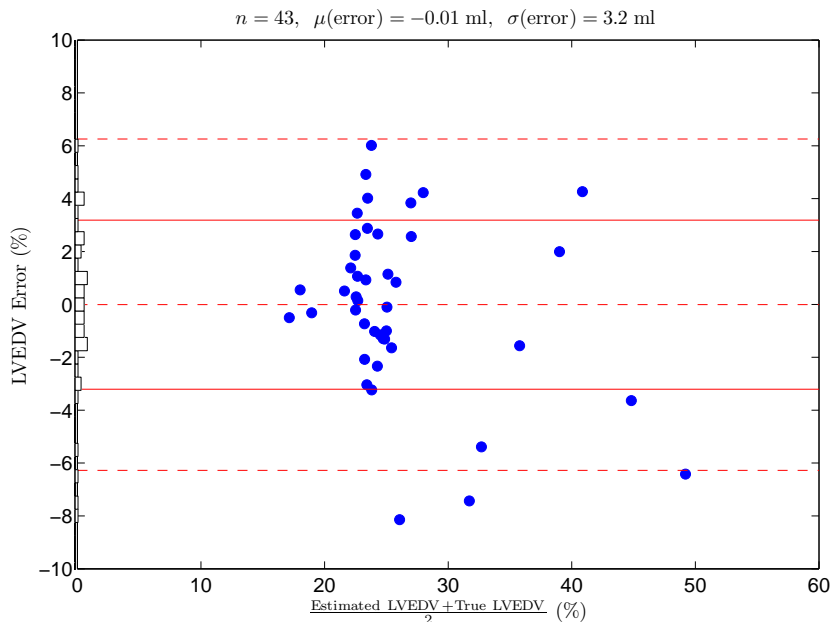


Figure 6.8: Bland-Altman plot of LVEDV estimation error (using cABP and mean calibration) versus the mean of true and estimated LVEDV (using cABP) over the three dogs. The horizontal lines in the plot are the mean error, and the 1-SD and 2-SD lines.

6.10 Combining Estimates of CO, TPR, EF, and LVEDV

In the ICU, we envision providing beat-to-beat estimates of CO, TPR, EF, and LVEDV to clinicians, allowing them to quickly decide on therapeutic interventions, particularly for hypotensive ICU patients with a combination of hypovolemia, sepsis, or cardiac failure.

We plot time series of estimated CO, TPR, EF, and LVEDV for dogs 1, 2, 3, in Figs. 6.9, 6.10, and 6.11, respectively. Each estimate was obtained under conditions described in this chapter and in Chapter 5.

In Fig. 6.9, when dobutamine is infused, we see a rapid increase in EF and a rapid decrease in both true and estimated TPR, while LVEDV stays approximately constant. Later in the record, when phenylephrine is infused, TPR increases, and as a result LVEDV increases.

In Fig. 6.10, when dobutamine is infused, we see a rapid increase in EF and a rapid decrease in TPR, while LVEDV stays approximately constant. Later in the record, during the progressive hemorrhage, TPR and LVEDV increase very rapidly. During the volume infusion, TPR and LVEDV gradually increase. During the hemorrhage and volume infusion portions of data, EF stays approximately constant.

In Fig. 6.11, it is very difficult to make reasonable deductions about the dog’s cardiovascular state given that CO, mean cABP, EF, and LVEDV do not vary much during the experiment.

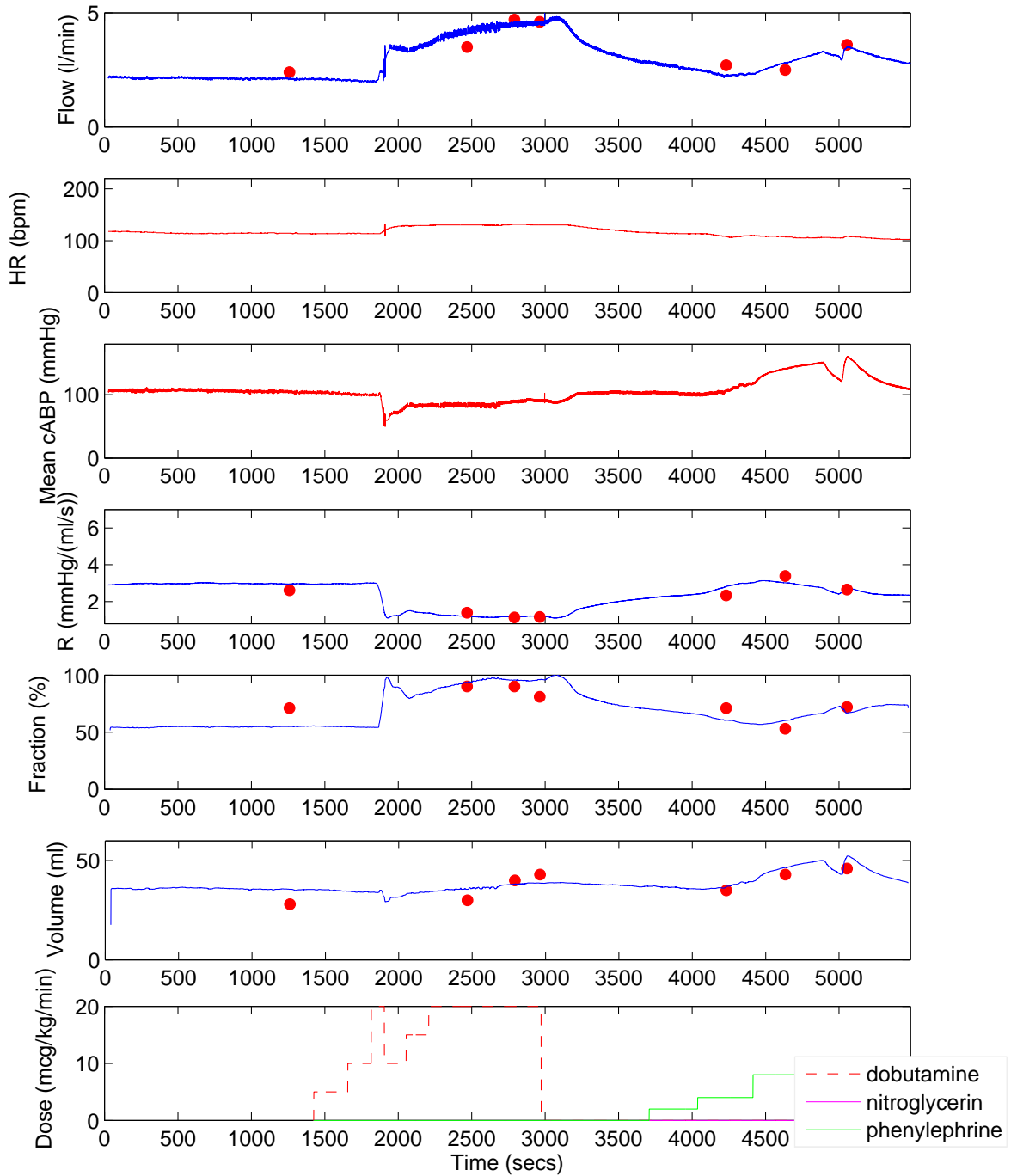


Figure 6.9: True and estimated CO, HR, mean cABP, true and estimated TPR, true and estimated EF, true and estimated LVEDV, and IV infusions for dog 1. The cABP waveform was used for each estimate.

Continuous Monitoring of Left Ventricular Ejection Fraction and End-Diastolic Volume

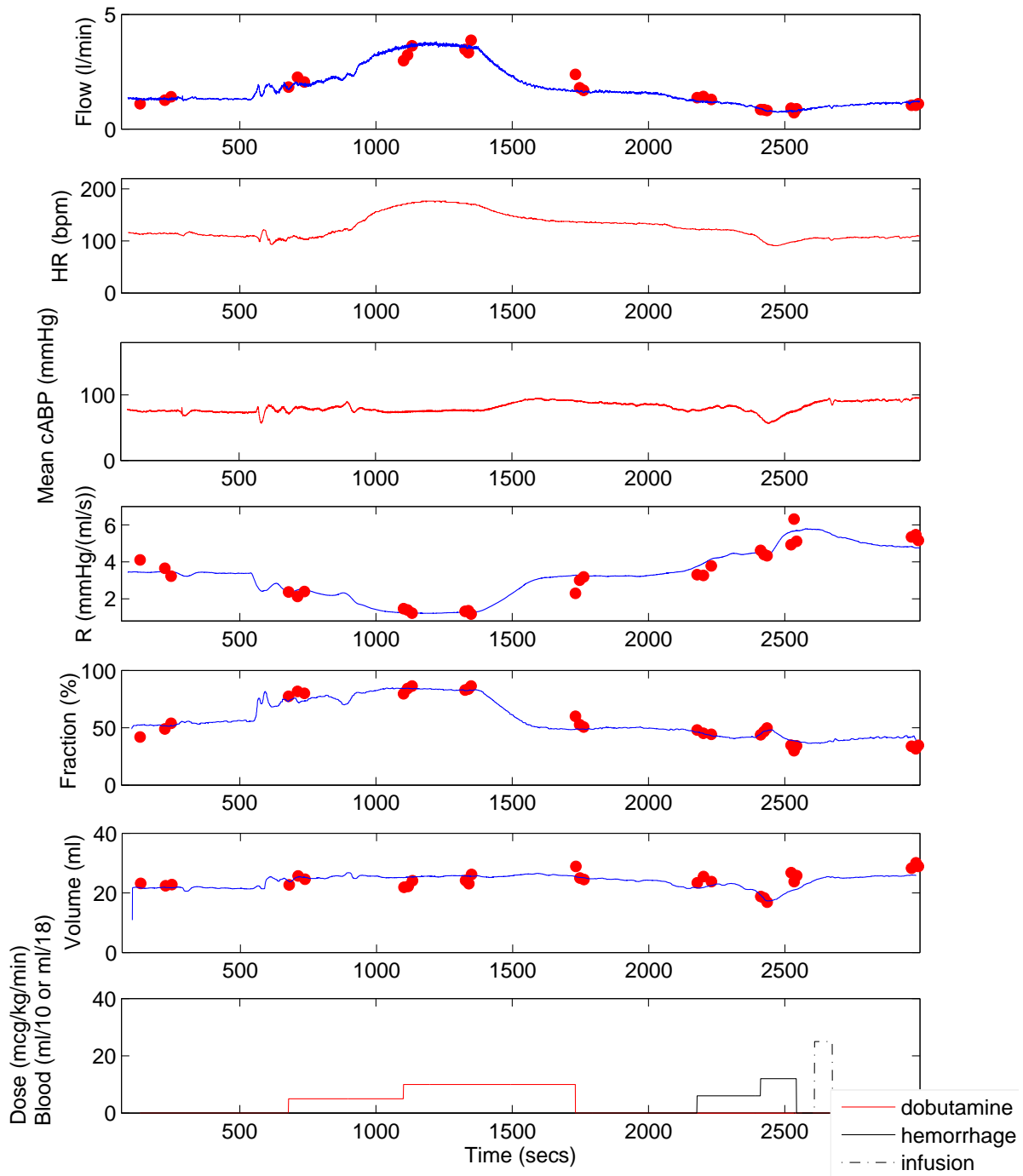


Figure 6.10: True and estimated CO, HR, mean cABP, true and estimated TPR, true and estimated EF, true and estimated LVEDV, and IV infusions for dog 2. The cABP waveform was used for each estimate.

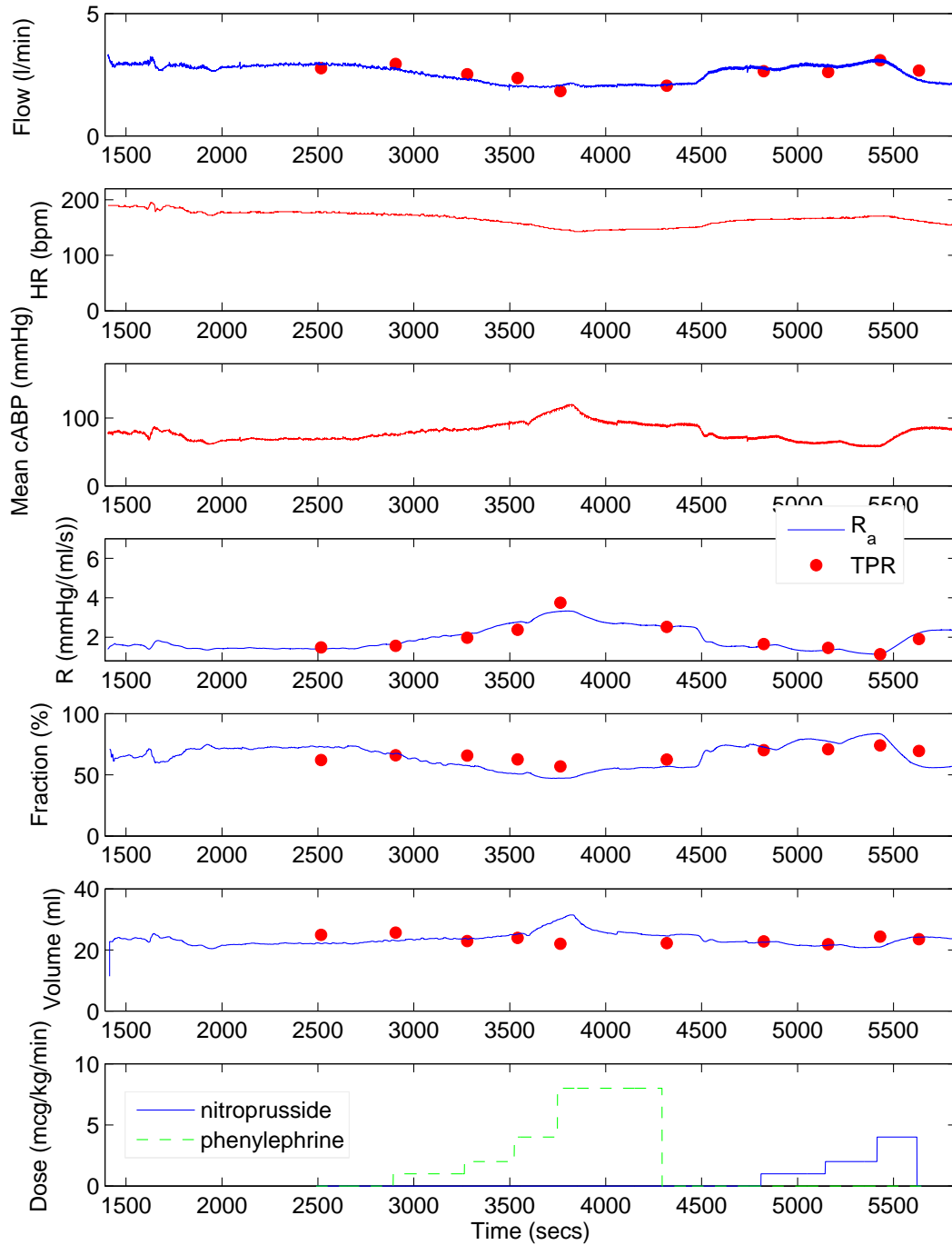


Figure 6.11: True and estimated CO, HR, mean cABP, true and estimated TPR, true and estimated EF, true and estimated LVEDV, and IV infusions for dog 3. The cABP waveform was used for each estimate.

6.11 Conclusions and Future Work

In this chapter, we described a novel beat-to-beat model-based method for continuously estimating left ventricular ejection fraction and left ventricular end-diastolic volume from central or peripheral arterial blood pressure waveforms. Our estimation methods require at least a single-point calibration to a reference EF or LVEDV measurement. Nevertheless, the methods have clear physiological bases, can be implemented using minimally-invasive arterial blood pressure measurements, and are computationally efficient making it easily implementable in real time.

We applied the method to a canine data set in which reference echocardiography-based ventricular volume measurements were available. The resulting RMSNEs on the data set, 13% for left ventricular ejection fraction, and 12% for left ventricular end-diastolic volume, are quite reasonable, especially given that our method does not require the entire arterial blood pressure wavelet in each beat. These errors are on the order of those obtained using another EF estimation method [27, 120], however, that method does not require a calibration factor. In future work, we intend to explore the bias errors that creep into our EF and LVEDV estimates, and we hope that this exploration will result in a calibration-free methods for estimating EF and LVEDV.

We concluded this chapter with a preview of one of the research directions we would like to pursue, namely, combining our estimates of CO, TPR, EF, and LVEDV to make sense of ICU patient data. As we lack the gold-standard annotated data for doing this research in a meaningful way, it would be prudent to carry out mammalian experiments in the laboratory through which more cardiac output, ejection fraction, left-ventricular end-diastolic volume, and arterial blood pressure data could be collected. This data could be collected for a variety of disease states and therapeutic interventions. Our model-based estimation methods would be even more strongly validated.

Part IV

Conclusions, Future Work, and Appendices

Conclusions

MODERN intensive care units suffer from an information overload problem, in which a vast and varied amount of physiological data is collected but little effort is placed in organizing, integrating, and interpreting the wealth of data. The clinician's task of data interpretation and integration is further complicated by the highly dynamic physiological state of ICU patients and the fact that the clinicians cannot devote too much time to any one ICU patient.

The research presented in this thesis attempted to address this information overload problem by using cardiovascular dynamics models and model-based estimation schemes to track important clinical variables. By tracking these variables, some of which are currently not continuously monitored in the ICU, we hope to present information to clinicians in a more organized manner, and also to reduce the frequency of invasive measurements performed on ICU patients. In particular, our hope was to be able to track variables that would help us distinguish between sepsis, hypovolemia, and cardiac problems.

We have come a long way towards estimating clinically important variables – cardiac output (CO), total peripheral resistance (TPR), left ventricular ejection fraction (EF), and left ventricular end-diastolic volume (LVEDV) – especially in terms of validating our model-based estimation methods with animal and human data. Yet, as with many theses, the research presented here generated more questions that need to be addressed, while providing answers to only some of those we posed earlier.

In this chapter, we conclude this report with a summary of the thesis contributions and a description of future research directions.

7.1 Summary of Contributions

The main contributions described in this thesis report are:

1. The development and application of averaging methodology to existing lumped-parameter pulsatile electrical circuit models of cardiovascular dynamics. The resulting averaged models – discrete-time beat-to-beat averaged and continuous-time cycle-averaged models – are capable of tracking cardiovascular dynamics on timescales larger than a single cardiac beat.

2. The development and application of the beat-to-beat averaged Windkessel model to estimate cardiac output and total peripheral resistance from a central or peripheral arterial blood pressure waveform. We validated this estimation method on two animal data sets – a porcine data set and a canine data set. In addition, we validated the method on two human ICU data sets – a MIMIC I patient data set with 12 patients and a MIMIC II patient data set with 120 patients. The errors obtained on application of our CO estimation method are well within the margin of clinically-acceptable error.
3. The use of the steady-state ventricular pressure-volume relationship in the development and application of a novel method for estimating left ventricular ejection fraction and left ventricular end-diastolic volume from a central or peripheral arterial blood pressure waveform. We applied these estimation methods to a canine data set, again obtaining errors that are clinically-acceptable.

7.2 Summary of Thesis Document

In Part I (Chapters 1 and 2) of this thesis, we gave an introduction to, and background for, the thesis research. In Chapter 1, we placed the thesis research in context, and provided a description of the thesis aims and contributions. We gave an overview of the MIT BRP and the MIMICU group within that partnership. We also included details on the MIMIC II ICU patient database, explaining which signals are routinely collected and the potential implications for researchers who might use these signals. We ended the chapter with the specific aims and contributions of this thesis research, and an outline of the thesis document. In Chapter 2 we gave a brief overview of cardiovascular physiology. In particular, we gave a brief description of the circulatory system and the mechanisms which control mean arterial blood pressure.

In Part II (Chapters 3 and 4), we described lumped-parameter electrical circuit models of cardiovascular dynamics. In particular, we described pulsatile, discrete-time beat-to-beat averaged, and continuous-time cycle-averaged models, many of which we developed. In Chapter 3 we described pulsatile models of cardiovascular dynamics. The well-known Windkessel model was introduced in this chapter. We showed how electrical circuit analogs for the cardiovascular system can be used to create models such as the modified Windkessel model, the cardiovascular simulator (CVSIM), and its derivatives – the simple cardiovascular simulator (CVSIMple) and the simple pulsatile cardiovascular model (SPCVM). We introduced the averaging methodology in Chapter 4 and applied it to some of these pulsatile models to obtain averaged models of cardiovascular dynamics. We illustrated these averaging techniques on the linear, time-invariant Windkessel model and also showed how one could cycle-average a nonlinear time-varying model such as the SPCVM.

In Part III (Chapters 5, and 6), we described our model-based estimation methods for cardiac output, total peripheral resistance, left-ventricular ejection fraction, and left-ventricular end-diastolic volume. In Chapter 5, we showed how the beat-to-beat averaged Windkessel model from Chapter 4 can be used to estimate cardiac output and total peripheral resistance. We validated this method using two animal and two human ICU patient data sets. The method was shown to be *robust* i.e., in all the data sets, our

method performed *better* than all the other CO estimation methods implemented, with a mean RMSNE of at most 15%. We presented a novel method for estimating left ventricular ejection fraction based on the steady-state left ventricular pressure-volume relationship in Chapter 6. As an extension of our EF estimation method, we also estimated left ventricular end-diastolic volume. Both methods were tested on a canine data set with three dogs and 43 reference echocardiography-based EF and LVEDV measurements. The resulting mean RMSNE of at most 13% is within the margin of clinically-acceptable error.

Part IV (Chapters 7 and the Appendices) concludes this thesis with a summary of the thesis research, main contributions, and potential avenues for further research. In the appendices, we give a description of the notation used in this thesis (Appendix A), and have placed ancillary material, such as derivations (Appendices B, C, D), and programming scripts (Appendices E and F).

7.3 Suggestions for Future Work

While we have come a long way towards demonstrating the benefits of computational models of cardiovascular dynamics in the ICU, there are many possible future research directions that we motivated through the research presented in this report. We describe some of these below.

Model-Based Estimation Methods Our model-based estimation methods for CO, EF, and LVEDV still need to be perfected. As mentioned in Chapters 5, we need to evaluate our results using the mean absolute normalized error criterion. In addition, as we mentioned in Chapter 6, the bias errors in our EF and LVEDV estimates need to be carefully analyzed. This analysis could potentially lead to the discovery of a calibration-free model-based method for estimating EF and LVEDV. While our estimation methods could easily report relative changes in these three variables, clinicians will be more accepting of our estimates if we provided absolute values of CO, EF, and LVEDV without any calibration.

Animal Studies There is a lack of gold-standard (appropriately measured and recorded) CO, EF, and LVEDV data in the MIMIC II database, something that we did not foresee at the beginning of this project. It would be prudent to carry out animal experiments in the laboratory through which more ejection fraction and left-ventricular end-diastolic volume and pressure data could be collected. In the same spirit, more animal data on cardiac output and ejection fraction and left-ventricular end-diastolic volume (and pressure) for various pathologies and therapeutic interventions should be collected. Our model-based estimation methods would then be more strongly validated.

Clinical Studies Before our CO estimation method progresses to a clinical setting, we need to perform studies with *human* subjects in which we determine how exactly to set nominal values for the calibration constants (γ_1 , γ_2) for our CO estimate. This study would, hopefully, take into account some of the pathologies we would encounter in the ICU, perhaps by using human subjects who suffer from cardiovascular disease.

Conclusions

Averaged Models While we have demonstrated the beat-to-beat and cycle-averaging methodologies in simple pulsatile models, it would be beneficial if we could show how to *modularize* our averaging methods, i.e., apply the methods in a modular fashion to linear or even nonlinear circuit elements. This would make the method more applicable to multi-compartment models, such as CVSIM. In addition, in the case of cycle-averaged models, other system identification techniques, such as adaptive observers and identifiers should be investigated.

Fluid Responsiveness One of the key problems in the ICU is determining a patient’s fluid responsiveness, i.e., how well a patient will respond to a bolus fluid infusion, or to the administration of a drug that reduces the body’s circulating blood volume. Fluid infusion is the main intervention for hypovolemia, while fluid removal is a key intervention for congestive heart failure [3]. We have performed some preliminary animal experiments in which we tried to determine how changes in the animals’ fluid balance relate to the respiratory modulation of the arterial blood pressure waveform [134]. Much work remains to be done – at the very least more animal studies could be performed to more carefully collect data on the respiratory modulation of ABP.

Clinical Reasoning Systems The emphasis in this thesis was on lumped-parameter electrical circuit models of cardiovascular dynamics. Very little work has been done on how to combine the outputs of our models and model-based estimation schemes to generate pathophysiological hypotheses in the ICU. This *model integration* step is essential, and a large part of our group’s future research effort would be best focused on this project.

We hope that our results will encourage other researchers to perform the studies suggested, and that the results in this thesis will contribute to the development of a next-generation patient monitoring system.

Appendix A

Nomenclature

A.1 Chapter 1

ICU	Intensive care unit
U.S.	United States of America
ABP	Arterial Blood Pressure
ECG	Electrocardiogram
BRP	Bioengineering Research Partnership
MIT	Massachusetts Institute of Technology
MIMIC	Multi-parameter Intelligent Monitoring for Intensive Care
LCP	Laboratory for Computational Physiology
CSAIL	Computer Science and Artificial Intelligence Laboratory
PHI	Protected Health Information
CVP	Central Venous Pressure
PAP	Pulmonary Artery Pressure
HR	Heart Rate
MAP	Mean Arterial Blood Pressure
SAP	Systolic Arterial Blood Pressure
DAP	Diastolic Arterial Blood Pressure
DPAP	Diastolic Pulmonary Artery Blood Pressure
PCWP	Pulmonary Capillary Wedge Pressure
CO	Cardiac Output
CHF	Congestive Heart Failure
TPR	Total Peripheral Resistance
SVR	Systemic Vascular Resistance
MIMICU	Model-based Monitoring for the Intensive Care Unit
LEES	Laboratory for Electromagnetic and Electronic Systems
AI	Artificial Intelligence
BBN	Bayesian Belief Network
HMM	Hidden Markov Model
EF	Left ventricular Ejection Fraction
LVEDV	Left Ventricular End-Diastolic Volume
LVEDP	Left Ventricular End-Diastolic Pressure

A.2 Chapter 2

CV	Cardiovascular
CVS	Cardiovascular System
SA	Sino-Atrial
AV	Atrio-Ventricular
MI	Myocardial Infarction
EDV	End-Diastolic Volume
ESV	End-Systolic Volume
EDP	End-Diastolic Pressure
ESP	End-Systolic Pressure
Preload	Pressure at the inlet of an atrium in the heart
Afterload	Pressure at the outlet of a ventricle in the heart
LV	Left Ventricular
RV	Right ventricular
SV	Stroke Volume
C_d	End-diastolic ventricular compliance
C_{es}	End-systolic ventricular compliance
LVESP	Left Ventricular End-Systolic Pressure
Q_d	Ventricular dead volume
V_{th}	Intrathoracic pressure
RVEDP	Right Ventricular End-Diastolic Pressure
VR	Venous Return
V_a	Arterial blood pressure
NTS	Nucleus tractus solitarius
ANS	Autonomic nervous system
RAP	Right Atrial Transmural Pressure
NO	Nitric Oxide
GTP	Guanosine triphosphate

A.3 Chapter 3

I	Blood flow
V	Blood pressure
Q	Blood volume
D	Heart valve
R	Vascular or valvular resistance
C	Vascular or ventricular compliance
L	Blood inertia
E	Elastance
R_a	Arterial resistance or TPR
C_a	Arterial compliance in Windkessel model
PP	Pulse Pressure
T (or T_n)	Duration of (n^{th}) cardiac cycle
f (or f_n)	Heart rate (in n^{th} cardiac cycle) in beats/min
t_n	Onset time of n^{th} cardiac cycle
$C_{a,p}$	Proximal arterial compliance in the modified Windkessel model
$C_{a,d}$	Distal arterial compliance in the modified Windkessel model
L_a	Blood inertia in modified Windkessel model
$V_{a,p}$	Proximal arterial blood pressure in the modified Windkessel model
$V_{a,d}$	Distal arterial blood pressure in the modified Windkessel model
I_L	Blood flow through L_a in the modified Windkessel model
CVSIM	Cardiovascular Simulator
CVSIMple	Simple cardiovascular simulator
SPCVM	Simple Pulsatile Cardiovascular Model
Q_h	Ventricular volume in CVSIMple or SPCVM
V_v	Venous blood pressure in CVSIMple or SPCVM
V_a	Arterial blood pressure
I_1	Blood flow through R_1 in CVSIMple or SPCVM
I_2	Blood flow through R_2 in CVSIMple or SPCVM
I_a	Blood flow through R_a
C_v	Venous compliance in CVSIMple or SPCVM
R_1	Inlet valve resistance in CVSIMple or SPCVM
R_2	Outlet valve resistance in CVSIMple or SPCVM
E_h	Ventricular elastance in CVSIMple or SPCVM
E_s	End-systolic elastance in CVSIMple or SPCVM
E_d	End-diastolic elastance in CVSIMple or SPCVM
T_d	Duration of diastole
T_s	Duration of systole
s_1	switching function for position 1 for the SPCVM switch
s_2	switching function for position 2 for the SPCVM switch
s_3	switching function for position 3 for the SPCVM switch
s_D	switching function for the diode in the SPCVM

A.4 Chapter 4

LVP	Left Ventricular Pressure
LTI	Linear and Time-Invariant
τ (or τ_n)	Time constant in Windkessel-type models (in the n^{th} cardiac cycle)
T (or T_n)	Duration of (n^{th}) cardiac cycle
f (or f_n)	Heart rate (in n^{th} cardiac cycle) in beats/min
t_n	Onset time of n^{th} cardiac cycle
X_n	X in the n^{th} cardiac cycle
\bar{V}_{an}	Mean ABP in the n^{th} cardiac cycle in the Windkessel model
ΔV_{an}	Equal to $V_a(t_{n+1}) - V_a(t_n)$ where n refers to the n^{th} cardiac cycle
$\bar{V}_{a,pn}$	Mean proximal ABP in the n^{th} cardiac cycle of the modified Windkessel model
$\Delta V_{a,pn}$	Equal to $V_{a,p}(t_{n+1}) - V_{a,p}(t_n)$ where n refers to the n^{th} cardiac cycle
$\bar{V}_{a,dn}$	Mean distal ABP in the n^{th} cardiac cycle of the modified Windkessel model
$\Delta V_{a,dn}$	Equal to $V_{a,d}(t_{n+1}) - V_{a,d}(t_n)$ where n refers to the n^{th} cardiac cycle
X_{ak}	Index- k cycle-average of X_a or $\langle X_a(t) \rangle_k$
X_{ak}^{R}	Real part of Index- k cycle-average of X_a or $\langle X_a(t) \rangle_k^{\text{R}}$
X_{ak}^{I}	Imaginary part of Index- k cycle-average of X_a or $\langle X_a(t) \rangle_k^{\text{I}}$
t_{D}	Diode turn-on time in the SPCVM
X_{a0}	Index-0 cycle-average of X_a
V_{a0}	Index-0 arterial blood pressure in the cycle-averaged Windkessel model
$V_{a,p0}$	Index-0 proximal arterial blood pressure in the cycle-averaged modified Windkessel model
$V_{a,d0}$	Index-0 distal arterial blood pressure in the cycle-averaged modified Windkessel model
I_{L0}	Index-0 blood flow through L_a in the cycle-averaged modified Windkessel model
$Q_{\text{h}0}$	Index-0 ventricular volume in the Index-0 CAM
$V_{\text{v}0}$	Index-0 venous blood pressure in the Index-0 CAM
V_{a0}	Index-0 arterial blood pressure in the Index-0 CAM
CAM	Cycle-Averaged Model
VP	Ventricular Pressure
PRU	Peripheral Resistance Unit (=1 mmHg/(ml/s))

A.5 Chapter 5

CO	Cardiac Output
ABP	Arterial Blood Pressure
ECG	Electrocardiogram
TPR	Total Peripheral Resistance
HR	Heart Rate
MAP	Mean Arterial Blood Pressure
SAP	Systolic Arterial Blood Pressure
DAP	Diastolic Arterial Blood Pressure
TPR	Total Peripheral Resistance
R_a	Arterial resistance or TPR
C_a	Arterial compliance in Windkessel model
PP	Pulse Pressure
T (or T_n)	Duration of (n^{th}) cardiac cycle
t_n	Onset time of n^{th} cardiac cycle
$C_{a,p}$	Proximal arterial compliance in modified Windkessel model
$C_{a,d}$	Distal arterial compliance in modified Windkessel model
L_a	Blood inertia in modified Windkessel model
$V_{a,p}$	Proximal arterial blood pressure in modified Windkessel model
$V_{a,d}$	Distal arterial blood pressure in modified Windkessel model
I_L	Blood flow through L_a in the modified Windkessel model
V_a	Arterial blood pressure in the Windkessel model
I_a	Blood flow through R_a
LTl	Linear and Time-Invariant
τ (or τ_n)	Time constant in Windkessel-type models (in the n^{th} cardiac cycle)
X_n	X in the n^{th} cardiac cycle
$\overline{V_{an}}$	Mean ABP in the n^{th} cardiac cycle in the Windkessel model
$\overline{V_{a,pn}}$	Mean proximal ABP in the n^{th} cardiac cycle of the modified Windkessel model
$\overline{V_{a,dn}}$	Mean distal ABP in the n^{th} cardiac cycle of the modified Windkessel model
ΔV_{an}	Equal to $V_a(t_{n+1}) - V_a(t_n)$ where n refers to the n^{th} cardiac cycle
UCO	Uncalibrated Cardiac Output
ECO	Estimated Cardiac Output
TCO	True (or reference) Cardiac Output
RMSNE	Root-Mean-Square-Normalized-Error
MANE	Mean Absolute Normalized Error
cABP	central Arterial Blood Pressure
rABP	radial Arterial Blood Pressure
fABP	femoral Arterial Blood Pressure
IV	Intravenous
B2BVI	Beat-to-Beat Variability Index
NECO	Naïve Estimated Cardiac Output
SHNECO	Sample-and-Holde Naïve Estimated Cardiac Output
LVESV	Left Ventricular End-Systolic Volume
LVEDV	Left Ventricular End-Diastolic Volume
ΔTCO	Range of True Cardiac Output measurements
POE	Provider-Order-Entry (medications)

A.6 Chapter 6

EF	Left ventricular Ejection Fraction
LVEDV	Left Ventricular End-Diastolic Volume
CO	Cardiac Output
TPR	Total Peripheral Resistance
SV	Stroke Volume
PCWP	Pulmonary Capillary Wedge Pressure
MRI	Magnetic Resonance Imaging
Echo	Echocardiography image
ICU	Intensive Care Unit
C_d	End-diastolic ventricular compliance
C_{be}	Before-ejection ventricular compliance
C_s	Peak-systolic ventricular compliance
C_{es}	End-systolic ventricular compliance
V_{th}	Intrathoracic pressure
SAP	Systolic Arterial Blood Pressure
DAP	Diastolic Arterial Blood Pressure
SV'	Estimated stroke volume
C_a	Arterial compliance in the Windkessel-type models
LVEDV'	Estimated left ventricular end-diastolic volume
Q_d	Ventricular dead volume
LVEDP	Left Ventricular End-Diastolic Pressure
LVESP	Left Ventricular End-Systolic Pressure
X_n	X in the n^{th} cardiac cycle
T (or T_n)	Duration of (n^{th}) cardiac cycle
t_n	Onset time of n^{th} cardiac cycle
$\overline{V_{an}}$	Mean ABP in the n^{th} cardiac cycle in the Windkessel model
τ (or τ_n)	Time constant in Windkessel-type models (in the n^{th} cardiac cycle)
ΔV_{an}	Equal to $V_a(t_{n+1}) - V_a(t_n)$ where n refers to the n^{th} cardiac cycle
RMSNE	Root-Mean-Square-Normalized-Error
MANE	Mean Absolute Normalized Error
SH X	Sample-and-Hold Estimator for quantity X
δ	calibration constant for ejection fraction
ϵ	calibration constant for left ventricular end-diastolic volume
cABP	central Arterial Blood Pressure
carABP	carotid Arterial Blood Pressure
fABP	femoral Arterial Blood Pressure

A.7 Chapter 7

ICU	Intensive Care Unit
CO	Cardiac Output
TPR	Total Peripheral Resistance
EF	Left Ventricular Ejection Fraction
LVEDV	Left Ventricular End-Diastolic Volume
MIMIC	Multi-parameter Intelligent Monitoring for Intensive Care
BRP	Bioengineering Research Partnership
CVSIM	Cardiovascular Simulator
CVSIMple	Simple Cardiovascular Simulator
SPCVM	Simple Pulsatile Cardiovascular Model
RMSNE	Root-Mean-Square-Normalized-Error
MANE	Mean Absolute Normalized Error
γ_1	first calibration constant for the pressure-dependent arterial compliance
γ_2	second calibration constant for the pressure-dependent arterial compliance

CVSIM Equations and Parameters

The equations for the CVSIM model corresponding to Fig. 3.7 are as follows:

$$\frac{dQ_{h,l}}{dt} = I_{il} - I_{ol} \quad (\text{B.1})$$

$$\frac{dV_a}{dt} = \frac{I_{ol} - I_a}{C_a} \quad (\text{B.2})$$

$$\frac{dV_v}{dt} = \frac{I_a - I_{ir}}{C_v} \quad (\text{B.3})$$

$$\frac{dQ_{h,r}}{dt} = I_{ir} - I_{or} \quad (\text{B.4})$$

$$\frac{dV_{pa}}{dt} = \frac{I_{or} - I_{pa}}{C_{pa}} \quad (\text{B.5})$$

$$\frac{dV_{pv}}{dt} = \frac{I_{pa} - I_{il}}{C_{pv}} \quad (\text{B.6})$$

where the various flow rates are given by:

$$I_{il} = \begin{cases} \frac{V_{pv} - V_{h,l}}{R_{il}} & \text{if } V_{pv} > V_{h,l} \\ 0 & \text{otherwise} \end{cases} \quad (\text{B.7})$$

$$I_{ol} = \begin{cases} \frac{V_{h,l} - V_a}{R_{ol}} & \text{if } V_{h,l} > V_a \\ 0 & \text{otherwise} \end{cases} \quad (\text{B.8})$$

$$I_a = \frac{V_a - V_v}{R_a} \quad (\text{B.9})$$

$$I_{ir} = \begin{cases} \frac{V_v - V_{h,r}}{R_{ir}} & \text{if } V_v > V_{h,r} \\ 0 & \text{otherwise} \end{cases} \quad (\text{B.10})$$

$$I_{or} = \begin{cases} \frac{V_{h,r} - V_{pa}}{R_{or}} & \text{if } V_{h,r} > V_{pa} \\ 0 & \text{otherwise} \end{cases} \quad (\text{B.11})$$

$$I_{pa} = \frac{V_{pa} - V_{pv}}{R_{pv}} \quad (\text{B.12})$$

CVSIM Equations and Parameters

Description	Parameter	Nominal Value
Systemic vascular resistance	R_a	1.0 mmHg/(ml/s) or PRU
Inflow resistance for right ventricle	R_{ir}	0.01 PRU
Outflow resistance for right ventricle	R_{or}	0.003 PRU
Pulmonary arterial resistance	R_{pa}	0.08 PRU
Inflow resistance for left ventricle	R_{il}	0.01 PRU
Outflow resistance for left ventricle	R_{ol}	0.006 PRU
Systemic arterial compliance	C_a	1.6 ml/mmHg
Systemic venous compliance	C_v	100 ml/mmHg
Pulmonary arterial compliance	C_{pa}	4.3 ml/mmHg
Pulmonary venous compliance	C_{pv}	8.4 ml/mmHg
Left ventricular end-diastolic elastance	$E_{d,l}$	0.1 mmHg/ml
Left ventricular end-systolic elastance	$E_{s,l}$	2.5 mmHg/ml
Right ventricular end-diastolic elastance	$E_{d,r}$	0.1 mmHg/ml
Right ventricular end-systolic elastance	$E_{s,r}$	$\frac{5}{6}$ mmHg/ml
Zero-pressure filling volume in left ventricular compartment	$Q_{h,l}(0)$	15 ml
Zero-pressure filling volume in right ventricular compartment	$Q_{h,r}(0)$	15 ml
Zero-pressure filling volume in systemic arterial compartment	$Q_a(0)$	715 ml
Zero-pressure filling volume in systemic venous compartment	$Q_v(0)$	2500 ml
Zero-pressure filling volume in pulmonary arterial compartment	$Q_{pa}(0)$	90 ml
Zero-pressure filling volume in pulmonary venous compartment	$Q_{pv}(0)$	400 ml
Length of one heart beat	T	$\frac{5}{6}$ s
Intrathoracic Pressure	V_{th}	-4 mmHg
Total Blood Volume	Q_{tot}	5000 mL

Table B.1: Nominal parameters of the CVSIM model. These parameters are based on a literature review in [49]. Ranges for these parameters can be found in [34].

The elastance of the left and right ventricles, respectively, are given by:

$$E_{h,l}(t) = \begin{cases} \frac{1}{2}(E_{s,l} - E_{d,l}) \left(1 - \cos\left(\frac{\pi t}{0.3\sqrt{T}}\right)\right) + E_{d,l} & \text{for } 0 \leq t \leq 0.3\sqrt{T} \\ \frac{1}{2}(E_{s,l} - E_{d,l}) \left(1 - \cos\left(\frac{2\pi(t-0.3\sqrt{T})}{0.3\sqrt{T}}\right)\right) + E_{d,l} & \text{for } 0.3\sqrt{T} \leq t \leq \frac{0.9\sqrt{T}}{2} \\ E_{d,l} & \text{for } \frac{0.9\sqrt{T}}{2} \leq t \leq T \end{cases} \quad (\text{B.13})$$

$$E_{h,r}(t) = \begin{cases} \frac{1}{2}(E_{s,r} - E_{d,r}) \left(1 - \cos\left(\frac{\pi t}{0.3\sqrt{T}}\right)\right) + E_{d,r} & \text{for } 0 \leq t \leq 0.3\sqrt{T} \\ \frac{1}{2}(E_{s,r} - E_{d,r}) \left(1 - \cos\left(\frac{2\pi(t-0.3\sqrt{T})}{0.3\sqrt{T}}\right)\right) + E_{d,r} & \text{for } 0.3\sqrt{T} \leq t \leq \frac{0.9\sqrt{T}}{2} \\ E_{d,r} & \text{for } \frac{0.9\sqrt{T}}{2} \leq t \leq T \end{cases} \quad (\text{B.14})$$

The nominal CVSIM parameters (see [8, 49]) are as follows:

Circuit Analysis for the SPCVM

The SPCVM operates in four different regions during a single cycle. These four regions correspond to the four stages (isovolumic contraction, ejection, isovolumic relaxation, and filling) of the cardiac cycle. In each region, based on the states of the switch and diode listed in Table 3.3, there is a circuit defining the SPCVM. Figure C.1 shows the circuits in the four regions of operation of the SPCVM.

If the diode switching times were fixed, the SPCVM would be a periodically time-varying system and a rich set of analysis tools could be applied to the circuit (see [135] and [136] for examples of such tools). Using Q_h , V_a , and V_v as state variables, we see that each of the circuits is linear.

In regions I (isovolumic contraction) and III (isovolumic relaxation), the charge in the time-varying capacitor is constant ($\dot{Q}_h = 0$) as there is no blood flow into or out of the heart. In these regions, we have a linear system given by:

$$\frac{d}{dt} \begin{bmatrix} Q_h \\ V_a \\ V_v \end{bmatrix} = \begin{bmatrix} 0 & 0 & 0 \\ 0 & \frac{-1}{R_a C_a} & \frac{1}{R_a C_a} \\ 0 & \frac{1}{R_a C_v} & \frac{-1}{R_a C_v} \end{bmatrix} \begin{bmatrix} Q_h \\ V_a \\ V_v \end{bmatrix}. \quad (\text{C.1})$$

In region II (ejection) there is blood flow out of the heart and thus Q_h is not constant. A state space description of the system in region II is:

$$\frac{d}{dt} \begin{bmatrix} Q_h \\ V_a \\ V_v \end{bmatrix} = \begin{bmatrix} \frac{-E_h(t)}{R_2} & \frac{1}{R_2} & 0 \\ \frac{E_h(t)}{R_2 C_a} & \frac{-(R_2 + R_a)}{R_2 R_a C_a} & \frac{1}{R_a C_a} \\ 0 & \frac{1}{R_a C_v} & \frac{-1}{R_a C_v} \end{bmatrix} \begin{bmatrix} Q_h \\ V_a \\ V_v \end{bmatrix}. \quad (\text{C.2})$$

Finally, by analyzing the third circuit in Fig. C.1, we obtain a state space model for region IV (filling) as:

$$\frac{d}{dt} \begin{bmatrix} Q_h \\ V_a \\ V_v \end{bmatrix} = \begin{bmatrix} \frac{-E_h(t)}{R_1} & 0 & \frac{1}{R_1} \\ 0 & \frac{-1}{R_a C_a} & \frac{1}{R_a C_a} \\ \frac{E_h(t)}{R_1 C_v} & \frac{1}{R_a C_v} & \frac{-(R_1 + R_a)}{R_1 R_a C_v} \end{bmatrix} \begin{bmatrix} Q_h \\ V_a \\ V_v \end{bmatrix}. \quad (\text{C.3})$$

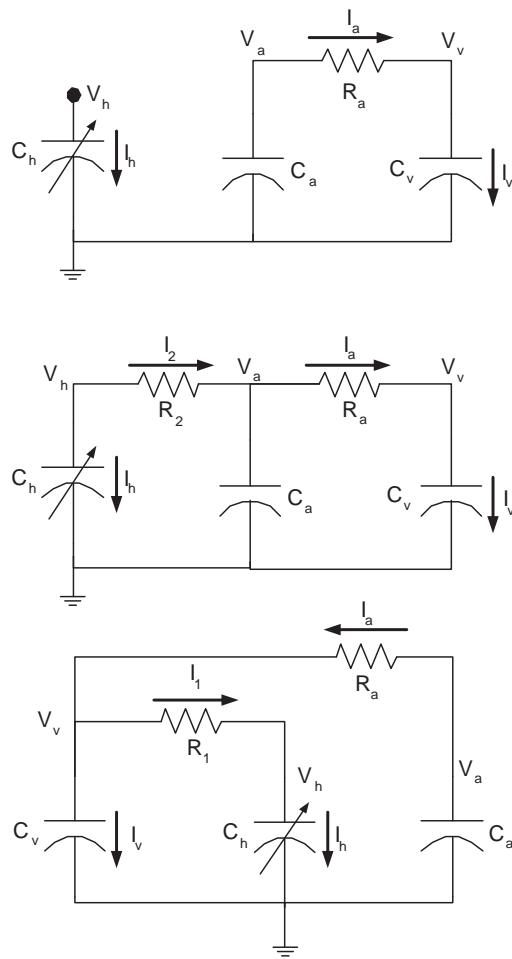


Figure C.1: SPCVM circuits for the different regions of operation: the top circuit is for regions I and III, the middle circuit is for region II, and the bottom circuit is for region IV.

Ancillaries for the Index-0 Cycle-Averaged Model

D.1 Expressions used in the Index-0 Model

Here, we give the expressions used for $\mathcal{C}(S_{10}, S_{D0}(t), p)$ and $\mathbf{d}(S_{10}, S_{D0}(t), S_{11}, S_{D1}, \mathbf{X}_1, \mathbf{X}_2, p)$. These expressions were derived using the approximations in (4.35)-(4.40), and can be evaluated using the parameters in Table 3.1.

The entries of the 3×3 matrix

$$\mathcal{C}(S_{10}, S_{D0}(t), p) = \begin{bmatrix} c_{11} & c_{12} & c_{13} \\ c_{21} & c_{22} & c_{23} \\ c_{31} & c_{32} & c_{33} \end{bmatrix}$$

are as follows:

$$c_{11} = -\frac{S_{10}E_{h0}}{R_1} - \frac{S_{D0}E_{h0}}{R_2} - 2\frac{S_{D1}^R E_{h1}^R}{R_2} - 2\frac{S_{D1}^I E_{h1}^I}{R_2} - 2\frac{S_{11}^R E_{h1}^R}{R_1} - 2\frac{S_{11}^I E_{h1}^I}{R_1}; \quad (\text{D.1})$$

$$c_{12} = \frac{S_{D0}}{R_2}; \quad (\text{D.2})$$

$$c_{13} = \frac{S_{10}}{R_1}; \quad (\text{D.3})$$

$$c_{21} = \frac{S_{D0}E_{h0}}{C_a R_2} + 2\frac{S_{D1}^R E_{h1}^R}{C_a R_2} + 2\frac{S_{D1}^I E_{h1}^I}{C_a R_2}; \quad (\text{D.4})$$

$$c_{22} = -\frac{R_2 + R_a S_{D0}}{C_a R_2 R_a}; \quad (\text{D.5})$$

$$c_{23} = \frac{1}{C_a R_a}; \quad (\text{D.6})$$

$$c_{31} = \frac{S_{10}E_{h0}}{C_v R_1} + 2\frac{S_{11}^R E_{h1}^R}{C_v R_1} + 2\frac{S_{11}^I E_{h1}^I}{C_v R_1}; \quad (\text{D.7})$$

$$c_{32} = \frac{1}{C_v R_a}; \quad (\text{D.8})$$

$$c_{33} = -\frac{R_a S_{10} + R_1}{C_v R_1 R_a}. \quad (\text{D.9})$$

The entries of the 3×1 vector

$$\mathbf{d}(S_{10}, S_{D0}(t), S_{11}, S_{D1}, \mathbf{X}_1, \mathbf{X}_2, p) = \begin{bmatrix} d_1 \\ d_2 \\ d_3 \end{bmatrix}$$

are given below. The expressions simplify somewhat under the reasonable assumption that V_{v1}^R and V_{v1}^I are negligibly small:

$$\begin{aligned} d_1 = & -2(Q_{h1}^R E_{h1}^R + Q_{h1}^I E_{h1}^I) \left(\frac{S_{10}}{R_1} + \frac{S_{D0}}{R_2} \right) - 2(Q_{h2}^R E_{h2}^R + Q_{h2}^I E_{h2}^I) \left(\frac{S_{10}}{R_1} + \frac{S_{D0}}{R_2} \right) \\ & - 2 \left(\frac{S_{D1}^R E_{h0} Q_{h1}^R + S_{D1}^I E_{h0} Q_{h1}^I}{R_2} \right) - 2 \left(\frac{S_{11}^R E_{h0} Q_{h1}^R + S_{11}^I E_{h0} Q_{h1}^I}{R_1} \right) \\ & - 2 \left(\frac{S_{D1}^R V_{a1}^R + S_{D1}^I V_{a1}^I}{R_2} \right) + 2 \left(\frac{S_{11}^R V_{v1}^R + S_{11}^I V_{v1}^I}{R_1} \right) \\ & - 2 \left(\frac{S_{11}^R}{R_1} + \frac{S_{D1}^R}{R_2} \right) \left(Q_{h2}^R E_{h1}^R + Q_{h2}^I E_{h1}^I \right) - 2 \left(\frac{S_{11}^I}{R_1} + \frac{S_{D1}^I}{R_2} \right) \left(Q_{h1}^R E_{h2}^R + Q_{h1}^I E_{h2}^I \right) \\ & - 2 \left(\frac{S_{11}^I}{R_1} + \frac{S_{D1}^I}{R_2} \right) \left(Q_{h2}^R E_{h1}^I - Q_{h2}^I E_{h1}^R \right) - 2 \left(\frac{S_{11}^R}{R_1} + \frac{S_{D1}^R}{R_2} \right) \left(Q_{h1}^R E_{h2}^I - Q_{h1}^I E_{h2}^R \right). \end{aligned} \quad (\text{D.10})$$

$$\begin{aligned} d_2 = & 2S_{D0} \left(\frac{Q_{h1}^R E_{h1}^R + Q_{h1}^I E_{h1}^I}{C_a R_2} \right) + 2S_{D0} \left(\frac{Q_{h2}^R E_{h2}^R + Q_{h2}^I E_{h2}^I}{C_a R_2} \right) \\ & + 2 \left(\frac{S_{D1}^R E_{h0} Q_{h1}^R + S_{D1}^I E_{h0} Q_{h1}^I}{C_a R_2} \right) - 2 \left(\frac{S_{D1}^R V_{a1}^R + S_{D1}^I V_{a1}^I}{C_a R_2} \right) \\ & + 2 \frac{S_{D1}^R}{C_a R_2} \left(Q_{h2}^R E_{h1}^R + Q_{h2}^I E_{h1}^I \right) + 2 \frac{S_{D1}^I}{C_a R_2} \left(Q_{h1}^R E_{h2}^R + Q_{h1}^I E_{h2}^I \right) \\ & + 2 \frac{S_{D1}^I}{C_a R_2} \left(Q_{h2}^R E_{h1}^I - Q_{h2}^I E_{h1}^R \right) + 2 \frac{S_{D1}^R}{C_a R_2} \left(Q_{h1}^R E_{h2}^I - Q_{h1}^I E_{h2}^R \right). \end{aligned} \quad (\text{D.11})$$

$$\begin{aligned} d_3 = & 2S_{10} \left(\frac{Q_{h1}^R E_{h1}^R + Q_{h1}^I E_{h1}^I}{C_v R_1} \right) + 2S_{10} \left(\frac{Q_{h2}^R E_{h2}^R + Q_{h2}^I E_{h2}^I}{C_v R_1} \right) \\ & + 2 \left(\frac{S_{11}^R E_{h0} Q_{h1}^R + S_{11}^I E_{h0} Q_{h1}^I}{C_v R_1} \right) - 2 \left(\frac{S_{11}^R V_{v1}^R + S_{11}^I V_{v1}^I}{C_v R_1} \right) \\ & + 2 \frac{S_{11}^R}{C_v R_1} \left(Q_{h2}^R E_{h1}^R + Q_{h2}^I E_{h1}^I \right) + 2 \frac{S_{11}^I}{C_v R_1} \left(Q_{h1}^R E_{h2}^R + Q_{h1}^I E_{h2}^I \right) \\ & + 2 \frac{S_{11}^I}{C_v R_1} \left(Q_{h2}^R E_{h1}^I - Q_{h2}^I E_{h1}^R \right) + 2 \frac{S_{11}^R}{C_v R_1} \left(Q_{h1}^R E_{h2}^I - Q_{h1}^I E_{h2}^R \right). \end{aligned} \quad (\text{D.12})$$

D.2 Charge Conservation in the Simple Pulsatile Cardiovascular Model

In this section we present results on charge conservation in the index-0 cycle-averaged model. First, we show that there is charge conservation in the SPCVM. Second, we prove that the (constant) total charge in the SPCVM and the index-0 component of the total charge in the index-0 cycle-averaged SPCVM are equal.

By applying the index-0 cycle-average operator, $\langle \bullet \rangle_0$, to the SPCVM equations, we obtain:

$$\frac{dQ_{h0}}{dt} = -\frac{\langle s_1(V_h - V_v) \rangle_0}{R_1} - \frac{\langle s_D(V_h - V_a) \rangle_0}{R_2} \quad (\text{D.13})$$

$$C_a \frac{dV_{a0}}{dt} = \frac{\langle s_D(V_h - V_a) \rangle_0}{R_2} - \frac{V_{a0} - V_{v0}}{R_a} \quad (\text{D.14})$$

$$C_v \frac{dV_{v0}}{dt} = \frac{\langle s_1(V_h - V_v) \rangle_0}{R_1} + \frac{V_{a0} - V_{v0}}{R_a}. \quad (\text{D.15})$$

By summing the left-hand sides of (D.13), (D.14) and (D.15), we obtain:

$$\frac{dQ_{\text{tot}0}}{dt} = \frac{dQ_{h0}}{dt} + C_a \frac{dV_{a0}}{dt} + C_v \frac{dV_{v0}}{dt} = 0 \quad (\text{D.16})$$

where $Q_{\text{tot}0}$ is the index-0 component of the total charge in the index-0 cycle-averaged model. This result shows that for any given approximation for S_{D0} , and any E_h , C_a , C_v , R_1 , R_2 , and R_a , the total charge in the index-0 cycle-averaged model is conserved.

Let Q_{tot} be the total charge in the SPCVM. By definition, we have:

$$Q_{\text{tot}} = Q_h + C_a V_a + C_v V_v. \quad (\text{D.17})$$

Applying the linear operator $\langle \bullet \rangle_0$ to (D.17) yields:

$$Q_{\text{tot}0} = Q_{\text{tot}} = Q_{h0} + C_a V_{a0} + C_v V_{v0}. \quad (\text{D.18})$$

since Q_{tot} is constant.

The right-hand side of (D.18) is, by definition, the total charge in the index-0 cycle-averaged model. Thus:

$$Q_{\text{tot}} = Q_{\text{tot}0}. \quad (\text{D.19})$$

D.3 Higher-Order Approximations for the Cycle-Averages

We present expressions for the index-0 cycle-averaged model in which the index-0, index-1, and index-2 cycle-averages are not assumed to be negligible. We only derive these expressions for the index-0 and index-1 cycle-averages of the product of two signals $x(t)$ and $y(t)$. The extension of the results to three

Ancillaries for the Index-0 Cycle-Averaged Model

signals proceeds in complete analogy.

A useful expression for index- k averages that allows simplification of expressions for higher-index cycle-averages is that for any signals $x(t)$ and $y(t)$, the following relation holds:

$$X_{-k}Y_k + X_kY_{-k} = 2(X_k^R Y_k^R + X_k^I Y_k^I) . \quad (\text{D.20})$$

If we assume that the index-2 cycle-averages are not negligible, by applying (4.33), we have that:

$$\langle xy \rangle_0 = X_0 Y_0 + 2(X_1^R Y_1^R + X_1^I Y_1^I) + 2(X_2^R Y_2^R + X_2^I Y_2^I) . \quad (\text{D.21})$$

$$\langle xy \rangle_1^R = X_0 Y_1^R + X_1^R Y_0 + X_2^R Y_1^R + X_2^I Y_1^I + X_1^R Y_2^R + X_1^I Y_2^I . \quad (\text{D.22})$$

$$\langle xy \rangle_1^I = X_0 Y_1^I + X_1^I Y_0 + X_2^R Y_1^I - X_2^I Y_1^R + X_1^R Y_2^I - X_1^I Y_2^R . \quad (\text{D.23})$$

which would require changing $\mathcal{C}(S_{10}, S_{D0}(t), p)$ and $\mathbf{d}(S_{10}, S_{D0}(t), S_{11}, S_{D1}, \mathbf{X}_1, \mathbf{X}_2, p)$. In simulations, we observed that the improvement in results does not justify using such higher-order terms in the index-0 cycle-averaged model, except for Q_h and E_h .

MATLAB implementation for the SPCVM

```

% SPCVM.m
global T alpha beta Es Ed Ts R1 R2 Ca Cv

t0=0; tf=60; Es=2.5; Ed=0.1; T=1; Ts=T/3; alpha=0.5*T; beta=Ts;
Ca=2; Cv=100; R1=0.03; R2=0.01; tstep=0.02;

x0=[127.383 91.2281 15.0337];

options = odeset('MaxStep',tstep);
[t,x]=ode45(@getSPCVM,t0:tstep:tf, x0, options);

Qh=x(:,1); Va=x(:,2); Vv=x(:,3);

time=t';

for m=1:length(time)
    ttemp=mod(time(m),T);%(time(m)-floor(time(m)))/T;
    if ttemp<=(T/3)
        E(m)=((Es-Ed)*ttemp)/Ts+Ed;
    end
    if (ttemp>(T/3))&(ttemp<=(T/2))
        E(m)=(1/(T/6))*(Ed-Es)*ttemp+3*Es-2*Ed;
    end
    if ttemp>(T/2)
        E(m)=Ed;
    end
end
Vh=Qh' .*E;
function dx=getSPCVM(t,x)
ttemp=mod(t,T);

if ttemp<=(T/3)
    E=((Es-Ed)*ttemp)/Ts+Ed;
end if (ttemp>(T/3))&(ttemp<=(T/2))
    E=(1/(T/6))*(Ed-Es)*ttemp+3*Es-2*Ed;
end if ttemp>(T/2)
    E=Ed;
end

```

MATLAB implementation for the SPCVM

```
if ttemp<alpha
    q1=0;
else
    q1=1;
end

if ttemp<beta
    q2=1;
else
    q2=0;
end

if ((x(1)*E)>=x(2))&(q2==1)
    qd=1;
else
    qd=0;
end

if t>=15
    R3=2;
    if t>=30
        R3=1;
        if t>=45
            R3=0.5;
        end
    end
else
    R3=1;
end

dx1=(-(q1/R1) - (qd/R2))*E*x(1) + (qd/R2)*x(2) + (q1/R1)*x(3) ;
dx2=(qd*E/(Ca*R2))*x(1) + (-1/(Ca*R3)-qd/(Ca*R2))*x(2)+...
(1/(Ca*R3))*x(3) ;
dx3=(q1*E/(Cv*R1))*x(1) + (1/(Cv*R3))*x(2) +...
(-q1/(Cv*R1)-1/(Cv*R3))*x(3) ;

dx=[dx1;dx2;dx3];
```

MATLAB implementation for the index-0 CAM

```

% index0CAM.m
global T alpha beta Es Ed Ts R1 R2 Ca Cv

t0=0; tf=60; Es=2.5; Ed=0.1; T=1; Ts=T/3; alpha=0.5*T; beta=Ts;
Ca=2; Cv=100; R1=0.03; R2=0.01; tstep=1;

% initial conditions
x0=[127.383 91.2281 15.0337];

options = odeset('MaxStep',tstep);

[t,x]=ode45(@getindex0CAM, t0:tstep:tf, x0, options);

Qh_mfav0=x(:,1); Va_mfav0=x(:,2); Vv_mfav0=x(:,3);

time=t';

E_0=0.700120374; E_1R=-0.09133141072612; E_1I=-0.47387465212172;
E_2R=-0.2052; E_2I=0.1185;

Qh_1R = 18.68684392876221; Qh_1I = 10.71078134657849; Qh_2R =2.0333;
Qh_2I =-2.5241;

% Calculate the correct form of <Vh> :
Vh_mfav0=Qh_mfav0*E_0 + 2*Qh_1R*E_1R + 2*Qh_1I*E_1I + 2*Qh_2R*E_2R
+ 2*Qh_2I*E_2I;

function dx=getindex0CAM(t,x)

if t>=15
    R3=1.4;
    if t>=30
        R3=1;
        if t>=45
            R3=0.6;
        end
    end
else
    R3=1;

```

MATLAB implementation for the index-0 CAM

```
end

q1_avg=(alpha); q1_1R=-9.99999999841267e-5;
q1_1I=-(1/(2*pi))*(cos(2*pi*q1_avg)-1);

E_0=0.700120374; E_1R=-0.09133141072612; E_1I=-0.47387465212172;
E_2R=-0.2052; E_2I=0.1185;

Qh_1R = 18.68684392876221; Qh_1I = 10.71078134657849; Qh_2R =2.0333;
Qh_2I =-2.5241;

Vh_1R=2.95889924835524; Vh_1I=-27.81509469786276;

Vv_1R=-0.0866; Vv_1I=-0.0333;

Va_1R= -4.95043425370244; Va_1I= -3.62999310428362;

td=(T*Ed/(3*(Es-Ed)))*((x(2)/x(3))-1); qd_avg=beta-td/T;
qd_1I=-(1/(2*pi))*(cos(2*pi*(beta-0.2557))-cos(2*pi*beta));
qd_1R=(1/(2*pi))*(sin(2*pi*beta)-sin(2*pi*(beta-0.2557)));

a11= -(q1_avg/R1) - (qd_avg/R2))*E_0 - 2*qd_1R*E_1R/R2 -
2*qd_1I*E_1I/R2 - 2*q1_1R*E_1R/R1 - 2*q1_1I*E_1I/R1;

a12=qd_avg/(R2); a13= (q1_avg/R1);

b1= (2*Qh_1R*E_1R + 2*Qh_1I*E_1I + 2*Qh_2R*E_2R + ...
2*Qh_2I*E_2I)*(-(q1_avg/R1) - (qd_avg/R2)) - 2*qd_1R*E_0*Qh_1R/R2...
- 2*qd_1I*E_0*Qh_1I/R2 - 2*q1_1R*E_0*Qh_1R/R1...
-2*q1_1I*E_0*Qh_1I/R1 + (2*qd_1R*Va_1R + 2*qd_1I*Va_1I)/R2...
+(2*q1_1R*Vv_1R + 2*q1_1I*Vv_1I)/R1 -2*((q1_1R/R1)+...
(qd_1R/R2))*(Qh_2R*E_1R+Qh_2I*E_1I+Qh_1R*E_2R+Qh_1I*E_2I)...
-2*((q1_1I/R1) + (qd_1I/R2))*(Qh_2R*E_1I - Qh_2I*E_1R +...
Qh_1R*E_2I - Qh_1I*E_2R);

dx1=a11*x(1) + a12*x(2) + a13*x(3) + b1 -195.813036461240;

a21= (qd_avg/(Ca*R2))*E_0 + 2*qd_1R*E_1R/(Ca*R2) +...
2*qd_1I*E_1I/(Ca*R2); a22= (-1/(Ca*R3)-qd_avg/(Ca*R2));

a23=(1/(Ca*R3));

b2= (qd_avg/(Ca*R2))*(2*Qh_1R*E_1R + 2*Qh_1I*E_1I... +
2*Qh_2R*E_2R+ 2*Qh_2I*E_2I) + 2*qd_1R*E_0*Qh_1R/(Ca*R2) +...
2*qd_1I*E_0*Qh_1I/(Ca*R2)- (2*qd_1R*Va_1R...
+2*qd_1I*Va_1I)/(Ca*R2)...
+2*(qd_1R/(Ca*R2))*(Qh_2R*E_1R+Qh_2I*E_1I+Qh_1R*E_2R+Qh_1I*E_2I)...
+ 2*(qd_1I/(Ca*R2))*(Qh_2R*E_1I - Qh_2I*E_1R + Qh_1R*E_2I -...
```

$Qh_1I * E_2R$);

$dx2 = a21 * x(1) + a22 * x(2) + a23 * x(3) + b2 + 73.741741338509$;

$a31 = (q1_avg / (Cv * R1)) * E_0 + (2 * q1_1R * E_1R + 2 * q1_1I * E_1I) / (Cv * R1)$;

$a32 = (1 / (Cv * R3))$; $a33 = (-q1_avg / (Cv * R1) - 1 / (Cv * R3))$;

$b3 = (q1_avg / (Cv * R1)) * (2 * Qh_1R * E_1R + 2 * Qh_1I * E_1I + 2 * Qh_2R * E_2R \dots$

$+ 2 * Qh_2I * E_2I) + 2 * q1_1R * E_0 * Qh_1R / (Cv * R1) + \dots$

$2 * q1_1I * E_0 * Qh_1I / (Cv * R1) - (2 * q1_1R * Vv_1R \dots$

$+ 2 * q1_1I * Vv_1I) / (Cv * R1) + \dots$

$2 * (q1_1R / (Cv * R1)) * (Qh_2R * E_1R + Qh_2I * E_1I + Qh_1R * E_2R + Qh_1I * E_2I) \dots$

$+ 2 * (q1_1I / (Cv * R1)) * (Qh_2R * E_1I - Qh_2I * E_1R + Qh_1R * E_2I \dots$

$- Qh_1I * E_2R)$;

$dx3 = a31 * x(1) + a32 * x(2) + a33 * x(3) + b3 + 0.483295537842$;

$dx = [dx1; dx2; dx3]$;

Bibliography

- [1] Y. Donchin, D. Gopher, M. Olin, Y. Badihi, M. Biesky, C. L. Sprung, R. Pizov, and S. Cotev, “A look into the nature and causes of human errors in the intensive care unit,” *Critical Care Medicine*, vol. 23, pp. 294–300, 1995.
- [2] S. Lawless, “Crying wolf: false alarms in a pediatric ICU,” *Critical Care Medicine*, vol. 22, pp. 981–984, 1994.
- [3] P. L. Marino, *The ICU book*. Lippincott, Williams and Wilkins, 2nd ed., 1998.
- [4] R. G. Mark, G. C. Verghese, and P. Szolovits, “NIH/NIBIB Bioengineering Research Partnership Proposal.” <http://mimic.mit.edu>, September 2003.
- [5] G. B. Moody and R. G. Mark, “A database to support development and evaluation of intelligent intensive care monitoring,” in *Computers in Cardiology*, vol. 23, pp. 657–660, 1996.
- [6] “Projected supply, demand, and shortages of registered nurses: 2000-2020,” U.S. Department of Health and Human Services, July 2002.
- [7] M. Saeed, C. Lieu, G. Raber, and R. Mark, “MIMIC II: a massive temporal ICU patient database to support research in intelligent patient monitoring,” in *Computers in Cardiology*, vol. 29, 2002.
- [8] Z. Samar, *Cardiovascular parameter estimation using a computational model*. S.M. Thesis, Electrical Engineering and Computer Science, MIT, June 2005.
- [9] H. Swan, W. Ganz, J. Forrester, H. Marcus, G. Diamond, and D. Chonette, “Catheterization of the heart in man with the use of a flow-directed balloon-tipped catheter,” *New England Journal of Medicine*, vol. 283, pp. 447–451, 1970.
- [10] C. Renjifo, *Exploration, processing and visualization of physiological signals from the ICU*. M.Eng. Thesis, Electrical Engineering and Computer Science, MIT, June 2005.
- [11] J. Blachowicz, J. Wojcicki, P. Ladyzynski, K. Slomka, and G. Opolski, “A novel approach to the alarm system for monitoring of the patient state in cardiac intensive care unit,” in *Proceedings of the IFAC Modelling and Control in Biomedical Systems Conference*, 2000.
- [12] B. M. Dawant, S. Uckun, E. J. Manders, and D. P. Lindstrom, “The SIMON project: model-based signal acquisition, analysis, and interpretation in intelligent patient monitoring,” *IEEE Engineering in Medicine and Biology Magazine*, pp. 82–91, December 1993.
- [13] J. Roberts, *Bayesian networks for cardiovascular modeling*. SM Thesis, Electrical Engineering and Computer Science, MIT, June 2006.
- [14] J. M. Roberts, T. A. Parlikar, T. Heldt, and G. C. Verghese, “Bayesian networks for cardiovascular modeling,” *Proceedings of the 28th Annual IEEE Engineering in Medicine and Biology Conference*, pp. 205–209, September 2006.

BIBLIOGRAPHY

- [15] T. A. Parlikar and G. C. Verghese, “A simple cycle-averaged model of cardiovascular dynamics,” in *Proceedings of the 27th Annual Conference of the IEEE Engineering in Medicine and Biology Society*, pp. 5490–5494, September 2005.
- [16] T. A. Parlikar, T. Heldt, and G. C. Verghese, “Cycle-averaged models of cardiovascular dynamics,” *IEEE Transactions on Circuits and Systems I: Fundamental Theory and Applications*, vol. 53, no. 11, pp. 2459–2468, 2006.
- [17] S. Francis, *Continuous estimation of cardiac output and arterial resistance from arterial blood pressure waveforms using a third-order Windkessel model*. M.Eng. Thesis, Electrical Engineering and Computer Science, MIT, June 2007.
- [18] S. X. Li, *Probabilistic network models for cardiovascular monitoring*. M.Eng. Thesis, Electrical Engineering and Computer Science, MIT, June 2007.
- [19] Z. Lu and R. Mukkamala, “Continuous cardiac output and left atrial pressure monitoring by pulmonary artery pressure waveform analysis,” *Proceedings of the 28th Annual IEEE Engineering in Medicine and Biology Conference*, pp. 214–217, September 2006.
- [20] L. H. Opie, *Drugs for the heart*. W. B. Saunders and Company, 2nd (Expanded) ed., 1987.
- [21] L. S. Costanzo, *Physiology*. W.B. Saunders, 2nd ed., 2002.
- [22] R. M. Berne, M. N. Levy, B. M. Koeppen, and B. A. Stanton, *Physiology*. Mosby, 5th ed., 2004.
- [23] R. M. Berne and M. N. Levy, *Cardiovascular physiology*. Mosby Physiology Monograph Series, 8th ed., 2001.
- [24] L. W. J. Bogert and J. van Lieshout, “Non-invasive pulsatile arterial pressure and stroke volume changes from the human finger,” *Experimental Physiology*, vol. 90, no. 4, pp. 437–446, 2005.
- [25] J. Keener and J. Sneyd, *Mathematical physiology*. Springer-Verlag, 1998.
- [26] J. Levick, *An introduction to cardiovascular physiology*. Arnold, 3rd ed., 2000.
- [27] R. Mukkamala, J. Kuiper, J. Sala-Mercardo, R. Hammond, J.-K. Kim, L. W. Stephenson, and D. S. O’Leary, “Continuous cardiac output and left atrial pressure monitoring by pulmonary artery pressure waveform analysis,” *Proceedings of the 28th Annual IEEE Engineering in Medicine and Biology Conference*, pp. 620–623, September 2006.
- [28] J. P. Curtis, S. Sokol, Y. Wang, S. Rathore, D. T. Ko, F. Jadbabaie, E. L. Portnay, S. J. Marshalko, M. J. Radford, and H. M. Krumholz, “The association of left ventricular ejection fraction, mortality, and cause of death in stable outpatients with heart failure,” *Journal of the American College of Cardiology*, vol. 42, no. 4, pp. 736–742, 2003.
- [29] K. Sagawa, H. Suga, and K. Nakayama, “Instantaneous pressure-volume ratio of the left ventricle versus instantaneous force-length relation of papillary muscle,” in: *Cardiovascular system dynamics*. The MIT Press, 1978.
- [30] A. C. Guyton, C. Jones, and T. G. Coleman, *Circulatory physiology: cardiac output and its regulation*. W.B. Saunders Company, 2nd ed., 1973.
- [31] K. Schmidt-Nelson, *Animal physiology*. Cambridge University Press, 5th ed., 1998.
- [32] D. Gross, *Animal models in cardiovascular research*. Kluwer Academic Publishers, 1994.

- [33] R. Mukkamala, *A forward model-based analysis of cardiovascular system identification methods*. Ph.D. Thesis, Electrical Engineering and Computer Science, MIT, June 2000.
- [34] T. Heldt, *Modeling of the cardiovascular response to orthostatic stress*. Ph.D. Thesis, Division of Health Sciences and Technology, MIT, September 2004.
- [35] O. Frank, “Die Grundform des arteriellen Pulses. Erste Abhandlung. Mathematische Analyse,” *Z. f. Biol.*, vol. 37, pp. 485–526, 1899.
- [36] K. Sagawa, R. K. Lie, and J. Schaefer, “Translation of Otto Frank’s paper ‘Die Grundform des arteriellen Pulses,’” *Journal of Molecular and Cellular Cardiology*, vol. 22, pp. 253–277, 1990.
- [37] O. Frank, “Schätzung des Schlagvolumens des menschlichen Herzens auf Grund der Wellen- und Windkesseltheorie,” *Z. f. Biol.*, vol. 90, pp. 405–409, 1930.
- [38] A. Noordergraaf, “Development of an analog computer for the human systemic circulatory system,” in *Circulatory Analog Computers* North-Holland Publishing Company, 1963.
- [39] B. W. Smith, J. G. Chase, G. M. Shaw, and R. I. Nokes, “Experimentally verified minimal cardiovascular system model for rapid diagnostic assistance,” *Control Engineering Practice*, vol. 13, no. 9, 2005.
- [40] B. W. Smith, J. G. Chase, R. I. Nokes, G. M. Shaw, and G. Wake, “Minimal haemodynamic system model including ventricular interaction and valve dynamics,” *Medical Engineering and Physics*, vol. 26, pp. 131–139, 2004.
- [41] T. Heldt, J. L. Chang, J. J. S. Chen, G. C. Verghese, and R. G. Mark, “Cycle-averaged dynamics of a periodically-driven, closed loop circulation model,” *Control Engineering Practice*, vol. 13, no. 9, pp. 1163–1171, 2005.
- [42] J. J. S. Chen, T. Heldt, G. C. Verghese, and R. G. Mark, “Analytical solution to simplified circulatory model using piece-wise linear elastance function,” in *Computers in Cardiology*, vol. 30, pp. 259–262, 2003.
- [43] A. C. Guyton and T. G. Coleman, “Quantitative analysis of the pathophysiology of hypertension,” *Circulation Physiology*, vol. 24, no. 5 (Suppl. I): I-1, pp. 1–19, 1969.
- [44] A. C. Guyton, T. G. Coleman, A. W. Cowley, J.-F. Liard, R. A. Norman, and R. D. Manning, “Systems analysis of arterial pressure regulation and hypertension,” *Annals of Biomedical Engineering*, vol. 1, no. 4, pp. 254–281, 1972.
- [45] A. C. Guyton, T. G. Coleman, and H. J. Granger, “Circulation: overall regulation,” *Annual Review of Physiology*, vol. 34, pp. 13–46, 1972.
- [46] J. G. Defares, J. J. Osborn, and H. H. Hara, “Theoretical synthesis of the cardiovascular system. Study I: the controlled system,” *Acta Physiol. Pharmacol. Neerl.*, vol. 12, pp. 189–265, 1963.
- [47] M. F. Snyder, V. C. Rideout, and R. J. Hillestad, “Computer modeling of the human systemic arterial tree,” *Journal of Biomechanics*, vol. 1, pp. 341–353, 1968.
- [48] M. F. Snyder and V. C. Rideout, “Computer simulation studies of the venous circulation,” *IEEE Transactions on Biomedical Engineering*, vol. BME-16, October 1969.
- [49] T. L. Davis and R. G. Mark, “Teaching physiology through interactive simulation of hemodynamics,” in *Computers in Cardiology*, pp. 649–652, September 1990.

BIBLIOGRAPHY

- [50] R. Beeukes and N. Braslow, "The cardiovascular analog trainer: a real time physiological simulator," *Physiol. Teacher*, vol. 3, no. 3, pp. 4–7, 1974.
- [51] N. A. Peterson and K. Campbell, "Teaching cardiovascular intergrations with computer laboratories," *The Physiologist*, vol. 28, no. 3, pp. 159–169, 1985.
- [52] M. Ursino, "A mathematical model of carotid baroregulation in pulsating conditions," *IEEE Transactions on Biomedical Engineering*, vol. 46, no. 4, pp. 382–392, 1999.
- [53] T. G. Coleman, "Mathematical analysis of cardiovascular function," *IEEE Transactions on Biomedical Engineering*, vol. BME-32, pp. 289–294, April 1985.
- [54] W. Welkowitz, Q. Cui, Y. Qi, and J. B. Kostis, "Noninvasive estimation of cardiac output," *IEEE Transactions on Biomedical Engineering*, vol. 38, pp. 1100–1105, November 1991.
- [55] J. E. Tsitlik, H. R. Halperin, A. S. Popel., A. A. Shoukas, F. C. P. Yin, and N. Westerhof, "Modeling the circulation with three-terminal electrical networks containing special nonlinear capacitors," *Annals of Biomedical Engineering*, vol. 20, no. 595-616, 1992.
- [56] T. Heldt, E. B. Shim, R. D. Kamm, and R. G. Mark, "Computational modeling of the cardiovascular response to orthostatic stress," *Journal of Applied Physiology*, vol. 92, pp. 1239–1254, March 2002.
- [57] R. Mukkamala, A. Reisner, H. Hojman, R. Mark, and R. Cohen, "Continuous cardiac output monitoring by peripheral blood pressure waveform analysis," *IEEE Transactions on Biomedical Engineering*, vol. 53, no. 3, pp. 459–467, 2006.
- [58] Z. Lu and R. Mukkamala, "Continuous cardiac output monitoring in humans by invasive and noninvasive peripheral blood pressure waveform analysis," *Journal of Applied Physiology*, vol. 101, no. 2, pp. 598–608, 2006.
- [59] J. W. Clark, R. S. Ling, R. Srinivasan, J. S. Cole, and R. C. Pruett, "A two-stage identification scheme for the determination of the parameters of a model of left heart and systemic circulation," *IEEE Transactions on Biomedical Engineering*, vol. BME-27, pp. 20–29, January 1980.
- [60] M. Guarini, J. Urzua, A. Cipriano, and W. Gonzalez, "Estimation of cardiac function from computer analysis of the arterial pressure waveform," *IEEE Transactions on Biomedical Engineering*, vol. 45, pp. 1420–1428, December 1998.
- [61] R. W. deBoer, J. M. Karemaker, and J. Strackee, "Hemodynamic fluctuations and baroreflex sensitivity in humans: a beat-to-beat model," *American Journal of Physiology Heart and Circulation Physiology*, vol. 253, no. 3, pp. H680–H689, 1987.
- [62] O. Frank, "Die Theorie der Pulswelle," *Z. Biol.*, vol. 85, pp. 91–130, 1927.
- [63] N. Stergiopoulos, B. E. Westerhof, and N. Westerhof, "Total arterial inertance as the fourth element of the Windkessel model," *American Journal of Physiology*, pp. H81–H88, 1999.
- [64] G. Liljestr and and E. Zander, "Vergleichende Bestimmung des Minutenvolumens des Herzens beim Menschen mittels der Sickoxydulmethode und durch Blutdruckmessung," *Z. Exp. Med.*, vol. 59, pp. 105–122, 1928.
- [65] K. H. Wesseling, J. R. C. Jansen, J. J. Settels, and J. J. Schreuder, "Computation of aortic flow from pressure in humans using a nonlinear, three-element model," *Journal of Applied Physiology*, vol. 74, pp. 2566–2573, 1993.

- [66] D. McDonald, *Blood flow in arteries*. The Williams and Wilkins Company, 2nd ed., 1974.
- [67] A. Noordergraaf, *Circulatory system dynamics*. Academic Press, 1978.
- [68] E. T. Ozawa, *A numerical model of the cardiovascular system for clinical assessment of the hemodynamic state*. Ph.D. thesis, Division of Health Sciences and Technology, MIT, September 1996.
- [69] P. Hallock and I. C. Benson, “Studies on the elastic properties of human isolated aorta,” *J. Clin. Invest.*, vol. 16, pp. 595–602, 1937.
- [70] D. Seals, “Habitual exercise and the age-associated decline in large artery compliance,” *Exerc. Sport Sci. Rev.*, vol. 31, no. 2, pp. 68–72, 2003.
- [71] J. van Lieshout and K. H. Wesseling, “Continuous cardiac output monitoring by pulse contour analysis?,” *British Journal of Anaesthesia*, vol. 86, no. 4, pp. 467–468, 2001.
- [72] M. Bourgeois, B. Gilbert, D. Donald, and E. Wood, “Characteristics of aortic diastolic pressure decay with application to continuous monitoring of changes in peripheral vascular resistance,” *Circulation Research*, vol. 35, no. 1, pp. 56–66, 1974.
- [73] M. Bourgeois, B. Gilbert, G. Bernuth, and E. Wood, “Continuous determination of beat-to-beat stroke volume from aortic pressure pulses in the dog,” *Circulation Research*, vol. 39, no. 1, pp. 15–24, 1976.
- [74] D. Chemla, J.-L. Hebert, C. Coirault, K. Zamani, I. Suard, P. Colin, and Y. Lecarpentier, “Total arterial compliance estimated by stroke volume-to-aortic pressure pulse ratio in humans,” *Journal of Applied Physiology Heart and Circulation Physiology*, pp. H500–H505, 1998.
- [75] Z. Liu, K. Brin, and F. Yin, “Estimation of total arterial compliance: an improved method and evaluation of current methods,” *Journal of Applied Physiology Heart and Circulation Physiology*, pp. H588–H600, 1986.
- [76] R. Burattini, R. Fogliardi, and K. Campbell, “Lumped model of terminal aortic impedance in the dog,” *Annals of Biomedical Engineering*, vol. 22, pp. 381–391, 1994.
- [77] G. Toorop, N. Westerhof, and G. Elzinga, “Beat-to-beat estimation of peripheral resistance and arterial compliance during pressure transients,” *Journal of Applied Physiology Heart and Circulation Physiology*, pp. H1275–H1283, 1987.
- [78] N. Stergiopoulos, J.-J. Meister, and N. Westerhof, “Simple and accurate way for estimating total and segmental arterial compliance: the pulse pressure method,” *Annals of Biomedical Engineering*, vol. 22, pp. 392–397, 1994.
- [79] N. Stergiopoulos, J.-J. Meister, and N. Westerhof, “Evaluation of methods for estimation of total arterial compliance,” *Journal of Applied Physiology Heart and Circulation Physiology*, pp. H1540–H1548, 1995.
- [80] W. Laskey, H. Parker, V. Ferrari, W. Kussmaul, and A. Noordergraaf, “Estimation of total systemic arterial compliance in humans,” *Journal of Applied Physiology*, vol. 69, pp. 112–119, 1990.
- [81] C. Quick, D. Berger, and A. Noordergraaf, “Apparent arterial compliance,” *Journal of Applied Physiology Heart and Circulation Physiology*, vol. 274, pp. 1393–1403, 1998.

BIBLIOGRAPHY

- [82] R. Mukkamala, K. Toska, and R. J. Cohen, "Noninvasive identification of the total peripheral resistance baroreflex," *American Journal of Physiology Heart and Circulation Physiology*, vol. 284, pp. H947–H959, March 2003.
- [83] R. Mukkamala and R. J. Cohen, "A forward model-based validation of cardiovascular system identification," *American Journal of Physiology Heart and Circulation Physiology*, vol. 281, pp. H2714–H2730, December 2001.
- [84] G. Rosenberg, W. M. Phillips, D. L. Landis, and W. S. Pierce, "Design and evaluation of the Pennsylvania State University mock circulation system," *ASAIO Journal*, vol. 4, pp. 41–49, 1981.
- [85] H. Suga, "Time course of left ventricular pressure-volume relationship under various end-diastolic volume," *Japan Heart Journal*, vol. 10, pp. 509–515, 1969.
- [86] H. Senzaki, C. H. Chen, and D. A. Kass, "Single-beat estimation of end-systolic pressure-volume relation in humans," *Circulation*, vol. 94, pp. 2497–2506, 1994.
- [87] H. Suga, "Theoretical analysis of a left ventricular pumping model based on the systolic time-varying pressure-volume ratio," *IEEE Transactions on Biomedical Engineering*, vol. BME-18, pp. 47–55, January 1971.
- [88] H. Suga, "Left ventricular time-varying pressure-volume ratio in systole as an index of myocardial inotropism," *Japan Heart Journal*, vol. 12, pp. 153–160, 1971.
- [89] F. S. Grodins, "Integrative cardiovascular physiology: a mathematical synthesis of cardiac and blood vessel hemodynamics," *The Quarterly Review of Biology*, vol. 34, pp. 93–116, June 1959.
- [90] F. Kappel and R. O. Peer, "Fundamental regulation processes in the cardiovascular system," *Journal of Mathematical Biology*, vol. 31, pp. 611–631, 1993.
- [91] D. Boyers, J. Cuthbertson, and J. Luetscher, "Simulation of the human cardiovascular system: A model with normal response to change in posture, blood loss, transfusion, and autonomic blockade," *Simulation*, vol. 18, pp. 197–205, 1972.
- [92] H. Raymundo, A. M. Scher, D. S. O'Leary, and P. D. Sampson, "Cardiovascular control by arterial and cardiopulmonary baroreceptors in awake dogs with atrioventricular block," *American Journal of Physiology*, vol. 257, no. 26, pp. H2048–H2058, 1989.
- [93] J. E. A. James and M. D. B. Daly, "Comparison of the reflex vasomotor responses to separate and combined stimulation of the carotid sinus and aortic arch baroreceptors by pulsatile and non-pulsatile pressures in the dog," *American Journal of Physiology*, vol. 209, no. 2, pp. 257–293, 1970.
- [94] H. Unbehauen and G. Rao, *Identification of continuous systems*. North-Holland, 1987.
- [95] M. Shinbrot, "On the analysis of linear and nonlinear systems," *Transactions of the ASME*, vol. 79, pp. 547–552, 1957.
- [96] G. C. Verghese, *Dynamic modeling and control in power electronics*, pp. 1413–1424. The Control Handbook, Boca Raton: IEEE Press, 1996.
- [97] S. R. Sanders, J. M. Noworolski, X. Z. Liu, and G. C. Verghese, "Generalized averaging method for power conversion circuits," *IEEE Transactions on Power Electronics*, vol. 6, pp. 251–259, April 1991.
- [98] V. A. Caliskan, G. C. Verghese, and A. M. Stankovic, "Multi-frequency averaging of dc/dc converters," *IEEE Transactions on Power Electronics*, vol. 14, pp. 124–133, January 1999.

- [99] J. G. Kassakian, M. F. Schlecht, and G. C. Verghese, *Principles of Power Electronics*. Addison-Wesley, 1991.
- [100] S. R. Sanders, “On limit cycles and the describing function method in periodically switched circuits,” *IEEE Transactions on Circuits and Systems-I: Fundamental Theory and Applications*, vol. 40, pp. 564–572, September 1993.
- [101] G. Foote, S. Schabel, and M. Hodges, “Pulmonary complications of the flow-directed balloon-tipped catheter,” *New England Journal of Medicine*, vol. 290, pp. 927–931, 1974.
- [102] M. Matthay and K. Chatterjee, “Bedside catheterization of the pulmonary artery: risks compared with benefits,” *Annals of Internal Medicine*, vol. 109, pp. 826–834, 1988.
- [103] J. Bender, M. Smith-Meek, and C. E. Jones, “Routine pulmonary artery catheterization does not reduce morbidity and mortality of elective vascular surgery: results of a prospective, randomized trial,” *Annals of Surgery*, vol. 226, pp. 229–237, 1997.
- [104] G. R. Bernard, G. Sopko, F. Cerra, R. Demling, H. Edmunds, S. Kaplan, L. Kessler, H. Masur, P. Parsons, D. Shure, C. Webb, H. Weidemann, G. Weinmann, and D. Williams, “Pulmonary artery catheterization and clinical outcomes,” *Journal of the American Medical Association*, vol. 283, pp. 2568–2572, 2000.
- [105] H. R. Warner, H. J. C. Swan, D. C. Connolly, R. G. Tompkins, and E. H. Wood, “Quantitation of beat-to-beat changes in stroke volume from the aortic pulse contour in man,” *Journal of Applied Physiology*, vol. 5, p. 495, 1953.
- [106] J. Herd, N. Leclair, and W. Simon, “Arterial pressure pulse contours during hemorrhage in anesthetized dogs,” *Journal of Applied Physiology*, vol. 21, no. 6, pp. 1864–1868, 1966.
- [107] R. M. Cundick and R. M. Gardner, “Clinical comparison of pressure-pulse and indicator-dilution cardiac output determination,” *Circulation*, vol. 62, no. 2, pp. 371–376, 1980.
- [108] J. van Lieshout and J. Jansen, “Continuous cardiac output monitoring by blood pressure analysis,” *Journal of Applied Physiology*, vol. 102, p. 826, February 2007.
- [109] T. Parlikar, G. V. Ranade, T. Heldt, and G. C. Verghese, “Model-based method for continuous determination of cardiac output and peripheral vascular resistance.” MIT Technology Licensing Office case number 12560. Provisional patent filed on May 16, 2007.
- [110] G. Langewouters, K. Wesseling, and W. Goedhard, “The static elastic properties of 45 human thoracic and 20 abdominal aortas in vitro and the parameters of a new model,” *Journal of Biomechanics*, vol. 17, pp. 425–435, 1984.
- [111] Y. Tardy, J.-J. Meister, F. Perret, H. Brunner, and M. Arditi, “Noninvasive estimation of the mechanical properties of peripheral arteries from ultrasonic and photoplethymographic measurements,” *Clinical Physiology and Physiological Measurements*, vol. 12, pp. 39–54, 1991.
- [112] O. Godje, P. Lamm, C. Schmitz, M. Theil, and B. Reichart, “Continuous, less invasive, hemodynamic monitoring in intensive care after cardiac surgery,” *Thoracic Cardiovascular Surgery*, vol. 46, pp. 242–249, 1998.
- [113] J. X. Sun, A. T. Reisner, M. Saeed, and R. G. Mark, “Estimating cardiac output from arterial blood pressure waveforms: a critical evaluation using the MIMIC II database,” in *Computers in Cardiology*, vol. 32, pp. 295–298, 2005.

BIBLIOGRAPHY

- [114] D. Altman and J. Bland, "Measurement in medicine: the analysis of method comparison studies," *The Statistician*, vol. 32, pp. 307–317, 1983.
- [115] J. Bland and D. Altman, "Statistical methods for assessing agreement between two methods of clinical measurement," *Lancet*, vol. I, pp. 307–310, 1986.
- [116] W. Zong, T. Heldt, G. Moody, and R. Mark, "An open-source algorithm to detect onset of arterial blood pressure pulses," *Computers in Cardiology*, vol. 30, pp. 259–262, 2003.
- [117] W. Zong, G. Moody, and D. Jiang, "A robust open-source algorithm to detect onset and duration of QRS complexes," *Computers in Cardiology*, vol. 30, pp. 737–740, 2003.
- [118] R. Mukkamala and A. Reisner, "Reply to van Lieshout and Jansen," *Journal of Applied Physiology*, vol. 102, p. 827, February 2007.
- [119] T. Heldt, "Continuous blood pressure-derived cardiac output monitoring – should we be thinking long-term?," *J. Appl. Physiol.*, vol. 101, no. 2, pp. 373–374, 2006.
- [120] G. Swamy, B. Olivier, J. Kuiper, and R. Mukkamala, "Continuous ejection fraction estimation by model-based analysis of an aortic pressure waveform: comparison to echocardiography," *29th Annual Conference of the IEEE Engineering in Medicine and Biology Conference*, August 2007 (in press).
- [121] W. Zong, G. B. Moody, and R. G. Mark, "Reduction of false blood pressure alarms by use of electrocardiogram blood pressure relationships," *Computers in Cardiology*, vol. 26, pp. 305–308, 1999.
- [122] W. Zong, G. B. Moody, and R. G. Mark, "Reduction of false arterial blood pressure alarms using signal quality assessment and relationships between the electrocardiogram and arterial blood pressure," *Medical and Biological Engineering and Computing*, vol. 42, September 2004.
- [123] T. A. Parlikar, T. Heldt, R. Mukkamala, and G. C. Verghese, "Model-based method for continuous determination of cardiac ejection fraction and ventricular end-diastolic volume." MIT Technology Licensing Office case number 12677. Provisional patent filed on May 16, 2007.
- [124] G. Cintron, G. Johnson, G. Francis, F. Cobb, and J. Cohn, "Prognosis significance of serial changes in left ventricular ejection fraction in patients with congestive heart failure," *Circulation*, vol. 87, no. 6, pp. 17–23, 1993.
- [125] B. Sridhara, S. Bhattacharya, X. Liu, P. Broadhurst, and A. Lahiri, "Rate of change of left ventricular ejection fraction during exercise is superior to the peak ejection fraction for predicting functionally significant coronary artery disease," *British Heart Journal*, vol. 70, pp. 507–512, 1993.
- [126] X. Bosch and P. Theroux, "Left ventricular ejection fraction to predict early mortality in patients with non-ST segment elevation acute coronary syndromes," *American Heart Journal*, vol. 150, pp. 215–220, 2005.
- [127] L. W. Stevenson and J. H. T. *et al.*, "Importance of hemodynamic response to therapy in predicting survival with ejection fraction < 20% secondary to ischemic or nonischemic dilated cardiomyopathy," *American Journal of Cardiology*, vol. 66, pp. 1348–1354, 1990.
- [128] B. Massie, T. Ports, and K. C. *et al.*, "Long-term vasodilator therapy for heart failure: clinical response and its relationship to hemodynamic measurements," *Circulation*, vol. 63, pp. 269–278, 1981.

- [129] A. E. Steimle, L. W. Stevenson, C. Chelimsky-Fallick, G. C. Fonarow, M. A. Hamilton, J. D. Moriguchi, A. Kartashav, and J. H. Tillisch, “Sustained hemodynamic efficacy of therapy tailored to reduce filling pressures in survivors with advanced heart failure,” *Circulation*, vol. 96, pp. 1165–1172, 1997.
- [130] D. Weilenmann, H. Rickli, F. Follath, W. Kiowski, and H. Brunner-La Rocca, “Noninvasive evaluation of pulmonary capillary wedge pressure by BP response to the valsalva maneuver,” *Chest*, vol. 122, pp. 140–145, 2002.
- [131] C. Corsi, R. M. Lang, F. Veronesi, L. Weinert, E. G. Caiani, P. MacEneaney, C. Lamberti, and V. Mor-Avi, “Volumetric quantification of global and regional left ventricular function from real-time three-dimensional echocardiographic images,” *Circulation*, vol. 112, pp. 1161–1170, 2005.
- [132] A. S. Gopal, M. J. Schnellbaecher, Z. Shen, L. M. Boxt, J. Katz, and D. L. King, “Freehand three-dimensional echocardiography for determination of left ventricular volume and mass in patients with abnormal ventricles: comparison with magnetic resonance imaging,” *Journal of the American Society of Echocardiography*, vol. 10, no. 8, pp. 853–861, 1997.
- [133] J. Rumberger, T. Behrenbeck, M. Bell, J. Breen, D. L. Johnston, D. R. Holmes, and M. Enriquez-Sarano, “Determination of left ventricular ejection fraction: a comparison of available imaging methods,” *Mayo Clinic Proceedings*, vol. 72, pp. 860–870, 1997.
- [134] G. V. Ranade, *Respiratory modulation of the arterial blood pressure waveform*. 6.UAP Report, Electrical Engineering and Computer Science, MIT, June 2007.
- [135] J. A. Richards, *Analysis of periodically time-varying systems*. Springer-Verlag, 1983.
- [136] I. W. Sandberg, “A stability criterion for linear networks containing time-varying capacitors,” *IEEE Transactions on Circuit Theory*, pp. 1–11, March 1965.